Quarterdiurnal Tide in the Middle Atmosphere

Von der Fakultät für Physik und Geowissenschaften
der Universität Leipzig
genehmigte
DISSERTATION
zur Erlangung des akademischen Grades

Doctor rerum naturalium

Dr. rer. nat.,

vorgelegt

von Master of Science, Christoph Geißler

geboren am 09.01.1991 in Halle (Saale)

Gutachter:
Prof. Dr. Christoph Jacobi
Prof. Dr. Erdal Yiğit

Tag der Verleihung: 22.03.2021

Bibliographische Beschreibung

Geißler, Christoph
Quarterdiurnal Tide in the Middle Atmosphere
Universität Leipzig, Dissertation
234 S., 100 Lit., 143 Abb., 2 Tab.

Kurzzusammenfassung

In der mittleren und oberen Atmosphäre spielen atmosphärische solare Gezeiten eine wichtige Rolle für die Dynamik und den Vertikaltransport von Energie und Impuls aus der Stratosphäre. Angeregt werden sie primär durch Absorption solarer Strahlung in der Troposphäre und Stratosphäre. Dabei entsprechen die Perioden der solaren Gezeiten den harmonischen Anteilen der täglichen Variation solarer Strahlung. Mittlerweile sind die täglichen, halbtägigen und dritteltägigen Gezeiten relativ gut erforscht, was bei der vierteltägigen Gezeit nicht der Fall ist. Die Informationen über diese Gezeit sind bislang rudimentär vor allem bzgl. einer globalen Klimatologie als auch der Details über möglichen Anregungsmechanismen und Wechselwirkungen. Dies ist darauf zurückzuführen, dass die Amplituden sehr klein sind und eine hohe zeitliche Auflösung für die Analyse benötigt wird. Die vierteltägige Gezeit wurde bislang von bodengebundenen Instrumenten und mit Fernerkundungsgsmethoden beobachtet, welche bislang lediglich einen räumlich und zeitlich begrenzten Überblick über die vierteltägige Gezeit boten. Da es nicht möglich ist die Beiträge der einzelnen Anregungen zu messen, muss sich numerischer Modelle als mächtiges Werkzeug bedient werden. Mit numerischen Modellen ist es möglich die verschiedenen Anregungsmechanismen zu separieren und ihre Beiträge für die vierteltägige Gezeit zu analysieren. Modellstudien lieferten bislang kein umfassendes Bild der QDT und berücksichtigten auch keine vierteltägige Schwerwellenanregungen. Diese Arbeit soll das Wissen zu diesem Thema erweitern, indem ein nichtlineares, mechanistisches, globales Zirkulationsmodell genutzt wird. Es wird eine umfassende numerische Studie durchgeführt, um die Wichtigkeit und das Zusammenspiel der drei vierteltägigen Anregungsmechanismen zu untersuchen, das sind die direkte solare Anregung, nichtlineare Wechselwirkung zwischen Gezeiten und Schwerewellen-Gezeiten-Wechselwirkungen. Erstmalig werden Anregungsterme, die über die Erwärmungsraten hinausgehen, selbst analysiert und quantifiziert und die Wechselwirkungen der vierteltägigen Gezeiten aus den unterschiedlichen Quellen untersucht. Darüber hinaus werden verschiedene Gezeitenmoden untersucht, um Interaktionen der vierteltätigen Gezeit aus den unterschiedlichen Anregungsmechanismen zu identifizieren. Darüber hinaus werden mit Hilfe der theoretischen Hough-Moden diejenigen Moden der vierteltägigen Gezeit abgeleitet, die in den Modellsimulationen maßgeblich für die meridionale Struktur verantwortlich sind. Diese aufwändige und umfassende Modellstudie analysiert die Anregungsmechanismen und deren Interaktion der vierteltägigen Gezeit. Die Arbeit hilft somit das Verständnis über die Wellenausbreitung der mittleren Atmosphäre auf ein neues Niveau zu heben.

Bibliographic Description

Geißler, Christoph
Quarterdiurnal Tide in the Middle Atmosphere
Universität Leipzig, Dissertation
234 pp., 100 bibl., 143 fig., 2 tab.

Abstract

In the middle and upper atmosphere atmospheric solar tides play an important role in the dynamics and vertical transport of energy and momentum from the stratosphere. They are primarily excited by absorption of solar radiation in the troposphere and stratosphere. The periods of the solar tides correspond to the harmonic components of the daily variation of solar radiation. Meanwhile, the diurnal, semidiurnal and terdiurnal tides have been relatively well studied, which is not the case with the quarterdiurnal tide. The knowledge about this tide is so far rudimentary, especially with regard to global climatology and details of possible excitation mechanisms and interactions. This is due to the fact that the amplitudes are very small and a high temporal resolution is required for the analysis. The quarterdiurnal tide has been observed by ground-based instruments and remote sensing methods, which until now have only provided a spatially and temporally limited overview of the quarterdiurnal tide. Since it is not possible to measure the contributions of the individual excitations, numerical models must be used as a powerful tool. With the numerical models it is possible to separate the different excitation mechanisms and to analyse their contributions for the quarterdiurnal tide. Model studies so far did not provide a comprehensive picture of QDT and did not consider QDT gravity wave excitation. This work is intended to extend the knowledge on this topic by using a nonlinear, mechanistic, global circulation model. A comprehensive numerical study will be carried out to investigate the importance and the interaction of the three quarterdiurnal excitation mechanisms, i.e. direct solar excitation, nonlinear tidal interactions and gravity

wave tidal interactions. For the first time, excitation terms beyond the heating rates will be analyzed and quantified and the interactions of the quarterdiurnal tides from different sources will be investigated. Furthermore, different tidal modes will be investigated to identify quarterdiurnal tide interactions from the different excitation mechanisms. Furthermore, the theoretical Hough modes are used to derive those quarterdiurnal modes that are significantly responsible for the meridional structure in the model simulations. This elaborate and comprehensive model study analyses the excitation mechanisms and their interaction of the quarter-day tide. The work thus helps to raise the understanding of wave propagation in the middle atmosphere to a new level.

Contents

1. Tides in the Middle Atmosphere - An Introduction

Middle Atmosphere

The middle atmosphere includes the area from the tropopause to the lower thermosphere. The temperature profile is characterized by three layers. Above the tropopause the stratosphere is located with an increase of temperature in the middle stratosphere due to the absorption of solar ultra violet (UV) radiation by ozone. The temperature reaches a maximum at 50 km altitude, the stratopause. In the overlying mesosphere, the temperature decreases again up to a altitude of 85 km, where the temperature minimum marks the mesopause. The lowest temperatures are reached in the summer polar mesopause, which is due to the adiabatic cooling during large-scale ascents of the air masses. In winter, a warming in the polar regions is detected by the sinking of the air masses. The thermosphere is located above the mesopause. The temperature in this region increases strongly by the UV absorption of molecular oxygen and to a much lesser degree by the Rayleigh friction. The temperature climatology from CIRA 86 is shown in Fig. 1.1a for January after Fleming et al. (1990). The characteristic profile of the zonal mean zonal wind of the middle atmosphere results mainly from the thermal wind equation. The climatology of the zonal wind is represented by CIRA 86 in Fig. 1.1b for January. The wind systems are opposite in the hemispheres in summer and winter. In the troposphere the westerly wind jets of the midlatitudes are shown. Above these, up to approximatly 90 km, the summer easterly wind jet is located in the stratosphere and mesosphere at up to $60\,ms^{-1}$. In the winter hemisphere the westerly wind jet reaches up to 100 km and $100\,ms^{-1}$. Again there is a wind reversal above 100 km with westerly wind in the summer hemisphere and easterly wind in the winter hemisphere up to 120 km altitude.

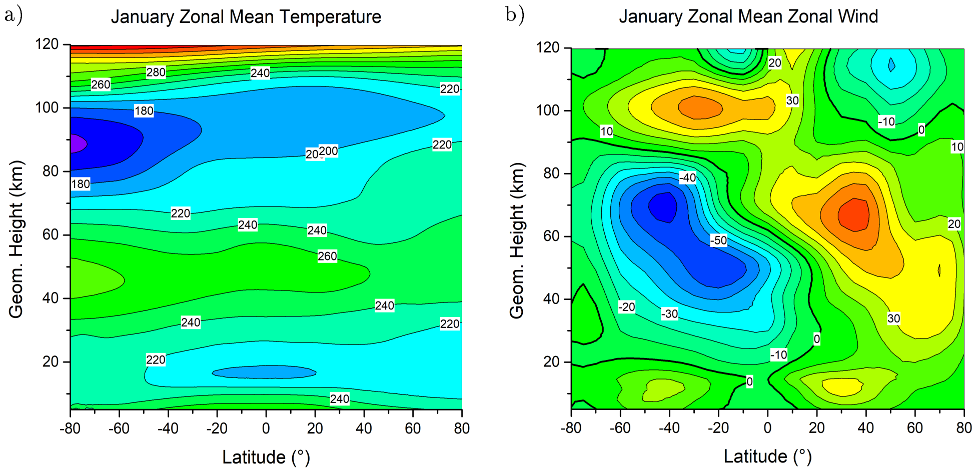

Figure 1.1.: CIRA 1986 climatology of zonal mean temperature (a) and zonal wind (b) in January after Fleming et al. (1990).

Waves in the Middle Atmosphere

The cause for this are atmospheric waves, which are ubiquitous in the middle atmosphere. The amplitudes of the atmospheric waves increase with decreasing density. In the upper atmosphere, there are damped by molecular diffusion. The atmospheric waves can be divided into different types depending on their scale. Small-scale waves, such as the internal gravity waves (GWs), are generated by the topography, instabilities in the atmospheric stratification and achieving the balance between buoyancy and gravity. Large scale waves, such as Planetary waves (PWs) and atmospheric tides exist as well. PWs, also called Rossby waves, are global normal modes that are caused by the beta-effect. The beta-effect describes the northerly gradient of potential vorticity.

Tides in the Middle Atmosphere

Atmospheric tides arise as a result of thermal heating of the atmosphere through the daily cycle of solar radiation. Another source of atmospheric tides is also the gravitational force of the moon, with the effect of the moon being much weaker on the atmosphere than on the ocean. The dynamics of the upper mesosphere and lower thermosphere (MLT) are strongly influenced through atmospheric waves, especially solar tides (Forbes, 1982a,b;

Forbes et al., 1994; Manson et al., 1989; Hagan et al., 1995; Jacobi et al., 1999; Pancheva et al., 2002; Yiğit and Medvedev, 2015). Tides are global-scale oscillations with periods of a solar day (24 h) and its harmonics (12 h, 8 h, 6 h), which mainly result from absorption of solar radiation by water vapor in the troposphere and ozone in the stratosphere (Chapman and Lindzen, 1970; Andrews et al., 1987; Xu et al., 2012). Because of the decrease of density and conservation of energy, the tidal amplitudes increase with height (Chapman and Lindzen, 1970; Andrews et al., 1987) and reach a maximum in the MLT region before they dissipate. Tides with larger periods like diurnal tides (DTs), semidiurnal tides (SDTs) and terdiurnal tides (TDTs) usually have larger amplitudes than short-period tides like the quarterdiurnal tide (QDT). This is why in the past the QDT attracted less attention than the relatively well understood DT, SDT and TDT. Atmospheric tides can be further classified into migrating and non-migrating tides. Migrating tides are sun-synchronous, which means that the harmonics in time and space are equal (Andrews et al., 1987; Hagan et al., 1995). Non-migrating tides are caused by topography and tropospheric heat sources, that are geographically fixed (Andrews et al., 1987) or nonlinear interactions between migrating tides (Teitelbaum and Vial, 1991), or between solar tides and planetary (Beard et al., 1999) or gravity waves (Miyahara and Forbes, 1991). The variation of solar heating over a day forms the basis of thermally-induced tides. The thermal heating has its maximum during noon and is zero during the night. This diurnal cycle can for instance be splitted with a Fourier Transformation into its harmonics with periods of 24 h, 12 h, 8 h, 6 h, etc. These are called diurnal tide (DT), semidiurnal tide (SDT) (Chapman and Lindzen, 1970; Manson et al., 1989), terdiurnal tide (TDT) (Revah, 1970; Cevolani and Bonelli, 1985) and quarterdiurnal tide (QDT). This produces waves that propagate through the atmosphere. Observations show that the SDT has the largest amplitudes above 100 km in the midlatitudes and equator regions (Chapman and Lindzen, 1970; Manson et al., 1989). This is also visible in the results of the temperature amplitudes of DT (Fig. 1.3a, c) and SDT (Fig. 1.3e, g) of the Global Scale Wave Model (GSWM; Hagan et al., 2001; GSWM, 2020). The DT amplitudes are smaller than the SDT amplitudes above 100 km but larger below. The wavelength of the tides can be derived directly from the phases. Phases are shown in Fig. 1.3b, d for DT and 1.3g, h for SDT in local time. The wavelength can be determined by determining the vertical distance between two altitudes with the same phase at one latitude. Recognize that the wavelengths are shorter for the DT (30 km) than for the SDT (100 km), which is why it is not possible to generate a DT in the ozone layer of the stratosphere by heating due to absorption of solar UV radiation. The reason for that is a destructive interference between the troposphere excited DT and the DT from the ozone layer in the stratosphere (Andrews et al., 1987). According to GSWM in the mesosphere and lower thermosphere (MLT) region, the DT reaches the maximum amplitudes in temperature during the equinoxes and above the equator with 30 K in the lower stratosphere at 100 km. In the zonal wind, the maxima of the amplitudes are in the low latitudes of both hemispheres reach $50\,ms^{-1}$. For the SDT the GSWM shows the maximum temperature amplitudes at 125 km with 50 K and for the zonal wind at 110 km with $60\,ms^{-1}$. A climatology of the TDT is shown in Lilienthal et al. (2018) and Lilienthal (2019) from model simulations. The greatest amplitudes in the MLT region for temperature and zonal wind occurred in April and October in the middle latitudes and equator between 110 km and 140 km. Temperature amplitudes reached over 12 K and those of the zonal wind up to $15\,ms^{-1}$.

At the beginning of the 19^{th} century, Pierre-Simon Laplace first mathematically described the horizontal structure of the tides. He focused on the equations describing the motion of a shallow ocean of constant depth on a rotating planet. Building on this, Hough and Darwin (1898) used these foundations to adapt them to a spherically stratified atmosphere on a rotating planet. Thus, all the particles in the system are ecited to carry out a uniform wave motion, the Eigenfrequencies of the Earth. These frequencies are not the Eigenvalues and Eigenfunctions for atmospheric tides but the equivalent depths, which are similar to the ocean depths of Laplace's description. Eigenvalues and Eigenfunctions solve the Laplace's tidal equation, as an eigenvalue problem. The tidal equation can be written as (e.g., Andrews et al. (1987)):

$$L\hat{\Phi} + \gamma\hat{\Phi} = 0 \tag{1.1}$$

$\hat{\Phi}$	Geopotential amplitude
$\gamma \equiv 4\Omega^2 a^2/gh$	Lamb's parameter

Where L is the second-order ordinary differential operator:

$$L = \frac{d}{d\mu}\left[\frac{(1-\mu^2)}{\sigma^2-\mu^2}\frac{d}{d\mu}\right] - \frac{1}{\sigma^2-\mu^2}\left[\frac{-s(\sigma^2+\mu^2)}{\sigma(\sigma^2-\mu^2)} + \frac{s^2}{1-\mu^2}\right]. \tag{1.2}$$

s	zonal nondimensionalized wavenumber
$\sigma = 2\pi/2\Omega P$	nondimensionalized frequency parameter in radians
P	wave period
$\Omega = 2\pi/86164\,s^{-1}$	rotation rate of the Earth
$\mu = sin\phi$	$-1 \leq \mu \leq 1$
ϕ	latitude

As boundary condition, $\hat{\Phi}$ must be bounded at the poles ($\mu \pm 1$). Under these conditions, the Laplace's tidal equation is a Eigenvalue problem for specified s and σ (Andrews et al., 1987). This problem can be solved numerically for Eigenvalues $\gamma_n^{(\sigma,s)}$ and Eigenfunctions $\Theta_n^{(\sigma,s)}$, which are called Hough-functions:

$$L\Theta_n^{(\sigma,s)} + \gamma\Theta_n^{(\sigma,s)} = 0. \tag{1.3}$$

n	integer values
Θ_n	Hough-functions

The Hough-function are the solution of the Laplace tidal equations. At the same time they describe the meridional structure of the Eigenmodes. The equation for the vertical structure is the following (Andrews et al., 1987):

$$\frac{d^2W}{dz^2} + \left(\frac{N^2}{gh} - \frac{1}{4H^2}\right)W = 0. \tag{1.4}$$

W	vertical function
$g = 9.81\,ms^{-1}$	acceleration due to gravity

h	equivalent depth
N	Brunt-Väisälä frequency
H	scale height
z	altitude

Lower boundary conditions are given:

$$\frac{dW}{dz} + \left(\frac{R\overline{T}(0)}{gh} - \frac{1}{2}\right)\frac{W}{H} = 0\bigg|_{z=0}. \tag{1.5}$$

$R = 287JK^{-1}kg^{-1}$	gas constant for dry air

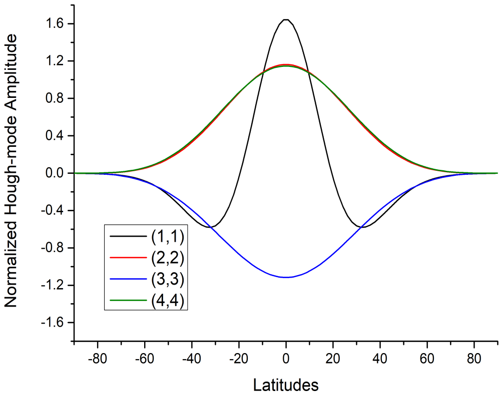

Figure 1.2.: Normalized Hough modes for the DT ($s = 1, n = 1, \sigma = \frac{1}{2}$) in black, SDT ($s = 2, n = 2, \sigma = 1$) in red, TDT ($s = 3, n = 3, \sigma = \frac{3}{2}$) in blue and QDT ($s = 4, n = 4, \sigma = 2$) in green with a latitudinal resolution of 2.5°.

Examples for the computed Hough functions using the Chebyshev method (Wang et al., 2016) are shown in Fig. 1.2 for the DT $s = 1,\ n = 1,\ \sigma = \frac{1}{2}$, SDT $s = 2,\ n = 2,\ \sigma = 1$, TDT $s = 3,\ n = 3,\ \sigma = \frac{3}{2}$ and QDT $s = 4,\ n = 4,\ \sigma = 2$. These are the first symmetric modes for the DT, SDT, TDT and QDT. For the DT (see Fig. 1.3a-d) the first symmetric Hough mode explains the global structure of the amplitudes with maxima at the equator and at low latitudes. The SDT amplitudes from Fig. 1.3e-h cab only partially be explained by the first Hough mode, since only the maximum at the equator is represented. Therefore, higher Hough modes of SDT will play an important role. The same applies to the TDT, where the first Hough mode also just explains the equatorial maximum, but not the maxima at the midlatitudes. The higher Hough modes with a finer meridional structure could play a larger role, if the meridional resolution of the model is higher and could lead to besser meridional structure of the QDT amplitudes.

For the QDT amplitudes a detailed view on a global climatology were necessary, as well as for the poorly understood forcing mechanisms of QDT. These shortcomings are the subject of this thesis.

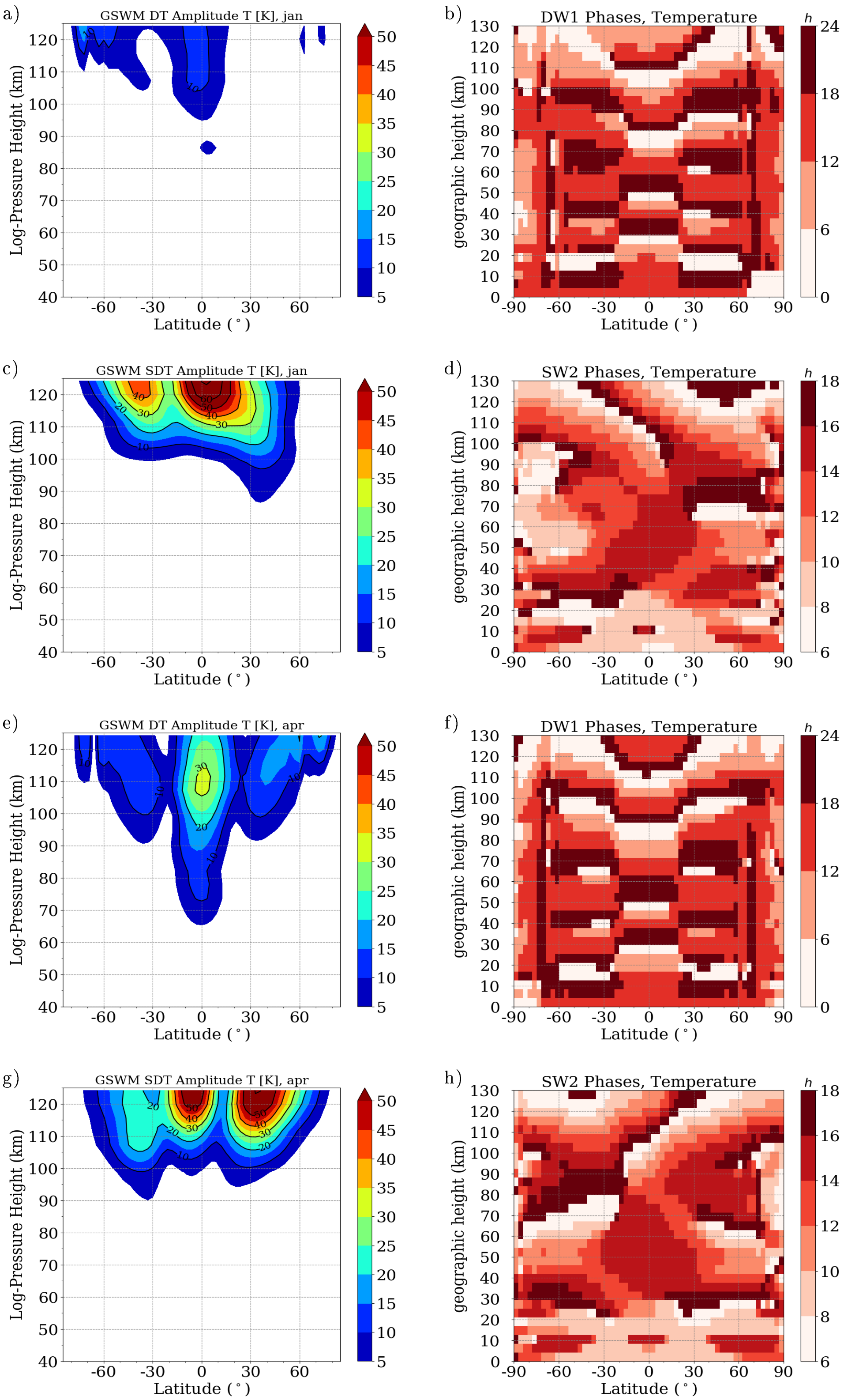

Figure 1.3.: GSWM migrating DT temperature amplitudes (a, e) and phases (b, f) and migrating SDT temperature amplitudes (c, g) and phases (d, h) for January (a - d) and April (e - f). Available at GSWM (2020).

2. Quarterdiurnal Solar Tides

For the first time, Revah (1970) was able to prove QDT in meteor radar (MR) measurements over Garchy, France. Since then, there have been just a few studies on the characteristics of QDT in the MLT region, mainly from radar and satellite measurements. Later, further measurement methods and model simulations followed. An overview of the measuring methods and the results obtained are given below.

2.1. Forcing of Quarterdiurnal Tides

2.1.1. Overview of the different Forcing Mechanisms

Andrews et al. (1987) defined atmospheric tides as global-scale oscillations, which can be divided into migrating and nonmigrating tides. Migrating tides, like DTs, SDTs, TDTs and QDTs, are mainly caused by the diurnal heating due to the absorption of solar ultraviolet radiation by atmospheric water vapor and ozone. Andrews et al. (1987) showed that the DT is mainly forced in the troposphere by the absorption of solar radiation of water vapor. A forcing by absorption of the solar radiation due to ozone also takes place. The SDT, on the other hand, is forced in the lower stratosphere due to the absorption of solar radiation through ozone. The DT amplitudes are smaller as seen in Fig. 1.3 due to destructive interference in the ozone heating region, so that the excitation from the absorption of solar radiation by water vapor in the troposphere is more effectively. Troposphere and stratosphere are also important for the solar forcing of the TDT, as Lilienthal et al. (2018) could show. Generally, as a typical characteristic of solar forced tides, it can be assumed that the phases are regular and wavelengths are relatively long (Fellous et al., 1975; Bernard et al., 1981).

Other excitation processes were release of latent heat in clouds and upward propagating temperature waves from the sensible heat flux of the Earth into the atmosphere (Cevolani and Bonelli, 1985).

Simulations of gravity wave - tide interactions were performed by Ribstein and Achatz

(2016), but they did not analyze higher harmonics than the SDT. Liu et al. (2006) as well showed an interaction between tides and gravity waves from a bicoherence spectrum analysis. This was mainly found for the upper height gates considered. Lilienthal and Jacobi (2019) found also interactions between DT, SDT and gravity waves that can force a TDT. Such analyses have not been carried out for the QDT so far.
Nonmigrating components of the tides or higher harmonics may also arise from nonlinear interactions. Miyahara and Forbes (1991) demonstrated such a mechanism for the TDT, but without consideration of the QDT. Liu et al. (2006) showed nonlinear interactions between atmospheric tides at midlatitude radar measurements. Lilienthal and Jacobi (2019) also showed that nonlinear interactions between DT, SDT occured. Nonlinear interactions between DTs, SDTs and TDTs can be an important forcing mechanism of QDTs, which is suggested by Smith et al. (2004).

2.1.2. Theoretical Consideration of the Nonlinear Forcing Mechanism

Nonlinear interactions describes an interaction between two primary waves, that produces secondary waves. These secondary waves are the sum or difference of the primary frequencies and wavenumbers (Beard et al., 1999). The model after Beard et al. (1999) describes nonlinear terms as quadratic system. A signal $y_1(t)$ has also to pass through a quadratic system $y_2(t) = y_1(t) + \alpha y_1^2(t)$ with α as a constant. The signal is defined as:

$$y_1(t) = A_1 cos(\omega_1 t + \psi_1) + A_2 cos(\omega_2 t + \psi_2) \tag{2.1}$$

Together with the quadratic system this results in:

$$\begin{aligned} y_2(t) = {} & A_1 cos(\omega_1 t + \psi_1) + A_2 cos(\omega_2 t + \psi_2) \\ & + 0.5\{A_1^2[1 + cos(2(\omega_1 t + \psi_1))] + A_2^2[1 + cos(2(\omega_2 t + \psi_2))] \\ & + 2A_1A_2[cos((\omega_1 + \omega_2)t + (\psi_1 + \psi_2))] + 2A_1A_2[cos((\omega_1 - \omega_2)t + (\psi_1 - \psi_2))]\} \end{aligned} \tag{2.2}$$

A_i .... amplitude of wave i

ω_i .... angular frequency of wave i

t .... time

ψ_i .... phase of wave i

Fig. 2.2 consists of three terms that describe the possible nonlinear interactions. The amplitudes from this equation should not be assumed to be exact, since these equations only describe the general mechanism of the interactions, but do not take into account the wave propagation. In the first term, waves are self-excited that have the same frequencies as the primary waves. The second term describes the doubling of the frequency of the secondary waves from the primary waves and in the third term secondary waves are excited, which have a frequency that results from the sum or the difference of the primary waves. This results in the following options to excite a QDT (Forbes et al., 2008):

$$\underbrace{cos(2\Omega t + 2\varphi)}_{\text{migrating SDT}} \cdot \underbrace{cos(2\Omega t + 2\varphi)}_{\text{migrating SDT}} \Rightarrow \underbrace{cos(4\Omega t + 4\varphi)}_{\text{migrating QDT}} + ... \tag{2.3}$$

$$\underbrace{cos(\Omega t + \varphi)}_{\text{migrating DT}} \cdot \underbrace{cos(3\Omega t + 3\varphi)}_{\text{migrating TDT}} \Rightarrow \underbrace{cos(4\Omega t + 4\varphi)}_{\text{migrating QDT}} + ... \tag{2.4}$$

φ .... longitude

Equations 2.3 and 2.4 give no information about the amplitudes. But it follows from there two equations that a QDT can only arise through a nonlinear interaction between DT and TDT or two SDTs, whereby the wavenumber results from the sum of the respective primary waves.

Such nonlinear interactions could be verified by Smith et al. (2004) in model simulations. Evidence in radar or satellite measurements is still pending. Smith et al. (2004) used the ROSE model to carry out simulations for the QDT between 80 km and 100 km. The model included solar and nonlinear forcing of tides and the gravity wave interaction with tides. DT and SDT are used for the lower boundary conditions by the Global Scale Wave Model (GSWM, 2020), the QDT is forced directly. Smith et al. (2004) showed the annual QDT amplitudes for the reference run, for the simulation without solar forcing of the QDT and for the run without boundary forcing of all tides except the QDT. All three runs show maxima in autumn and winter months and minima in spring and summer. It is interesting that for the simulation without nonlinear forcing, the amplitudes in all seasons are minimally larger than in the reference run. This leads to a decrease of the QDT amplitudes in the reference run from nonlinear interaction. This indicates interference between the differently excited QDT. But note, that the nonlinear interactions play an important role in the dynamics of the middle atmosphere and possible also for the appearance of the QDT.

In addition, the vertical wavelength of the nonlinear forced QDT can be calculated after Younger et al. (2002) and Deepa et al. (2006), which applied this for the TDT. For the QDT the calculation is analogous:

$$\lambda_6 = \frac{\lambda_{24}\lambda_8}{\lambda_{24} + \lambda_8} \tag{2.5}$$

$$\lambda_6 = \frac{\lambda_{12}^2}{2\lambda_{12}} \tag{2.6}$$

λ_6	vertical wavelength of the QDT
λ_8	vertical wavelength of the TDT
λ_{12}	vertical wavelength of the SDT
λ_{24}	vertical wavelength of the DT

For the interaction between DT and TDT, the vertical wavelength can be calculated according to equation 2.5 and for the interaction between two SDT according to equation 2.6.

2.2. Observations and Model Study of the QDT

As described in the chapter 2.1 about the forcing of the QDT, the solar, nonlinear and gravity wave forcing of the QDT exists. The QDT, which is excited by the individual forcings cannot be measured, only the result of all forcings together. For the investigation of the MLT region there are different possibilities.

Radar Measurements

One option is the RADAR (=RAdio Detection And Ranging). Radio waves are emitted into the atmosphere, which are scattered due to refractive index variations caused by electron density and electrons. For example, electrons are formed in the tail when meteors (meteor radar) burn up in the upper atmosphere. Free electrons occur in the ionosphere and also scattered the waves from the radar. The scattered wave is then detected by the radar. From the obtained information, distance, angle and velocity of the ion / electron can be determined. With the MR method, the reflection takes place at the ionisation traces and not at the free electrons. The MR method provides information at an altitude of 80 - 100 km, with the MFR method in altitudes of 60 - 100 km. Based on long-term measurements of MR wind data from Collm (51° N, 13° E) and Obninsk (55° N, 37° E), Jacobi et al. (2017b) carried out trend studies and compiled a climatology of the QDT amplitudes in the zonal and meridional wind. The QDT amplitudes reached their maximum above Collm in the autumn and winter months, as well as in April. In the altitude range of 82 km to 97 km, an increase in amplitude with altitude was observed. The long-term trend at both stations generally shows an increase in QDT amplitudes, which was significantly positive in November, January, February and April and May. Guharay et al. (2018) evaluated three different MR measurements in the MLT region over Brazil. They were able to find the largest QDT amplitudes in the zonal wind in late summer and autumn and a vertical wavelength of 20 km. Jacobi et al. (2017b) could prove similar vertical wavelengths in summer. Liu et al. (2020) investigated three different MR measurements in the southern midlatitutdes between 2005 and 2018. QDT amplitudes between 0.5 ms^{-1} and 4 ms^{-1} were measured. The largest amplitudes were seen during the winter months (June-August) and the smallest amplitudes during the summer months. Further meteor radar measurements, which could prove a QDT, were carried out by Liu et al. (2006) in China and by Kovalam and Vincent (2003) in Australia. Smith et al. (2004) studied meteor radar wind observations from Esrange (60° N, 21° E), which shows the largest QDT amplitudes in winter with smaller amplitudes at the lower latitudes. In addition to their radar measurements, Smith et al. (2004) conducted a model study, in which they found a non-linear interaction between DT and SDT, which again forced a QDT. Jacobi et al. (2018) found something similar with a bispectral analysis.

LIDAR and Airglow Measurements

Another measuring system is LIDAR (= LIght Detection And Ranging), which uses a laser beam instead of a radio wave. The lidar has the advantage over the radar that it has a higher vertical and temporal resolution and can measure from the ground up to the MLT region. Other ground-based instruments measure airglow emission, which describe mesospheric temperature variability. Measuring systems can also be housed in satellites in order to be able to create a global climatology. This has the limitation of a lower temporal resolution. Thus, day to day variations and small fluctuations can not be resolved for a particular location from satellites. Using lidar temperature measurements, She et al. (2002) studied the MLT region in Fort Collins (41° N, 105° W) and also found a QDT. In the airglow intensities and temperatures in the winter of the southern polar mesopause region, Sivjee and Walterscheid (1994) discovered a QDT oscillation. This QDT is excited from absorption of solar radiation from stratospheric ozone or a nonlinear interaction between migrating tides in the lower atmosphere.

Thermosphere and Ionosphere Measurements

In 1988, Tong et al. (1988) showed, based on measurements of the electron density of the ionosphere, that a signature of QDT was present in the winter above Arecibo. Morton et al. (1993) later found, also for Arecibo, that the QDT in the wind had a significant influence on the distribution of electrons in the ionosphere. They explained this with a nonlinear frequency doubling of the SDT. Oikonomou et al. (2014) found also effects of a QDT in measurements at Cyprus in the ionospheric sporadic E layers. Earlier this was observed by Lee et al. (2003) over Taiwan. Jacobi et al. (2019) analyzed QDT signatures in lower ionospheric sporadic E occurrence rates. They mainly found maxima during early and late winter at middle latitudes, which coincided with modeled QDT vertical shear maxima of the zonal wind.

Satellite Measurements

Satellite-based measurements with a Microwave Limb Sounder (MLS), Xu et al. (2012) investigated the QDT excited from absorption of solar radiation from stratospheric ozone. They found higher QDT amplitudes during solstices (especially in winter) than on equinoxes. Xu et al. (2014) investigated the MLT region using Broadband Emission Radiometry (SABER) measurements of the Thermosphere-Ionosphere-Mesosphere Energetics and Dynamics (TIMED) satellite. They conclude that the observed QDT must have arisen from the interaction of nonmigrating DT and TDT. Liu et al. (2015) also looked at the SABER/TIMED temperature data and found a migrating QDT with amplitudes increasing with altitude. Further maxima of the QDT amplitudes were found in the low latitudes (30 °N/S) and above the equator. Azeem et al. (2016) investigated temperature measurements from the Near-Infrared Spectrometer (NIRS) instrument on Remote Atmospheric and Ionospheric Detection System experiment on the International Space Station and the Sounding of the Atmosphere using Broadband Emission Radiometry (SABER). Therefore, they found significant QDT amplitudes in the low- and midlatitudes that showed the structure of the QDT Hough modes.

State of Research

The current state of research is that the excitation of QDT is mainly owing to direct solar forcing (Chapman and Lindzen, 1970; Smith and Ortland, 2001; Xu et al., 2012). In addition, QDT can be excited by a nonlinear interaction of DT, SDT and TDT (Fellous et al., 1975; Manson and Meek, 1986; Teitelbaum et al., 1989; Younger et al., 2002; Xu et al., 2014). An excitation of the QDT via an interaction of gravity waves has not been investigated so far but was demonstrated for the TDT (Miyahara and Forbes, 1991; Lilienthal et al., 2018; Lilienthal and Jacobi, 2019), which allows the implication of similar mechanisms for the QDT. From the meteor radar and satellite measurements, it can be summarized for the QDT temperature and zonal wind amplitudes that there are maxima of the QDT in the low and middle latitudes. These reach 5 K at 100 km and up to 30 K at 130 km altitude in the temperature and up to 15 ms^{-1} at 120 km altitude in the zonal wind.

2.3. Summary and Outlook

The QDT has been observed from meteor radars, lidars, airglow and satellites. These observations only covers a limited altitude, latitude and longitude and / or time range, which is due to the measurement techniques. Radar measurements only give an overview at a specific location. So far, satellite measurements have only been available for a limited time and SABER does not have a polar orbit, so polar caps are missing. In addition, the small amplitudes are difficult to evaluate from the satellite data. With the model simulations of Smith et al. (2004), the measurements confirmed that direct solar forcing and nonlinear interactions play an important role in the excitation of the QDT. The current QDT climatology consists of measurements from some meteor radars and satellites, as well as the model simulations from Smith et al. (2004). A global overview of the QDT ampliutudes is therefore only possible with reservations and cannot be represented for the excitation mechanisms. The aim of this work is to provide a global overview of the structure of the QDT using model simulations that should be close to reality as possible and so provide a climatology from ensemble simulations for the first time. This work aims to go into more detail here and validate the results of Smith et al. (2004). This includes the dominant excitation mechanisms (solar heating, nonlinear tidal interactions, and gravity wave - tidal interactions). Similar to Smith et al. (2004), the individual forcing mechanisms are removed separately. This enables an exact overview of the structure and contribution of each forcing in the overall amplitude of the QDT and provides information about possible interactions between different excitation mechanisms. The following two chapters introduce the model, mathematical and numerical methods.

3. The Middle and Upper Atmosphere Model (MUAM)

3.1. Introduction

The Middle and Upper Atmosphere Model (MUAM; Pogoreltsev et al., 2007; Pogoreltsev, 2007) is used to investigate the forcing mechanisms of the migrating QDT with wavenumber 4. MUAM is a 3-D, primitive equation, mechanistic global circulation model based on the earlier Cologne Model of the Middle Atmosphere - Leipzig Institute for Meteorology (COMMA-LIM) described by Jakobs et al. (1986), Fröhlich et al. (2003) and Jacobi et al. (2006). COMMA-LIM was based on a hemispherical model of the stratosphere and mesosphere from Rose (1983). The vertical domain was extended by Jakobs et al. (1986) to 150 km and ion drag, molecular heat conduction, dynamic viscosity and an extended GW parameterization from Lindzen (1981) is added. The radiation routines for solar heating are inserted by Berger (1994) after Strobel (1978), Liou (1992), and Mlynczak and Solomon (1993) and also the infrared (IR) cooling according to Fomichev and Shved (1985). COMMA-LIM was mainly used and optimized for atmospheric chemistry at Cologne University. In the last years a sum of changes are done, such as by Pogoreltsev et al. (2007) the change from Leapfrog to Matsuno integration scheme. The upper boundary is increased up to about 160 km in log-pressure height and a new thermosphere GW parameterization is introduced according to Yiğit et al. (2008) and coupled with the existing linear Lindzen-type scheme. Recent versions of the MUAM model are described by Lilienthal et al. (2017, 2018), Lilienthal and Jacobi (2019), Jacobi et al. (2019) and Samtleben et al. (2019).

3.2. Numerical Properties

Integration Scheme and Temporal Resolution

The model uses a Matsuno scheme (Matsuno, 1966) for solving the time integration. The Leapfrog scheme is used in COMMA-LIM. In general the numerical approximation for a parameter Φ for a multi-stage scheme is the following:

$$\frac{\Phi^{n+1} - \Phi^n}{\Delta t} = \beta F(\tilde{\Phi}^{n+1}) + (1 - \beta) F(\Phi^n) \tag{3.1}$$

Φ^n	parameter at time step n
Δt	time interval
$F(\Phi) = \frac{d\Phi}{dt}$	temporal derivative of Φ
$\alpha,\ \beta$	constants defining the scheme

with

$$\tilde{\Phi}^{n+1} = \Phi^n + \alpha \Delta t F(\Phi^n). \tag{3.2}$$

This solves Eq. 3.1 for Φ^{n+1}

$$\Phi^{n+1} = \Phi^n + \beta \Delta t F(\tilde{\Phi}^{n+1}) + (1 - \beta) \Delta t F(\Phi^n) \tag{3.3}$$

It applies to the Matsuno scheme that $\alpha = \beta = 1$:

$$\Phi^{n+1} = \Phi^n + \Delta t F \tilde{\Phi}^{n+1} \tag{3.4}$$

and

$$\tilde{\Phi}^{n+1} = \Phi^n + \Delta t F(\Phi^n) \tag{3.5}$$

Eq. 3.4 describes the backward scheme (first stage) while Eq. 3.5 shows the equivalent to the Euler/forward scheme. For this reason the Matsuno scheme is called forward-backward or Euler-backward scheme, which is an implicit method. Important for the stability of the numerical simulation is the Courant-Friedrich Lewy (CFL) condition, which is tested at each model time step:

$$C = u\frac{\Delta t}{\Delta x} \leq C_{max} \tag{3.6}$$

C	Courant number (dimensionless)
C_{max}	maximum Courant number for stability
u	velocity of the process
Δx	spatial resolution
Δt	temporal resolution

$C_{max} = 1$ is given for the Matsumo integration scheme, so that applies:

$$u \leq \frac{\Delta x}{\Delta t} \tag{3.7}$$

For this reason in the model version of Lilienthal et al. (2018) and all versions before (Lilienthal et al., 2017; Lilienthal and Jacobi, 2019; Jacobi et al., 2018; Samtleben et al., 2019) a time step of 225 s was used. In the current configuration with 56 levels and 72 latitudes the time step is 120 s.

Spatial Resolution

All previous work with the MUAM was done with a horizontal resolution of 5.0° in latitudes and 5.625° in the longitudes, which results in a horizontal model grid of 36×64 (Lilienthal et al., 2017, 2018; Lilienthal and Jacobi, 2019; Lilienthal, 2019; Jacobi et al., 2018; Samtleben et al., 2019). In the frame of this thesis, the horizontal resolution was increased to 2.5° in latitude while a resolution of 5.625° in longitudes was retained, which results in a horizontal model grid of 72×64 (Geißler et al., 2020). The model reaches from the surface at 1000 hPa to 160 km log-pressure height, with a constant scale height of $H = 7\,\mathrm{km}$ and a vertical resolution of 2.842 km or 56 altitude levels. The altitude levels can be chosen between 48 and 60. In the version of this thesis 56 altitude level were chosen. With the nondimensional logarithmic pressure height x, the number of levels have a constant distance of $\Delta x = 0.4$. The nondimensional logarithmic pressure height is given by

$$x = -ln\left(\frac{p}{p_s}\right). \tag{3.8}$$

p .... pressure

$p_s = 1000\ hPa$ .... surface pressure

The logarithmic pressure height z at each level follows from this

$$x = H \cdot x = -ln\left(\frac{p}{p_s}\right). \tag{3.9}$$

$H = 7\ km$ .... scale height

Note, that the scale height H is assumed to be constant, which results in a difference between geometric altitude and logarithmic pressure altitude. These differences are small below 100 km but increase with height (see Tab. 3.1).

Table 3.1.: Nondimensional logarithmic pressure height x, the logarithmic pressure height z, the geometric height z_{geom} and the geopotential height z_{geopot} after Pogoreltsev et al. (2007) corresponding to their vertical levels.

level	x	z	z_{geom}	z_{geopot}
29	11.6	81 km	≈ 80 km	≈ 80 km
36	14.4	101 km	≈ 95 km	≈ 95 km
56	22.4	158 km	≈ 240 km	≈ 300 km

Initial Conditions

The middle and upper atmosphere model MUAM does not include typical features of the troposphere such as surface temperature and wind, clouds, orography, aerosols or latent heat release. Therefore, in the lowermost 30 km, i.e. in the lowest 10 model levels, the zonal mean temperatures $\overline{T_{MUAM}}$ of the model are nudged to monthly mean zonal mean temperature fields $\overline{T_{ERA}}$ of European Reanalyses (ERA)-Interim (Dee et al., 2011; ERA-Interim, 2018). The nudging term is introduced as follows:

$$\left.\frac{\partial T}{\partial t}\right|_{z<30km} = \frac{eff_{,nudge}}{t_{nudge}}(\overline{T_{MUAM}} - \overline{T_{ERA}}) \tag{3.10}$$

$\frac{\partial T}{\partial t}$ ....tendency term of the temperatures in MUAM

eff_{nudge} ....spin-up factor for nudging efficiency

$\overline{T_{ERA}}$ ....interpolated zonal mean monthly mean ERA-Interim temperature

$\overline{T_{MUAM}}$ ....zonal mean model temperature

t_{nudge} ....tuning parameter for nudging

with

$$eff_{nudge} = 1 - exp{-}(t/t_{nudge})^2. \tag{3.11}$$

In the model, Eq. 3.10 describes a tendency term of the prognostic equations. The nudging is performed only in the first 10 height levels, the first level is at an log-pressure altitude of 1.421 km. Monthly mean zonal mean temperature and geopotential fields from ERA-Interim reanalysis data (ERA-Interim, 2018; Dee et al., 2011) are given at the lower boundary of 1000 hPa. ERA-Interim data were used because they offer a good availability in terms of time and space (Lilienthal, 2019). In order to avoid interaction between stationary planetary waves (SPW) and tides, SPWs were not considered in this model version, even if these could be taken into account in the model (Jacobi et al., 2015).

Initialization and Spin-up

In the first time step of the model simulation, the atmosphere is initialized with a zero wind profile and standard atmosphere temperature profile (Pogoreltsev et al., 2007), which is independent on the day of the year. Above 130 km the initialization temperature profile is constant. A model run starts with a spin-up time of 120 model days. In that time the heating rates are zonally averaged, which means there are no tides. In this time only the background circulation is formed, through the boundary conditions and GWs. The nudging strength is continuously increased over time. This is described by the factor eff_{nudge} in Eq. 3.11, which is shown in Fig. 3.1 after Lilienthal (2019). After that, further 90 model days are simulated with zonally variable heating rates, so that there is tidal forcing now. The following results are analyzed from the last 30 model days (180-210). In this time period the tidal amplitudes remain almost constant and show only small day-to-day variations (Lilienthal, 2019). Lower atmosphere mean temperatures are nudged during the entire model run. However, since only zonal means are modified, tidal forcing and propagation remains possible. The declination in this model version is fixed to the 15th day of the respective month.

3.3. Model Physics

Model Equations

In MUAM the basic dynamics are given by primitive equations on a sphere in log-pressure coordinates. In a log-isobaric system the pressure p_0 at a certain altitude z can be de-

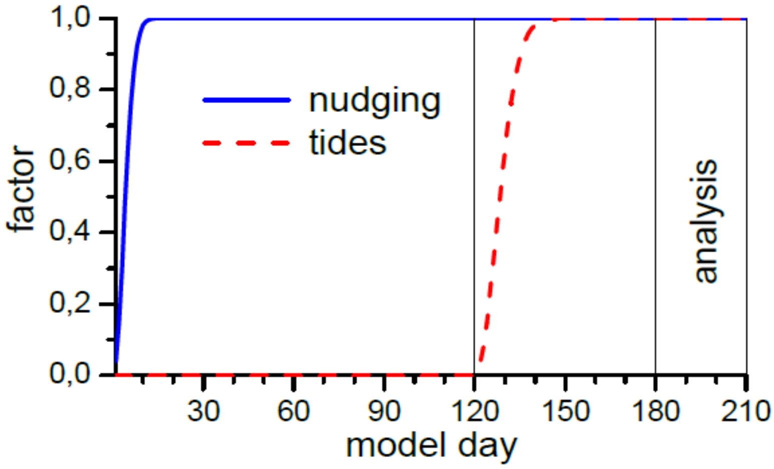

Figure 3.1.: Nudging efficiency and solar heating rates and their spin-up time in the model run. Taken from Lilienthal (2019).

scribed as following:

$$p_0 = p_s \ \ exp(-z/H). \tag{3.12}$$

p_0 .... pressure at respective altitude

$p_s = 1000\ hPa$ .... surface pressure

The horizontal wind components u and v are calculated from the Navier-Stokes Equations. The behavior of the temperature is based on the first law of thermodynamics and the continuity equation, which describes the conservation of mass in the system, provides the vertical wind w. The hydrostatic assumption says that acceleration due to gravity is much larger than the vertical acceleration, so that the vertical component of Coriolis force can be neglected (Fröhlich, 2005). The earth radius r is given as constant and it is $z \ll r$. The density is given by the gas law. The model equations are written in flux form for implementation in the model. This ensures the compliance of the upper and lower boundary if the vertical wind is handled correctly here (Fröhlich, 2005). Accelerations and heating of the system, which are unresolved are derived from several parameterizations, indicated by the vertical bar behind the derivative (Jakobs et al., 1986):

$$\begin{aligned}\frac{\partial u}{\partial t} =& -\frac{1}{r\cos\varphi}\frac{\partial u^2}{\partial\lambda} - \frac{1}{r\cos\varphi}\frac{\partial}{\partial\varphi}(uv\cos\varphi) - \frac{1}{\rho_0}\frac{\partial}{\partial z}(\rho_0 uw) + \left(f + \frac{u}{r}\tan\varphi\right)v \\ & -\frac{1}{r\cos\varphi}\frac{\partial\phi}{\partial\lambda} + \left.\frac{\partial u}{\partial t}\right|_{bidif} + \left.\frac{\partial u}{\partial t}\right|_{eddif} + \left.\frac{\partial u}{\partial t}\right|_{ion} + \left.\frac{\partial u}{\partial t}\right|_{GW}\end{aligned} \tag{3.13}$$

$$\begin{aligned}\frac{\partial v}{\partial t} =& -\frac{1}{r\cos\varphi}\frac{\partial uv}{\partial\lambda} - \frac{1}{r\cos\varphi}\frac{\partial}{\partial\varphi}(v^2\cos\varphi) - \frac{1}{\rho_0}\frac{\partial}{\partial z}(\rho_0 vw) + \left(f + \frac{u}{r}\tan\varphi\right)u \\ & -\frac{1}{r}\frac{\partial\phi}{\partial\varphi} + \left.\frac{\partial v}{\partial}t\right|_{bidif} + \left.\frac{\partial v}{\partial t}\right|_{eddif} + \left.\frac{\partial v}{\partial t}\right|_{ion} + \left.\frac{\partial v}{\partial t}\right|_{GW}\end{aligned} \tag{3.14}$$

$$\begin{aligned}\frac{\partial T}{\partial t} =& -\frac{1}{r\cos\varphi}\frac{\partial uT}{\partial\lambda} - \frac{1}{r\cos\varphi}\frac{\partial}{\partial\varphi}(vT\cos\varphi) - \frac{1}{\rho_0}\frac{\partial}{\partial z}(\rho_0 wT) + \frac{RwT}{m'c_pH} + \left.\frac{\partial T}{\partial t}\right|_{sol} + \left.\frac{\partial T}{\partial t}\right|_{ir} \\ & + \left.\frac{\partial T}{\partial t}\right|_{New} + \left.\frac{\partial T}{\partial t}\right|_{nudge} + \left.\frac{\partial T}{\partial t}\right|_{bidiff} + \left.\frac{\partial T}{\partial t}\right|_{molcon} + \left.\frac{\partial T}{\partial t}\right|_{GW} + \left.\frac{\partial T}{\partial t}\right|_{PW}\end{aligned} \tag{3.15}$$

u	zonal wind
v	meridional wind
w	vertical wind
T	temperature
ρ_0	density
ϕ	geopotential
φ	geographic latitude
λ	geographic longitude
f	Coriolis parameter
R	gas constant for dry air
r	earth radius
m'	ratio of the molecular weights of air at level z and $z = 0$
c_p	specific heat at constant pressure

The acronyms *bidif* and *eddif* describe the tendency terms of the parameterization of the biharmonic and eddy diffusion. The *ion*-term in the tendency equation indicates the parameterization of ionospheric processes like ion drag, Lorentz deflection and Rayleigh friction. The *molcon*-term in the tendency equation represents the molecular conduction and the *nudge*-term the nudging of ERA_Interim zonal mean temperature after Eq. 3.10. The parameterization of the gravity waves and traveling planetary waves in the tendency equation is indicated with the GW-term (Yiğit et al., 2008, 2009) and PW-term, whereby in this model version the term of the traveling planetary waves is zero. The *sol*-term describes the parameterization (Strobel, 1978) of heating due to solar radiation in the tendency equation. The *ir*-term and *New*-term indicate the heating due to infrared radiation and the Newtonian cooling.

This prognostic equations form the MUAM core dynamics. This includes the additional parameterizations for GWs and solar radiation, because they are crucial for a realistic simulation of the middle and upper atmosphere dynamics.

3.4. Parameterizations

Gravity Wave Parameterization

The gravity wave routine used in the model is based on a combination of the linear scheme of (Lindzen, 1981) for the middle atmosphere and the Yiğit-type scheme (Yiğit et al., 2008, 2009) for the thermosphere. The Lindzen-type scheme was introduced by Jakobs et al. (1986) in the model and includes the zonal and meridional accelerations of the mean flux by the breaking of gravity waves. The resulting heating and cooling rates are calculated on the basis of Medvedev and Klaassen (2003), also the efficiency of mechanical energy conversation into heat is considered (Huang and Smith, 1991). The breaking of gravity waves on multiple leves was explained by Fröhlich et al. (2003) and Fröhlich (2005). This parameterization is based on 48 waves initialized at 10 km altitude, traveling in eight directions with phase speed between 5 and 30 ms^{-1}. The linear scheme amplitudes have a latitudinal distribution with higher amplitudes in the winter hemisphere and smaller ones in the summer hemisphere (Fig. 3.2, left), because this represents the enhanced gravity wave activity during winter months. These waves do not effectively propagate beyond the lowermost thermosphere, therefore the Lindzen-type routine is coupled with the eddy diffusion coefficient through a modified nonlinear parameterization after Yiğit et al. (2008, 2009), initiated with gravity waves of higher horizontal phase speeds. To couple both routines, the Yiğit scheme has been adjusted and modified for the current MUAM version (Koval et al., 2018). The individually excited gravity waves are clearly separated through their different phase velocities. Yiğit et al. (2008) define a gravity wave spectrum in wavenumber with many large phase speeds and few small phase speeds, which is now adjusted to a broader wavelength spectrum. This includes 30 waves in total with equally distributed phase speeds in a range between $\pm 35\, ms^{-1}$ and $\pm 105\, ms^{-1}$. These gravity waves are launched at 10 km altitude. Fig. 3.2 shows (right) the spectral distribution of the initialized vertical momentum fluxes at this level. In the current model version, the configuration are set to zero for the gravity wave parameterization, the parameters for the coefficients of the Newtonian cooling, the collision frequency between ion and neutral particles and the electron density, so that they have no effect (Lilienthal, 2019; Geißler et al., 2020).

Now, the distribution of tendency terms from both gravity waves routines can be summed up to the total acceleration of the mean flow through gravity waves (Lilienthal et al., 2017, 2018; Lilienthal, 2019; Geißler et al., 2020). The results can be seen for zonal gravity wave acceleration for January (left) and April (right) in Fig. 3.3 as sum of both parameterizations. The linear scheme of Lindzen (1981) accounts of the middle atmosphere up to the mesopause ($< 100\ km$), the approach of Yiğit et al. (2008) leads to gravity wave acceleration in the thermosphere. For this and because of the different wave spectra, this results into breaking of small phase speeds gravity waves in the mesospheric jets and so, only fast traveling gravity waves are able to reach the thermosphere.

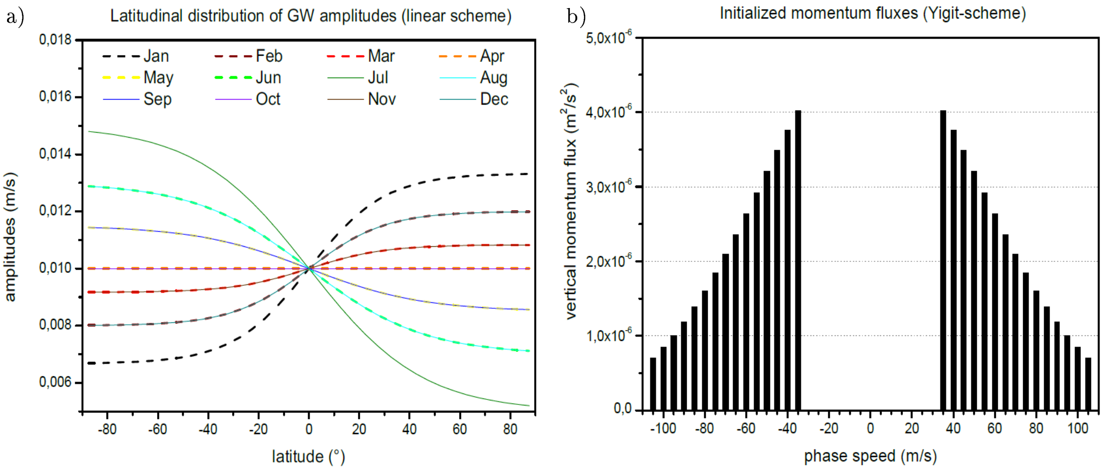

Figure 3.2.: Latitudinal distribution of gravity wave amplitudes in the linear parameterization for all months with mean value for all function of 0.01 ms^{-1} (left). Spectral distribution of gravity wave vertical momentum fluxes of the Yiğit parameterization at 10 km launch level (right). Taken from Lilienthal (2019).

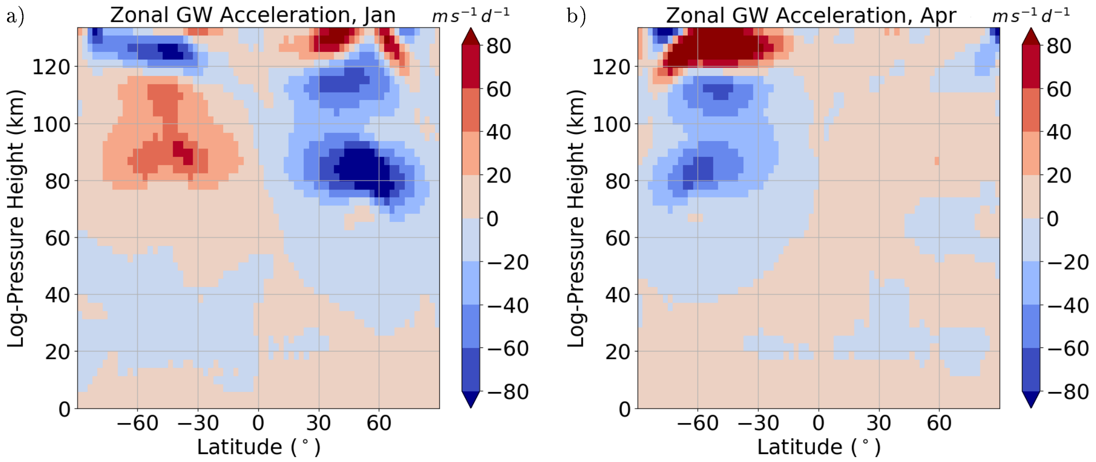

Figure 3.3.: Zonal gravity wave acceleration as combination of Lindzen-type and Yiğit-type parameterization for January (left) and April (rigth) for the year 2005 conditions.

Radiation Parameterization

The solar heating through absorption, including water vapor, carbon dioxide, ozone, oxygen, and nitrogen, in the middle atmosphere is parameterized after Strobel (1978) and is described by Fröhlich et al. (2003) and Fröhlich (2005) for the COMMA-LIM model, but it is the same for MUAM. The following shows a summary of the absorption bands of the chemical constituents and further improvements. The H_2O in the model, which is given as monthly zonal mean updated global constant volume mixing ratio, absorbs solar radiation in the troposphere and lower stratosphere. In MUAM it is parameterized after Liou (1992). Absorption happens for six wavelength intervals with the following central wavelengths: 0.94 μm, 1.1 μm, 1.38 μm, 1.87 μm, 2.7 μm and 3.2 μm. CO_2. Parameterization is done after Liou (1992). O_3 absorbs in Herzberg ($205 - 242$ nm), Hartley ($200 - 300$ nm), Huggins ($300 - 350$ nm) and Chappuis band ($450 - 700$ nm) located mainly in the stratosphere. Atomic oxygen and O_2 absorb in the Herzberg band in the stratosphere. In the thermosphere absorption takes place in the Extreme Ultra Violet (EUV) band ($5 - 105$ nm), Lyman-α line (121 nm), Schumann-Runge continuum ($125 - 175$ nm) and Schumann-Runge band ($175 - 205$ nm). N_2 absorption is only considered in the EUV band in the thermosphere. Chemical heating due to recombination reactions of oxygen and ozone is parameterized after Riese et al. (1994).

This model version uses only zonal mean water vapor mixing ratios at 1000 hPa from NCEP reanalyses (Ermakova et al., 2017). For higher levels the water vapor is analytically derived from the given data with the help of corresponding scale heights from NCEP reanalyses. Carbon dioxide is implemented as monthly mean mixing ratio according to the Mauna Loa Observatory data for 2005 between 377 ppm in September and 382 ppm in May as globally constant up to 87.5 km with an exponential decrease above (e.g., 380 ppm for February 2005, NOAA ESRL Global Monitoring Division, 2018; Thoning et al., 1989). Carbon dioxide is fixed for the ensemble runs from 2000 to 2010, because it is not intend to perform an CO_2 dependent trend analysis. That there is a trend in carbon dioxide is seen in Fig. 3.4b. These vertical carbon dioxide distribution is shown in Fig. 3.4a for different mixing ratios to see the behaviour of the decrease. Ozone is implemented as monthly mean zonal mean field of mixing ratios for the year 2005 up to 50 km altitude taken from MERRA-2 (Modern-Era Retrospective Analysis for Research and Application, version 2) reanalysis data (; MERRA-2, 2019). In the previous model versions from Lilienthal et al. (2018), Lilienthal and Jacobi (2019), Lilienthal (2019), and Jacobi et al. (2018) SPARC (Stratosphere-troposphere Processes And their Role in Climate) ozone data were used

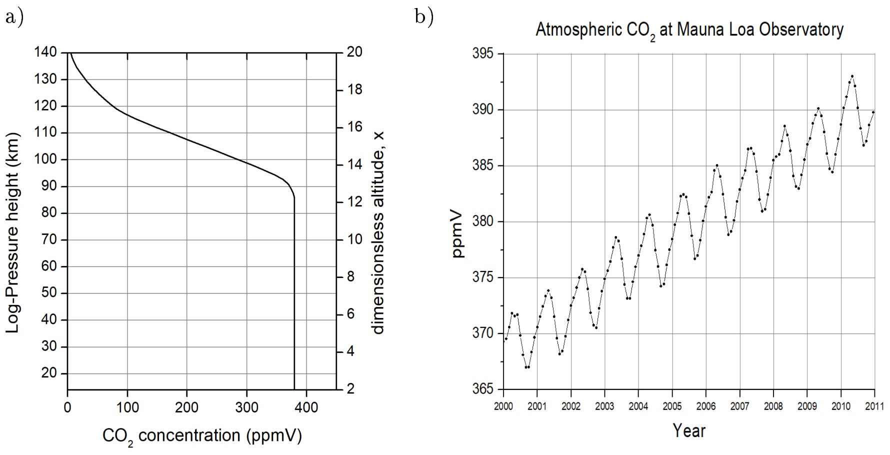

Figure 3.4.: Left: profile of carbon dioxide as implemented in MUAM model for a concentration of 380 ppmV. Right: monthly mean atmospheric carbon dioxide at Mauna Loa Observatory from 2000 to 2010. Source: `https://www.esrl.noaa.gov/gmd/ccgg/trends/`

(Randel and Wu, 2007; SPARC, 2020). The MERRA-2 ozone data provide a much better ozone distribution and mixing ratios than the SPARC ozone data. The ozone volume mixing ratios from MERRA-2 (left) and SPARC (rigth) are shown in Fig. 3.5 for January 2005 as latitude-altitude distribution. As for carbon dioxide, the ozone mixing ratios are fixed for the ensemble runs from 2000 to 2010 to avoid a trend dependent analysis.

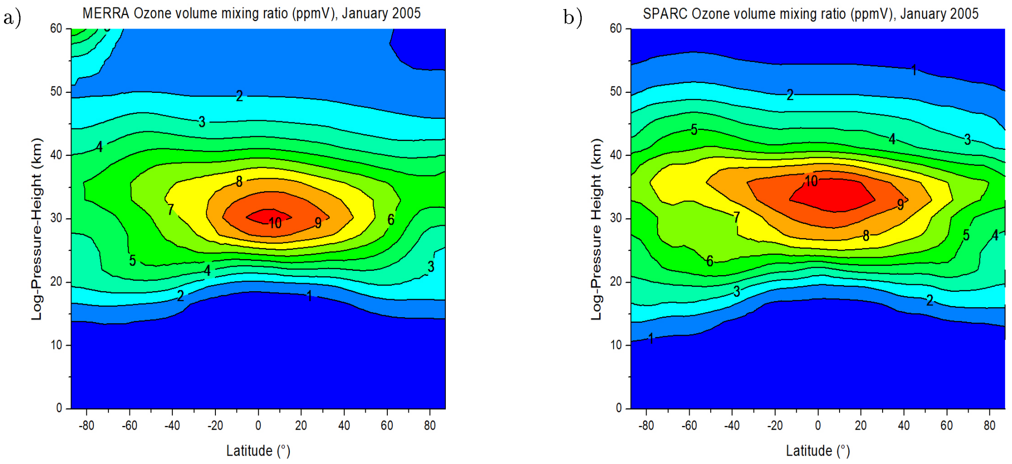

Figure 3.5.: Ozone volume mixing ratios from MERRA-2 (MERRA-2, 2019) data (left) and SPARC (SPARC, 2020) data (right) for January 2005.

The solar flux in the atmosphere, cooling and heating due to absorption and emission of IR by water vapor, ozone and carbon dioxide has to be balanced in MUAM by parameterization (Fröhlich, 2005; Lange, 2001). In the troposphere the cooling by water vapor is most important in the 6.3 μm band and parameterized in the MUAM after Chou et al. (1993). The important part of stratosphere cooling takes place by ozone. There is also small heating from IR radiation at about 25 km altitude from the 9.6 μm band. This is implemented according to Fomichev and Shved (1985). Carbon dioxide leads to a cooling and heating in the troposphere is parameterized after Fomichev et al. (1998) for the 15 μm band. In the stratosphere and lower mesosphere and MLT the radiative effect of carbon dioxide is implemented according to Chou et al. (1993) and Ogibalov et al. (2000).

3.5. Background Climatology

The model run consists of 210 model days. The following results of monthly means shows of the last 30 model days. The results are given as means of the 11 ensemble members (color shading), which based on the model simulations for the year 2000 - 2010. Carbon dioxide and ozone mixing ratios are constant for the year 2005 for the months January to December. The respective ERA-Interim reanalysis zonal mean temperatures for every year from 2000 - 2010 is used for nudging (Geißler et al., 2020). The following plots show the results from the reference run, which includes all forcing mechanisms of every tide and no filtering according to chapter 4. A sensitivity study is done in the following chapter 5, which leads to the best case scenario, the reference run (REF), that is presented now. Due to the fact, that these reanalysis data are nudged up to 30 km in the ensemble simulation the standard deviations (contour lines) may be considered as a measure for climatological year-to-year variability. This is seen in large standard deviations in the winter hemisphere due to the variability of the polar vortex. Corresponding to this fact the standard deviations are smaller during equinoxes. This is seen in Fig. 3.6 for the background climatology for zonal mean temperature (a, b), zonal (c, d) and meridional wind (e, f) for January (left) and July (right). The whole seasonal cycle of the year is shown in the supplement A1 for temperature in Fig. S1, zonal wind in Fig. S2 and meridional wind in Fig. S3. The model temperature shows general agreement with the empiricall climatology of COSPAR International Reference Atmosphere (CIRA 86) (Fleming et al., 1990) climatology for January and April. But in the winter polar region the temperatures in the MUAM simulation are higher than in the CIRA86 climatology. Largest standard deviation is seen in the northern polar region due to the variability of polar vortex.

The following discussion is taken from Geißler et al. (2020). The model zonal wind climatology agrees reasonably well with earlier empirical climatologies such as COSPAR International Reference Atmosphere (CIRA 86) (Fleming et al., 1990) or the radar-based Global Empirical Wind Model (GEWM) (Portnyagin et al., 2004; Jacobi et al., 2009) and the satellite-based URAS Reference Atmosphere Project (URAP) (Swinbank and Ortland, 2003). In winter the easterly jet of the summer hemisphere is weaker in comparison with the climatologies. The same is true for the equatorial easterly winds in April and October. The model temperature shows general agreement with the empirical CIRA 86 climatology. In winter the stratopause and mesopause temperatures above the equator and low latitudes are about 10 K lower than predicted by the CIRA 86 climatology. These differences are not seen in the comparison for October. MUAM produces a year-to-year variability (standard deviation σ) especially in the areas of the strongest jets of the northern mid-latitudes in winter (up to $\sigma(u) = 8\,\mathrm{ms}^{-1}$) and at the southern midlatitudes for the period from May to November (up to $\sigma(u) = 10\,\mathrm{ms}^{-1}$). The reason for this is the annual variability in the formation of the polar vortex, which affects the strength of the jets and the temperature at the high and midlatitudes. This variability causes fluctuation of a few K or ms^{-1}. Elsewhere, the standard deviation is very small, and mostly amounts to less than $\sigma(T) = 2\,\mathrm{K}$ ($\sigma(u) = 2\,\mathrm{ms}^{-1}$, $\sigma(v) = 0.5\,\mathrm{ms}^{-1}$). In comparison with the more recent Horizontal Wind Model (HWM14, Drob et al., 2015), the westerly wind jet in February in the middle atmosphere midlatitudes is much stronger ($+20\,\mathrm{ms}^{-1}$) in the MUAM simulation. The easterly wind jet in the mesosphere, on the other hand, is much weaker ($-35\,\mathrm{ms}^{-1}$) in the MUAM simulation than predicted from the HWM14. Also, the mesospheric wind reversal is at higher altitudes in HWM14 (100 km) than in the MUAM (80 km) simulation, especially in the northern hemisphere. Similarly, the wind jets in the mesopause and lower thermosphere region are much weaker in the MUAM run than in HWM14. A better agreement is seen for autumn regarding the strength of the wind jets. However, in contrast to winter, the wind reversal is seen at higher altitudes than in MUAM (80 km) than in HWM14 (70 km).

The meridional wind below 100 km corresponds to the Brewer-Dobson circulation, which is mainly directed from the summer pole to the winter pole. That means accordingly northward wind in January and southward wind in July. Some anomalies during May to August at 60° S with positive meridional wind are also reported by Lilienthal et al. (2017) and Lilienthal (2019). Lilienthal et al. (2017) describes this feature as a consequence of the GW distribution whose source level is implemented as a 2-D horizontal field instead of a zonal mean distribution. Fig. 3.7 shows the background climatology for temperature (a, d, g), zonal wind (b, e, h) and merdional wind (c, f, i) as time-latitude-plot for 90 km (top), 101 km (mid) and 109 km (bottom). Every plot shows the seasonal cycle with higher MLT region temperatures during winter seasons and the resulting Brewer-Dobson circulation in the meridional wind. In the zonal wind at 101 km and 109 km (e, h in Fig. 3.7) the MLT region easterly (winter) and westerly (summer) jets can be seen.

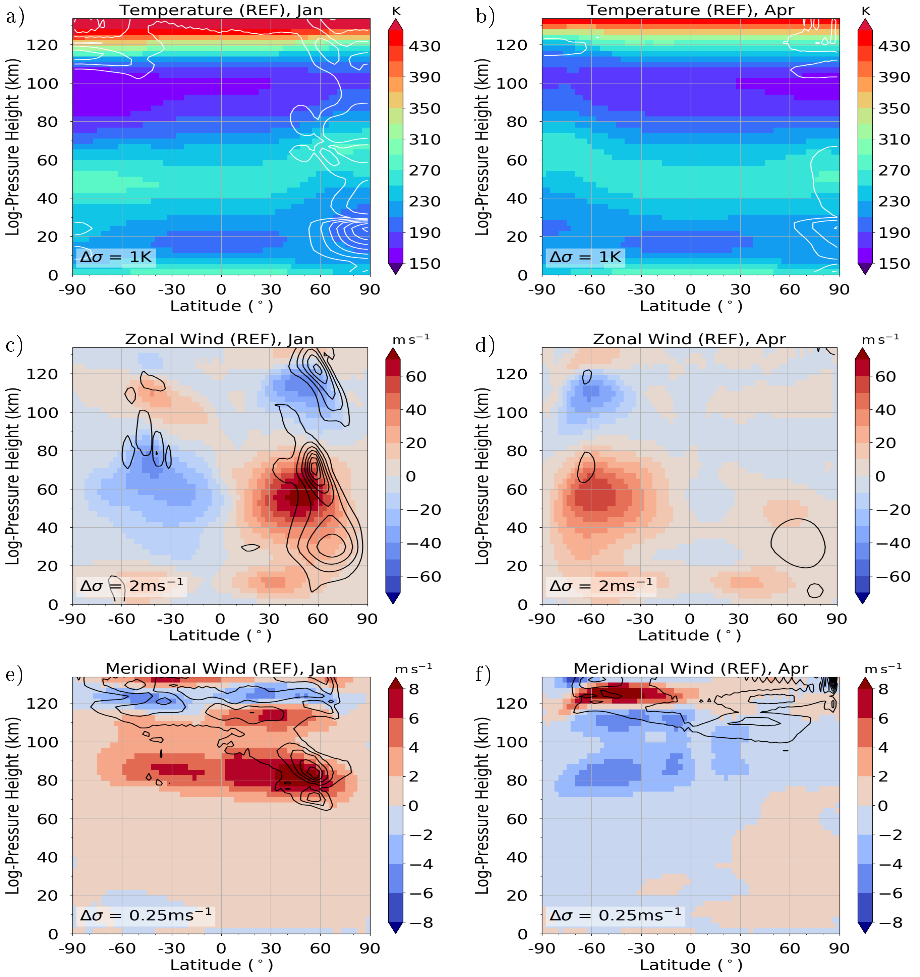

Figure 3.6.: The Background climatology is shown as color, black lines are standard deviation from ensemble runs. Left for January, right for April, top for temperature, mid for zonal wind, bottom for meridional wind.

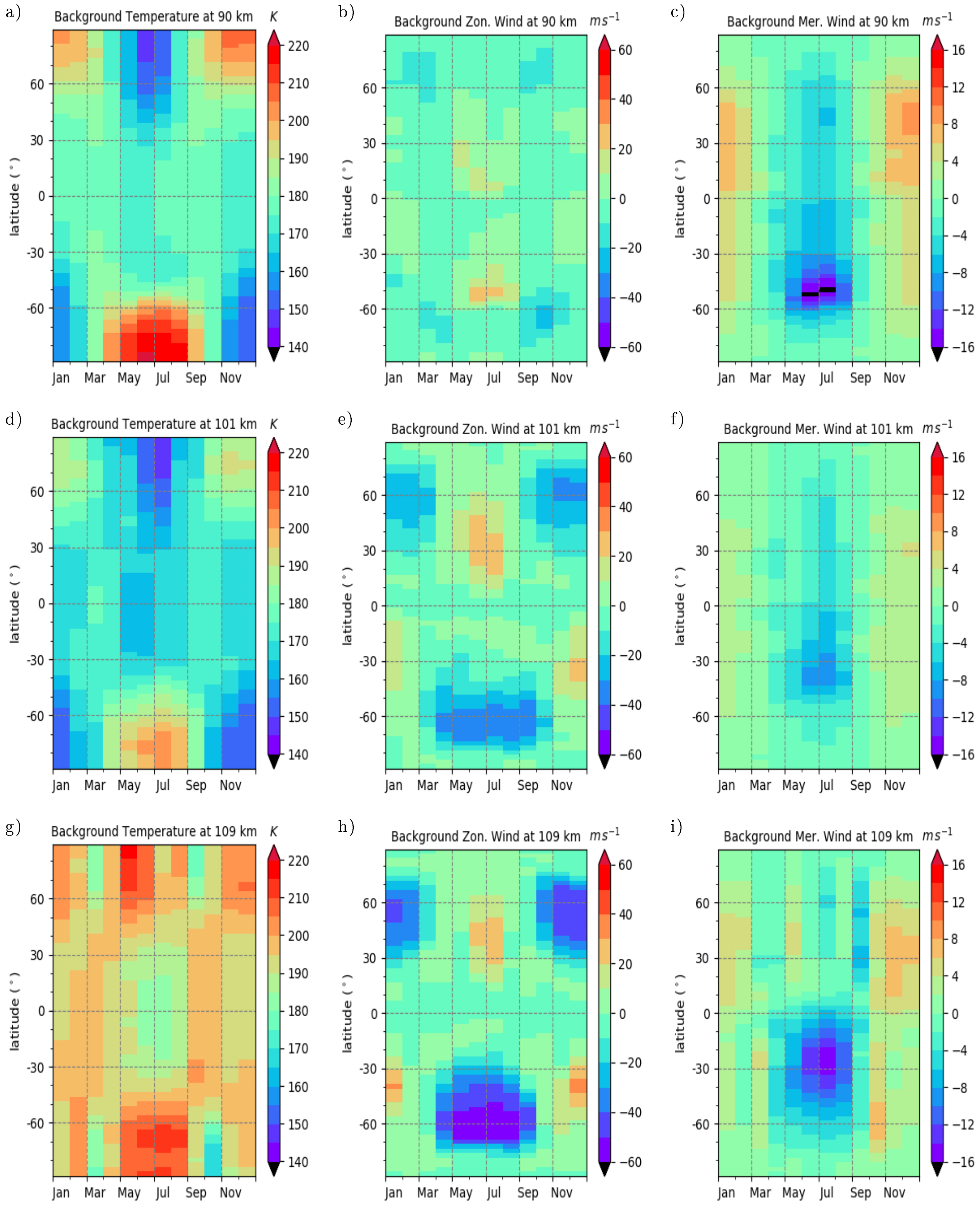

Figure 3.7.: Background climatology for temperature (a, d, g), zonal wind (b, e, h) and merdional wind (c, f, i) as time-latitude-plot for 90 km (top), 101 km (mid), 109 km (bottom).

4. Mathematical and Numerical Methods

4.1. Fast Fourier Transform

Solar tides, including the QDT, may be generated by three different mechanisms, named solar heating, nonlinear tide-tide interactions, and gravity wave - tidal interactions. More details of these forcing mechanisms and how they are represented in the MUAM model are described by Lilienthal et al. (2018) and Geißler et al. (2020). Here, it is essentially to follow their approach by removing different forcing mechanisms. To this end, a Fourier transform is a useful tool to remove the wavenumber 4 (which is equivalent to the migrating QDT, since there are no non-zonal structures for the migrating tides in this MUAM version) amplitude from the respective forcing term during each time step and at each model grid point. To remove the solar forcing mechanism, the wavenumber 4 heating was removed from the radiation parameterization scheme. To remove the nonlinear tide - tide interactions, the nonlinear terms are separated, which are essentially the advection terms in the momentum equation and the temperature equation as has been done in Lilienthal et al. (2018) and Geißler et al. (2020). Then the wavenumber 4 in these terms is removed. Since these advection terms are responsible for wave-wave interaction, this strategy effectively removes the QDT forcing through non-linear interaction. To remove gravity wave - tidal interaction, the total acceleration and heating through gravity wave oscillations of wavenumber 4 are removed. This approach was introduced by Lilienthal et al. (2018) and applied by Geißler et al. (2020).

The Fast Fourier Transform will play an important role to separate the different forcings of the QDT. For a better understanding, how this Transform works a short introduction will follow.

The Discrete Fourier Transform

A Fast Fourier Transformation offers the possibility of splitting a data set into its frequency components using spectral analysis. The following section is taken from Press et al. (1989). They assume that for a data set $h(t)$, the Fourier transform can be written as follows:

$$H(\omega) = \int_{-\infty}^{+\infty} h(t)\ e^{i\omega t}\ dt \tag{4.1}$$

with

h	data set as function of time
H	data set as function of frequency
t	time
f	frequency
ω	angular frequency

Suppose the data set has a length of N, it is possible to convert Eq. 4.1 into a discrete form:

$$H(f_n) = \sum_{k=0}^{N-1} h_k\ e^{2\pi i f_n t_k}\ \Delta \tag{4.2}$$

with

N	length of the (temporal) data set
k	number of (temporal) element
t_k	time at the k-th element
Δ	sampling interval (in real time)
h_k	(temporal) data at the k-th element
$n = -N/2...N/2$	number of element in frequency domain
$f_n = n/(N\Delta)$	sampling frequency for n-th element
$H(f_n)$	data at the n-th element in frequency domain

It is important that the upper and lower limits of n are determined by the Shannon-Nyquist sampling theorem and correspond to the critical frequency range. Using the relations $f_n = n/(N\Delta)$, $k = t_k/\Delta$ and W as complex number $W = e^{\frac{2\pi i}{N}}$ the Eq. 4.2 can be rewritten to:

$$H_n = \sum_{k=0}^{N-1} h_k W^{nk}. \tag{4.3}$$

Thus, the vector of h_k is multiplied by a matrix whose (n,k)th element is the constant W to the power $n \times k$. The matrix multiplication produces a vector result whose components are the H_n's. However, this matrix multiplication requires N^2 complex multiplications and the discrete Fourier transform appears to be an $O(N^2)$ process. A so-called Fast Fourier Transform can reduce this to $O(N \log_2 N)$, e.g. by applying the Danielson-Lanczos algorithm (Danielson and Lanczos, 1942).

Danielson-Lanczos Algorithm

Danielson and Lanczos (1942) show that a discrete Fourier Transform of length N can be rewritten as the sum of two discrete Fourier transforms, each of length $N/2$: the even- and the odd-numbered. According to Press et al. (1989), this results in:

$$H_n = \sum_{k=0}^{N-1} h_k \; e^{\frac{2\pi i k n}{N}} \tag{4.4}$$

$$= \underbrace{\sum_{k=0}^{N/2-1} h_{2k} \; e^{\frac{2\pi i n k}{N/2}}}_{even} + W^n \underbrace{\sum_{k=0}^{N/2-1} h_{2k+1} \; e^{\frac{2\pi i n k}{N/2}}}_{odd} \tag{4.5}$$

$$= \underbrace{H_n^e}_{N/2 \text{ data points}} + W^n \underbrace{H_n^o}_{N/2 \text{ data points}} \tag{4.6}$$

This scheme can be applied recursively on H_n^e and H_n^o so that four data sets of length $N/4$ are produced: H_n^{ee}, H_n^{eo}, H_n^{oe} and H_n^{oo} and so forth. This is the reason why the algorithm requires a data set where length N is an integer power of two, as said before. If the length of the data set is up to the next power of two. Since the MUAM has 64 longitudes, the data set has a length of exactly 2^6 and thus fulfills the requirements of a discrete Fourier transform.

4.2. Harmonic Analysis

To obtain the amplitudes and phases of the QDT, a harmonic analysis of the data is performed. This has been done for the last 30 days of each simulation and separately for each latitude and altitude. For example after Foreman and Henry (1989), the zonal wind field is composed of the superposition of the monthly mean zonal mean zonal wind and the migrating DT, SDT, TDT and QDT.

$$u_e(x,t) = \overline{u} + \sum_{i=1}^{4} \Big(a_i \sin(k_i x + \frac{2\pi}{P_i} t) + b_i \cos(k_i x + \frac{2\pi}{P_i} t) \Big) \tag{4.7}$$

u_e .... modeled zonal wind field

$\overline{u}$ .... monthly mean zonal mean zonal wind

x .... longitude in rad

t .... time

i .... index of tide (i-th harmonic)

a_i .... imaginary part coefficient

b_i .... real part coefficient

k_i .... wave number

$P_i = 6\ h$ .... period of the QDT

To find the best solution for a_i and b_i, a least-squares fit is used, which minimizes the quadratic differences between the expected wind field u_e and with current wind field u of the model output.

$$\sum_{x,t} (u(x,t) - u_e(x,t))^2 \rightarrow min \tag{4.8}$$

The same applies to the meridional wind and temperature. The amplitudes and phases of the tides can be derived from the real and imaginary parts as follows:

$$A_i = \sqrt{a_i^2 + b_i^2} \tag{4.9}$$

A_i .... amplitude

$$T_i = \arctan\left(\frac{a_i}{b_i}\right) \tag{4.10}$$

T_i .... phase A_4 and T_4 are the amplitude and phase of the migrating QDT.

5. MUAM: Sensitivity Studies

The sensitivity study will show how the results depend on the specific model settings. Special attention will be paid to the points that were changed in the context of this thesis and showed improvements for the QDT amplitudes. These include the horizontal and temporal resolution of the model, as well as the initial conditions through the assimilation of ERA-interim reanalysis data. As a conclusion of this study the optimal model settings for the investigation of the QDT will be found for the reference simulation (REF).

5.1. Influence of Horizontal Resolution on the Background Climatology and QDT amplitudes

In comparison to Lilienthal et al. (2018), Lilienthal and Jacobi (2019), and Lilienthal (2019) the latitudinal resolution of the MUAM model was increased from 36 latitudes to 72 latitudes. For this model experiment, the temporal resolution had to be increased to 120 s for the model run with 72 latitudes, while the model run with 36 latitudes has a temporal resolution of 225 s. In the following, a comparison is made with the older model version with 36 latitudes and shows the influence of this change on the background circulation. The changes in circulation and dynamics, especially in the mesosphere, have a decisive impact on the propagation of waves and thus on the tides in the MLT region, which will be treated later.

Background Climatology

The model runs with the different latitudinal resolutions have all forcings of tides enabled. As an example only the months January and April are shown.

Fig. 5.1 shows the temperature as color, white/black lines are standard deviation from the ensemble runs for January (a - c) and April (d - f), the REF run with a resolution of 72 latitudes (a, c) and the REF run with a resolution of 36 latitudes (b, d) and the differences

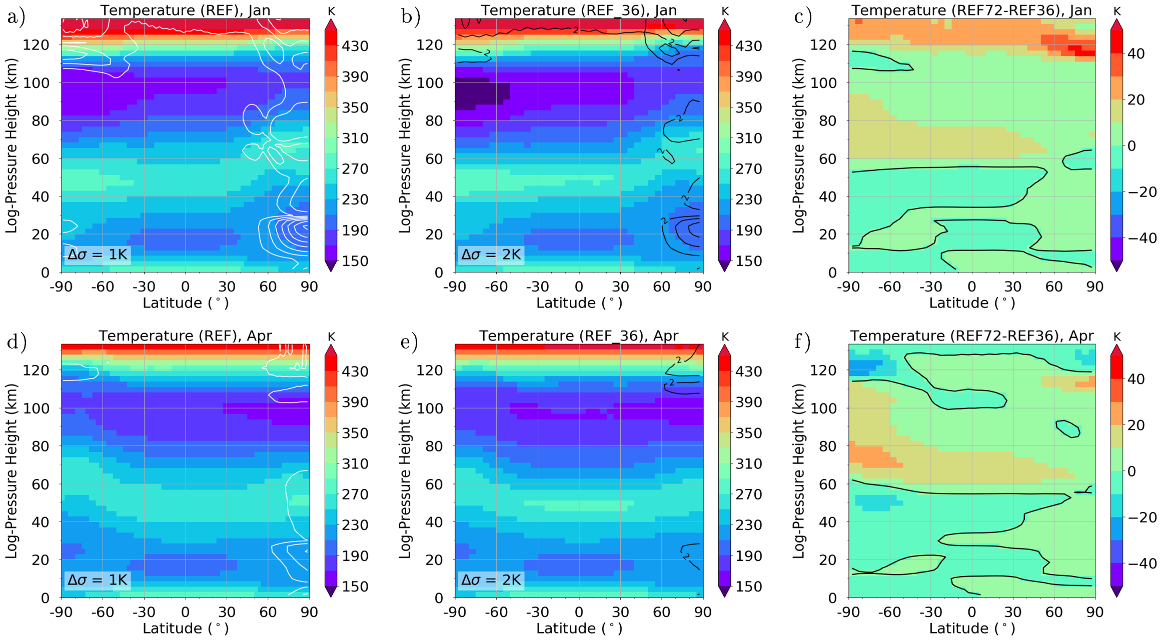

Figure 5.1.: Temperature is shown as color, white/black lines are standard deviations from the ensemble runs for January in the first line January and April in the second line. First column REF run with 72 latitudinal resolution and second row REF run with 36 latitudinal resolution, third row shows differences (REF72-REF36) between run with 72 latitudes and 36 latitudes.

(REF72-REF36) between the runs with 72 latitudes and 36 latitudes (c, e). In January and April, especially at southern hemisphere the stratosphere and stratopause are colder in the model run with 72 latitudinal resolution. At southern hemisphere mesosphere and mesopause both months are warmer for the higher latitudinal resolution run. Compared to the CIRA 86 climatology, this is a step in the wrong direction, since MUAM is now too warm, especially in the mesosphere, while the 36 latitude version agreed well with this climatology.

Fig. 5.2 shows the same as the Fig. 5.1, but for zonal wind. It can be seen, that the MLT region jets are a little weaker in January in the higher resolution model version, but in April the jets on southern hemisphere are stronger by up to 20 ms^{-1}. In contrast to this, the northern hemisphere shows weaker (up tp 15 ms^{-1}) jets in the new model version. The differences in the wind jets between the MUAM simulation and the CIRA

86, URAP and GEWM climatologies and the HWM14 model is still present but not that large compared with the older version.

Fig. 5.3 shows the same as Fig. 5.2 and Fig. 5.1 but for meridional wind. The meridional wind of the Brewer-Dobson circulation increases (up to $\sim 1\ ms^{-1}$) between 70 km and 100 km and decreases above by more than 50% in January. For April a similar behavior can be seen with an strong increase of 100% of the Brewer-Dobson circulation between 70 km and 100 km and a strong decrease above, especially at northern hemisphere by 100%. The better model resolution provides more realistic wind jets in the MLT region, but leads to slightly higher temperatures in the mesosphere compared to CIRA 86 and other climaologies.

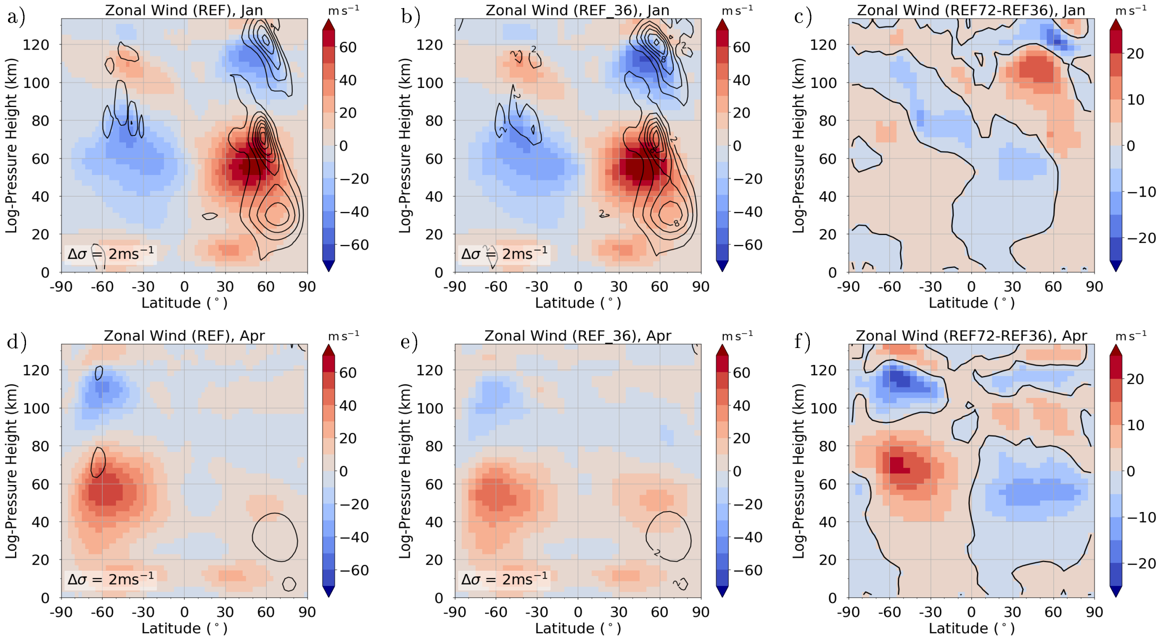

Figure 5.2.: Same as Fig. 5.1 but for zonal wind.

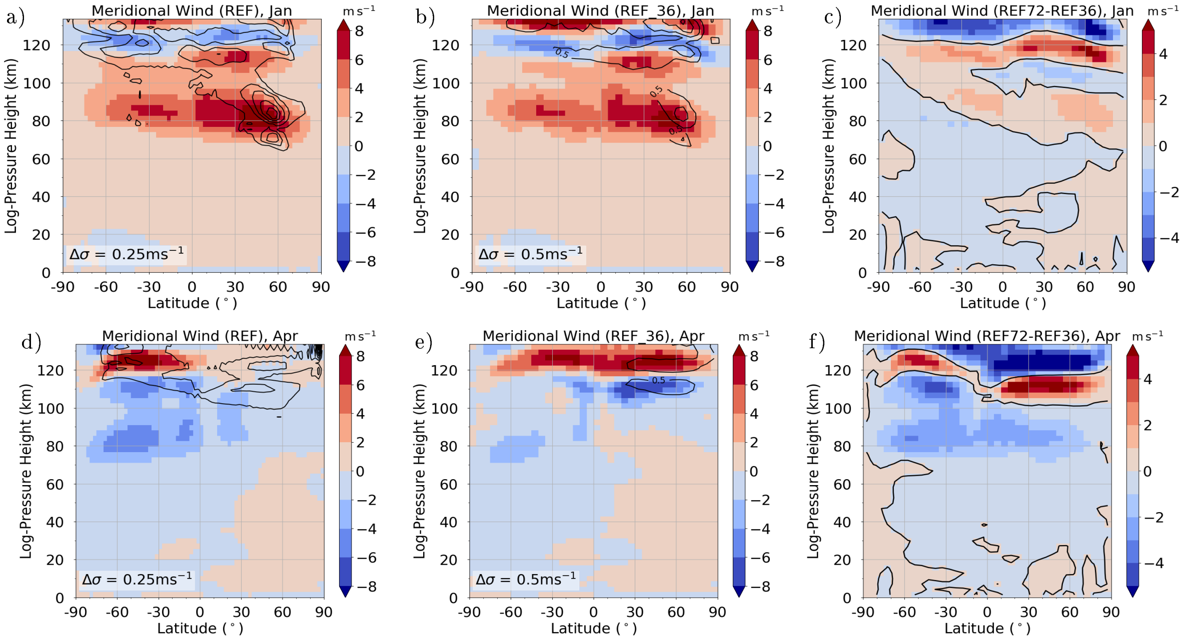

Figure 5.3.: Same as Fig. 5.1 and Fig. 5.2 but for meridional wind.

QDT Climatology

The main purpose of the resolution increase was to simulate the QDT more realistically. Therefore, the QDT structure is compared in the following to demonstrate the improvement of its structure and amplitudes. On the one hand, a change in the circulation leads to different propagation conditions of the tides in the atmosphere, on the other hand, the tides are also better spatially resolved. Since the QDT is a higher harmonic (Azeem et al., 2016) and has a finer meridional structure, this should be better represented with a better horizontal resolution. This includes all forcing mechanisms of the QDT in all runs. Fig. 5.4 shows the temperature amplitudes of the QDT as color, black lines are standard deviation from ensemble runs for January (top) and April (bottom), for the REF simulation with 72 grid points in latitude (left) and 36 grid points in latitude (right). The amplitudes are larger in the newer version than in the 36 latitudinal version. As expected, the structure of the QDT is better resolved in the meridional version and four maxima instead of two can now be seen. The standard deviation in April is also larger in the higher resolved model version, since spatial variability can now be better represented. Fig. 5.5 shows the same as Fig. 5.4 but for zonal wind QDT amplitudes. As with the temperatures, it can be seen in the new version that the amplitudes are larger overall, more meridional structure is visible and the standard deviation increased especially in April. In conclusion, it can be stated that the higher meridional resolution amplifies larger QDT amplitudes and provides a higher structural resolution (Azeem et al., 2016). The QDT amplitudes in the model are too small compared to measurements from satellites and radar and largest amplitudes occure during February and October (e.g., Liu et al., 2015; Azeem et al., 2016; Xu et al., 2012; Liu et al., 2020; Pokhotelov et al., 2018; Liu et al., 2020; Jacobi et al., 2017c; Guharay et al., 2018). Therefore the QDT amplitudes are shown in the following only for February and October. This effect of smaller QDT amplitudes was more pronounced in the model version with 36 latitudes than in the version with 72 latitudes. In the following chapter 6 a detailed discussion of the modeled QDT climatology with the literature can be found.

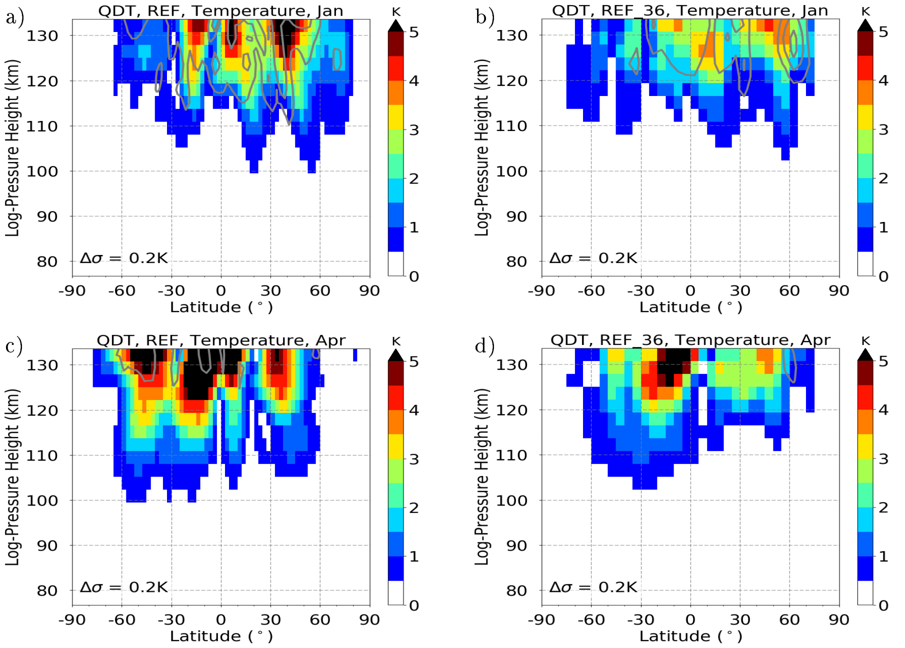

Figure 5.4.: Temperature amplitudes of the QDT are shown as color, black lines are standard deviations from ensemble runs for January (top) and April (bottom) and left for the REF simulation with 72 latitudes and right for 36 latitudes.

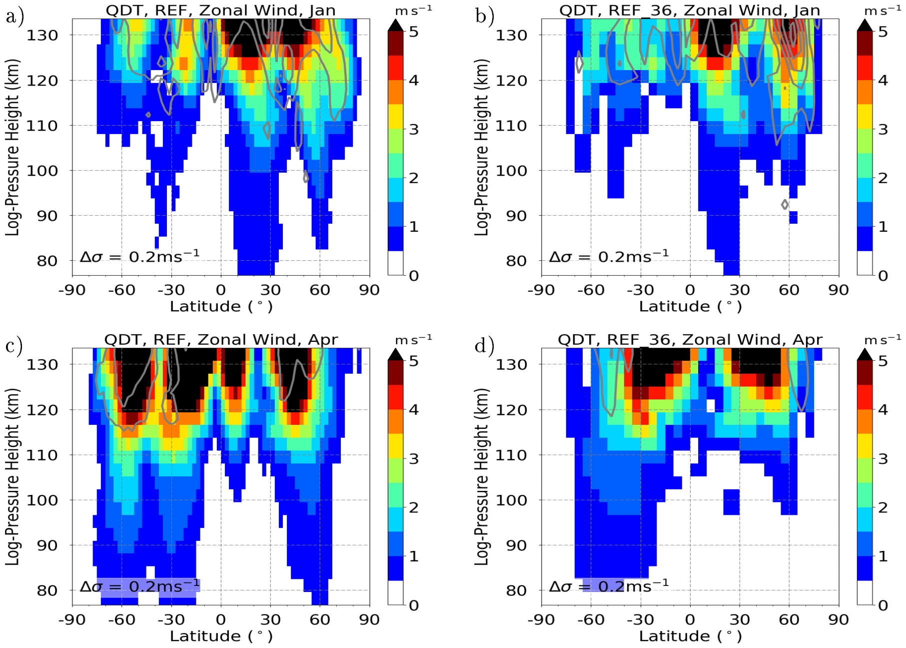

Figure 5.5.: Same as Fig. 5.4 but for zonal wind amplitudes of the QDT.

5.2. Influence of the Initial Conditions on the Background Climatology and QDT amplitudes

The MUAM allows an nudging of the initial conditions of the ERA-interim data from 2 to 80 km altitude. Depending on the nudging altitude this has a decisive effect on the dynamics of the modeled atmosphere in the model and thus on the propagation conditions of the QDT. In a further model experiment, the effect of a nudging height of the initial conditions between 10 km and 50 km is now being investigated.

Background Climatology

In the following figures five different plots are shown: the REF run with 72 latitudes resolution and 2005 conditions with an nudging altitude of 30 km and four differences between different simulations with nudging altitudes of 10 km, 20 km, 40 km and 50 km for 2005 conditions and the REF simulation. The influence of the different nudging altitudes of ERA-interim data of the initial conditions on the background circulation is shown in Fig. 5.6 for January for the REF run (a) and the differences for the nudging altitudes of 10 km, 20 km, 40 km and 50 km (b - e). To save computing time, ensemble calculations were not made for nudging altitudes of 10 km, 20 km, 40 km and 50 km. For the mesospheric jet between 40 km and 80 km altitude a significant decrease of wind speed in the northern hemisphere in January can be seen with higher nudging altitude. The westerly wind jet weakens the higher the lower boundary is nudged. Wind speeds decrease from about 100 ms^{-1} in the 10 km case to 70 ms^{-1} for the 50 km case, which is more in agreement with the CIRA 86 climatology with up to 65 ms^{-1}, see Fig. 1.1. At the same time, the easterly wind jet in the southern hemisphere increased by about 15 ms^{-1}. In the MLT region the opposite was seen, the easterly wind jet in the northern hemisphere decreased by about 10 ms^{-1} and the westerly wind jet in the southern hemisphere increased by about 10 ms^{-1}. This development is adequately pronounced in July, see Fig. 5.8.

Fig. 5.7 and 5.9 show the same as before for April and October. The higher the data of the lower boundary conditions are assimilated, the weaker the westerly wind jet is in both months. For the easterly wind jet this in only true for October. This applies both to the jets in the mesosphere and lower thermosphere.

Overall, an assimilation of ERA-interim data up to an altitude of 50 km provides more realistic wind speeds in the simulations in jets when compared to the CIRA 86 or HWM14 model climatology.

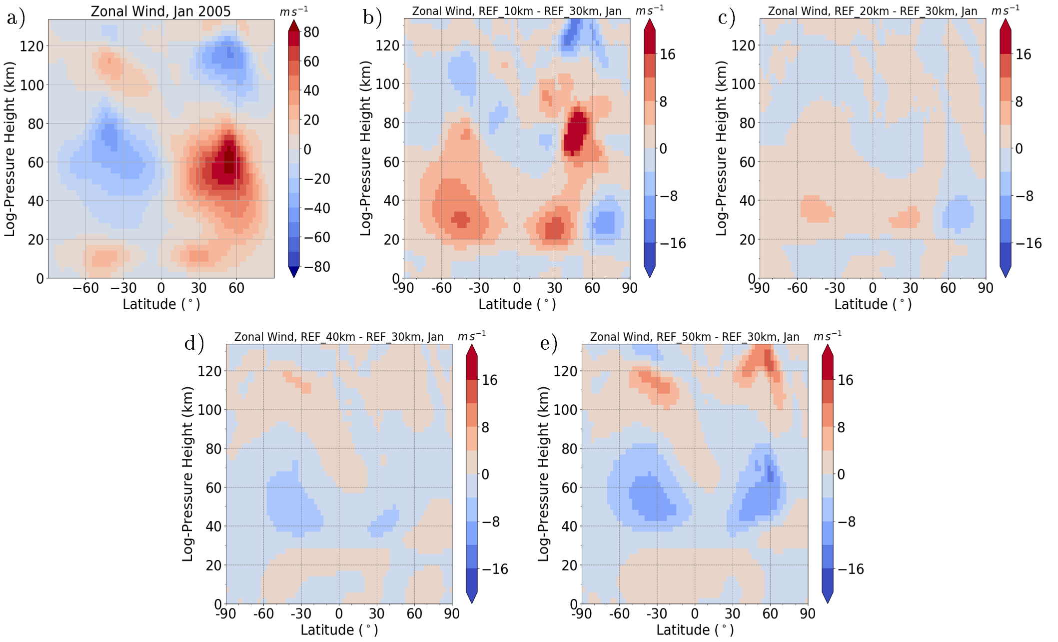

Figure 5.6.: REF run (30 km nudging altitude) zonal wind for January 2005 (left) and the differences between runs with different nudging altitudes of initial conditions 10 km, 20 km, 40 km, 50 km for 2005 conditions and REF run.

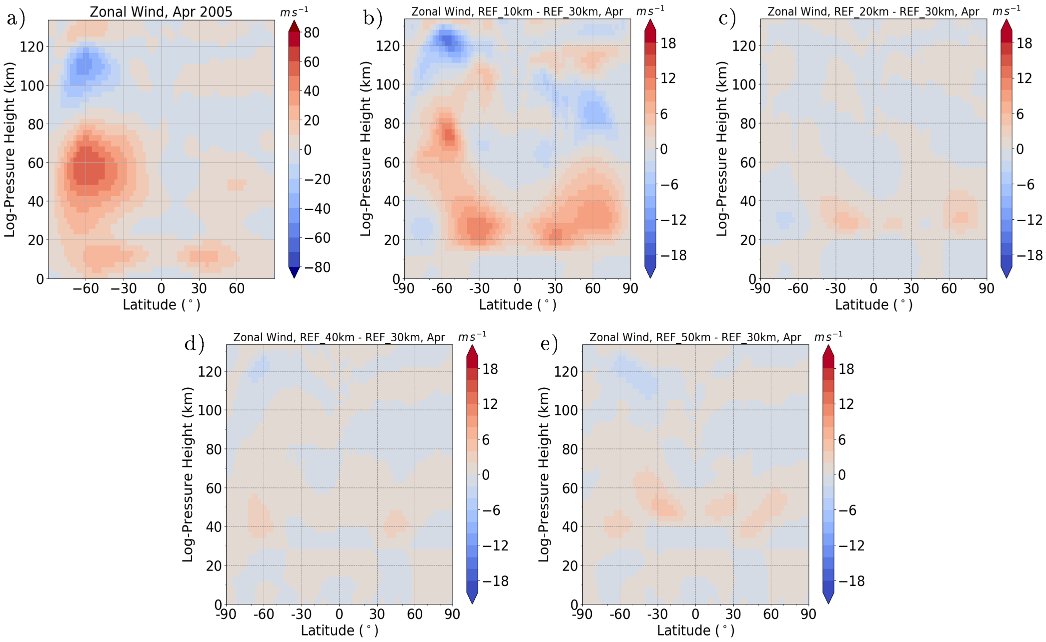

Figure 5.7.: Same like Fig. 5.6 but for April.

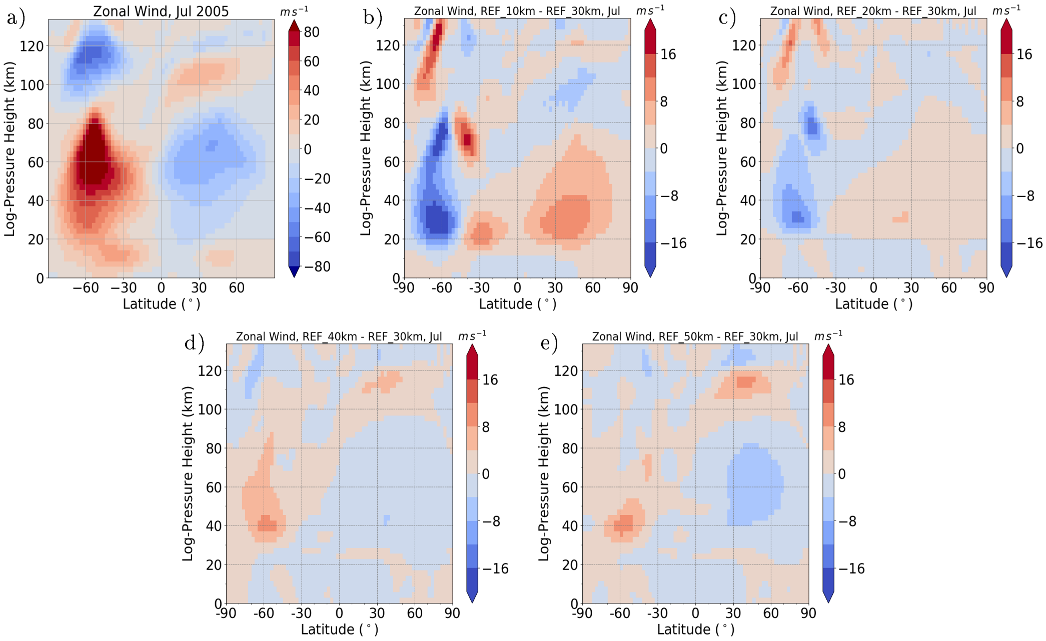

Figure 5.8.: Same like Fig. 5.6 but for July.

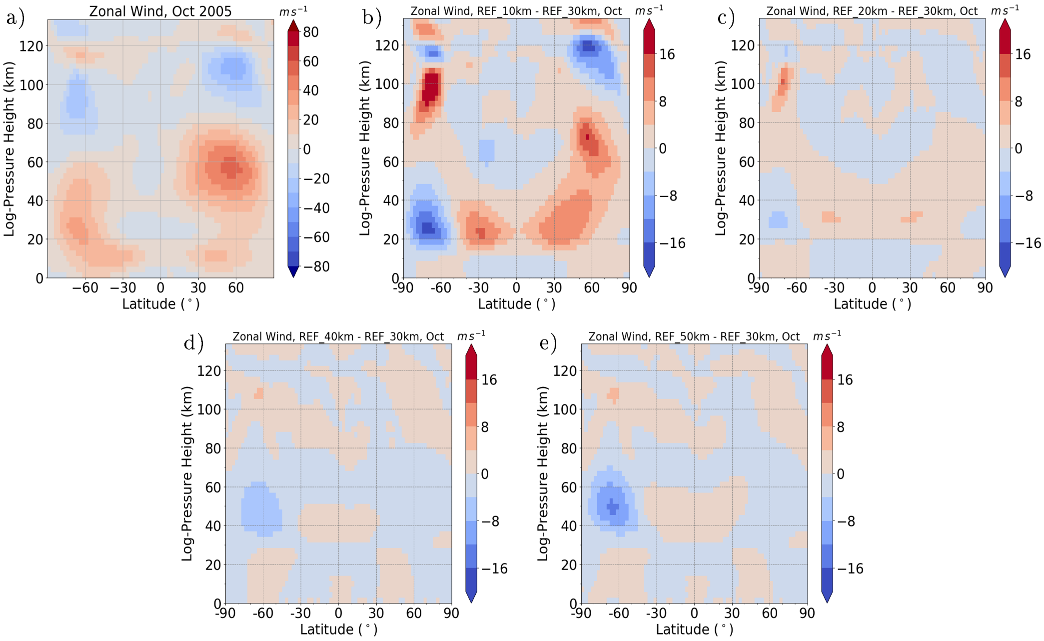

Figure 5.9.: Same like Fig. 5.6 but for October.

QDT Amplitudes

At next the effect of the assimilation altitude of the initial condition on the QDT amplitudes is investigated. This includes all forcing mechanisms of the QDT in all runs. For this purpose the QDT temperature amplitudes for February and October for the REF (assimilation up to 30 km) simulation for 2005 conditions (a) and the differences to the REF run for the runs with 10 km, 20 km, 40 km and 50 km (b - e) assimilation altitude and 2005 conditions are shown in Fig. 5.10 and 5.11. For February, especially in the southern hemisphere, a decrease of the amplitudes can be seen, the higher the data are assimilated. In the northern hemisphere the effect is smaller and mainly limited to lower latitudes. In October this behavior is not visible. There the amplitudes are largest at an assimilation altitude of 20 km. If one looks at the amplitudes in the zonal wind in Fig. 5.12 and 5.13, it can be seen that for February a massive decrease of the zonal wind QDT amplitudes occurs at an assimilation altitude of 50 km. This particularly pronounced in the southern hemisphere, as was already seen in the temperature amplitudes. For October the development of the zonal wind amplitude is also analogous to the temperature amplitudes. While at an assimilation altitude of 10 km the amplitudes are weaker than at 20 km or 40 km, especially in the northern hemisphere, a massive decrease of zonal wind amplitudes can be seen at an assimilation altitude of 50 km. The cause here are the decrease in the westerly wind jet and increase of the easterly wind jet below 80 km altitude in the mesosphere. This effect changes the propagation conditions of the QDT, which can difficultly propagate and this leads to a decrease of the amplitudes. Apparently a stronger easterly wind jet in the southern hemisphere causes a decrease in the QDT amplitudes in February and a too weak or too strong westerly wind jet in the northern hemisphere in October also causes small amplitudes. It is recommended to take a compromise between weaker jets and stronger QDT amplitudes, so that a nudging altitude of the initial conditions of 30 km is chosen in the REF simulations.

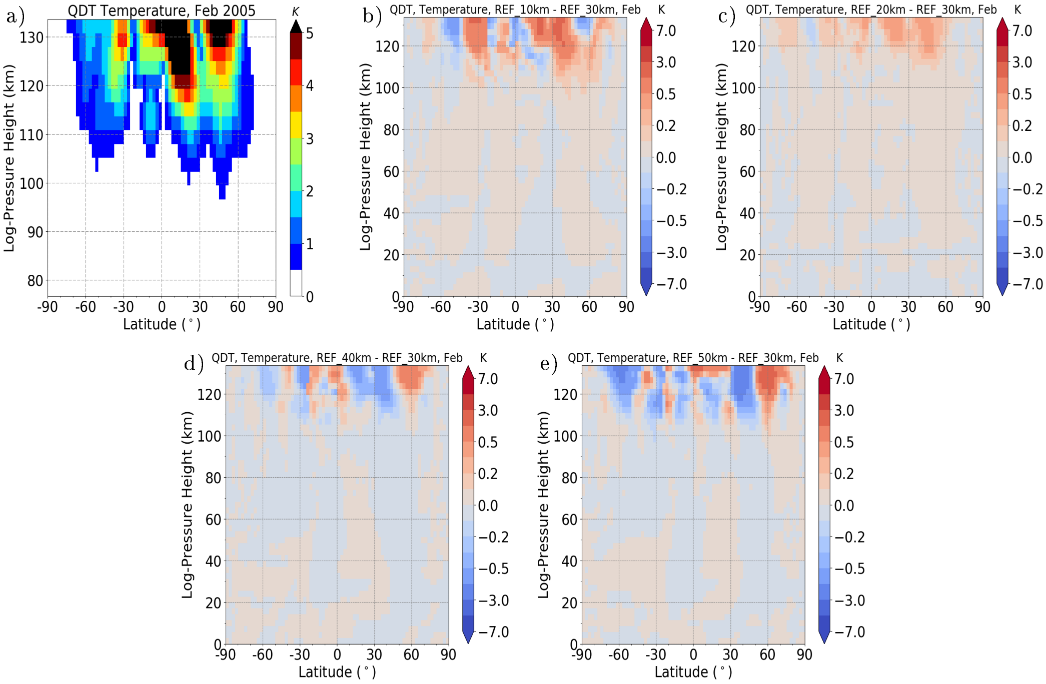

Figure 5.10.: REF run (30 km nudging altitude) QDT temperature amplitude for January 2005 (left) and the differences between runs with different nudging altitudes of initial conditions 10 km, 20 km, 40 km, 50 km for 2005 conditions and REF run.

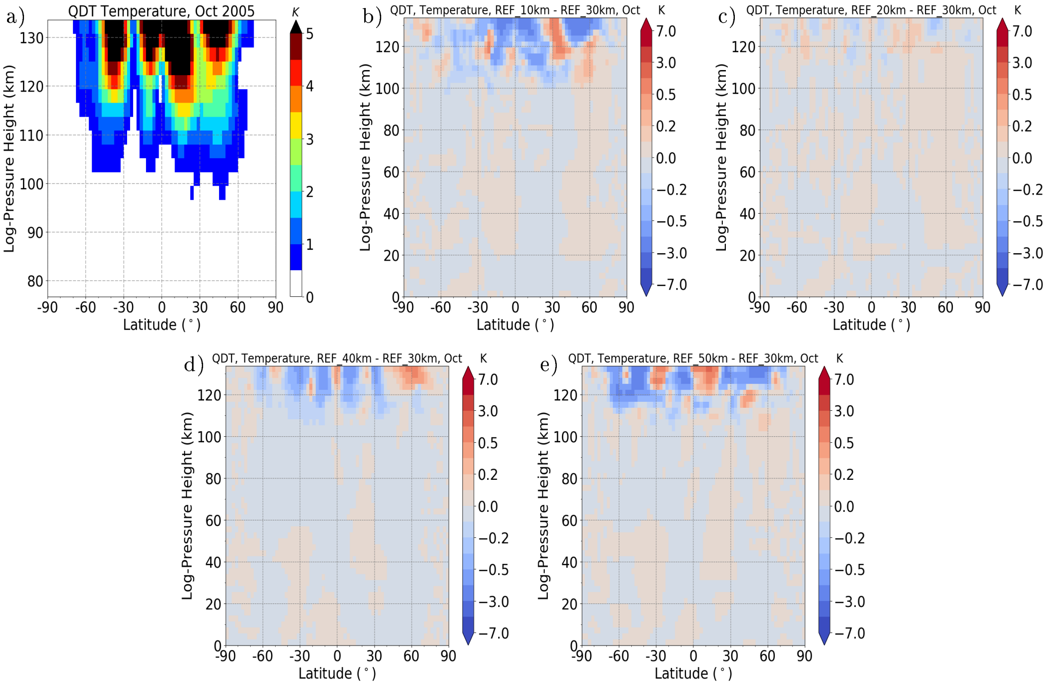

Figure 5.11.: Same like Fig. 5.10 but for October.

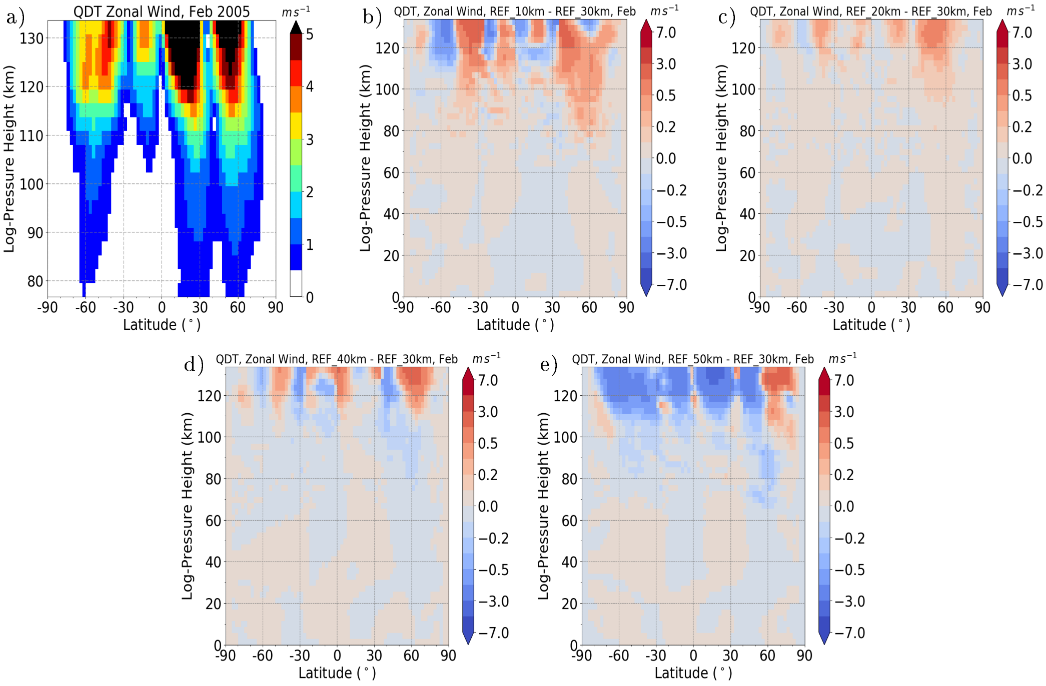

Figure 5.12.: Same like Fig. 5.6 but for QDT zonal wind amplitudes and for February.

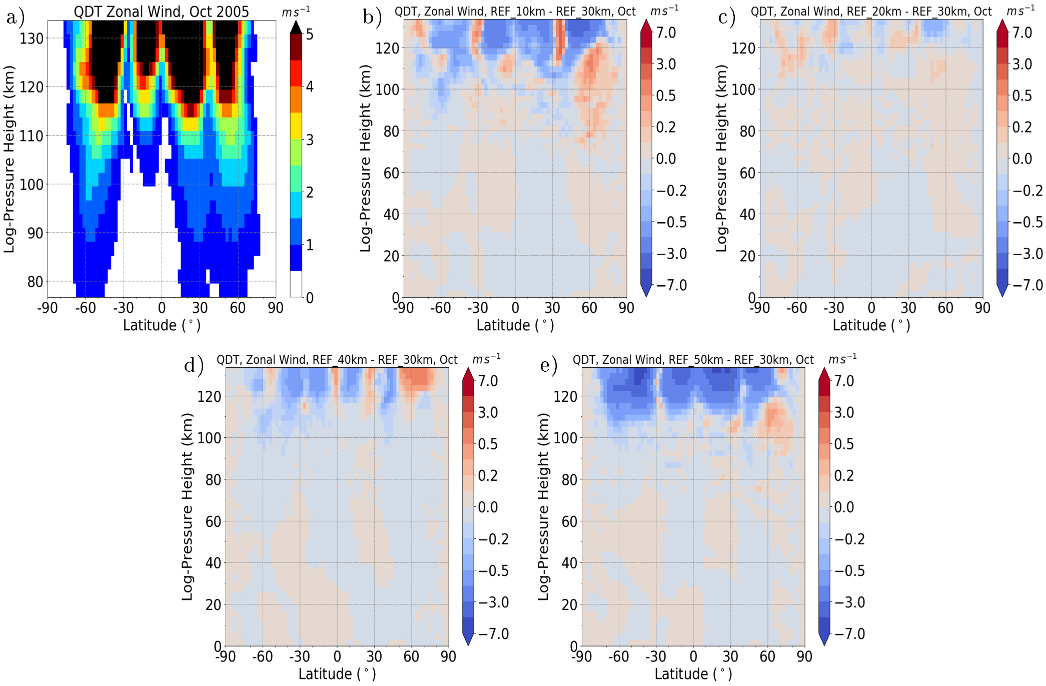

Figure 5.13.: Same like Fig. 5.6 but for QDT zonal wind amplitudes and for October.

5.3. Influence of temporal resolution on the Background Climatology and QDT amplitudes

Since the horizontal resolution of the model was increased, the time step of the model also had to be adjusted for a stable numerical simulation. The question is whether the changes that occurred were only caused by higher horizontal resolution or also by the time resolution changes. Therefore, simulations were carried out with different time steps. The time step can only be selected in a range in which the model works stable, when the model satisfies the Courant-Friedrich Lewy criterion, see chapter 3.2. The model version of Lilienthal et al. (2018) and Lilienthal and Jacobi (2019) had a time step of 225 s, the reference run of Geißler et al. (2020) and this dissertation has a time step of 120 s. In addition, a stable model simulation could be guaranteed for the following time steps: 40 s, 80 s, 150 s, 180 s. The influence of the time step on the background circulation is small compared to the assimilation altitude of the initial condition as described before. In the background temperature the difference is negligible, so that it is not shown here.

Background Climatology

As examples the zonal wind from the REF run for 2005 conditions and the differences to different time steps are shown for January in Fig. 5.14 and for July in Fig. 5.15. The reference run (a) is shown for 2005 conditions, the simulations for the time steps 40 s, 80 s, 150 s, 180 s refer also to 2005 conditions and are shown as differences (b - e) to the REF run (120 s). The model run with 40 s time step became unstable in July and is therefore not shown in Fig. 5.15. For January, the mesospheric jets of the northern hemisphere show a total increase of about 10 ms^{-1} between a time step of 40 s and 180 s. On the southern hemisphere, the easterly wind jet decreases of about 10 ms^{-1}. The structure of the jets is unaffected by the changes. This also applies to July, where the maxima of the jets only increase in the southern hemisphere by a total of about 5 ms^{-1} with larger time step, while in the northern hemisphere the effect is negligible. The maximum shifts minimally towards the equator in January and towards the poles in July the stronger the jet and the smaller the time step is. Therefore, the REF run (120 km) always seems to have the stronger zonal wind in the difference plots, but this is only due to the shifting and weakening of the maxima. In January at 60° N and an altitude of 70 km the effect is especially noticeable. For this reason the zonal wind for the different time steps is shown in Fig. 5.16 as example for January. For the zonal wind, it follows that a smaller time step compared to the climatology of CIRA 86 or HWM14 model provides more realistic wind speed for the jets of the mesosphere in January and July. However, a smaller time step also requires more computational effort, which must be carefully considered here. In summary, a smaller time step ensures better wind maxima in the jets of the mesosphere.

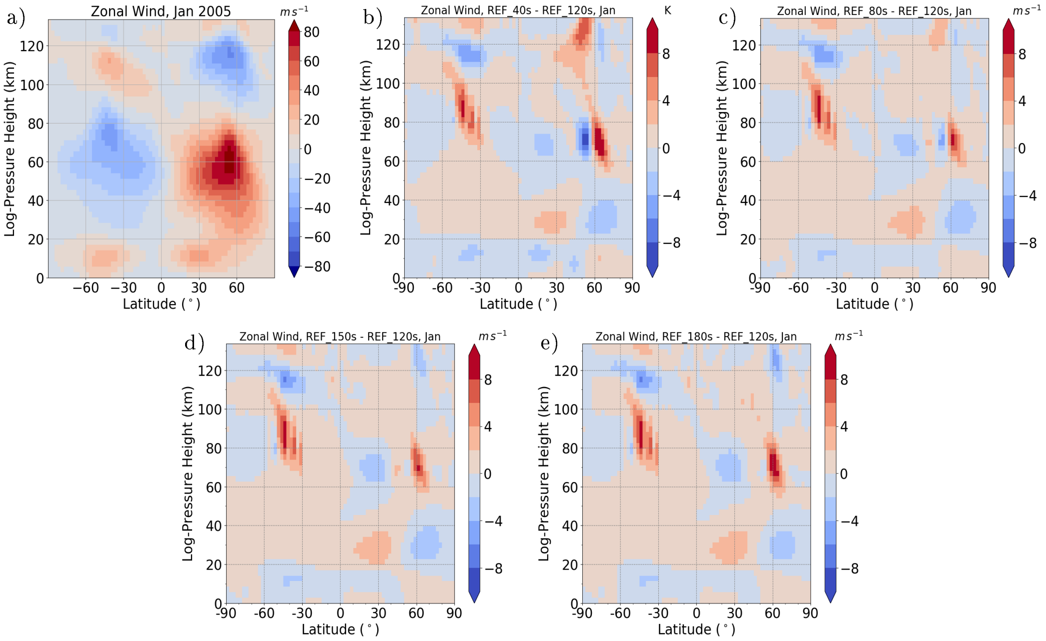

Figure 5.14.: Zonal wind in January for the REF run with a time step of 120 s and 2005 conditions and differences between REF (120 s) and 40 s, 80 s, 150 s, and 180 s.

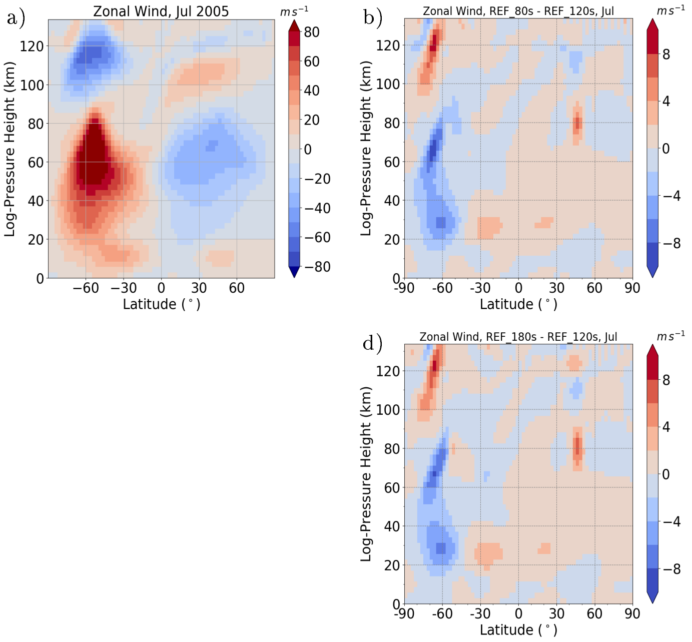

Figure 5.15.: Same as Fig. 5.14 but for July.

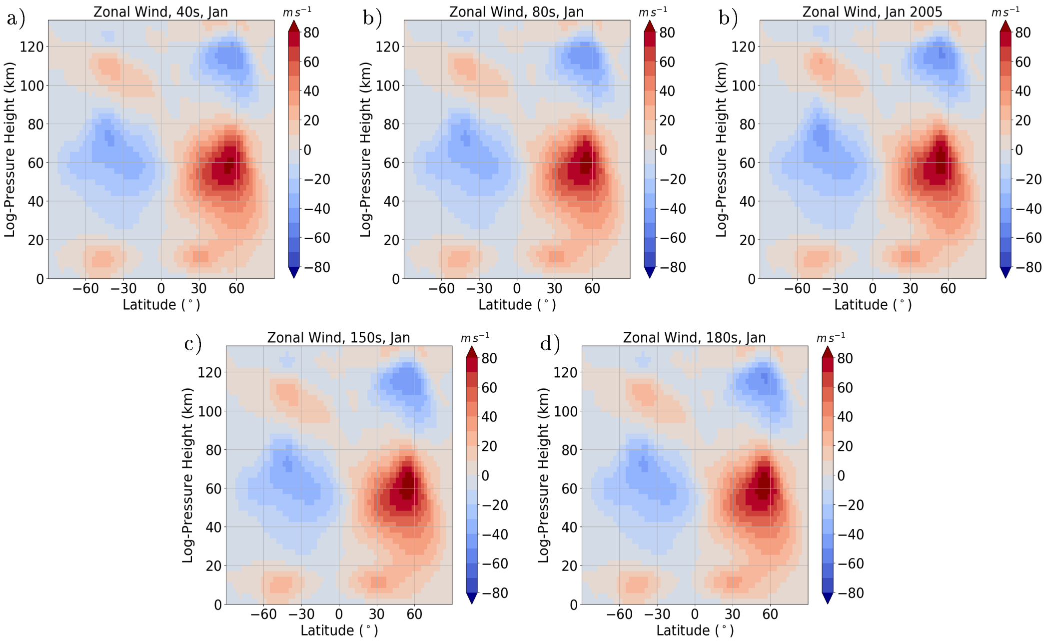

Figure 5.16.: Zonal wind in January for 2005 conditions and the time steps 40 s, 80 s, 120 s (REF), 150 s, and 180 s.

QDT Amplitudes

In Fig. 5.17 for February and in Fig. 5.18 for October the QDT temperature amplitudes for the REF run (a) with 120 s time step for the conditions of the years 2005 and the further runs as differences to the REF run with the time steps of 40 s, 80 s, 150 s, 180 s (b - e) for the year 2005 are shown. In October, the model simulation with a time step of 40 s became unstable and is not shown here. One can see in February (up to 5 K) and October (up to 4 K) that the smaller the time step the larger the amplitudes are. At the same time, this effect is particularly larger even below 120 km altitude, which could not be observed when changing the assimilation altitude.

In Fig. 5.19 and Fig. 5.20 the same representation as before is shown for February and October for the amplitudes of the QDT in the zonal wind. The same behavior as for the amplitudes in the temperature is also to be seen here. The larger the time step becomes, the smaller the QDT zonal wind amplitudes become in all altitudes, especially in the middle and high latitudes.

Here again, the cause seems to be the propagation conditions of the tides have changed, so that the tides can not propagate easily. Accordingly, for larger QDT amplitudes, a time step as small as possible would be preferred, but this would lead to a massive increase on the computing time of the simulations. A time step of 120 s had to be chosen as a compromise.

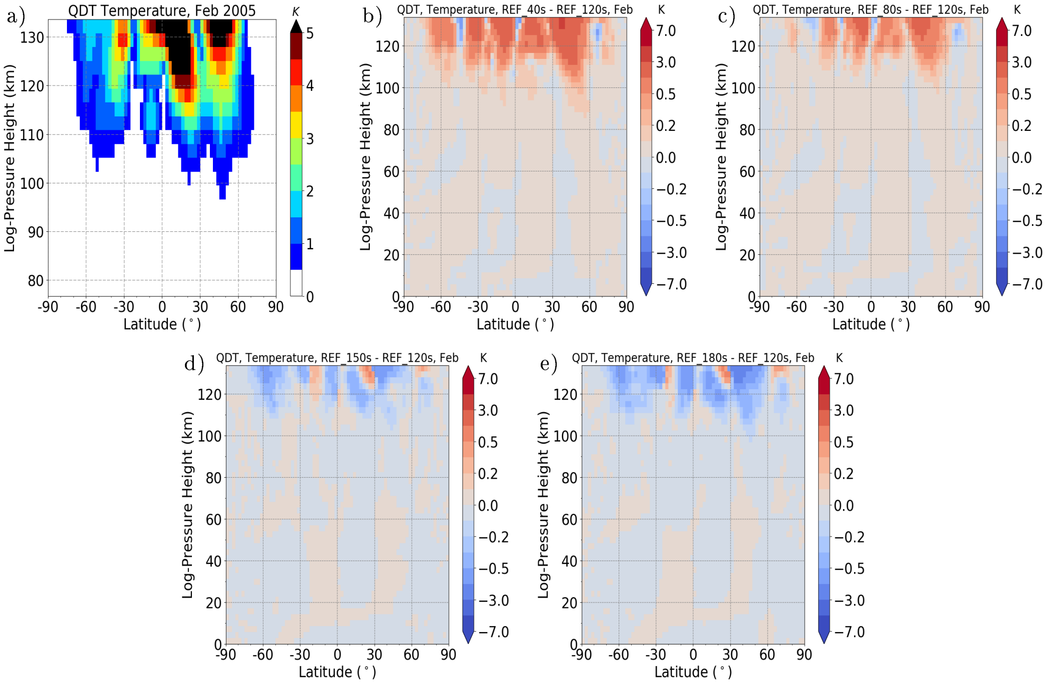

Figure 5.17.: QDT temperature amplitude in February for the REF run with a time step of 120 s and 2005 conditions and differences between REF (120 s) and 40 s, 80 s, 150 s, and 180 s.

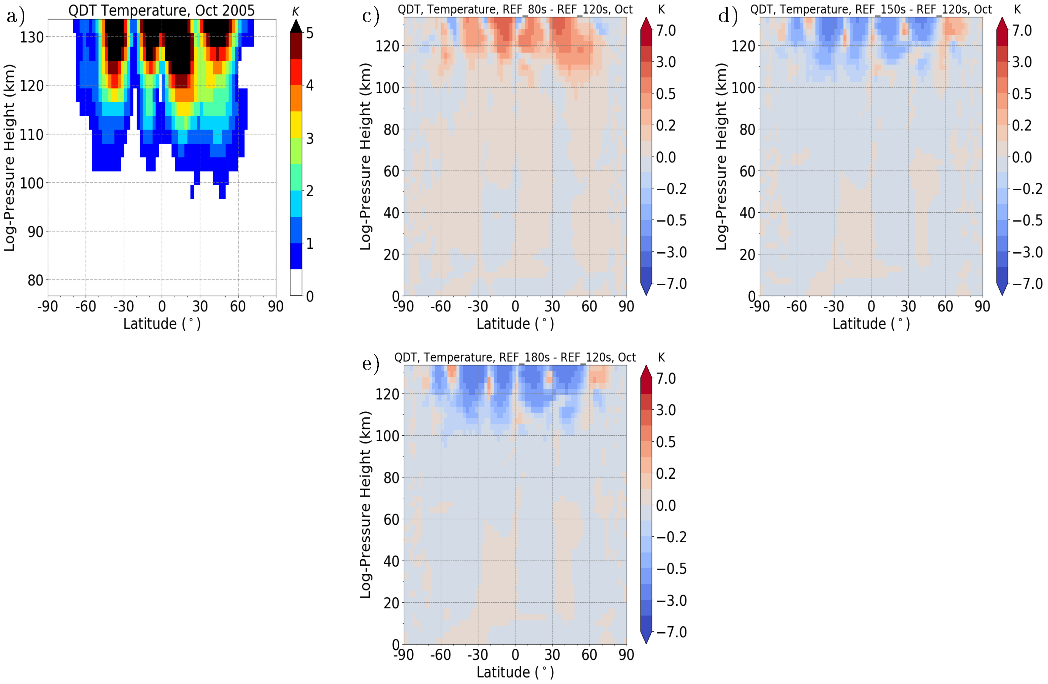

Figure 5.18.: Same as Fig. 5.17 but for October and without the 40 s run.

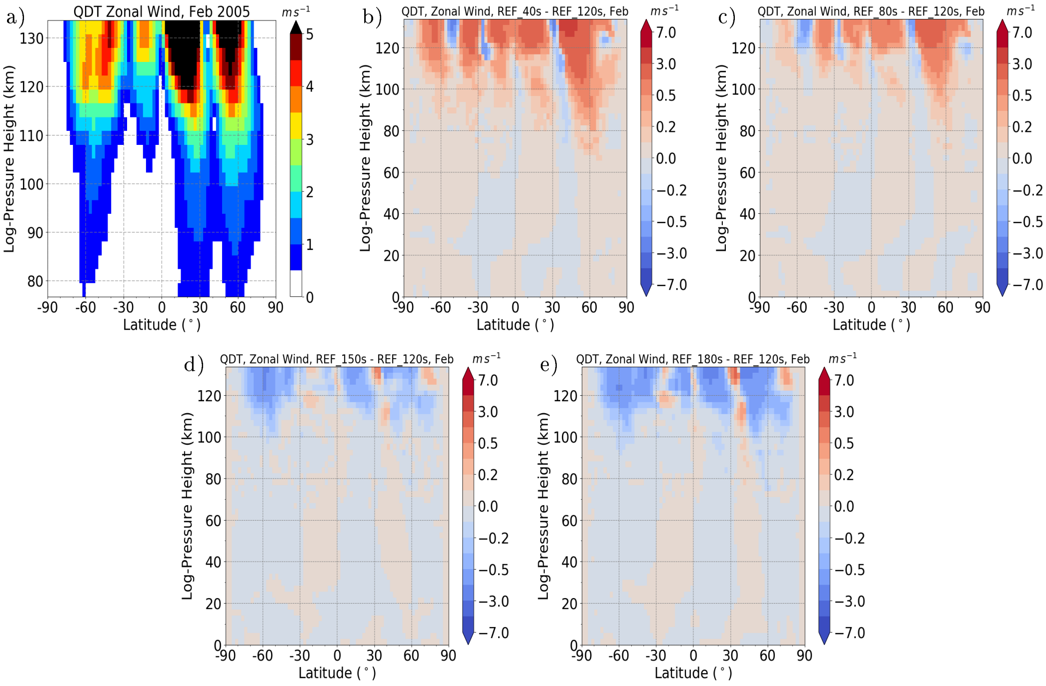

Figure 5.19.: Same as Fig. 5.17 but for zonal wind.

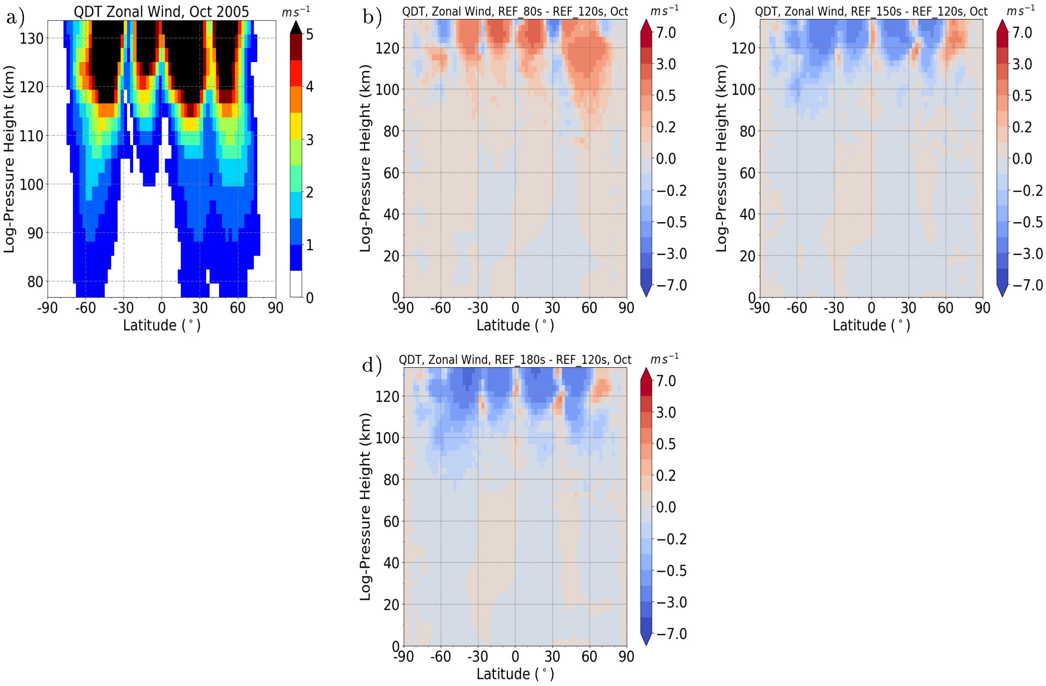

Figure 5.20.: Same as Fig. 5.17 but for October, zonal wind and without the 40 s run.

6. MUAM: Climatology of the Quarterdiurnal Tide

Now a detailed introduction to the reference simulation (REF) will be given, which contains all quarterdiurnal forcing mechanisms (direct solar, gravity-wave - tide interactions and nonlinear interactions). This includes the QDT amplitudes, phases and vertical wavelengths from the REF simulation. First results have already been shown in section 2.2 to demonstrate the sensitivity of the model. Doubling the meridional grid points (36 to 72 grid points) of the model led to better results in the background circulation an in the meridional resolution of the QDT amplitudes. For the altitude of the nudging of the lower boundary condition of ERA-INTERIM data it was shown that a balance of these effect has to be taken to get a more realistic background circulation and QDT amplitudes. Therefore, all following simulations are based on nudging of the ERA-INTERIM data up to 30 km height. A small time step (40 s or 80 s), on which the model runs stable, would also lead to better results. But that would lead to an excessive computation time to perform the full range of simulations necessary to fully investigate the QDT. A compromise with 120 s time step had to be chosen. These are the basic settings of all following model simulations.

For this purpose, the REF simulation results will be compared with observations from the literature, which have already been presented in chapter 2.2.

6.1. Amplitudes

Fig. 6.1 shows the QDT amplitude for the reference simulation as ensemble (2000-2010) for the months of February (left) and October (right) for temperature (top), zonal wind (mid) and meridional wind (bottom) as colored areas. The standard deviation resulting from the ensemble simulation is shown as gray lines. For all other months the figures are shown in the supplement, for the temperature in Fig. S4, zonal wind in Fig. S5 and meridional wind in Fig. S6 with the same specifications. It can be seen for the temperature amplitudes in Fig. 6.1, that there are four maxima above 110 km, two on each hemisphere. These are located in the low and middle latitudes, whereby those in the low latitudes of the respective winter hemisphere have the largest temperature amplitudes (6 K) in February, April, August and October. At 100 km altitude, amplitudes up to 0.5 K in temperature and 1.5 ms^{-1} in zonal wind are achieved. Thus, the modeled amplitudes are much smaller than reported from measurements (e.g., Liu et al., 2015; Azeem et al., 2016; Xu et al., 2012; Liu et al., 2020; Pokhotelov et al., 2018), i.e. satellite measurements reveal temperature amplitudes of 5 - 10 K, depending on season and altitude. The standard deviations are larger in months which show larger amplitudes, and also in the winter northern hemisphere, which is connected with the natural variability of the polar vortex. The meridional structure and the seasonal cycle of the QDT amplitudes are very similar at temperature and zonal wind. Here the amplitudes reaches up to 7 ms^{-1} in February, April, August and October. In the case of the meridional wind, on the other hand, a latitudinal dependent structure with five maxima can be seen, which are found in the low and middle latitudes of the respective hemisphere and above the equator. The largest amplitudes are found with up to 6 ms^{-1} in February, April, August and October. Also, for zonal wind, the modeled amplitudes (2 ms^{-1}) are much smaller at 100 km altitude than reported from radar data (e.g., Liu et al., 2020; Jacobi et al., 2017c; Guharay et al., 2018). Radar data show wind amplitudes of 2.5 - 5 ms^{-1}. A climatology of latitude-altitude-cross-section were only presented for single months and seasons for selected altitudes from satellite data, or from radar measurements for a certain latitude. Therefore, in Fig. 6.2 the temperature (left), zonal wind (mid) and meridional wind (right) amplitudes of the QDT are shown for the altitudes 90 km (top), 101 km (mid) and 109 km (bottom) as a latitude-time-cross-section.

The following discussion is taken from Geißler et al. (2020). For an overview of the seasonal cycle of the QDT, Fig. 6.2 shows the QDT temperature and wind amplitudes at about 101 km height. In the northern hemisphere, amplitudes increase in autumn and winter in the latitude ranges 20° N - 40° N and 50° N - 70° N, respectively. Maximum wind amplitudes in the northern hemisphere are seen in February and October; for the meridional wind the largest amplitudes are found in the 20° N - 40° N range, while zonal wind and temperature QDT amplitudes during these months are seen at 50° N - 70° N. In the southern hemisphere maximum amplitudes appear also during autumn and winter (April to October) between 20° S - 40° S and 50° S - 70° S. The higher latitude maximum is more strongly expressed than in the northern hemisphere.

Liu et al. (2015) showed a climatology of QDT temperature amplitudes from SABER/TIMED satellite data between 50° North and South over 10 years. The amplitudes presented by Liu et al. (2015) show maxima near 30° North and South and above the equator. Their QDT temperature amplitudes reach values of 0.5 K to 1.0 K between 70 km and 90 km, and at higher altitudes the amplitudes reach up to 4 K on an annual and long-term average. Thus, the amplitudes observed by Liu et al. (2015) are larger those of the MUAM simulation.

The QDT temperature amplitude maxima in February, April, May and August at 40° N from MUAM simulations in Fig. 6.2 and can be seen in every altitude and agree with the satellite measurements analyzed by Liu et al. (2015). Our simulated maximum in October, on the other hand, does not appear in the SABER/TIMED data. Also, the extrema at about 10° N in June, September and October as reported by Liu et al. (2015) do not match with the MUAM results, because the amplitudes in the model are much smaller than the amplitudes observed by satellites.

Model simulations of the QDT temperature amplitudes at 100 km altitude by Smith et al. (2004) show a similar seasonal and latitudinal amplitude maximum distribution as seen in the MUAM results. Again, however, the amplitudes in the model simulations from Smith et al. (2004) are larger than in the MUAM results. Amplitudes in the MUAM simulations tend to underestimate other results by a factor of about 2 or 3. The reason for this is that latent heat is not included as a QDT source in the model. In addition, the amplitudes of other tides (DT, SDT, TDT) are also too small compared to observations (Lilienthal et al., 2018; Geißler et al., 2020), so that nonlinear interaction processes are possibly underestimated. The amplitudes for the DT, SDT and TDT from the MUAM model are shown in the supplement for the zonal wind in January in Fig. S13. The latitude-dependent structure and the increase of the amplitudes with altitude is correctly reproduced by the MUAM model. However, the maxima of the DT and SDT amplitudes in MUAM are more than 50% lower than those of the GSWM at low latitudes and midlatitudes. Also, comparison with radar measurements (e.g., Manson et al., 1989; Pokhotelov et al., 2018) shows that the amplitudes of the DT and SDT are underestimated in MUAM.

Meteor radar measurements of zonal wind QDT amplitudes at 50°N by Jacobi et al. (2017c, 2018) show maxima in January and February, as well as in April and May, analogous to the MUAM simulations. The maxima in autumn seen in Fig. 6.2 b are also supported by their measurements. Also, the temporal and spatial distribution of zonal wind amplitudes by Smith et al. (2004) show good agreement with the MUAM simulations. The same is the case for the meridional wind amplitudes in Fig. 6.2 c.

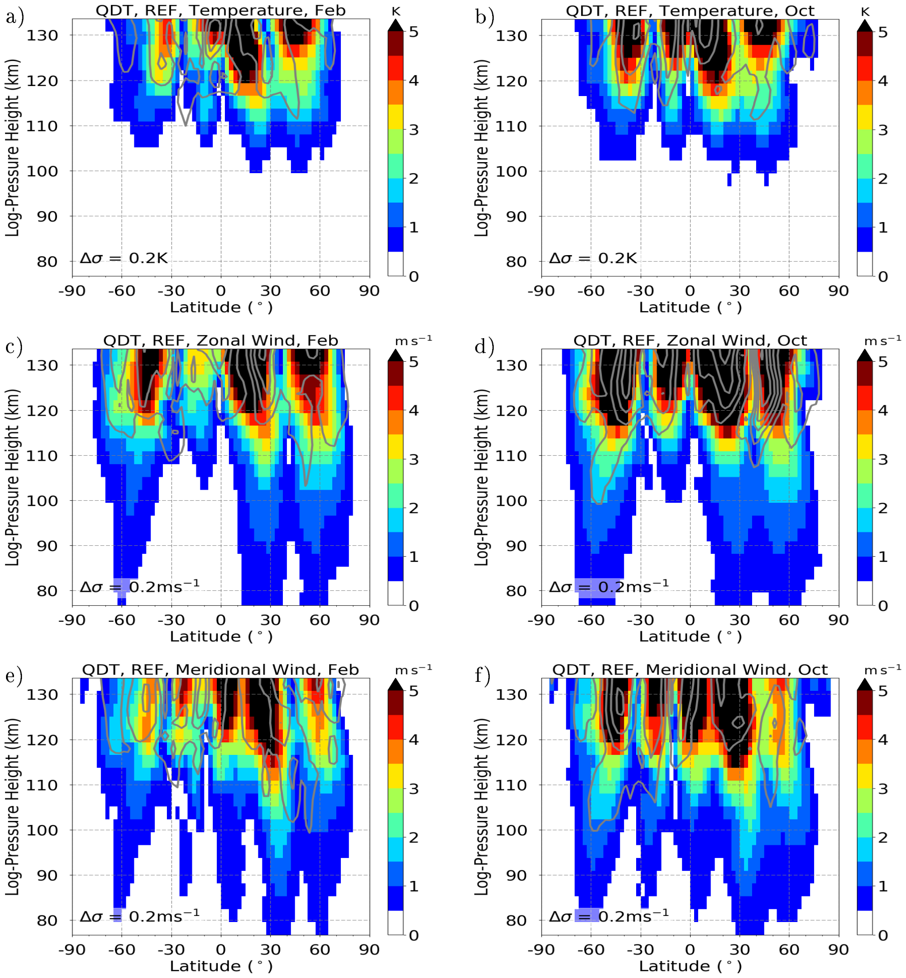

Figure 6.1.: QDT temperature amplitude climatology as color, black lines are standard deviation from ensemble runs. Left for January, right for April, top for temperature, mid for zonal wind, bottom for meridional wind.

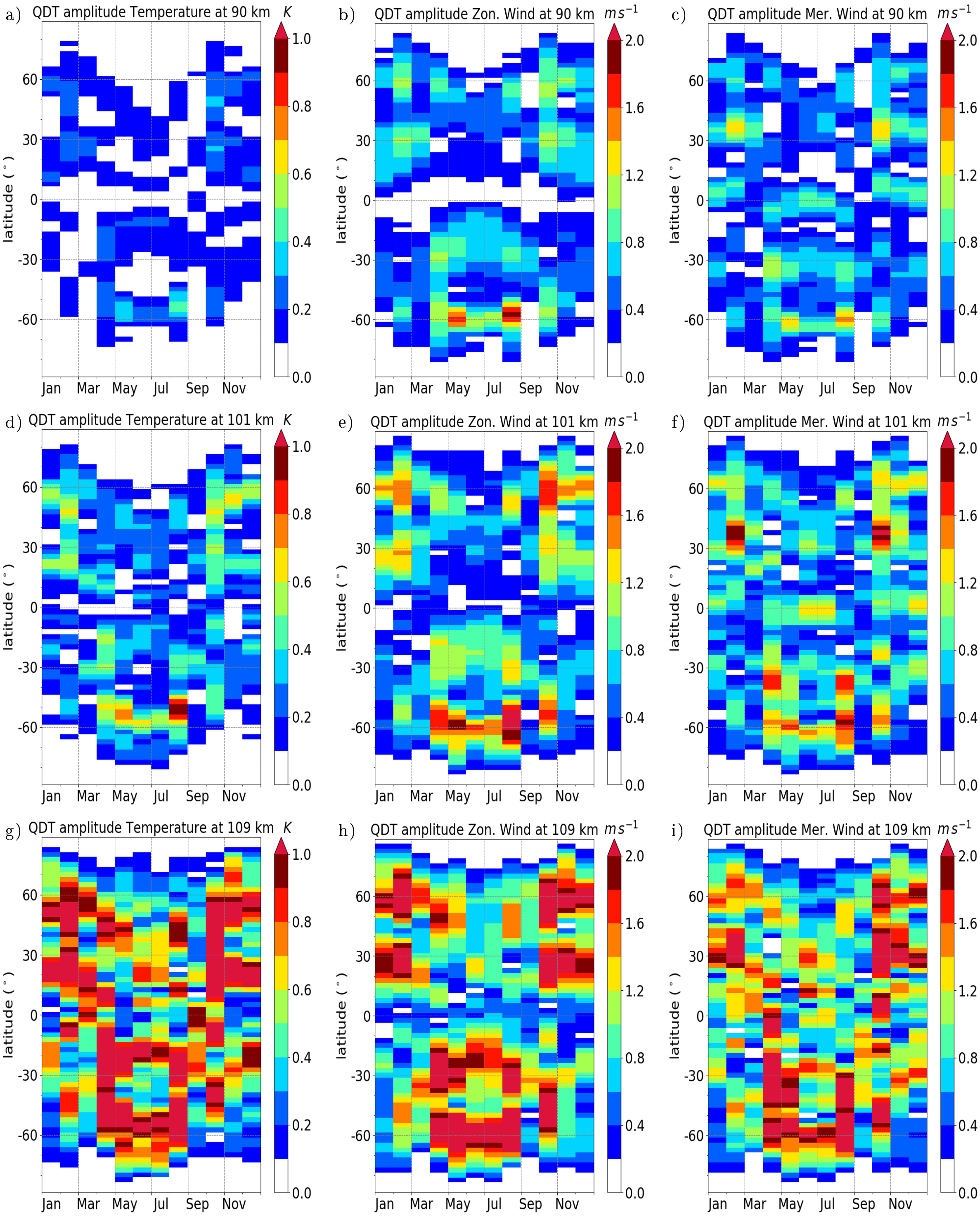

Figure 6.2.: QDT temperature (a,d,g), zonal wind (b,e,h) and merdional wind (c,f,i)amplitudes from the REF simulation as time-latitude-plot for 90 km (top), 101km (mid), 109 km (bottom).

6.2. Phases and Vertical Wavelengths

The phases of the QDT are more uniform in January and July than in April and October as shown in Fig. 6.3 for January and April and for all months for temperature in Fig. S7 for zonal wind in Fig. S8 and for meridional wind in Fig. S9 in the supplement. In January and July, the phases between ±30° are mostly constant up to an altitude of 110 km. In April the phases of QDT temperature and zonal wind amplitudes are symmetrical to the equator, whereas the phases of meridional wind are antisymmetric with an inversion at the equator. In comparison with the meteor radar measurements between 80 km and 100 km altitude from Smith et al. (2004) above Esrange ($68°N$) and Jacobi et al. (2017b) above Collm ($52°N$) the phases of the QDT show a good agreement with the result from the simulation.

Using the vertical phase gradient of the QDT, $\Delta\Phi_{QDT}/\Delta z$, the vertical wavelength λ_{QDT} can be derived as follows:

$$\lambda_{QDT} = \frac{P_{QDT}}{\Delta\Phi_{QDT}/\Delta z}. \tag{6.1}$$

λ_{QDT} .... vertical wavelength of the QDT
$\Delta\Phi_{QDT}$ .... vertical phase change of the QDT
Δz .... altitude range
$P_{QDT} = 6h$ .... period of the QDT

The vertical phase gradients are here derived from linear fits of the vertical phase profiles with a range of 30 km and the obtained values refer to the center of the vertical window. The altitude range is small enough to obtain vertical profiles of vertical wavelengths, but also large enough to cover magnitudes to 100 km of vertical wavelengths of tides. This has been done for all altitudes and latitudes, but only for correlation coefficients of the linear fit of $R \geq 0.6$ to avoid too much uncertainty. In addition, only phase gradients with a negative slope have been taken into account, as these can be interpreted as upward propagating waves. On the other hand, positive phase gradients indicate a downward propagating wave, but due to increase in density in the downward direction they have small effect on the circulation. The results are shown in Fig. 6.4 and for all months in the supplement Fig. S10 for temperature, in Fig. S11 for zonal wind and in Fig. S12 for meridional wind. In the low latitudes up to about 100 km large wavelengths of about 100 km can be recognized in the zonal wind, temperature and meridional wind only up to about 80 km. In the mid and high latitudes the wavelengths are clearly shorter with 20 km. Altogether the wavelength in the meridional wind is more irregular than in the temperature and zonal wind. The results for the phases for the DT, SDT and TDT are shown in the supplement for temperature, zonal wind and meridional wind for January in Fig. S14 and show shorter wavelengths for the DT and SDT compared to the QDT. Similar behavior is seen between QDT and TDT phases.

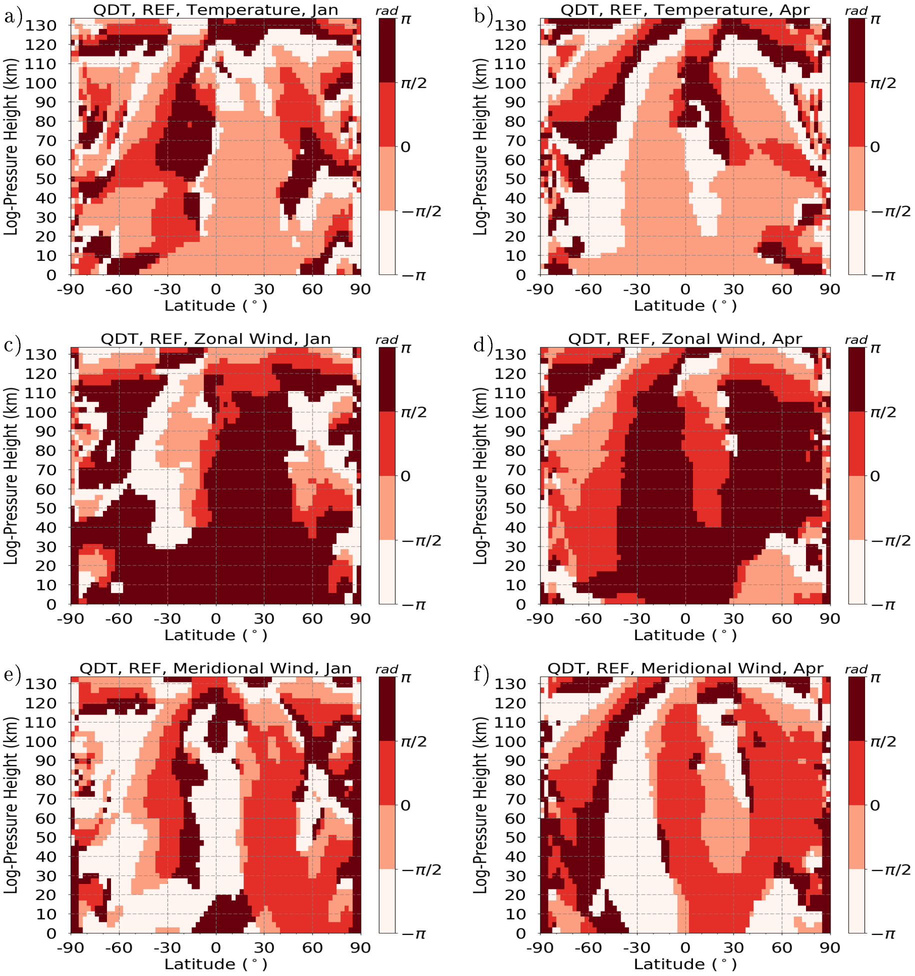

Figure 6.3.: QDT Phases temperature (top), zonal Wind (mid), meridional wind (bottom), left January, right April as color.

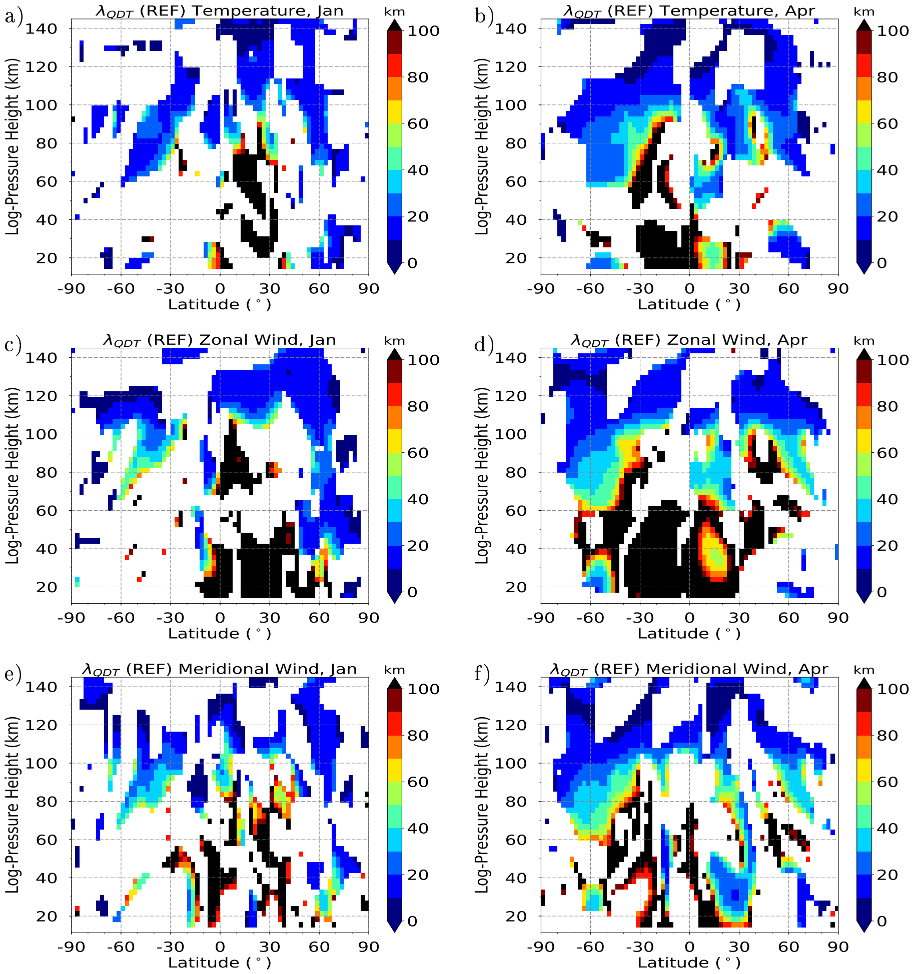

Figure 6.4.: QDT vertical wavelengths, which are a result of a linear fit of vertical phase gradients over a range of 30 km ($R^2 = 0.6$). Temperature (top), zonal Wind (mid), meridional wind (bottom), left January, right April.

6.3. QDT reconstruction with Hough modes

The Hough function are the solution of the Laplace tidal equations and describe the meridional structure of the Eigenmodes (Andrews et al., 1987). This was already described in chapter 1 and equation 1.4. We will now investigate which modes make up the QDT amplitude of the ensemble REF simulation. For this purpose, the meridional distributions of the first 10 Hough modes from the Chebyshev collocation method was calculated (Wang et al., 2016), which solve the Eigenvalue problem for the Laplace tidal equation. This method uses Chebyshev polynomials in the coordinate $\mu = \sin\phi$, which is equivalent to using an ordinary Fourier cosine or sine series in latitudes (Wang et al., 2016). Note, that the Chebyshev collocation method is a universal numerical method. The results for the first 10 Hough modes of the QDT are shown in Fig. 6.5 from mode (4,4) to (4,8) on the left side and from mode (4,9) to (4,13) on the right side. It can be seen, the higher the order of the mode, the finer the meridional structure. In order to determine the modes relevant for the ensemble REF simulation, a function F was defined which calculates the QDT amplitude from the Hough modes:

$$\begin{aligned} F(x,y,t) = {} & h_1(y)[p_1 \ \cos(kx+\omega t) + p_2 \ \sin(kx+\omega t)] \\ & + h_2(y)[p_3 \ \cos(kx+\omega t) + p_4 \ \sin(kx+\omega t)] \\ & + ... \\ & + h_{10}(y)[p_{19} \ \cos(kx+\omega t) + p_{20} \ \sin(kx+\omega t)]. \end{aligned} \tag{6.2}$$

With:

$h_1 ... h_{10}$ .... theoretical latitudinal distribution of Hough-mode 1 ... 10

$p_1 ... p_{20}$ .... fitting parameters

k .... wavenumber

x .... longitude

$\omega = \frac{2\pi}{T}$ .... angular frequency of QDT wave

t .... time

With a Least Squares Fit the optimal amplitude of the individual QDT Hough modes $h_a ... h_j$ was determined in order to obtain the total QDT amplitude that most closely correspond to the QDT from the model simulation (QDT_{MUAM}):

$$[F(x, y, t) - QDT_{MUAM}]^2 \rightarrow min. \tag{6.3}$$

The amplitudes of the individual modes can be calculated from the parameters $p_1 ... p_{20}$ after Eq. 6.4, which gives a reconstruction of the QDT amplitudes from the REF run:

$$\begin{aligned} h_a &= \sqrt{p_1^2 + p_2^2} \\ h_b &= \sqrt{p_3^2 + p_4^2} \\ &\ldots \end{aligned} \tag{6.4}$$

$h_a ... h_j$ … Hough modes 1...10 for reconstruction of QDT amplitudes from the REF run
$p_1 ... p_{20}$ …………………………………………………… fitting parameters

Fig. 6.6 shows the results of the vertical profiles of the individual Hough modes for January, April, July and October for the reconstruction of the REF simulation with 72 latitudes (left) and for the case with 36 latitudes (right) to show the differences in the

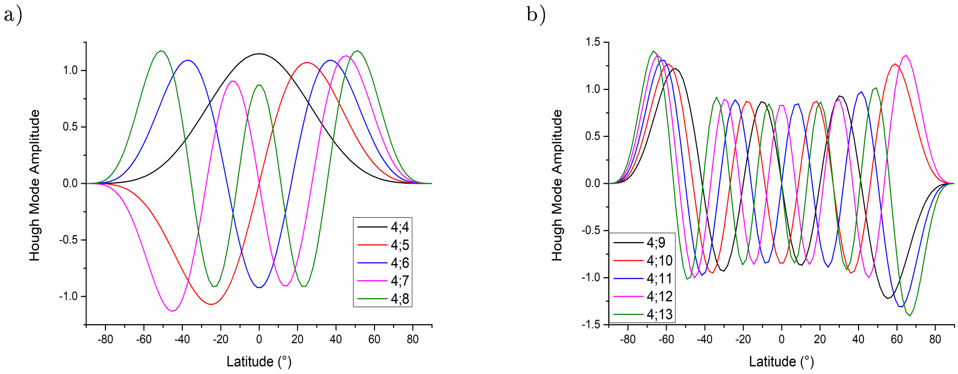

Figure 6.5.: Theoretically calculated QDT Hough modes amplitudes for mode (4,4) to (4,8) on the left and (4,9) to (4,13) on the right for 72 latitudes resolution after Chebyshev method (Wang et al., 2016).

new model version. For the case with 72 latitudes, the QDT Hough modes (4,5), (4,6), (4,7) and mostly also the Hough modes (4,9) and (4,10) dominate in all months for all altitudes. For the reconstruction with a meridional resolution of 36 latitudes there is a difference in the Hough modes compared to the 72 latitudinal reconstruction. Because of a coarser structure of the QDT amplitudes, the Hough modes (4,4), (4,5), (4,6) and (4,7) dominate.

The QDT modes have not been derived from model simulations so far, but only from satellite data which are investigated by Azeem et al. (2016), see also chapter 2.2. However, they were limited to a 60 day period from June to July of a single year and the latitudes between 30° S and 60° N. This makes a comparison with the ensemble model simulations difficult. In order to be able to make a meaningful comparison at all, the reconstruction was repeated for the case that only the latitude range between 30° S and 60° N and only the months June and July were considered. In addition, Azeem et al. (2016) has separated the altitude ranges and considered once the modes from 90 km to 120 km altitude and 120 km to 130 km altitude. The now reconstructed Hough modes are shown in Fig. 6.7 for June (left) and July (right) for up to 130 km (top) and above 130 km (bottom). The altitude ranges were chosen because in the overall profile (not shown here) a change of the predominant modes at an altitude of 130 km could be seen. Below 130 km, the Hough modes (4,4), (4,9), (4,10), (4,6), (4,7) and (4,11) dominate, above 130 km the Hough modes (4,6), (4,7), (4,9), (4,10), (4,4) and (4,5). At the same time, the dominant Hough modes in June and July are very similar below 130 km but differ fundamentally above 130 km altitude. Both differ from the reconstruction for the REF run, where the Hough modes (4,5), (4,6), (4,7), (4,9) and (4,10) dominated and that also for different months alike. This can be attributed to the limitation of the latitude and altitude ranges. For the altitudes up to 120 km Azeem et al. (2016) saw the Hough modes (4,4), (4,6) and (4,8) as dominating, which at least for the Hough mode (4,4) and partly for the mode (4,6) matches the results from the model simulations. The Hough modes (4,4), (4,6) and (4,7) were found to be dominant for the area above 120 km (Azeem et al., 2016). At least the Hough modes (4,6) and (4,7) also have a large part of the QDT amplitude in the reconstructed model results. Azeem et al. (2016) also notes that the Hough modes do not take nonlinear interactions into account and therefore a correct reproduction of the QDT amplitudes of the satellite data is difficult to achieve.

The results of the temperature reconstruction in MUAM are shown in Fig. 6.8 for the first 10 Hough modes. The reconstructed QDT amplitudes for the months January, April, July and October are shown on the left column, the amplitudes of the REF run in the middle and the differences between these two on the right. The reconstruction shows the meridional structure and the maxima and minima are very similar to the REF simulation. Accordingly, the differences are small between reconstruction and REF run, which are only ±0.2 K below 110 km altitude and ±0.6 K above 110 km altitude, which is also due to the increase of the QDT amplitude with altitude. Since the differences are small, the Hough modes from the Least Squares Fit show the optimal meridional structure and size of the amplitudes. Since the meridional resolution has been increased compared to earlier model versions, the influence of this change on the composition of the QDT Hough modes will be investigated. Therefore, the Least Squares Fit was performed with 36 latitudinal resolution and the results are shown in Fig. S15 in the supplement. Also, here the meridional structure and the maxima and minima could be reconstructed well, which leads to small differences (Fig. S15 right). However, there is a clear difference between different months, the differences in the months January and July are about twice as large as in April and October. Basically the behavior is similar to the case with 72 latitudes, that the differences above 110 km are much bigger than below.

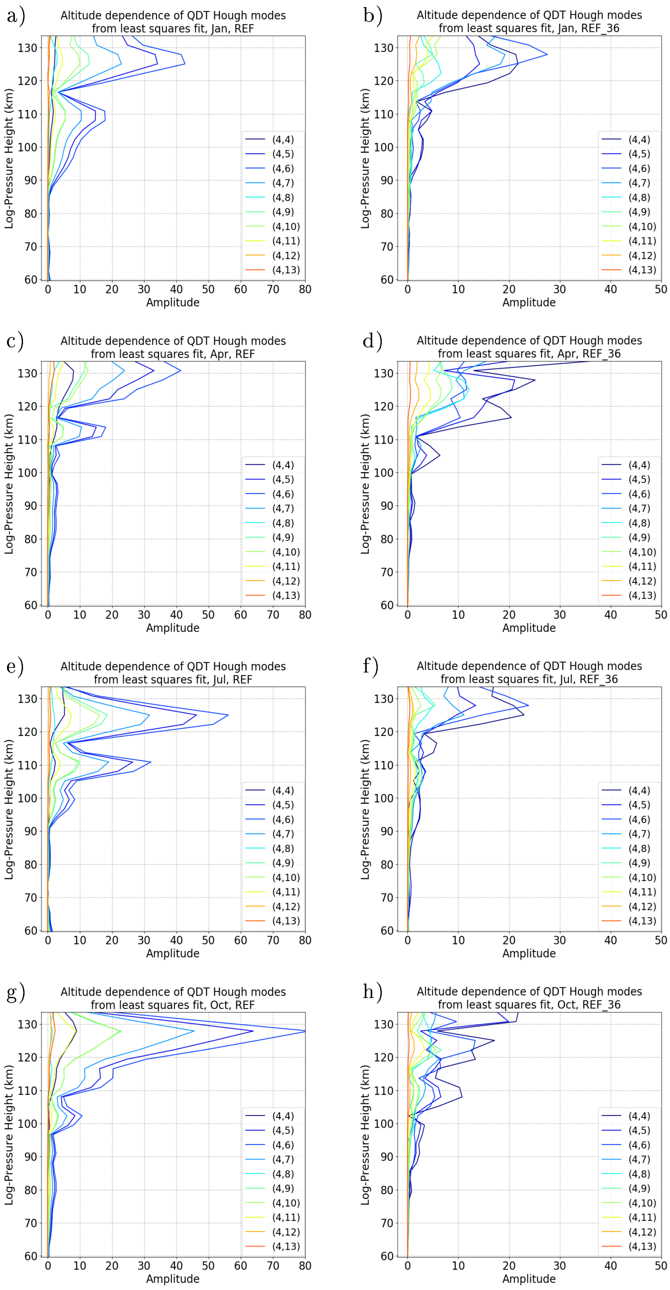

Figure 6.6.: Altitude dependence of the parameters (x1 to x10) from the calculations of Hough modes 1 to 10 with the least squares fit method with equation 6.2. For a resolution of 72 latitudes (left) and resolution of 36 latitudes (right) and January (top), April, July and October (bottom).

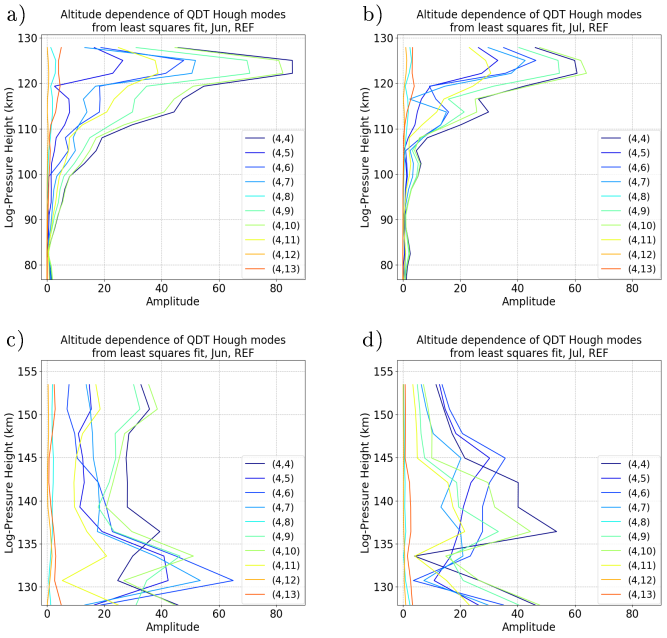

Figure 6.7.: Altitude dependence of the parameters (x1 to x10) from the calculations of Hough modes 1 to 10 with the least squares fit method with equation 6.2. Similar to Azeem et al. (2016) for June and July between 30° S and 60° N for altitudes up to 130 km (a, b) and for altitudes above 130 km (c, d).

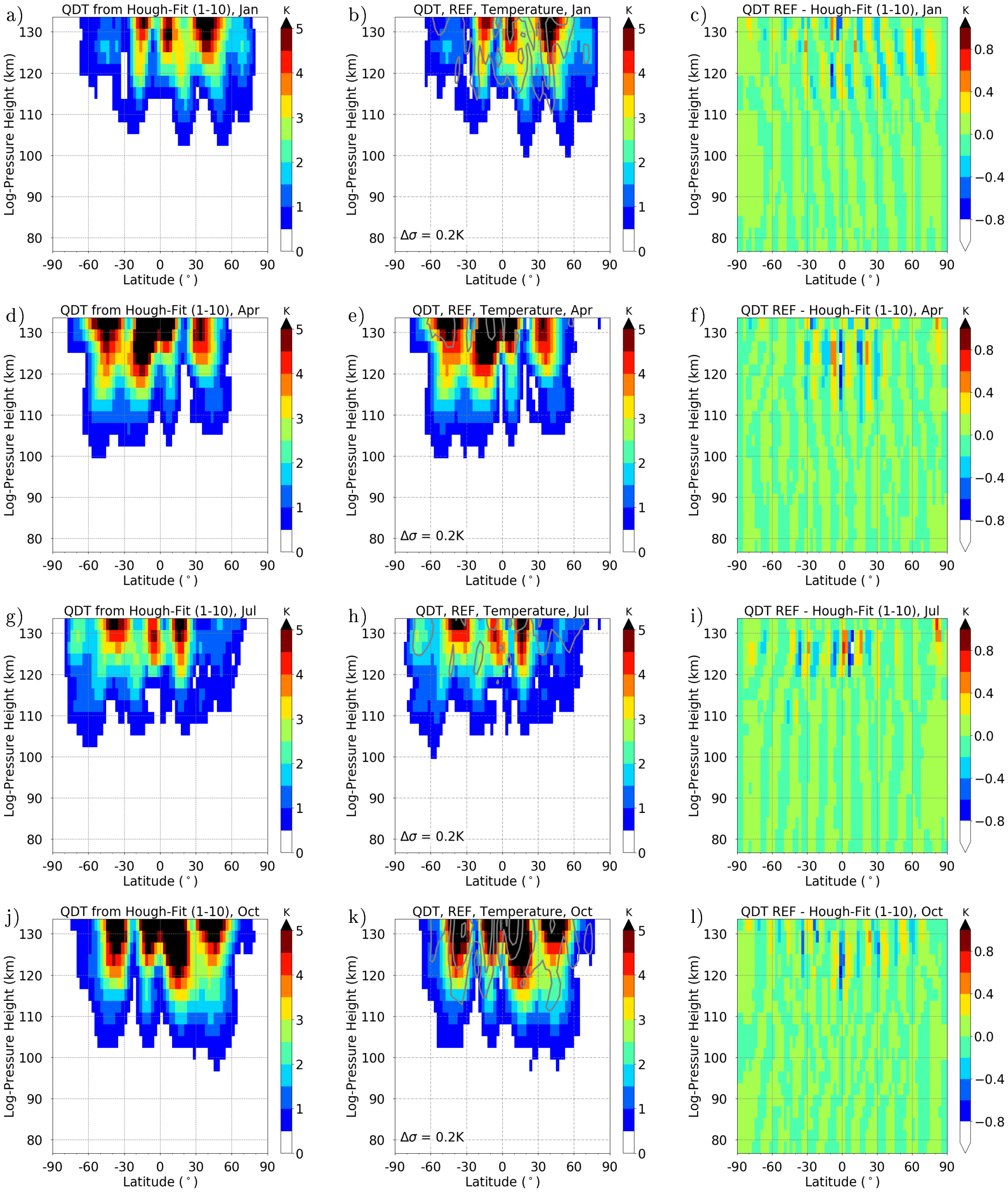

Figure 6.8.: Calculated QDT amplitudes for temperature from Hough modes 1 to 10 with the least squares fit method after Eq. 6.2 (left), REF simulation (mid) and differences between calculations and REF simulations (right) for a resolution of 72 latitudes. For January (top), April, July and October (bottom)

7. MUAM: The Quarterdiurnal Tide Forcing Mechanisms

The numerical model MUAM contains all dynamical features that are included in the prognostic equations. For MUAM these features are introduced in chapter 3.3 with the Eqs. 3.13 - 3.15. By analyzing all terms of the tendency equation of the migrating component of the quarterdiurnal tide, the excitation sources of the QDT can be determined. Some following results have already been shown and discussed in Geißler et al. (2020). These include the QDT climatology, the excitation terms of the QDT and the interactions of the different excitation mechanisms.

7.1. The Quarterdiurnal Forcing Terms

The solar forcing term Eq. 3.15 ($\left.{}^{\partial T}\!/\!{}_{\partial t}\right|_{sol}$) determines the non-zonal heating of the atmosphere. A harmonic analysis after Eq. 4.7 has applied to this tendency term to extract the migrating quarterdiurnal component of the direct solar heating (f_{sol}). The analysis of the migrating QDT component of the GW-tide interactions (f_{GW}) is done similar to the solar forcing. In MUAM GWs are the result of two coupled parameterizations (Lindzen, 1981; Yiğit et al., 2008), which were described in section 3.3. The results of these parameterizations are simply summed up in the tendency equations. In the tendency equations (Eqs. 3.13 - 3.15) nonlinear wave-wave interactions (f_{nlin}) appear as products of non-zonal parameters from u, v, w and T. Their separation and extraction is complicated and leads partly to numerical instabilities. For this reason the eddy diffusion, molecular conduction and Coriolis terms are neglected in the following. To understand the nonlinear interactions, as example the first term of the equation 3.13 is used. This term can be written as ${}^{\Delta u^2}\!/\!{}_{\Delta x}$ and Δu^2 can be divided into its parts like: $(\overline{u}_{i+1/2} + u'_{i+1/2})^2 - (\overline{u}_{i-1/2} + u'_{i-1/2})^2$. More details are described in Lilienthal (2019). In detail, the nonlinear interactions from the first term of equation 3.13 are as follows:

$$\begin{aligned}
\frac{\Delta u^2}{\Delta x} &= \frac{(\overline{u}_{i+1/2} + u'_{i+1/2})^2 - (\overline{u}_{i-1/2} + u'_{i-1/2})^2}{\Delta x(j)} \\
&= \underbrace{\frac{\overline{u^2}_{i+1/2} - \overline{u^2}_{i-1/2}}{\Delta x(j)}}_{zonal\ mean\ flow} + \underbrace{\frac{2\overline{u}_{i+1/2}u'_{i+1/2} - 2\overline{u}_{i-1/2}u'_{i-1/2}}{\Delta x(j)}}_{wave-mean\ flow\ interactions} + \underbrace{\frac{u'^2_{i+1/2} - u'^2_{i-1/2}}{\Delta x(j)}}_{wave-wave\ interactions}
\end{aligned} \tag{7.1}$$

The first term on the right side is related to the zonal mean flow, the second term represents wave-mean flow interactions and the last term includes the nonlinear wave-wave interactions.

All QDT forcing terms from the REF run, including the solar forcing, nonlinear forcing and the forcing resulting from gravity wave - tide interactions, are shown in Fig. 7.1 for January and Fig. 7.2 for April for thermal parameters (a-d) and wind parameters (e-h) as ensemble mean (2000-2010) and gray lines for standard deviation. All other months are shown in the supplement in Figs. S16 - S25. All these forcing terms in the MUAM tendency equations are scaled by the factor $exp[-z(2H)^{-1}]$ in order to account for the growth rate of the amplitudes with altitude due to decreasing density. Thus, the figures show the source regions of the QDT. However, from the parameters shown in Fig. 7.1 and 7.2 no statement about the propagation conditions of the QDT is possible because the tide might be trapped in the source region, not being able to propagate upwards (Lilienthal et al., 2018). In general, the QDT in-situ forcing in January and April shows a similar global distribution.

Fig. 7.1 shows the results for January and Fig. 7.2 for July for the temperature advection (a) and the nonlinear component of adiabatic heating (b) from Eq. 3.13 - Eq. 3.15, which are divided according to Eq. 7.1. Also shown is the heating related to dissipating gravity waves (c) from the tendency terms Eqs. 3.13 - 3.15 $\left.\partial T/\partial t\right|_{GW}$, $\left.\partial u/\partial t\right|_{GW}$ and $\left.\partial v/\partial t\right|_{GW}$ and direct solar heating (d) after $\left.\partial T/\partial t\right|_{sol}$ in Eq. 3.15. Note the different color scales to cover the maxima of all forcing terms. The thermal forcing (Fig. 7.1) of the QDT is dominated by direct solar heating in the troposphere and stratosphere (d). This is due to the absorption of solar radiation by water vapor in the troposphere and ozone in the stratosphere. In the mesosphere (80 - 110 km) nonlinear wave-wave interactions

(a) play the most important role and show maxima at the equator in the stratosphere, mesosphere and lower thermosphere. Nonlinear adiabatic heating (b) maximizes in the upper stratosphere and mesosphere at the equator. However, this forcing is about one order of magnitude smaller than the nonlinear forcing and therefore will be disregarded in the following. In the lower thermosphere, the strongest QDT generation second to solar heating takes place through gravity wave heating (c). Nevertheless, nonlinear effects continue to occur, and they are partly comparable in magnitude with the gravity wave forcing. The QDT acceleration terms in the momentum equations refer to the wind parameters shown in Fig. 7.1 e-h and 7.2 e-h, like the zonal (e) and meridional wind advection (f), the zonal (g) and meridional (h) acceleration due to gravity waves. In the troposphere, stratosphere and large parts of the mesosphere, the nonlinear forcing of both the zonal (e) and meridional (f) QDT wind dominates over the gravity wave forcing (g,h). Near the mesopause, gravity wave zonal and meridional forcing is more important than the nonlinear forcing in zonal and meridional wind. The zonal gravity wave forcing becomes relatively strong above 60 km at the northern middle latitudes. The gravity wave forcing plays a major role above 110 km, where it dominates over other nonlinear forcings. In the meridional component, the wind advection (f) outweighs the gravity wave forcing (h) at almost all altitudes. Figs. S26 - S31 in the supplement also show a comparison of the excitation terms between the model version with a resolution of 36 latitudes and the current version with 72 latitudes for January and April. Note that all excitation terms show slightly smaller excitation in the old model version in contrast to the version with 72 latitudes. This is a consequence of the numerical changes and explains the larger amplitudes of the QDT in the simulation with 72 latitudes.

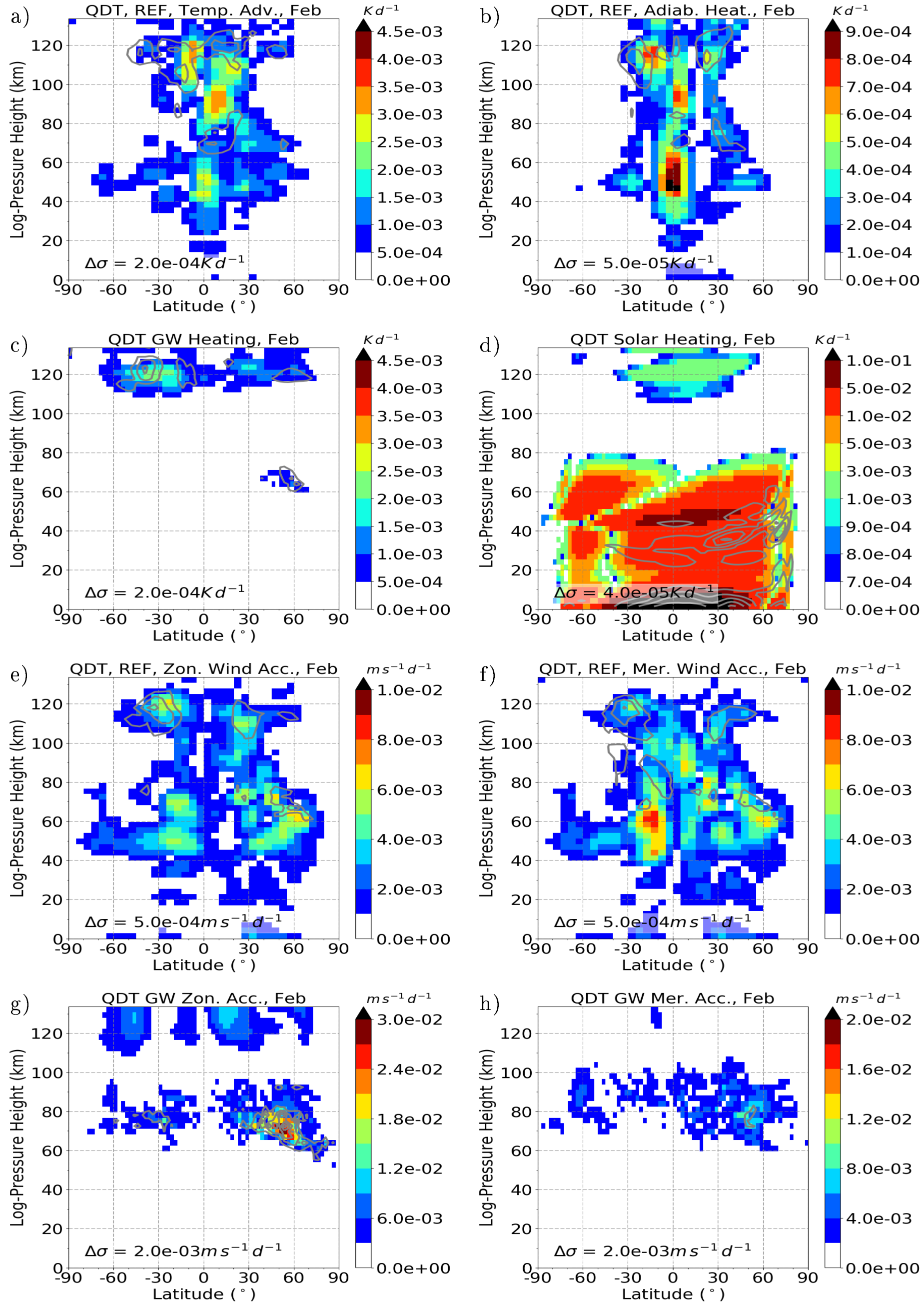

Figure 7.1.: Quarterdiurnal components of tendency terms for February in the REF simulation. Amplitudes are scaled by $\exp{-z(2H)^{-1}}$. Results are an average of the 11 ensemble members (shaded color). Standard deviations (σ) are added as grey contour lines. Temperature advection (nonlinear component), adiabatic heating (nonlinear component), heating due to gravity wave activity (tendency term from gravity wave parameterization), solar heating (tendency term from solar radiation parameterization), zonal wind advection (nonlinear component), meridional wind advection (nonlinear component), zonal and meridional acceleration due to gravity waves (tendency terms from gravity wave parameterization). Note that the color scales are different.

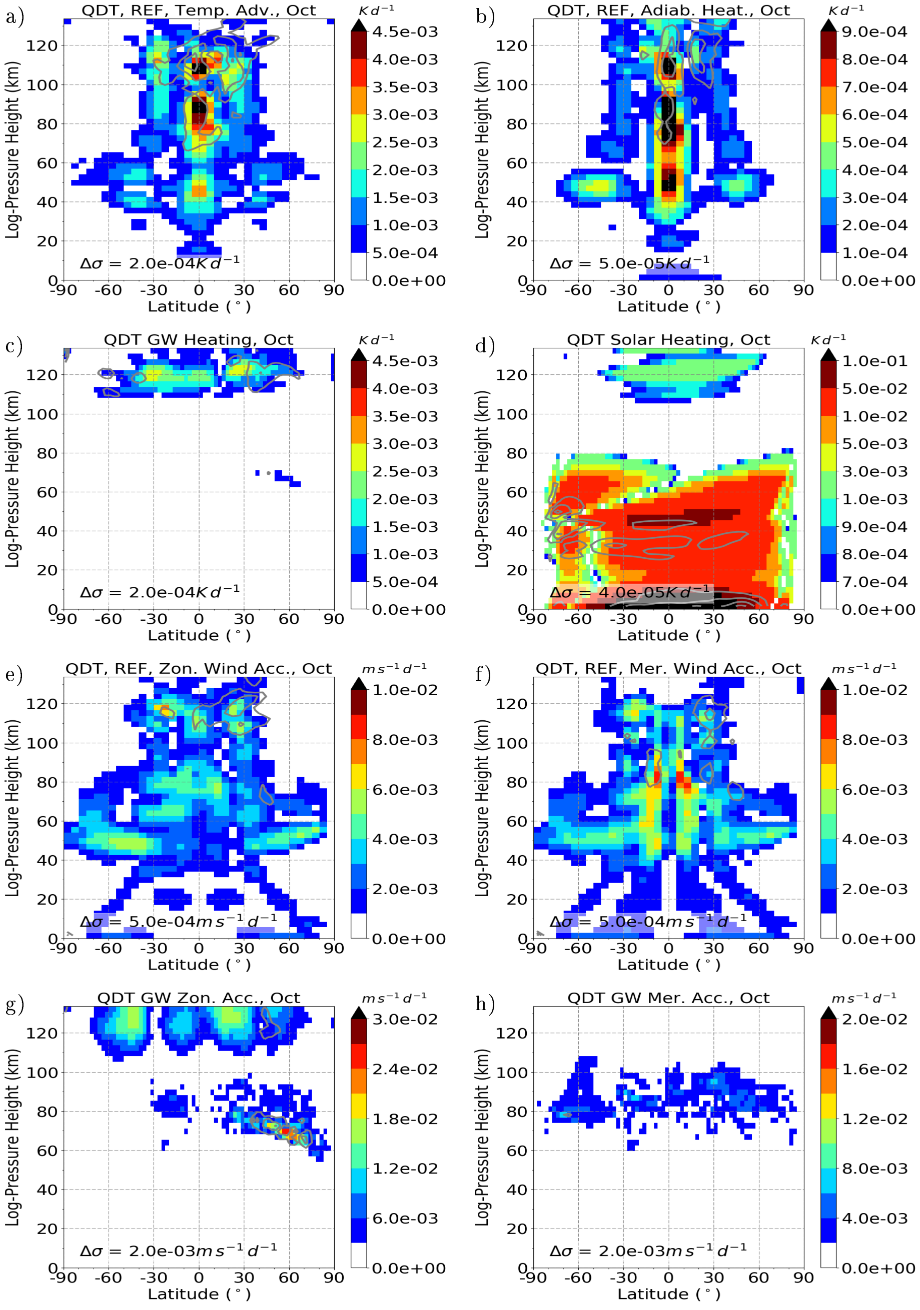

Figure 7.2.: Same as 7.2 but for October.

7.2. Model Experiments and Single Forcing Mechanisms

Solar tides in MUAM, including the QDT, may be generated by three different mechanisms, namely solar heating, nonlinear tide-tide interactions, and gravity wave - tidal interactions, as described in chapter 2 and 2.2 and by Lilienthal et al. (2018) and Geißler et al. (2020). In the following the different forcing mechanisms are removed separately, analogous to Geißler et al. (2020). To this end, a Fourier transform is used (see section 4) and the wavenumber 4 (which is equivalent to the migrating QDT, since there are no non-zonal structures at least for the migrating tides in this MUAM version) amplitude is removed from the respective forcing term during each time step and at each model grid point. To remove the solar forcing mechanism, the wavenumber 4 component heating was removed from all radiation parameterizations. To remove the nonlinear tide-tide interactions, the nonlinear terms are separated, which are essentially the advection terms in the momentum equation and the temperature equation as has been done in Lilienthal et al. (2018) and Geißler et al. (2020). Then the wavenumber 4 component in these terms are removed. Since these advection terms are responsible for wave-wave interaction, this strategy effectively removes the QDT forcing through non-linear interaction. To remove gravity wave - tidal interaction, the total acceleration and heating through gravity wave oscillations of wavenumber 4 are removed. Table 7.1 shows an overview of our simulations, in which different forcing mechanisms are eliminated separately: (i) SOL with no gravity wave - tidal interactions and no nonlinear interactions, (ii) NLIN, without solar forcing mechanism and without gravity wave - interactions, and (iii) GW without solar forcing and without nonlinear interactions. Effectively, these experiments represent model runs with only solar (SOL), nonlinear (NLIN), and gravity wave (GW) forcing of the QDT. Furthermore, two experiments were performed where only one process was removed, namely (iv) NO_NLIN with removed nonlinear interactions, and (v) NO_GW without gravity wave - tidal interaction.

Table 7.1.: Overview on the different model experiments. Activated QDT forcing is marked as ✓, disabled QDT forcing is marked as ✗.

Simulation	Solar forcing	Nonlinear forcing	Gravity wave forcing
SOL	✓	✗	✗
NLIN	✗	✓	✗
GW	✗	✗	✓
NO_NLIN	✓	✗	✓
NO_GW	✓	✓	✗
REF	✓	✓	✓

7.2.1. The Solar Forcing

In Fig. 7.3 a, c the QDT amplitudes and phases (b,d) of the SOL simulations for February and October are shown for temperature and in Fig. 7.4 for zonal wind. The amplitudes and phases for all months can be found in the supplement Figs. S32 - S35. The standard deviations from ensemble runs are given as gray lines. In this run, the gravity wave forcing mechanism and the nonlinear forcing mechanism have been removed from the terms of the model tendency equation. The QDT amplitudes in the SOL run look very similar to those of the REF run in terms of amplitude magnitude and distribution. This agrees well with Fig. 7.1 d and Fig. 7.2 d showing that direct solar forcing is the strongest forcing mechanism and dominates the QDT generation. On closer examination, the southern and northern hemisphere midlatitudes show even larger temperature and zonal wind amplitudes in the SOL run than in the REF run, especially in February. The differences of the QDT amplitudes between the SOL and REF simulation (SOL-REF) are shown in Fig. 7.5 for temperature (a,c) and zonal wind (b,d) for February and October and for all months in the supplement in Fig. S36 for temperature and Fig. S37 for the zonal wind. The areas with a significance level larger than 99% are dotted. Since the variability in the model only results from the changed initial conditions, which are based on monthly rather than daily averages, the significance is generally very high when comparing SOL and REF simulation. The amplitudes in zonal wind during spring and autumn tend to be slightly decreased in the SOL simulation but with similar global structure like those of the REF simulation. Fig. 7.6 shows the temperature (left), zonal wind (mid) and meridional wind (right) amplitudes of the QDT for the altitudes 90 km (top), 101 km (mid) and 109 km (bottom) as a latitude-time-cross-section. In comparison to the REF simulation from chapter 6 Fig. 6.2 there are no significant differences between SOL and REF simulation.

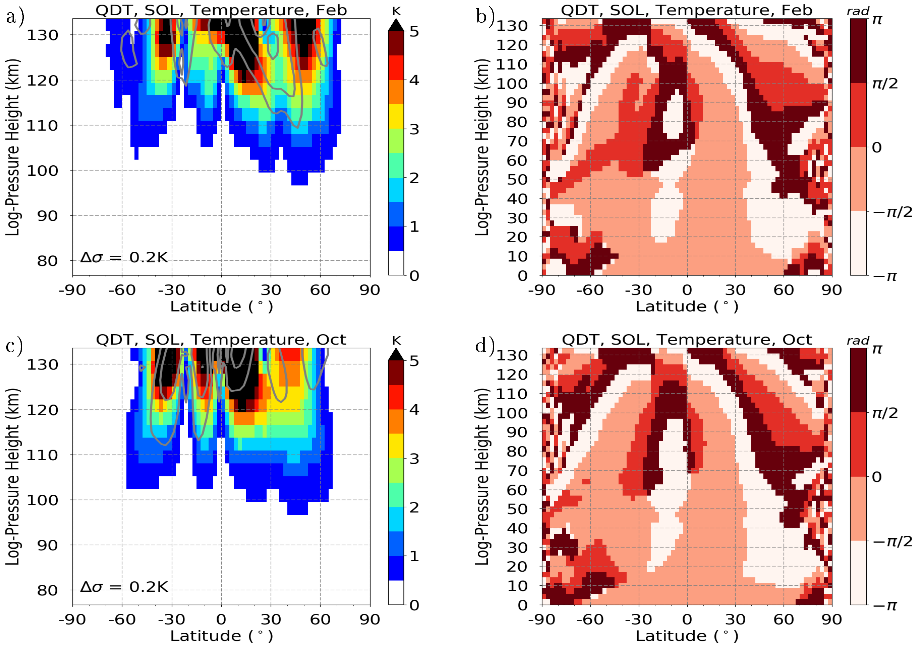

Figure 7.3.: QDT amplitudes (left) and phases (right) for temperature as color from the SOL simulation, grey lines show standard deviation ($\Delta\sigma = 0.2\ K$) from ensemble runs for February (top) and October (bottom).

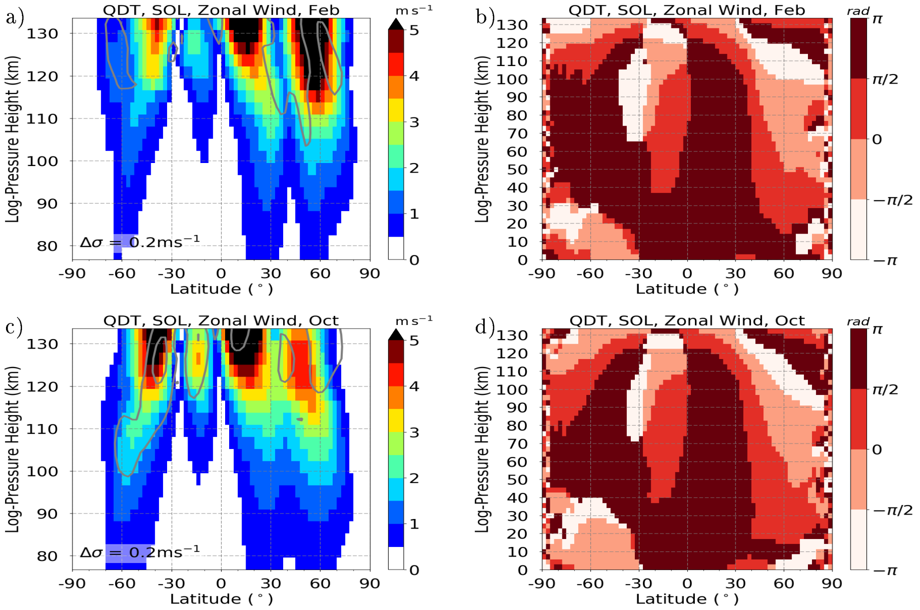

Figure 7.4.: QDT amplitudes (left) and phases (right) for zonal wind as color from the SOL simulation, gray lines show standard deviation ($\Delta\sigma = 0.2\ ms^{-1}$) from ensemble runs for February (top) and October (bottom).

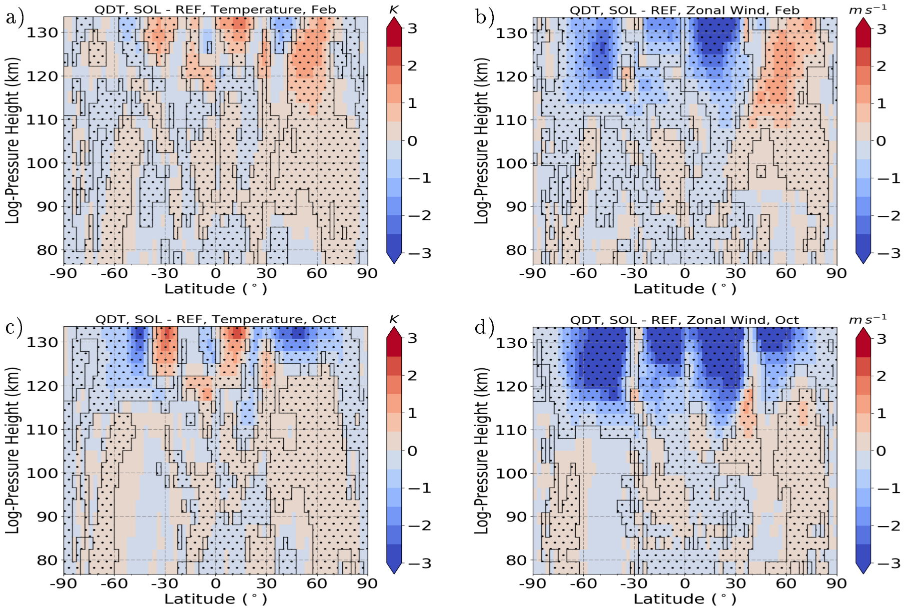

Figure 7.5.: QDT differences between SOL and REF simulation as color. Significance larger than 99% as dotted area. For February (top) and October (bottom), temperature (left), zonal wind (right).

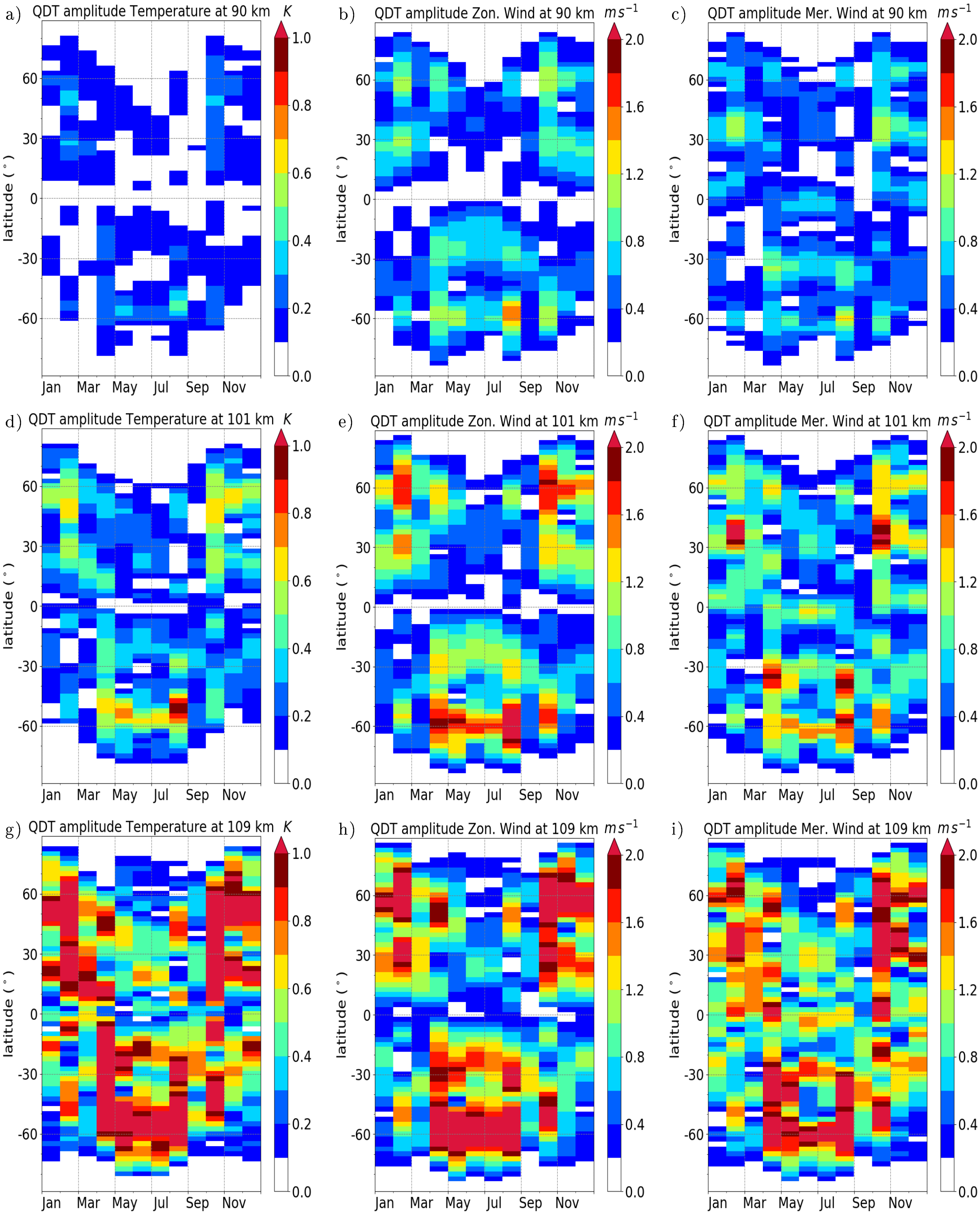

Figure 7.6.: SOL run QDT amplitudes for temperature (a,d,g), zonal wind (b,e,h) and merdional wind (c,f,i) as time-latitude-plot for 90 km (top), 101km (mid), 109 km (bottom).

7.2.2. The Gravity Wave Forcing

The GW run only contains the QDT gravity wave forcing and shows only small temperature amplitudes, up to 2.5 K in July, (Fig. 7.7 a, c) and phases (Fig. 7.7 b, d) for February and October compared to SOL and REF simulation. For other months see Fig. S38 and S39. The standard deviation from ensemble runs is given as grey lines. The zonal wind amplitudes (a, c) and phases (b, d) are shown in Fig. 7.8, for other months see Fig. S40 and S41. The differences of the QDT amplitudes between the SOL and REF simulation (SOL-REF) are shown in Fig. 7.9 for temperature (a, c) and zonal wind (b, d) for February and October and for all months in the supplement in Fig. S42 for temperature and Fig. S43 for zonal wind. The areas with a significance level larger than 99% are dotted. When comparing the phases of the GW run with the REF run, it is noticeable that they are less regular than in the REF and SOL run. REF and SOL run showed very similar phases, which were constant at the equator and low latitudes up to an altitude of 110 km with correspondingly large wavelengths. This is no longer visible in the GW run for temperature and zonal wind. The phases clearly differ from the REF run, i.e. vertical wavelengths are shorter (70 km) and the phase position and distribution have also changed. From 100 km altitude they become even smaller with just 20 km. Similar to the REF simulation, amplitudes gradually increase with height and maxima are located at northern low latitudes of the lower thermosphere, however, they are negligible below 115 km, what can be seen in Fig. 7.14. This is most likely due to the fact that gravity wave - tide interactions mainly take effect in the lower thermosphere. If one compares the amplitudes from the GW run (Fig. 7.14) with the REF run (Fig. 6.2) at 109 km altitude, one can see that the maxima are still found in the lower and middle latitudes. In addition, the GW run shows a maximum directly at the equator in the temperature amplitudes. The months with the maxima in the respective latitudes have also shifted and are no longer found in February, April, August and October, but in March and September. The different forcings therefore have a different meridional and temporal distribution of the maxima.

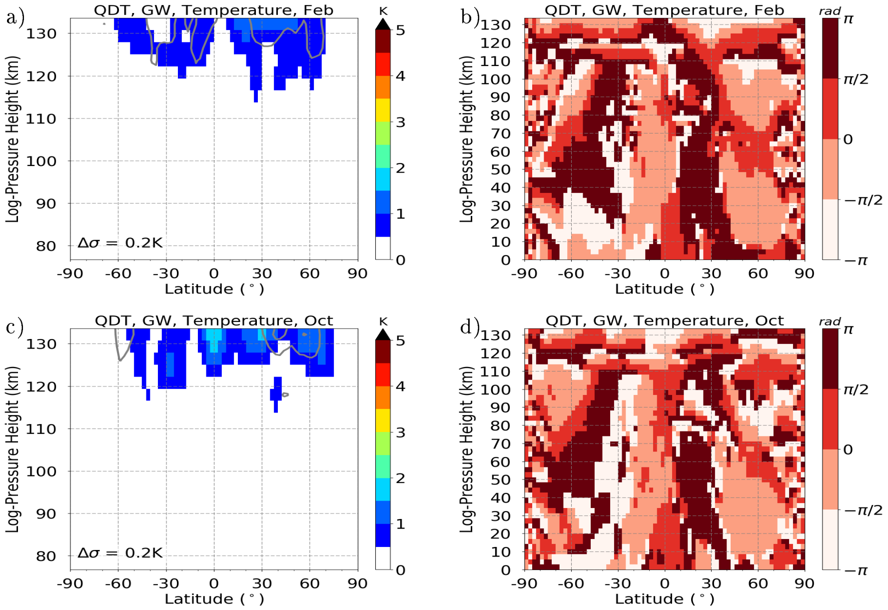

Figure 7.7.: QDT amplitudes (left) and phases (right) for temperature as color from the GW simulation, black lines show standard deviation from ensemble runs. Top February, bottom October.

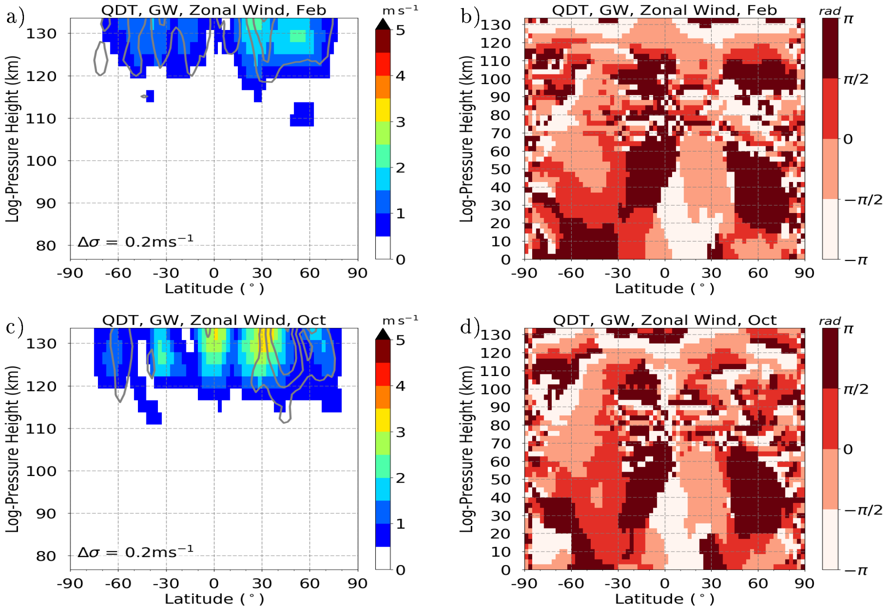

Figure 7.8.: QDT amplitudes (left) and phases (right) for zonal wind as color from the GW simulation, black lines show standard deviation from ensemble runs. Top February, bottom October.

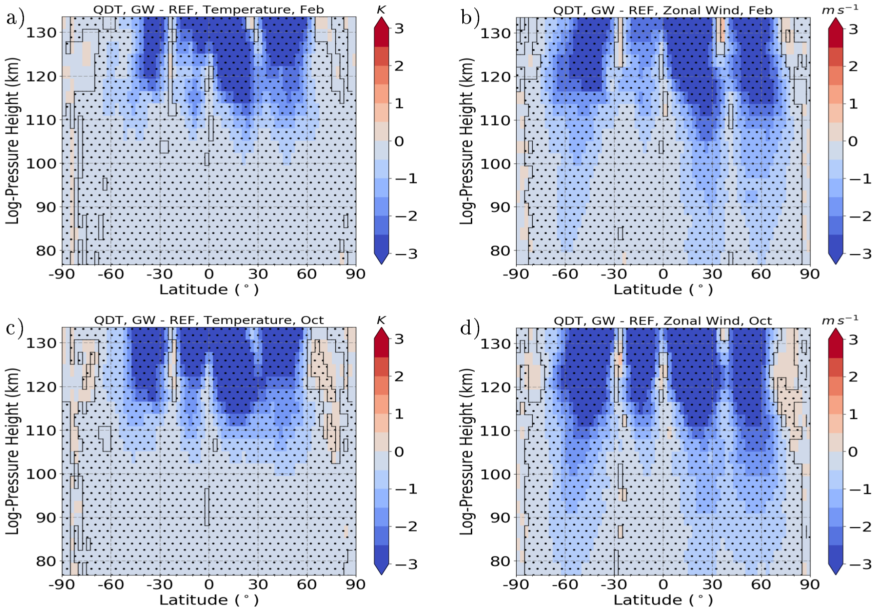

Figure 7.9.: QDT differences between GW and REF simulation as color. Significance larger than 99% as dotted area for February (top) and October (bottom), temperature (left), zonal wind (right)

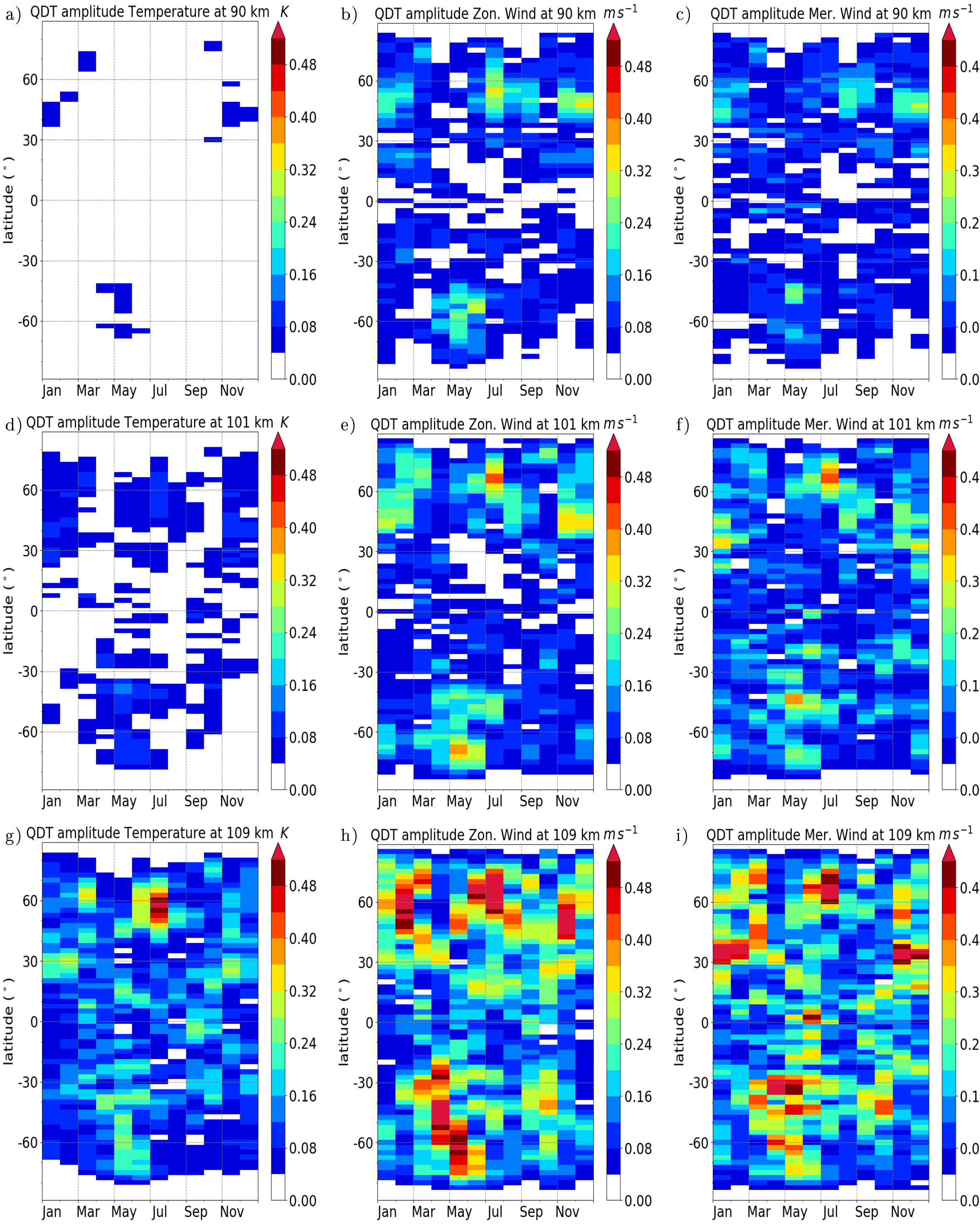

Figure 7.10.: GW run QDT amplitudes for temperature (a, d, g), zonal wind (b,e,h) and merdional wind (c, f, i) as time-latitude-plot for 90 km (top), 101km (mid), 109 km (bottom).

7.2.3. The Nonlinear Forcing

Figures 7.11 and 7.12 show the QDT amplitudes (a, c) and phases (b, d) for the temperature and zonal wind from the NLIN run for February and October. All other months are shown in the supplement Figs. S44 - S47. The standard deviation from ensemble runs is given as gray lines. This simulation contains only the forcing of nonlinear interactions. The amplitudes for the temperature component are comparable to those of the GW run with a maximum of 2 K (October). For the zonal wind component the amplitudes are even smaller than in the GW run with $2.0\,\mathrm{ms}^{-1}$ (June). For the NLIN simulation, only two maxima over the midlatitudes of both hemispheres can be identified. The same can be seen in the time-latitude distribution (Fig. 7.10) in the respective winter months. So the amplitudes are also much smaller compared to the REF run, which is shown in Fig. 7.13 for February and October with larger than 99% significance dotted and for all other months in the supplement Fig. S48 and S49. Keeping in mind that nonlinear tidal interactions mainly occur in the mesosphere (see Fig. 7.1 and 7.2), one may conclude that QDTs generated by this mechanism are trapped near their forcing region and cannot propagate further upward.

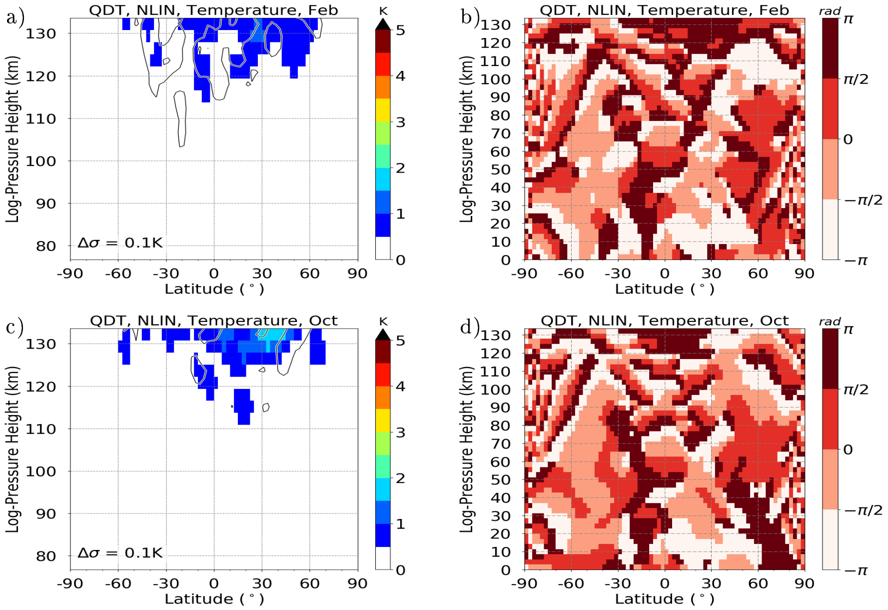

Figure 7.11.: QDT amplitudes (left) and phases (right) for temperature as color from the NLIN simulation, black lines show standard deviation from ensemble runs for February (top) and October (bottom).

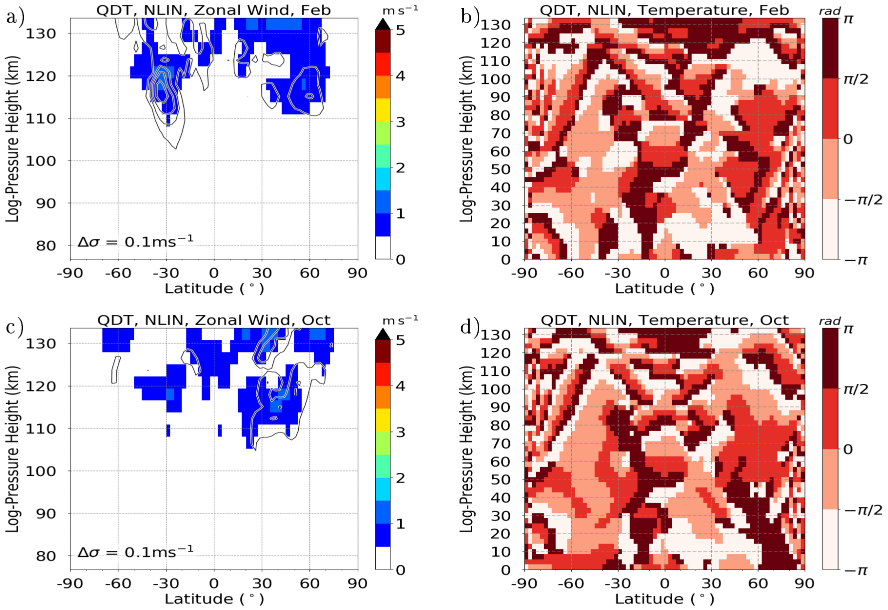

Figure 7.12.: QDT amplitudes (left) and phases (right) for zonal wind as color from the NLIN simulation, black lines show standard deviation from ensemble runs for February (top) and October (bottom).

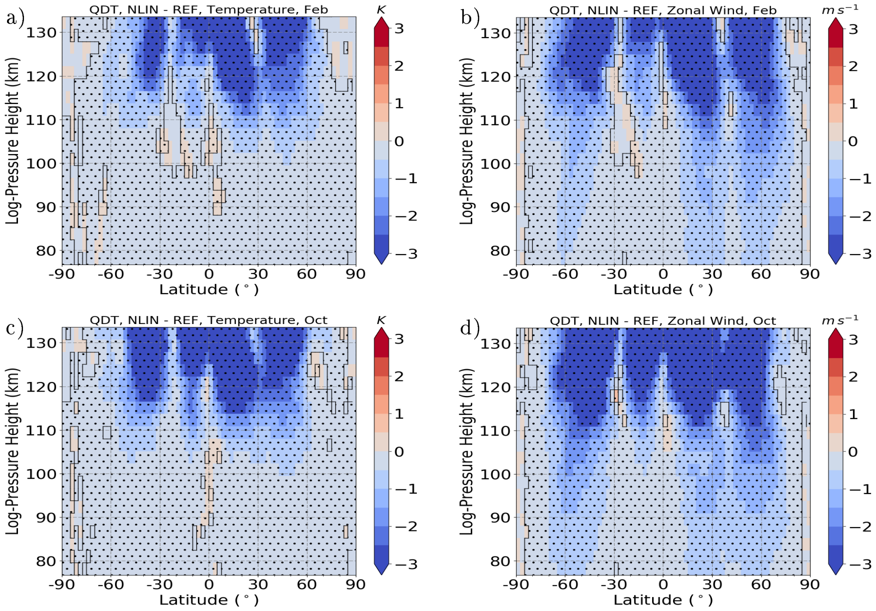

Figure 7.13.: QDT differences between NLIN and REF simulation as color. Significance larger than 99% as pointed area for February (top) and October (bottom), temperature (left) and zonal wind (right).

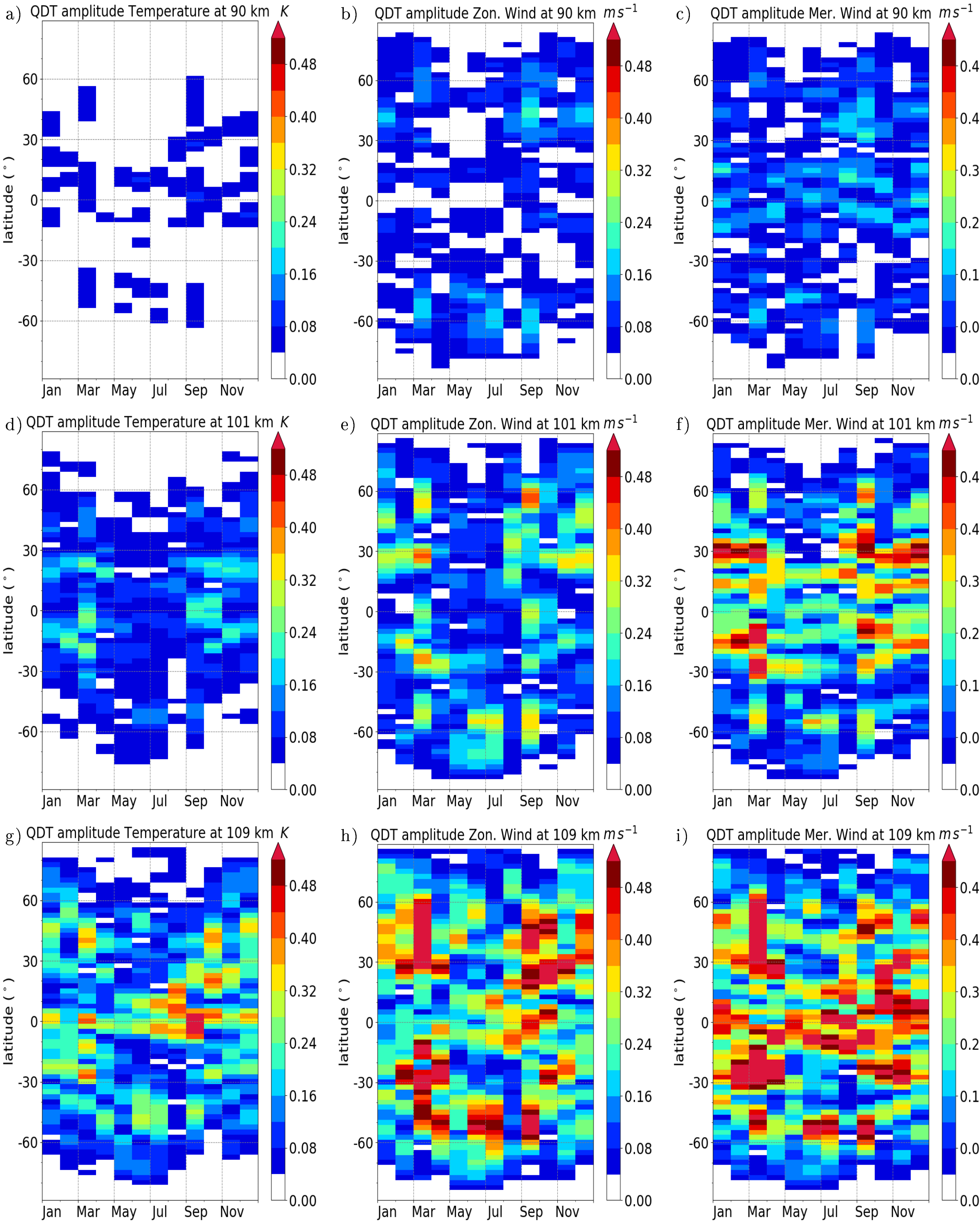

Figure 7.14.: NLIN run QDT amplitudes for temperature (a, d, g), zonal wind (b, e, h) and merdional wind (c, f, i) as time-latitude-plot for 90 km (top), 101km (mid), 109 km (bottom).

7.2.4. No Gravity Wave Forcing

A simulation was carried out where only the gravity wave forcing was turned off, this run is called NO_GW run. Fig. 7.15 and 7.16 show the QDT amplitudes (a, c) and phases (b,d) for the temperature and zonal wind from the NO_GW run for February and October. All other months are shown in the supplement Figs. S50 - S51. The standard deviation from ensemble runs is given as gray lines. The amplitudes and phases of the the REF and SOL run have a similar meridional structure. The amplitudes of the zonal wind are usually smaller than in the REF run, but especially in the temperature the amplitudes are partly larger than in the REF run. This is shown in Fig. 7.17 for February and October and for all other months in the supplement S54 and S55. Areas with larger than 99% significance are dotted.

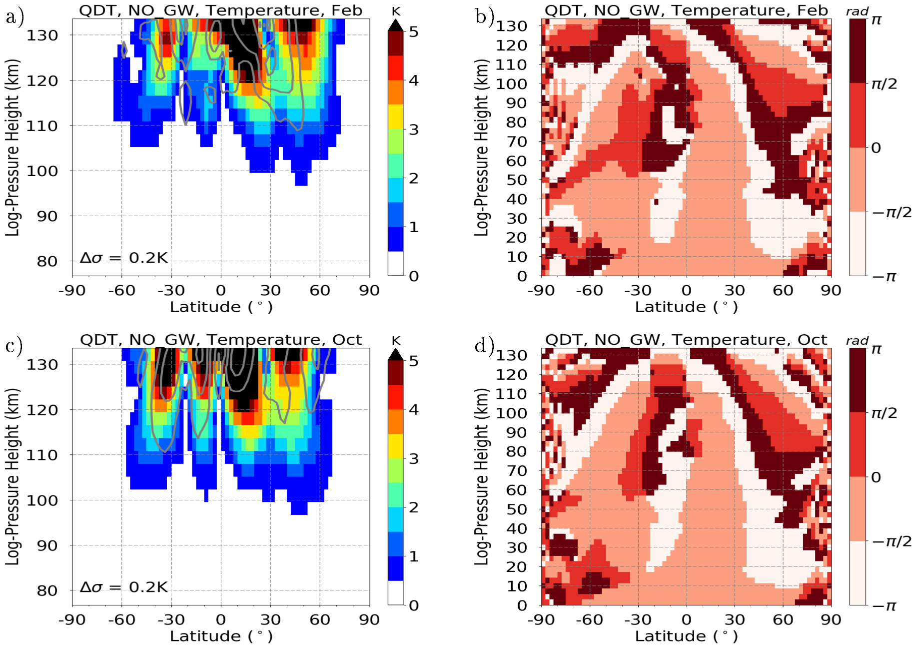

Figure 7.15.: QDT amplitudes (left) and phases (right) for temperature as color from the NO_GW simulation, grey lines show standard deviation from ensemble runs for February (top) and October (bottom).

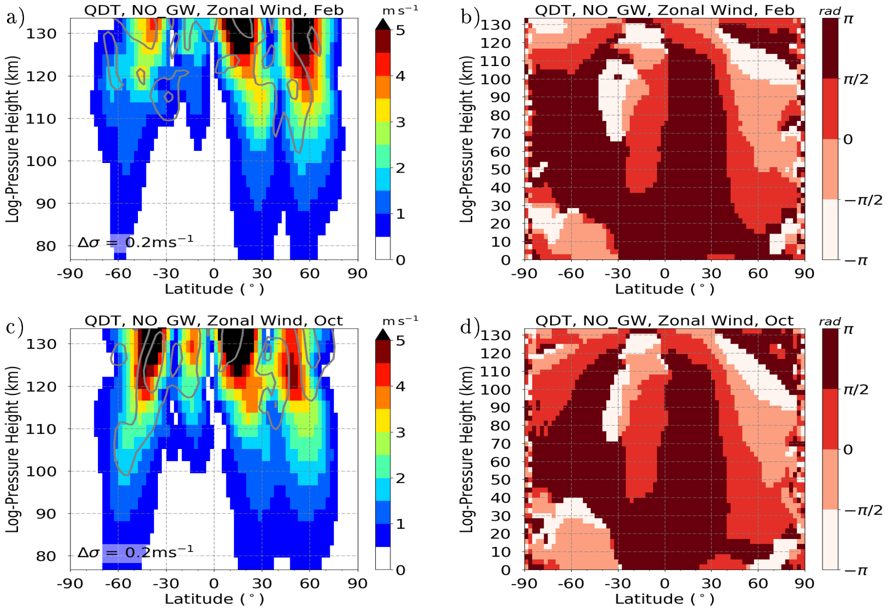

Figure 7.16.: QDT amplitudes (left) and phases (right) for zonal wind as color from the NO_GW simulation, black lines show standard deviation from ensemble runs for February (top) and October (bottom).

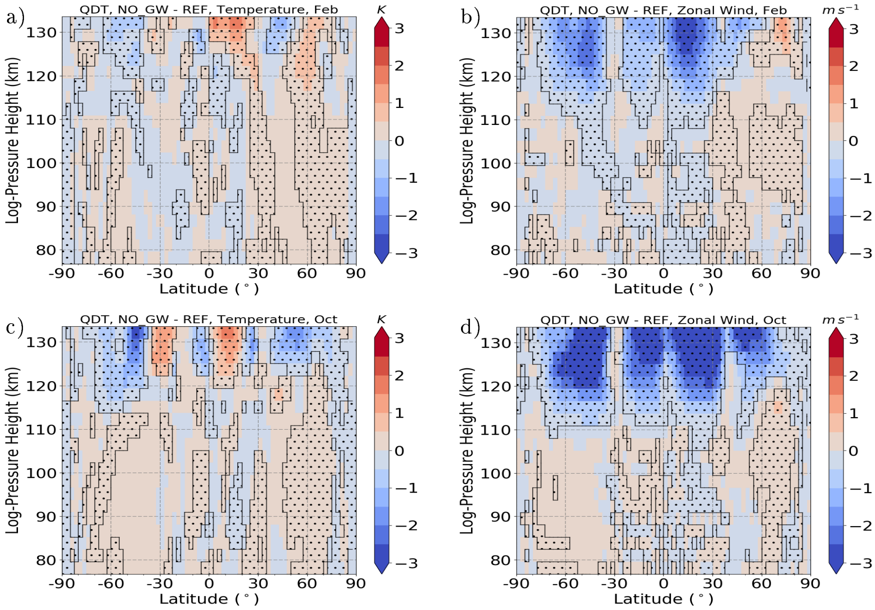

Figure 7.17.: QDT amplitude differences between NO_GW and REF simulation as color. Significance larger than 99% as dotted area. For February (top) and October (bottom), temperature (left) and zonal wind (right).

7.2.5. No Nonlinear Forcing

As for the gravity wave forcing in the NO_GW run, in this simulation just the QDT forcing from nonlinear interactions is disabled, this run is called NO_NLIN. Fig. 7.18 and 7.19 show the QDT amplitudes (a, c) and phases (b, d) for the temperature and zonal wind from the NO_NLIN run for February and October. All other months are shown in the supplement Figs. S56 - S59. The standard deviation from ensemble runs is given as gray lines. The amplitudes and phases, as before for the NO_GW run, are similar to those of the REF and SOL run in the meridional structure. But especially in the zonal wind the amplitudes are partly larger than in the REF run, like seen before in the NO_GW run. This is shown in Fig. 7.20 for February and October and for all other months in the supplement Fig. S60 and S61, where significance larger than 99% is dotted.

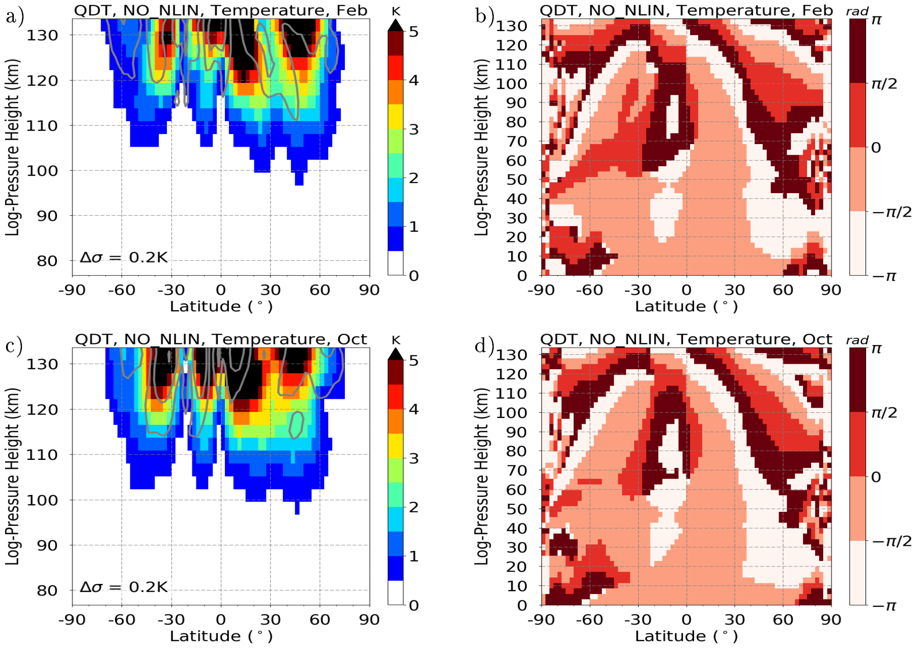

Figure 7.18.: QDT amplitudes (left) and phases (right) for temperature as color from the NO_NLIN simulation, black lines show standard deviation from ensemble runs. Top February, bottom October.

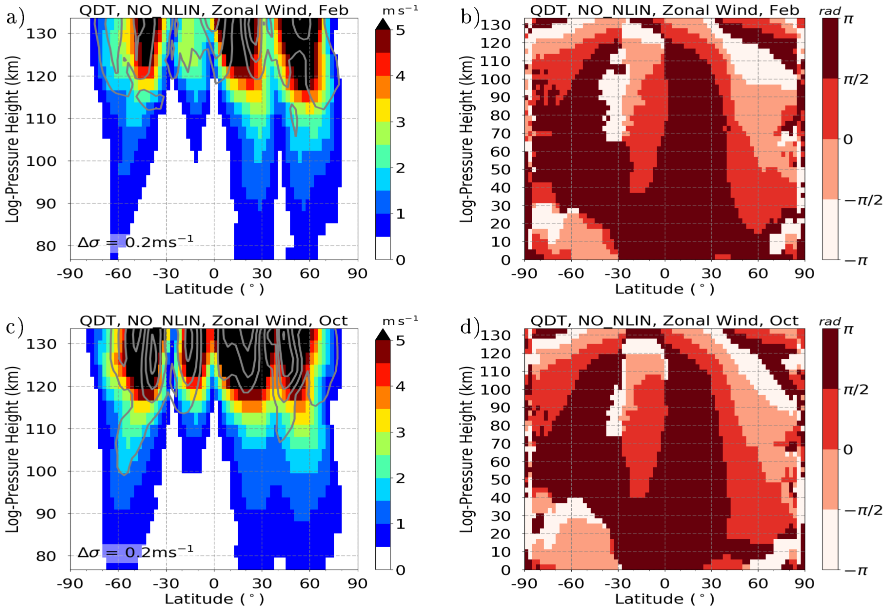

Figure 7.19.: QDT amplitudes (left) and phases (right) for zonal wind as color from the NO_NLIN simulation, black lines show standard deviation from ensemble runs. Top February, bottom October.

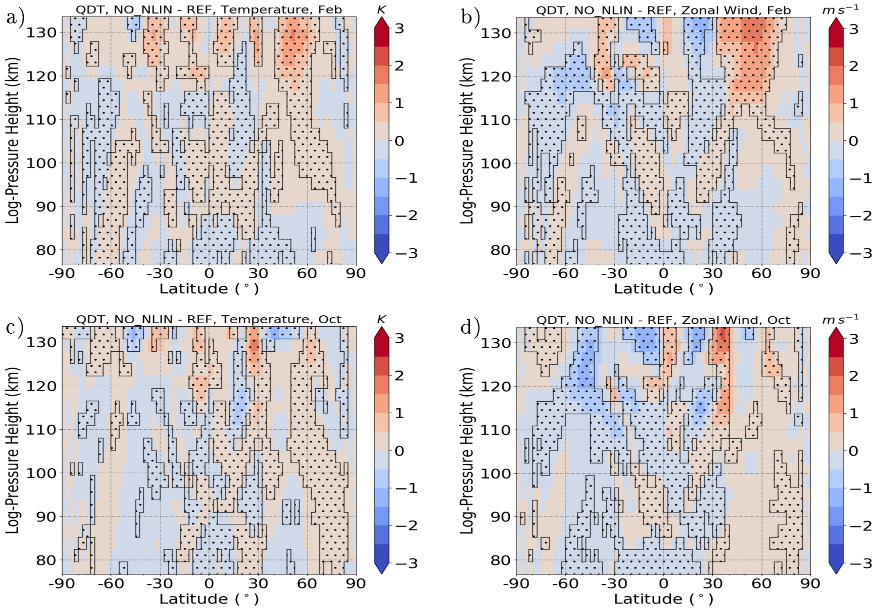

Figure 7.20.: QDT differences between NO_NLIN and REF simulation as color. Significance larger than 99% as dotted area. For February top and October bottom, temperature left, zonal wind right.

7.3. Hough modes in Model experiments

As in the section 6.3 the QDT amplitudes is to be reconstructed using the Hough modes and a Least Squares Fit according to Eq. 6.2. This time for the individual forcing in order to determine whether different modes are dominant in the individual forcing.

7.3.1. SOL Hough modes

The results of the reconstruction of the QDT temperature amplitudes for solar forcing and the first 10 Hough modes are shown in Fig. 7.21 for the months of January, April, July and October for the reconstruction (left), the SOL run, the altitude profile of the Hough modes with different colors for each mode and the differences between reconstruction and SOL run (right). The reconstruction shows good agreement with correspondingly small differences. Analogous to the reconstruction of the REF run, the largest deviations are shown in the areas with the largest amplitudes, but never exceed ±0.8 K. Since solar forcing is the most important QDT forcing and the meridional structure and minima and maxima are very similar to the REF simulation, with the result that the same Hough modes ((4,5), (4,6), (4,7), (4,9) and (4.10)) as in the REF run are dominant. Accordingly, the altitude dependence of the Hough modes is also very similar.

7.3.2. GW Hough modes

As before for the SOL run, a reconstruction of the first 10 Hough modes of the QDT temperature amplitudes was carried out for the GW run and the results are presented in Fig. 7.22, analogous to Fig. 7.21. The reconstruction is similarly good as in the previous comparisons, the differences are most ±0.2 K. Even if there are some differences in the altitude profile of the amplitudes compared to the SOL and REF run. The amplitudes of the modes are much smaller than for the REF and SOL run and die maxima are shown at lower altitudes (120 km) than in the REF and SOL run in January and April. In July and October the maxima in the GW modes are shifted 20 km upwards upward compared to REF and SOL run. But it can be seen that the modes (4,5), (4,6), (4,7), (4,9) and (4.10) are dominant, the same as in the REF and SOL run.

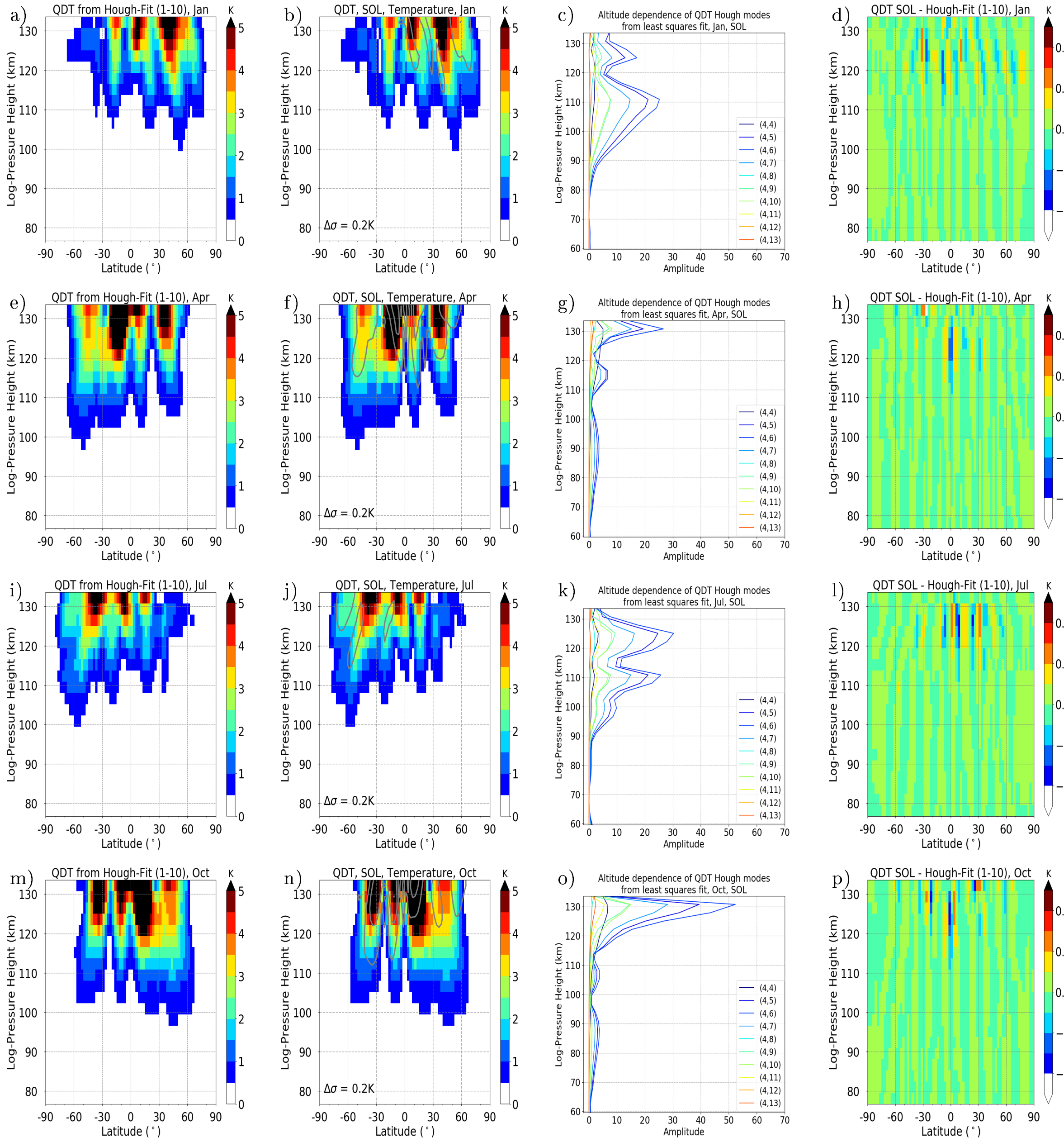

Figure 7.21.: Calculated SOL QDT temperature amplitudes from Hough modes 1 to 10 with the least squares fit method (left), SOL simulation, altitude dependence of QDT Hough modes and differences between calculations and REF simulations (right) for a resolution of 2.5 degrees in latitude. For January (top), April, July and October (bottom)

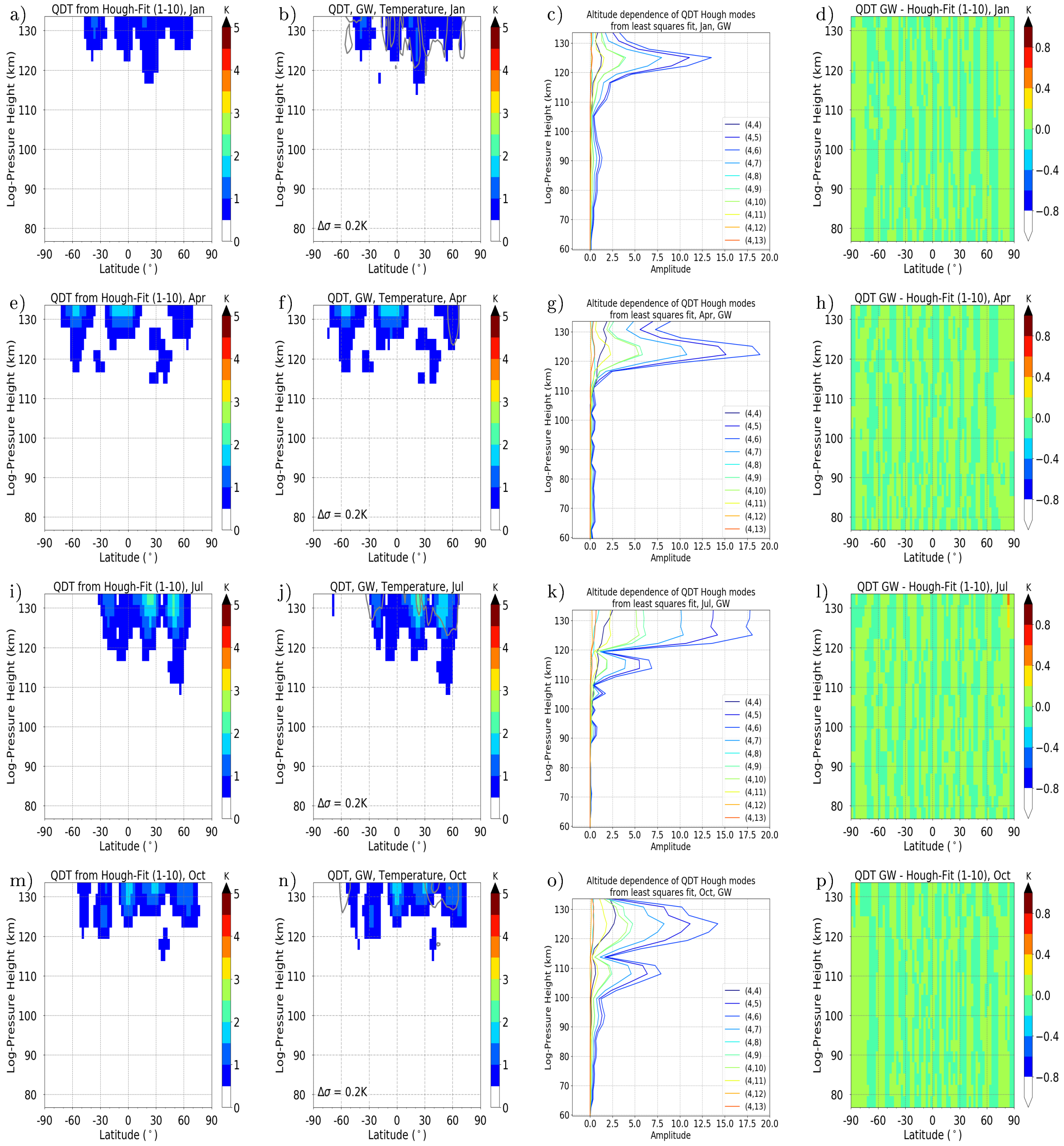

Figure 7.22.: Calculated GW QDT temperature amplitudes from Hough modes 1 to 10 with the least squares fit method (left), GW simulation, altitude dependence of QDT Hough modes and differences between calculations and REF simulations (right) for a resolution of 72 latitudes. For January (top), April, July and October (bottom)

7.3.3. NLIN Hough modes

As before, the reconstruction of the QDT temperatures amplitudes from the NLIN simulation was performed in the same way and the results are shown in Fig. 7.23. The altitude profile of the Hough modes differs from those of the SOL, GW and REF runs. The amplitudes are smaller than in the REF and SOL run, but similar to the GW run. The vertical structure shows also differences, the January changed similar to the GW run, so that the maximum is shifted downward to 120 km compared to the REF and SOL run, in April, July and October the maxima are shifted upward. But again the same Hough modes (4,5), (4,6), (4,7), (4,9) and (4.10) are determined.

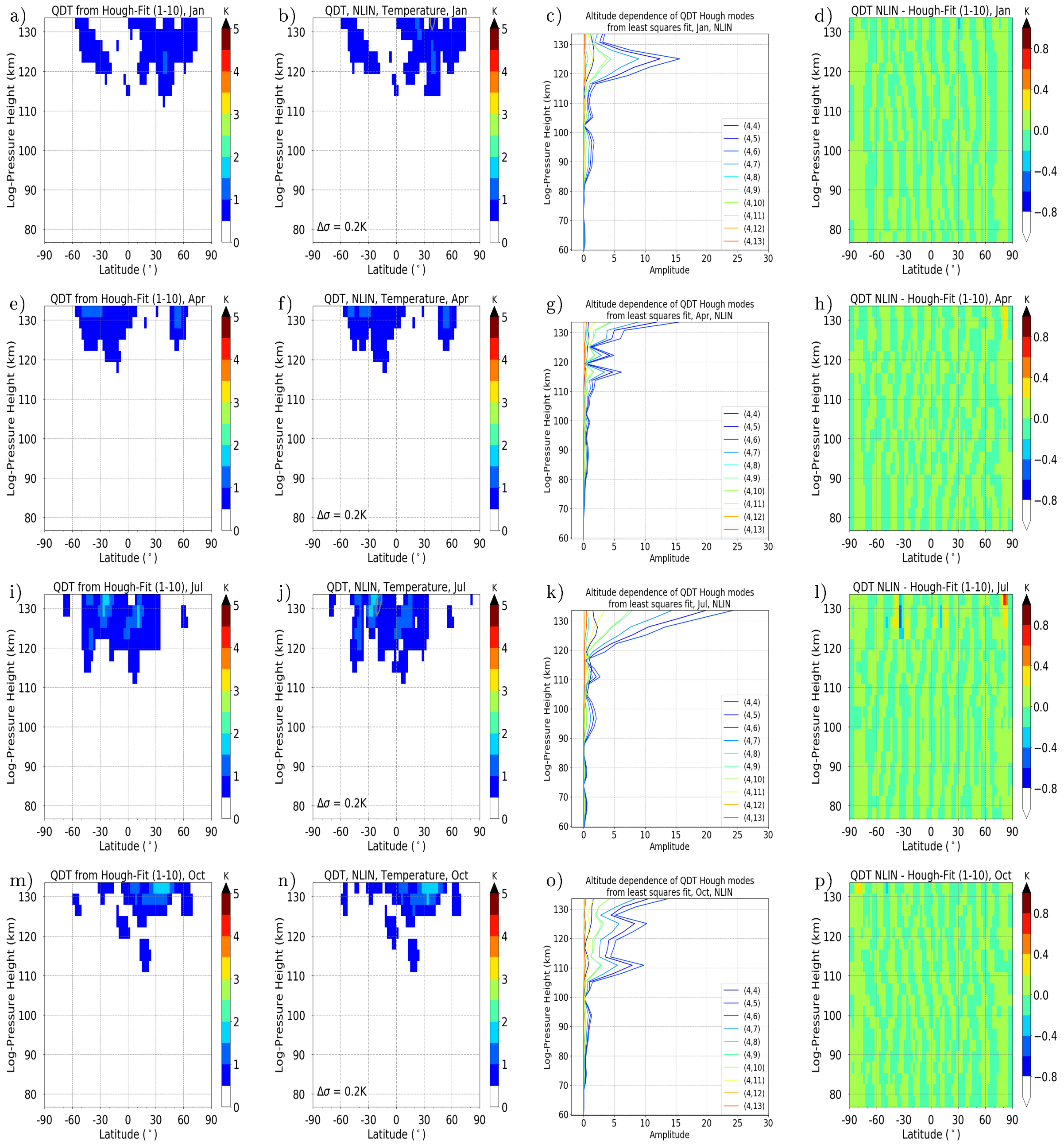

Figure 7.23.: Calculated NLIN QDT amplitudes for temperature from Hough modes 1 to 10 with the least squares fit method (left), GW simulation, altitude dependence of QDT Hough modes and differences between calculations and REF simulations (right) for a resolution of 72 latitudes. For January (top), April, July and October (bottom)

7.3.4. Hough modes: Seasonal cycle

The seasonal cycle of the individual Hough modes for the altitude of 120 km for the REF, SOL, GW and NLIN run is shown in Fig. 7.24. It can be seen that the Hough modes (4,5), (4,6), (4,7), (4,9) und (4.10) are dominant in all months and that solar forcing is the most important QDT forcing. Only in the autumn and winter months do the GW and NLIN run modes do have amplitudes comparable to REF and SOL run. So it can be summarized that the QDT temperature amplitude is always composed of the same Hough-modes, independent of the forcing. Comparing the seasonal cycle of the Hough modes of the REF run with the seasonal cycle of the amplitudes, it is noticeable that only the maxima and minima in February, September, October and November are shown correctly, but not in April and May. The same applies to the comparison of the SOL run with its Hough modes, whereby the amplitudes in autumn are underrepresented. The agreement is better when comparing the amplitudes of the GW and NLIN run with the respective Hough modes. Differences are only found from October to December, where the amplitudes are underrepresented in the GW run and overrepresented in the NLIN run. But the forcing of nonlinear QDT is important in December and January.

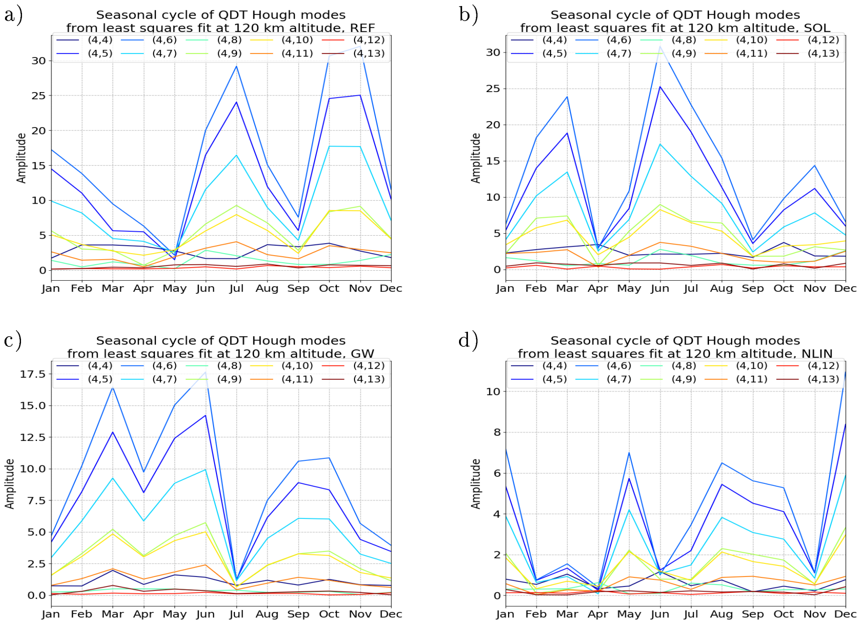

Figure 7.24.: Calculated seasonal cycle for QDT temperature Hough modes 1 to 10 with the least squares fit method for REF (a), SOL (b), GW (c) and NLIN (d) simulation.

7.4. Nonlinear Tidal Interactions

Nonlinear interactions between tides play an important role for the excitation of a QDT. Interactions between two SDTs or an DT and TDT can be considered as excitation of a QDT (see chapter 2.1). In order to determine which of these interactions is the dominant one, simulations were carried out in which the DT, SDT or TDT were removed in the model tendency terms with a FFT in order to prevent the respective interaction. These simulations are based on the conditions of 2005 and are not an ensemble run. The model configuration otherwise corresponds to that of the REF run. The following results do not consider the phases, because they are dominated by direct solar forcing of the QDT and are therefore similar with the REF and SOL simulation. The results are presented for January, as the strongest nonlinear interactions occur in the winter months.

7.4.1. Model run without SDT/SDT interaction

In the first case the SDT with wavenumber $k = 2$ was removed by an FFT, so that no SDT/SDT interaction is possible. Fig. 7.25 shows the result for January for the zonal wind (top) and temperature (bottom). On the left side the REF run is shown for comparison, the case without SDT in the middle and on the right side the difference between both. The meridional structure of the amplitudes is still visible, but in the case without SDT the amplitudes are larger (up to 1 K or 1 ms^{-1})in the northern mid- and southern low latitudes than in the REF run. Conversely, the amplitudes are smaller (up to 1 K or 1 ms^{-1}) in the low northern and southern midlatitudes. This effect is more pronounced in the amplitudes of the zonal wind than in the temperature. The interpretation is difficult, because some differences may be caused by comparing a single year with an ensemble mean. However, the differences in QDT amplitudes are sometimes larger than 33% of the amplitude, after the removal of an nonlinear forcing. Especially the increase in amplitudes can only be explained by an additional interaction between QDTs excited by different forcing mechanisms.

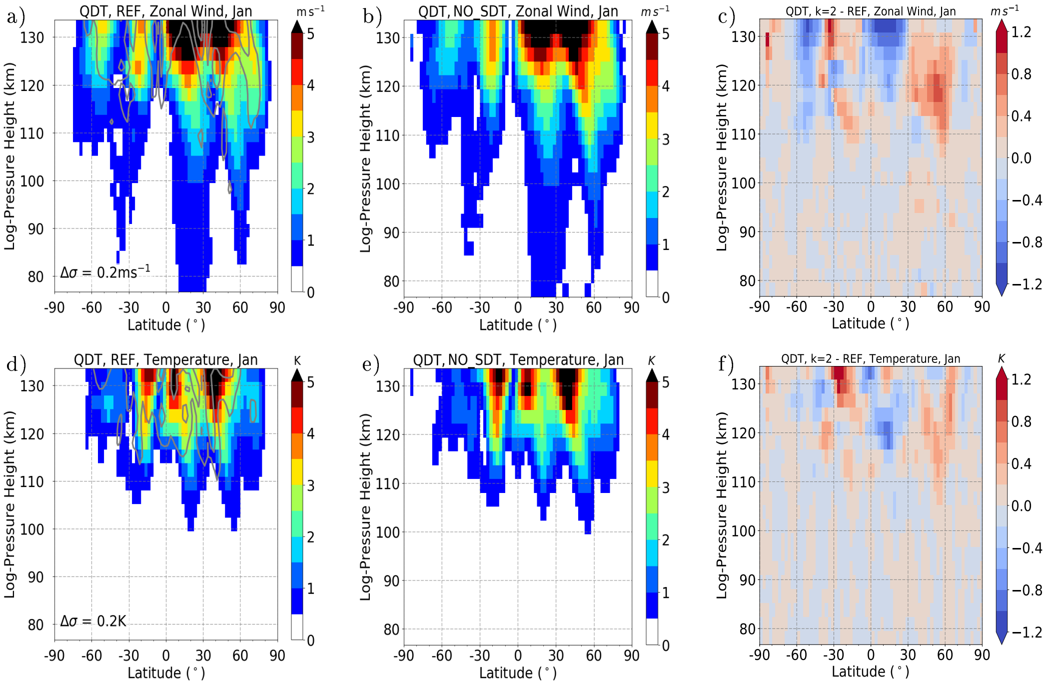

Figure 7.25.: QDT amplitudes from the REF run (left), without SDT (mid), differences (right). For zonal wind (top) and temperature (bottom) amplitudes.

7.4.2. Model run without DT/TDT interaction

As before for the SDT/SDT interaction, the same is now shown for the DT/TDT interaction for zonal wind (top) and temperature (bottom) in Fig. 7.26 for January. Note the different scaling of the differences between the run without DT/TDT interaction and the run without SDT/SDT interaction. The DT with wavenumber $k = 1$ and the TDT with wavenumber $k = 3$ is removed by a FFT. The meridional structure of the amplitudes is still visible, but in the case without SDT the amplitudes are larger (up to 1 K or 1 ms^{-1}) in the northern mid- and southern low latitudes than in the REF run and vice versa for the negative differences. The negative differences are now more pronounced than before in the SDT/SDT interaction and reach now up to 2 K or 2 ms^{-1}. From this it can be concluded that the part of the QDT from nonlinear tidal interactions is mainly due to the DT/TDT interaction. The excited QDT from SDT/SDT interactions is smaller, which can also be due to the possible interaction with the QDT from other forcing mechanisms. Jacobi et al. (2018) stated that the DT/SDT interaction was the stronger one, the investigation referred on the one hand only to a radar measurement at one point and to simulations with MUAM, which still had a lower merdional and a larger temporal resolution and therefore are only conditionally comparable with the current results.

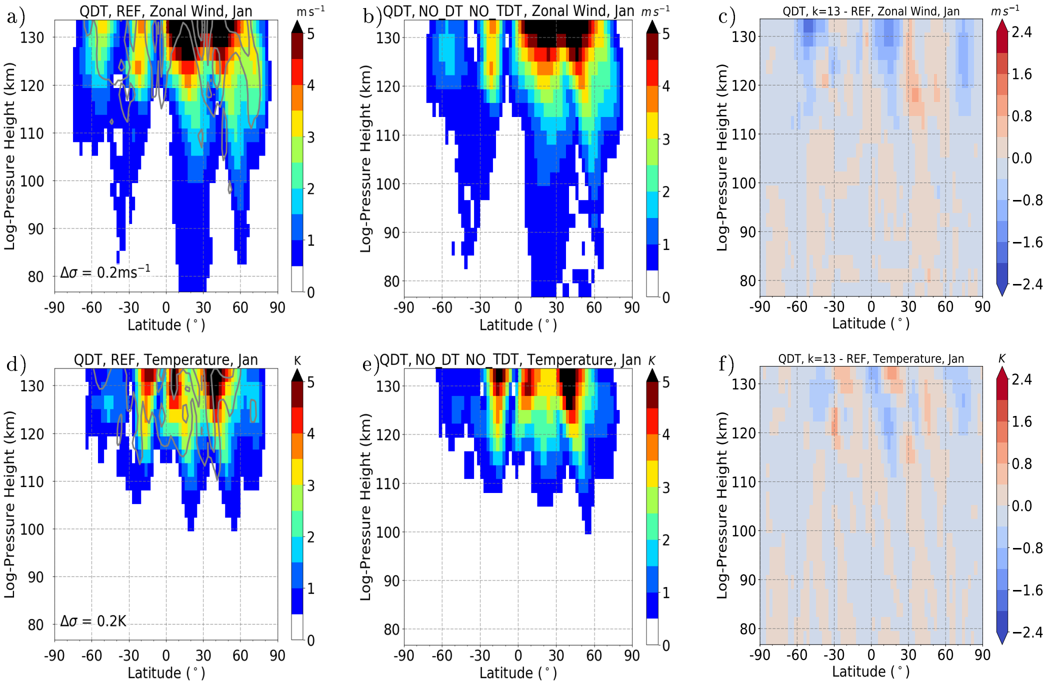

Figure 7.26.: QDT amplitudes from the REF run (left), without DT and TDT (mid), differences (right). For zonal wind (top) and temperature (bottom) amplitudes.

7.4.3. Model run without tide-tide interaction

In the next step a model simulation was carried out under the conditions of the year 2005, where all tidal interactions were excluded. That means, with using of an FFT, to remove the DT with wavenumber $k = 1$, SDT with wavenumber $k = 2$ and the TDT with wavenumber $k = 3$ from the model tendency terms. The results are shown in Fig. 7.27 as before for January for zonal wind (top) and temperature (bottom). It can be seen again that the meridional structure is preserved and that compared to the REF run the amplitudes in the low latitudes of the northern hemisphere and in the middle latitudes of the southern hemisphere become significantly larger, especially in the northern middle latitudes, which suggests an interaction of the QDT from different forcing mechanisms. The results from the run without tide-tide interaction should be similar to the NO_NLIN run. This is also the case for the meridional structure, as well as for the maxima of the amplitudes. Only in the higher latitudes the amplitudes in the NO_NLIN run are larger by 1.5 ms^{-1} and 1 K.

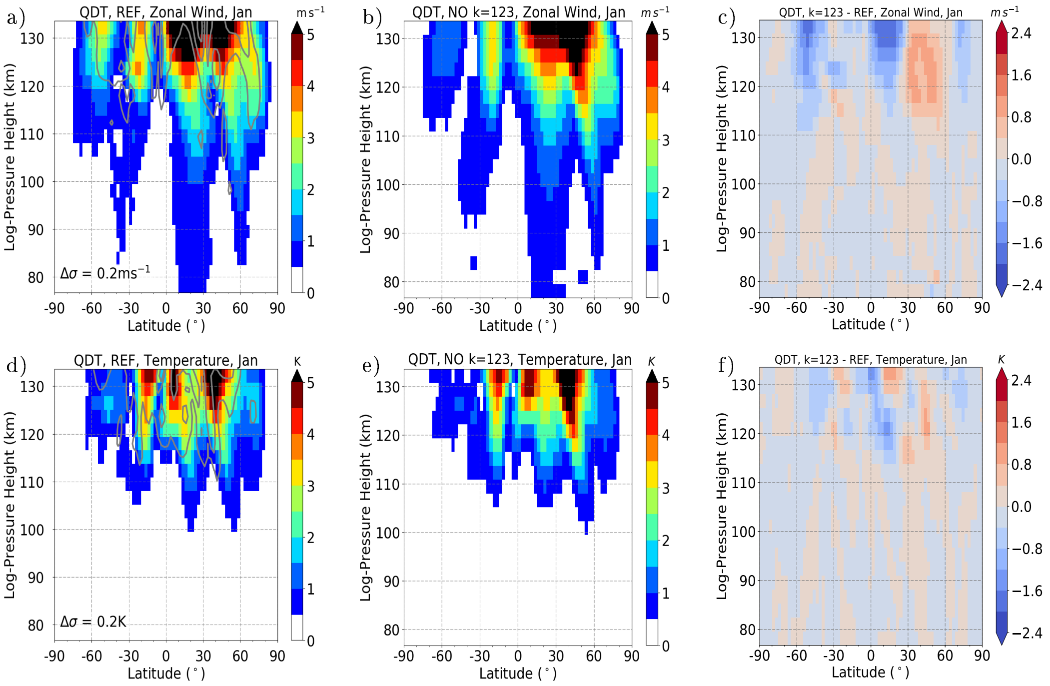

Figure 7.27.: QDT amplitudes from the REF run (left), without tide-tide interactions (mid), differences (right). For zonal wind (top) and temperature (bottom) amplitudes.

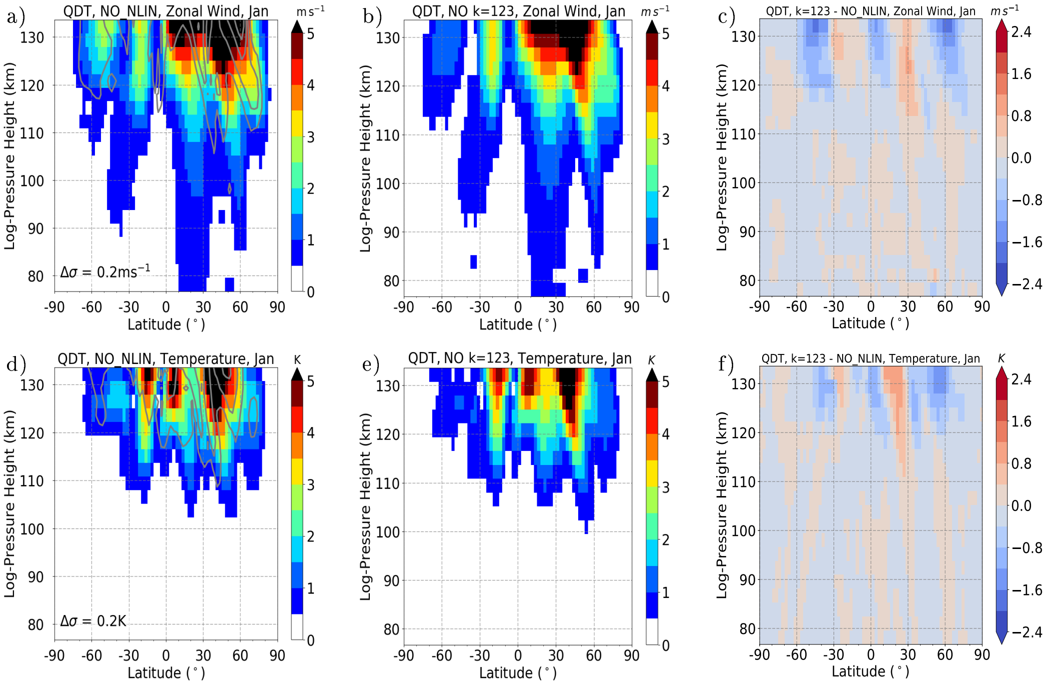

Figure 7.28.: QDT amplitudes from the NO_NLIN run (left), without tide-tide interactions (mid), differences (right). For zonal wind (top) and temperature (bottom) amplitudes.

7.5. Solar Tidal Interactions

The QDT, which is excited by direct solar forcing, is composed in the model primarily of the excitation by absorption of solar radiation from water vapor and ozone. In order to determine which forcing is the dominant one an FFT was applied to the radiation parameterization of the model, which removes the QDT ($k = 4$) caused by water vapor. For this purpose the configuration of the SOL run was used but only for the year 2005. The results for the QDT amplitudes and phases are shown in Fig. 7.29 for January for the run without ozone (right) and for the SOL run (left) and for temperature (a-d) and zonal wind (e-h). For January, because the effect is strongest this month, one can see for the temperature QDT amplitudes that in the case without water vapor forcing the amplitudes are larger than in the SOL run. This is particularly clear in the midlatitudes of the northern hemisphere, where the largest phase differences are found below 50 km altitude for zonal wind. These are now about 180° out of phase. This indicates a destructive interference in the SOL run between the QDTs excited by water vapor with the QDTs excited by ozone. For the zonal wind QDT amplitudes the differences are very similar in the northern hemisphere, but also in the southern midlatitudes a larger amplitude than in the SOL run is now visible. Here to the phases show a shift of 180° between the zonal wind QDTs excited by water vapor with the QDTs excited by ozone, which indicated the destructive interference. In summary, it can be stated that the part of the QDT amplitude in the SOL and REF run, which is caused by the excitation via the ozone, is the most dominant one. Because the QDT excited from water vapor from the troposphere is trapped below 20 km due to the destructive interference.

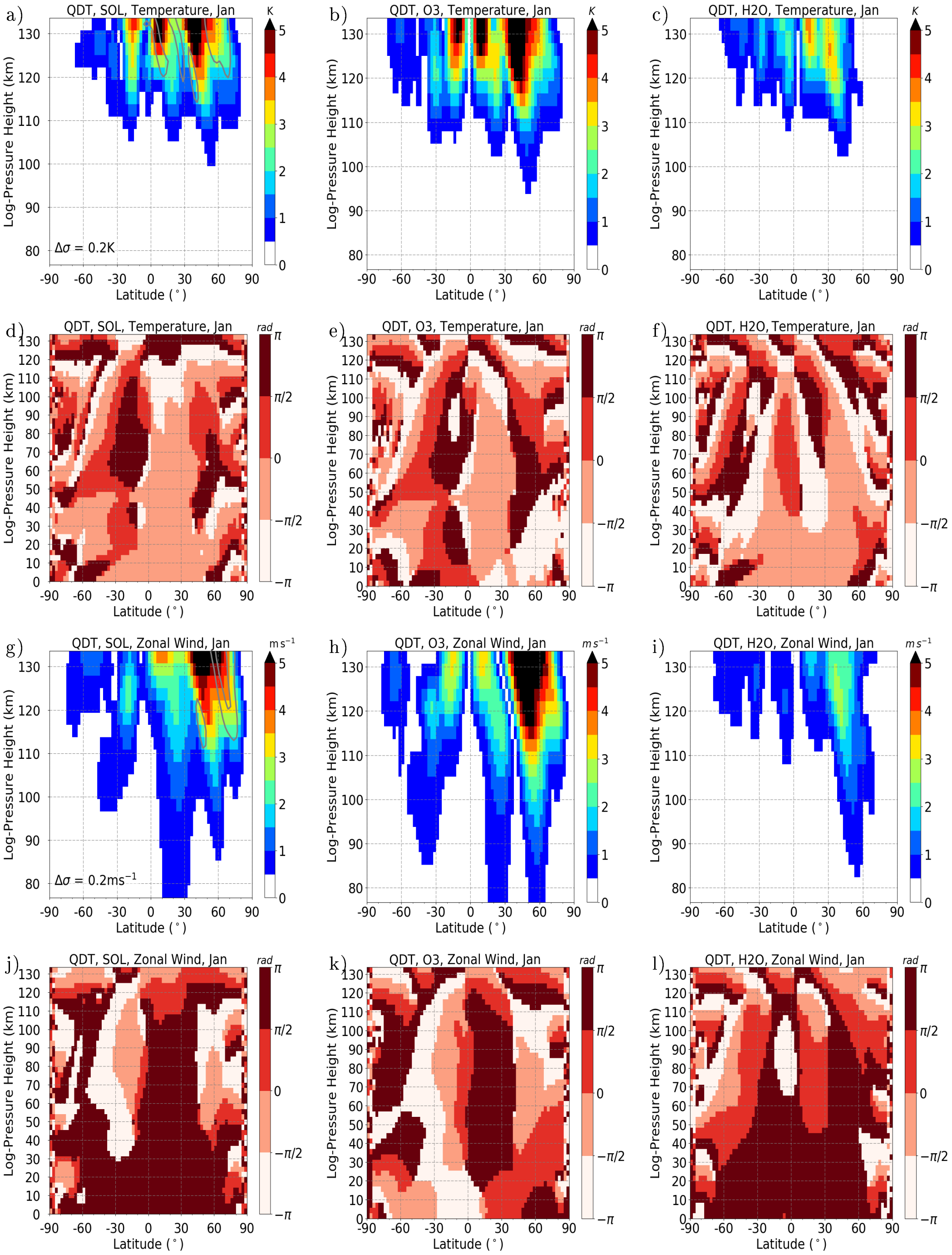

Figure 7.29.: Model run without direkt solar forcing from vater vapor (right), ozone (mid) and REF run for comparison (left). QDT amplitudes for January for temperature (a-c) and zonal wind (g-i) and phases for temperature (d-f) and zonal wind (j-l)

7.6. Interactions of Different Forcing Mechanisms

In section 7.5 was shown, that there are obviously interactions between QDTs, which were excited by different forcing. This will now be investigated in detail for interactions of direct solar forcing, nonlinear tidal interactions and gravity wave tidal interactions as excitation mechanisms. The analysis and discussion is analogous to Geißler et al. (2020). January and April are chosen, because these effects are strongest in this months.

7.6.1. Interaction between Nonlinear and Solar Forcing

The QDT amplitude differences are presented for January and April between the NO_NLIN and REF simulation for temperature in Fig. 7.30 a, b and for zonal wind in Fig. 7.30 c, d. The amplitudes are scaled with density to highlight the actual source region of the waves. All months are shown in the supplement Figs. S62 and S62. Here, the red (blue) areas denote larger amplitudes in NO_NLIN (REF) simulations. This means that in red areas the run with one removed forcing has larger amplitudes than the REF run. It can be concluded that the removed nonlinear forcing must have destructively interfered with other QDT from other forcings (like solar or gravity wave forcing). The NLIN run (only nonlinear forcing) case is expected to show small QDT amplitudes because of the weak nonlinear forcing. Without destructive interference, the NO_NLIN (without nonlinear forcing) simulation should show larger amplitudes than the NLIN run, but smaller ones than the REF run, because one forcing (nonlinear) is missing. Furthermore, the hatched areas denote destructive interference between the QDTs of NLIN and SOL, which are defined through their phases differences $\Delta\Phi = \Phi_{NLIN} - \Phi_{SOL}$:

$$120^\circ \leq \ \Delta\Phi \leq \ 240^\circ. \tag{7.2}$$

In case of a superposition of such destructively related NLIN and SOL waves, the amplitude of NO_NLIN is expected to be larger than in REF, because the nonlinear (NLIN) and solar (SOL) QDT of the REF run act against each other. Indeed, the observed regions for temperature (Fig. 7.30) and zonal wind (Fig. 7.31) in which the amplitudes in the NO_NLIN run are larger than in the REF simulation, and at the same time, destructive interference between the nonlinear and solar QDT corresponds to these positive amplitude differences. Thus, it can be concluded that the nonlinearly excited part of the QDT weakens the pure solar QDT amplitude in the REF simulation. The effect is more pronounced for the zonal wind than for temperature.

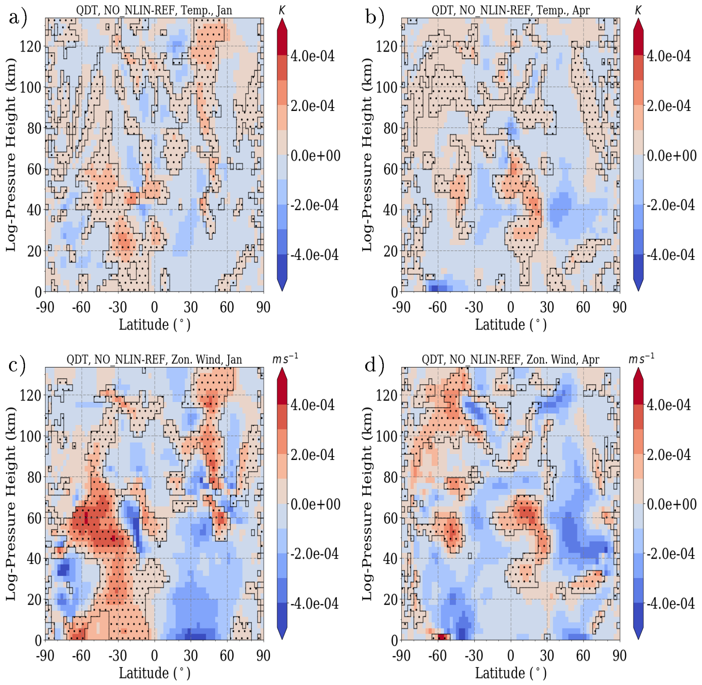

Figure 7.30.: Difference of QDT amplitudes between NO_NLIN and REF simulation, scaled by density. Areas of destructive interference (120° $\leq$ $\Delta\Phi$ $\leq$ 240°) between NLIN and SOL phases are hatched. For temperature (a, b) and zonal wind (c, d) for January (left) and April (right).

7.6.2. Interaction between Gravity wave and Solar Forcing

In addition to the interaction between nonlinear and solar QDT, an interaction between gravity wave - induced QDT and solar QDT is also possible. For this reason the respective results are shown in Fig. 7.31 a, b for temperature and in Fig. 7.31 c, d for zonal wind, analogue to Fig. 7.30. All months are shown in the supplement Fig. S64 and S65. Colors denote the differences between the NO_GW and the REF simulation, again scaled by the growth rate of the amplitudes with altitude. Red (blue) colors denote larger NO_GW (REF) amplitudes. Areas of destructive interference (see Eq. 7.2 with $\Delta\Phi = \Phi_{GW} - \Phi_{SOL}$) between the phases from the NO_GW and SOL run are hatched. The difference between NO_GW and REF run shows that the amplitudes in the NO_GW simulation are sometimes larger than in the REF run. This often happens in areas where destructive interference can be detected, but it is less well pronounced than in Fig. 7.30 for the nonlinear-solar QDT interaction. This means that the QDT owing to gravity wave - tide interactions also tends to act against the solar QDT which leads to a decline in QDT amplitude in the REF simulation for temperature and zonal wind where both forcing mechanisms are present. The interaction between GW and NLIN QDT is not shown separately because the interactions were negligible.

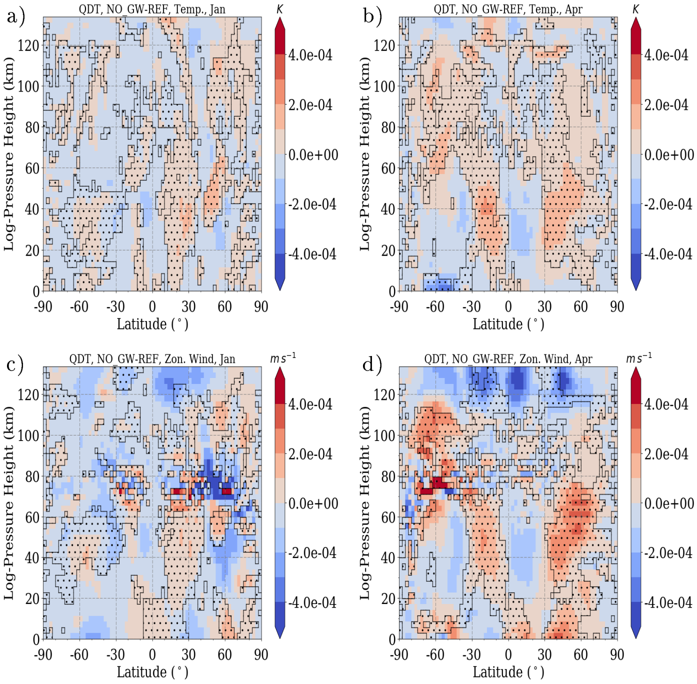

Figure 7.31.: Difference of QDT amplitudes between NO_NLIN and REF simulation, scaled by density. Areas of destructive interference ($120° \leq \Delta\Phi \leq 240°$) between NLIN and SOL phases are hatched. For temperature (a, b) and zonal wind (c, d) for January (left) and April (right).

7.7. Influence of Enhanced Forcing Mechanisms

So far only parts of the QDT from different forcings have been removed from the model tendency equation. In the next step, the existing QDT from the forcings is to be amplified. For this purpose, the QDT is extracted again from the tendency terms by an FFT analysis and added again with an amplification factor. This is done for each latitude, longitude, altitude and time step. This also shows the numerical stability of the model and how the propagation conditions behave with a changed background and what effects this has on the QDT amplitudes. All simulations are done for the conditions of the year 2005.

7.7.1. Influence of Enhanced Solar Forcing Mechanisms

For the case of increased solar forcing, the SOL run was used as a basis for this new experiment. In the SOL simulation, the QDT from nonlinear interactions and from gravity wave - tide interactions was removed by an FFT. In this new model experiment, the remaining direct solar forcing is increased, whereby 100% corresponds to the results of the SOL run and 200% corresponds to twice as strong forcing compared to the SOL run. Of course, this not only has influence on the resulting QDT, but also on the background circulation. Fig. 7.32 shows an overview over the results of this simulation. In Fig. 7.32 a (temperature) and d (zonal wind) the normalized latitudinally averaged (weighted by $\cos\phi$) QDT amplitudes are shown as vertical profile. The x-axis shows the ratio of the change between SOL (100%) and the run with 150% increase of the direct solar forcing. The average was calculated over all months, resulting in the annual variability, which is shown as inter-quartile range (boxes) and the mean value, shown as line in the box, as well as the error bars. In most altitude range exactly this can be observed, but between 120 km and 140 km the effect on the amplitude is smaller and stronger above 140 km than the expected 50%. The annual variability of temperature amplitudes is highest in the mesopause and thermosphere, while the highest values of zonal wind amplitudes are reached between 100 km and 130 km altitude. In 7.32 b (temperature) and e (zonal wind), the normalized vertically averaged (80-160 km) QDT amplitudes are shown in dependence of the amplification of forcing, with the different colors indicating different months. The points symbolize the data from the simulations and the line is the result of a linear fit for each month with the slope s given in the figure. It can be seen that the increase in all months is almost linear, so an amplification of the direct solar forcing by 10% leads to a 10% larger amplitude. In Fig. 7.32 c (temperature) and f (zonal wind) the effects on the background circulation are shown. The points show the simulation results as global average of the absolute change of zonal mean background parameter between 80 km and 160 km altitude. Also a linear fit is added for each month with given correlation coefficients. For temperature and zonal wind, there is a linear correlation between stronger direct solar forcing and changes in the background circulation for the months October to April. Between May and September, especially for zonal wind, the correlation is very weak. The results for January for every enhancement factor can be seen in the supplement in Fig. S66 for the background zonal wind and in Fig. S67 for the QDT zonal wind amplitudes. The decrease of QDT amplitudes in the SOL run at 130 km - 140 km altitude is due to nonlinear interactions with the nonlinear forced QDT between 120 km and 130 km altitude.

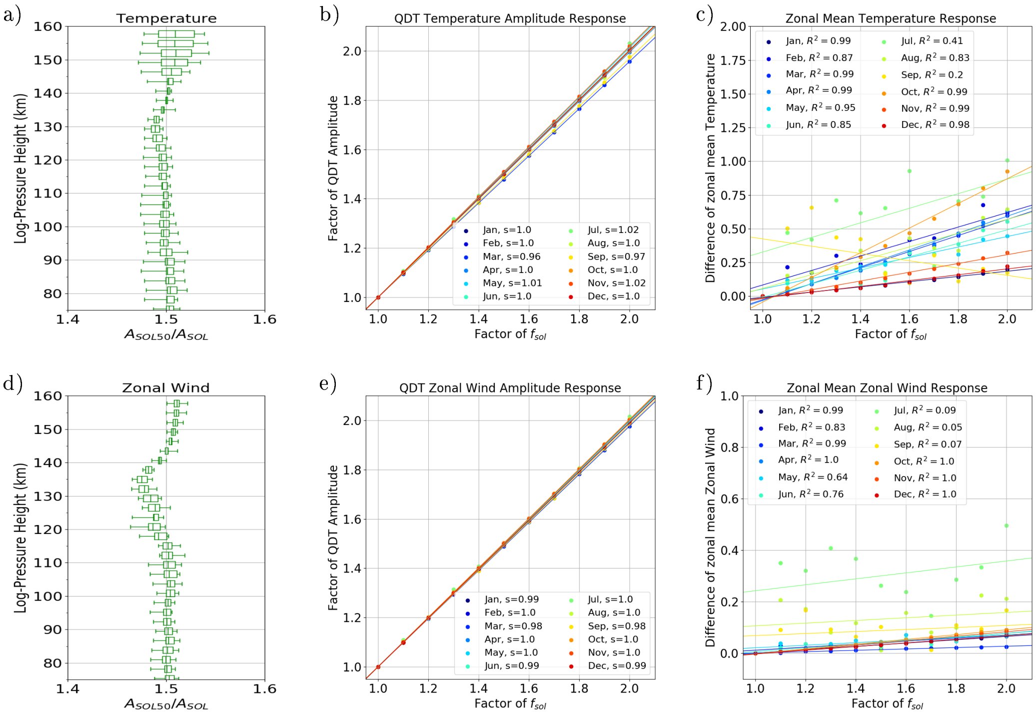

Figure 7.32.: Profiles of normalized latitudinal mean QDT amplitudes ratio (left), annual variability as inter-quartile range (boxes), mean value as line inside the box, and maximum/minimum range as error bars. Normalized, vertically averaged (80 - 160 km) QDT amplitudes for enhancements of f_{sol} in different colors for different months (mid). Dots show the simulations and line the linear fit for each month with correspond slope s. Global mean absolute change (80 - 160 km) of zonal mean background parameter with respect to SOL run (right). Linear fits for every month with correlation coefficient R^2. Top for temperature, bottom for zonal wind.

7.7.2. Influence of Enhanced Gravity Wave Forcing Mechanisms

The same like in section 7.7.1 for the SOL run was now done for the GW run. Only the forcing of the QDT due to the gravity wave - tide interaction is enabled and was increased from 100% of the GW run up to 200%. Fig. 7.33 shows an overview over the results of this simulation. In Fig. 7.33 a (temperature) and d (zonal wind) the normalized latitudinal averaged QDT amplitudes are shown as altitude profile. The x-axis indicated the ratio of the change between GW (100%) and the run with 150% increase of the gravity wave forcing. The average was calculated over all months, resulting in the annual variability, which is shown as inter-quartile range (boxes) and the mean value, shown as line in the box, as well as the error bars. For temperature and zonal wind this 50% can be only seen at 110 km to 120 km altitude. Above the effect is stronger and below it is weaker. This depends on the forcing of QDT from gravity wave, which is stronger in mesosphere above 110 km. The annual variability is highest for temperature and zonal wind above 120 km altitude. In 7.33 b (temperature) and e (zonal wind), the normalized vertical averaged (80-160 km) QDT amplitudes are shown according to the dependence of the amplification of forcing, with the different colors indicating different months. The points symbolize the data from the simulation. It can be seen that there is an linear increase but slope differs from month to month with the weakest increase in December and January. In Fig. 7.33 c (temperature) and f (zonal wind) the effects on the background circulation are shown. The points show the simulation results as global average of the absolute change of zonal mean background parameter between 80 km and 160 km altitude. The line corresponds to a linear fit for each month with given correlation coefficients. For temperature and zonal wind, there is a linear correlation for March and April and for October to December. But these correlation shows that there is just a weak influence of enhanced forcing on the background circulation, that differs from month to month. All other months show only noise. The results for every enhancement factor as example for January can be seen in the supplement in Fig. S68 for background zonal wind and in Fig. S69 for QDT zonal wind amplitudes.

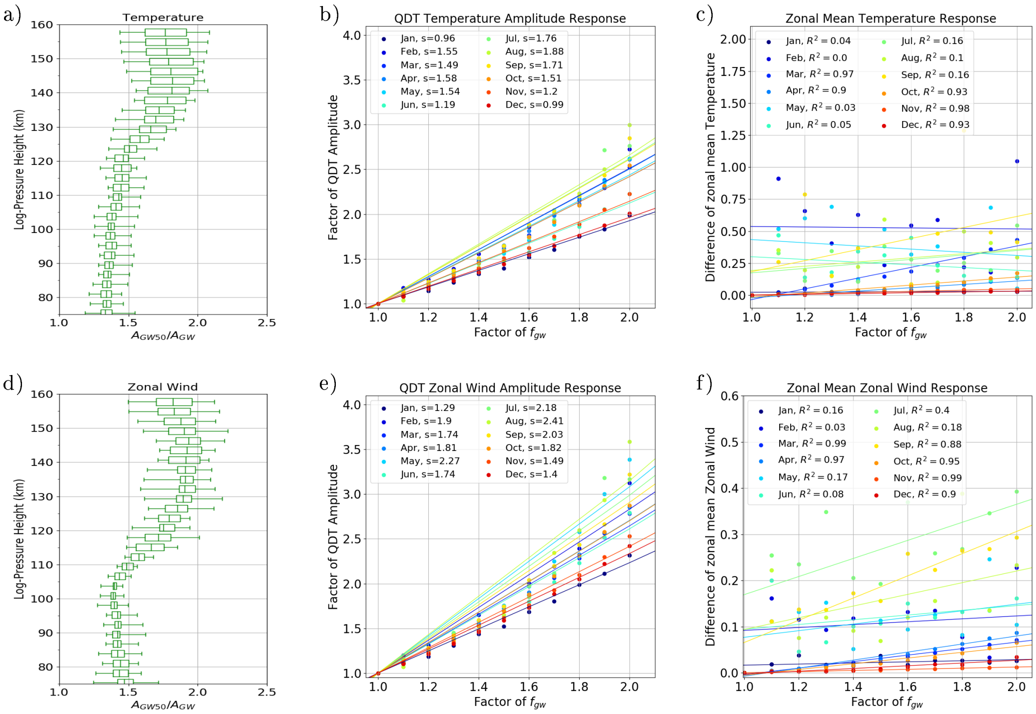

Figure 7.33.: Profiles of normalized latitudinal mean QDT amplitudes ratio (left), annual variability as inter-quartile range (boxes), mean value as line inside the box, and maximum/minimum range as error bars. Normalized, vertically averaged (80 - 160 km) QDT amplitudes for enhancements of f_{sol} in different colors for different months (mid). Dots show the simulations and line the linear fit for each month with correspond slope s. Global mean absolute change (80 - 160 km) of zonal mean background parameter with respect to GW run (right). Linear fits for every month with correlation coefficient R^2. Top for temperature, bottom for zonal wind.

7.7.3. Influence of Enhanced Nonlinear Forcing Mechanisms

The same as before for the SOL and GW run was now done for the NLIN run. Only the forcing of the QDT due to the nonlinear interactions takes place and was increased from 100% of the NLIN run up to 200%. Fig. 7.34 shows an overview over the results of this simulation. In Fig. 7.34 a (temperature) and d (zonal wind) the normalized latitudinal averaged QDT amplitudes are shown as altitude profile. The x-axis indicated the ratio of the change between GW (100%) and the run with 150% increase of the nonlinear forcing. The average was calculated over all months, resulting in the annual variability, which is shown as inter-quartile range (boxes) and the mean value, shown as line in the box, as well as the error bars. At an amplification of 50% it would be expected an amplification of the QDT amplitudes of 50%. In most altitude range exactly this can be observed, but above 120 km the effect on the amplitude is obviously smaller than the expected 50%, especially for zonal wind. This is to due nonlinear interactions between solar and nonlinear forced QDTs in this area. The annual variability of temperature amplitudes is the highest above 140 km altitude, while the highest values of zonal wind amplitudes are reached below 125 km altitude. In 7.34 b (temperature) and e (zonal wind), the normalized vertical averaged (80-160 km) QDT amplitudes are shown according to the dependence of the amplification of forcing, with the different colors indicating different months. The points symbolize the data from the simulations and the line is the result of a linear fit for each month with the slope s given. It can be seen that the increase in all months is almost linear. But in difference to the enhanced SOL run the increase is stronger in spring (March and April) and autumn (September and October) (up to $s = 1.19$ in September) and small during all summer months. In all other months an amplification of the nonlinear forcing by 10% leads more or less to a 10% larger amplitude. In Fig. 7.34 c (temperature) and f (zonal wind) the effects on the background circulation are shown. The points show the simulation results as global average of the absolute change of zonal mean background parameter between 80 km and 160 km altitude. The line corresponds to a linear fit for each month with given correlation coefficients. For temperature and zonal wind, there is no influence of enhanced forcing on the background circulation visible for all months. The results for every enhancement factor as example for January can be seen in the supplement in Fig. S70 for background zonal wind and in Fig. S71 for QDT zonal wind amplitudes.

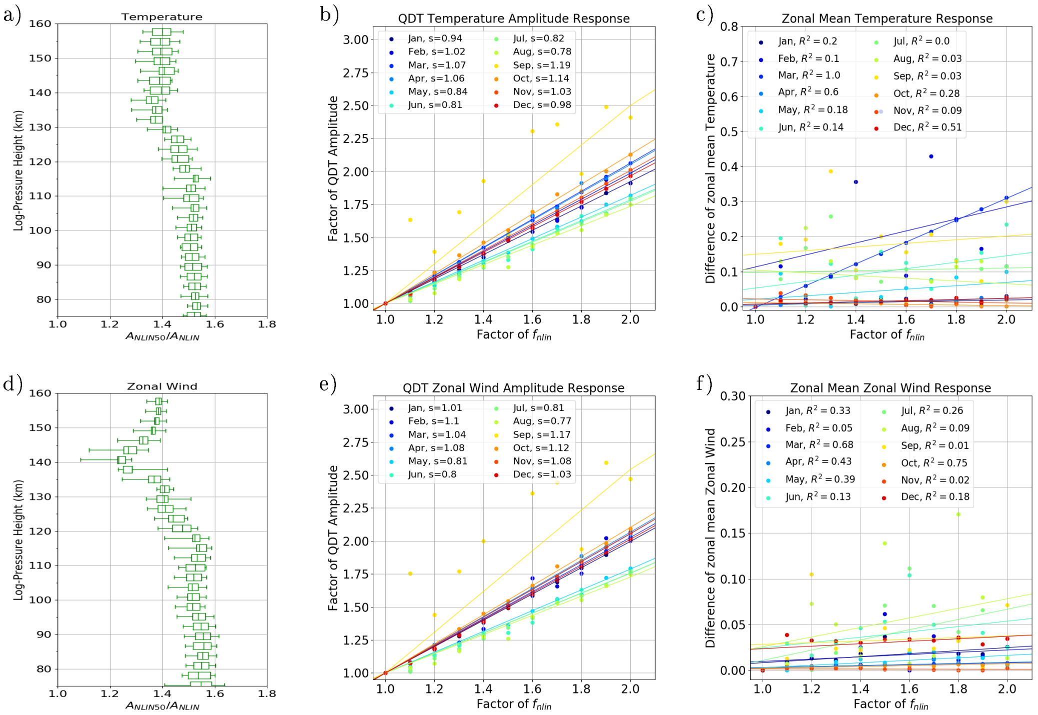

Figure 7.34.: Profiles of normalized latitudinal mean QDT amplitudes (left), annual variability as inter-quartile range (boxes), mean value as line inside the box, and maximum/minimum range as error bars. Normalized, vertically averaged (80 - 160 km) QDT amplitudes for enhancements of f_{sol} in different colors for different months (mid). Dots show the simulations and line the linear fit for each month with correspond slope s. Global mean absolute change (80 - 160 km) of zonal mean background parameter with respect to NLIN (right). Linear fits for every month with correlation coefficient R^2. Top for temperature, bottom for zonal wind.

8. Summary and Conclusion

In the sensitivity study carried out in the beginning in section 5, a compromise for a model configuration was found to obtain the most realistic background circulation and to increase the QDT amplitude in the model compared to earlier versions (Geißler et al., 2020; Geißler and Jacobi, 2018).

The results of the REF simulation show a consensus in the climatology of QDT in comparison with observations and other model studies. The amplitudes of the MUAM are relatively small for the QDT with up to $2.5\,\mathrm{ms}^{-1}$ in the zonal wind at 101 km altitude and $5.0\,\mathrm{ms}^{-1}$ at 120 km altitude in spring and autumn. For example, QDT amplitudes obtained from meteor radar measurements (Jacobi et al., 2017c) are up to three times larger than in the MUAM simulations. However, it is a known issue that numerical models tend to underestimate the tides in some regions and seasons (e.g., Smith, 2012; Pokhotelov et al., 2018; Geißler et al., 2020).

In the model simulations, the meridional structure of QDT amplitudes shows 3-4 maxima in the temperature and zonal wind component (5 in the meridional wind component). These are located at low (10°-30°) and middle latitudes (40°-70°) of the respective hemisphere (Geißler et al., 2020). These maxima at low and midlatitudes are also present in the NIRS and SABER temperature measurements (Liu et al., 2015; Azeem et al., 2016). Meteor radar measurements at northern midlatitudes (Jacobi et al., 2017c) confirm the shown QDT wind maxima in winter, spring and autumn. The maximum of the QDT wind amplitudes at low latitudes has been proven by meteor radar measurements over Brazil (Guharay et al., 2018). They show maxima below 100 km in spring and autumn like the MUAM simulations.

This thesis is focused on forcing mechanisms of the QDT. To this end, first all possible sources of the migrating QDTs are compared in the simulations following the approach of Lilienthal et al. (2018). These are (i) the absorption of solar radiation by water vapor and ozone, (ii) nonlinear tidal interactions between migrating DTs and TDTs and the self-interaction of migrating SDTs and (iii) nonlinear interactions between gravity waves and tides. This is the first time to present the global distribution of quarterdiurnal in-situ forcing from a numerical model. In summary, the solar forcing dominates in the troposphere and stratosphere, the nonlinear forcing predominates in the mesosphere and the gravity wave forcing mainly takes place in the mesosphere and thermosphere. These results do not allow to draw conclusions on the upward propagation of the QDT, but only show local excitation (Geißler et al., 2020).

For this reason, the idea of Smith et al. (2004) is adapted, who performed simulations with individual forcing mechanisms removed. In addition to Smith et al. (2004), the gravity wave - tide interactions are also considered. Some simulations are designed in a way that only a single forcing mechanism remains and the other two sources are removed (SOL, NLIN and GW), in other simulations only one of the sources was removed (NO_NLIN, NO_GW).

As a result, it could be found that the solar forcing mechanism is the most important and dominant one of all forcing mechanisms, since the removal of direct QDT solar heating (GW and NLIN runs) leads to a significant decrease in the QDT amplitude. Smith et al. (2004) came to the same conclusion, when they removed the QDT solar forcing in their simulations. In addition, in the direct solar forcing, which consists of excitation via water vapor and ozone, the QDT, which is excited from the ozone, is the dominant one due to some destructive interference from the QDT excited by water vapor in the troposphere and from the QDT excited by ozone in the stratosphere.

Additional (also see Geißler et al. (2020)) it is shown that the amplitudes resulting from the gravity wave forcing mechanism (GW) are smaller than the resulting amplitudes of the direct solar forcing (SOL), but larger than those from the nonlinear forcing mechanisms (NLIN). In agreement with the results of Smith et al. (2004), nonlinear tidal interactions seem to play a minor role for the total QDT amplitudes, although distinct sources of nonlinear quarterdiurnal in-situ excitation could be found in the mesosphere. This allows the conclusion that the QDT from local nonlinear forcing mechanisms can not propagate and is, to a large degree, trapped in the vertical domain. Significant nonlinear QDT amplitudes only exist in the thermosphere. In the temperature component, QDT amplitudes of the NLIN and GW simulation are comparable in magnitude. In the zonal wind component, they are smaller in NLIN than in GW. For the GW and NLIN simulations it can be note relatively short vertical wavelengths, accompanied by small QDT amplitudes, compared to the SOL and REF runs. It can be state that if the amplitudes are small, the vertical wavelength is shorter as well. Lilienthal et al. (2018) has found a similar relation for the vertical wavelengths of the TDT.

In the SOL simulation, which only contains the solar forcing, it can be see that the amplitudes are in some cases larger than in the REF run. A similar feature has been observed by Smith et al. (2004). Here, phase and amplitude differences between the different simulations are compared to investigate the physical explanation behind. The results show that the amplitudes in the simulations with removed forcing mechanisms (NO_NLIN and NO_GW) increase compared to REF in the same areas where destructive phase relations between the differently generated QDTs are detected. This leads to the conclusion that QDTs excited by different mechanisms counteract rather than enhance each other. Thus, removing an individual forcing mechanism in NO_NLIN or NO_GW also avoids the destructive interference and the remaining QDT can propagate freely, resulting in larger amplitudes.

This destructive relation appears to be more clear between the nonlinear tidal forcing and the direct solar forcing than between the gravity wave - induced forcing and the solar forcing. Note, however, that nonlinear tidal interactions generally have a smaller impact on the QDT than gravity wave - tide interactions, as described above.

Furthermore, a sensitivity study with respect to the strength of the individual forcing terms is done to contribute a better understanding of the forcing mechanisms and interactions. Thereby, their impact on QDT amplitudes and the background circulation is shown.

For direct solar forcing there is a linear connection between stronger forcing and the QDT amplitudes in temperature and zonal wind. So a 20% stronger forcing leads to 20% higher amplitudes. For the background circulation the correlation is also linear even it the effect is not as pronounced as with the amplitudes, except in the summer months when no correlation cloud be found. The same is true for the QDT amplitudes with stronger nonlinear interactions, the influence on the background circulation is negligible, as well as with stronger gravity wave forcing. The amplitudes show a slightly exponential increase with stronger gravity wave forcing.

Another investigation of this thesis concerned the important Hough modes of the QDT amplitude in the model simulations. Based on the first 10 Hough modes of the QDT, the field of the QDT temperature amplitudes was reconstructed with a Least Squares Fit and minimized differences to the model simulation. This allowed determining which Hough modes dominate and thus cause the meridional structure of the QDT amplitudes. For the REF simulation, there are the Hough modes (4,5), (4,6), (4,7), (4,9) and (4,10), which dominate all altitude ranges. A reconstruction was carried out analogous to the REF run for the SOL, NLIN and GW simulation, which has shown the dominant Hough modes are independent of the forcing and that the magnitude of the amplitude of the Hough modes in the altitude profiles differs between the forcings. A comparison was also made with the work of Azeem et al. (2016), which could only partially confirm the results of the dominant Hough modes.

9. Outlook

In the future, an implementation of a latent heat release parameterization according to Ermakova et al. (2019) and Jacobi et al. (2017a) to increase tidal amplitudes towards more realistic magnitudes. Nonmigrating tides are not considered in the model, this should be changed. This can be implemented by including SPWs in the model, using a three-dimensional ozone (Suvorova and Pogoreltsev, 2011) and water vapor distribution (Ermakova et al., 2017). At the moment, a version of the model with three-dimensional ozone is tested. A another important issue is the careful treatment of gravity waves, because we demonstrated that gravity waves are an important source of QDTs above the mesopause. In MUAM, gravity waves are currently implemented via two coupled parameterization. These two parameterizations could be replaced by the original whole atmosphere scheme, such as provided by Yiğit et al. (2008).

References

Andrews, D. G., C. B. Leovy, and J. R Holton (1987). *Middle atmosphere dynamics.* Vol. 40. Academic press, p. 489.

Azeem, I., R. L. Walterscheid, G. Crowley, R. L. Bishop, and A. B. Christensen (2016). Observations of the migrating semidiurnal and quaddiurnal tides from the RAIDS/NIRS instrument. *J. Geophy. Res.: Space Phys.*, 121 (5), 4626–4637. DOI: `10.1002/2015JA022240`.

Beard, A.G., N.J. Mitchell, P.J.S. Williams, and M. Kunitake (1999). Non-linear interactions between tides and planetary waves resulting in periodic tidal variability. *J. Atmos. Sol.-Terr. Phys.*, 61 (5), 363 –376. ISSN: 1364-6826. DOI: `10.1016/S1364-6826(99)00003-6`.

Berger, U. (1994). Numerische Simulation klimatologischer Prozesse und thermischer Gezeiten in der mittleren Atmosphäre. *Rep. Inst. Geophys. Meteorol. Univ. Köln.*

Bernard, R., J. L. Fellous, M. Massebeuf, and M. Glass (1981). Simultaneous meteor radar observations at Monpazier (France, 44°N) and Punta Borinquen (Puerto-Rico, 18°N). I—Latitudinal variations of atmospheric tides. *J. Atmos. Terr. Phys.*, 43 (5). Equatorial Aeronomy - I, 525 –533. ISSN: 0021-9169. DOI: `10.1016/0021-9169(81)90114-8`.

Cevolani, G. and P. Bonelli (1985). Tidal activity in the middle atmosphere. *Il Nuovo Cimento C*, 8 (5), 461–490. DOI: `10.1007/BF02582675`.

Chapman, S. and R. S. Lindzen (1970). Atmospheric Tides. *D. Reidel Publishing Company (Dordrecht, Holland).*

Chou, M.-D., W. L. Ridgway, and M. M-H. Yan (1993). One-Parameter Scaling and Exponential-Sum Fitting for Water Vapor and CO2 Infrared Transmission Functions. *J. Atmos. Sci.*, 50 (14), 2294–2303. DOI: `10.1175/1520-0469(1993)050<2294:OPSAES>2.0.CO;2`.

Danielson, G. C. and C. Lanczos (1942). Some improvements in practical Fourier analysis and their application to x-ray scattering from liquids. *J. Franklin Institute*, 233 (4), 365 –380. ISSN: 0016-0032. DOI: `10.1016/S0016-0032(42)90767-1`.

Dee, D. P., S. M. Uppala, A. J. Simmons, P. Berrisford, P. Poli, S. Kobayashi, U. Andrae, M. A. Balmaseda, G. Balsamo, P. Bauer, P. Bechtold, A. C. M. Beljaars, L. van de Berg, J. Bidlot, N. Bormann, C. Delsol, R. Dragani, M. Fuentes, A. J. Geer, L. Haimberger, S. B. Healy, H. Hersbach, E. V. Hólm, L. Isaksen, P. Kållberg, M. Köhler, M. Matricardi, A. P. McNally, B. M. Monge-Sanz, J.-J. Morcrette, B.-K. Park, C. Peubey, P. de Rosnay, C. Tavolato, J.-N. Thépaut, and F. Vitart (2011). The ERA-Interim reanalysis: configuration and performance of the data assimilation system. *Quart. J. Roy. Meteor. Soc.*, 137 (656), 553–597. DOI: `10.1002/qj.828`.

Deepa, V., G. Ramkumar, M. Antonita, K. K. Kumar, and M. N. Sasi (2006). Vertical propagation characteristics and seasonal variability of tidal wind oscillations in the MLT region over Trivandrum (8.5°N, 77°E): first results from SKiYMET Meteor Radar. *Ann. Geophys.*, 24 (11), 2877–2889. DOI: `10.5194/angeo-24-2877-2006`.

Drob, D. P., J. T. Emmert, J. W. Meriwether, J. J. Makela, E. Doornbos, M. Conde, G. Hernandez, J. Noto, K. A. Zawdie, S. E. McDonald, J. D. Huba, and J. H. Klenzing (2015). An update to the Horizontal Wind Model (HWM): The quiet time thermosphere. *Earth Space Sci.*, 2 (7). available at: `https://github.com/rilma/pyHWM14`, last acess: 10 September 2019, 301–319. DOI: `10.1002/2014EA000089`.

ERA-Interim (2018). Monthly mean temperature and geopotential fields on pressure levels 1979-date; Eurpoean Reanalysis Interim, available at: `https://apps.ecmwf.int/datasets/data/interim-full-moda/levtype=pl/`. compiled by Thoning, K. W., Kitzis, D. R. and Crotwell, A., Version 2015-12, updated annually.

Ermakova, T. S., O. G. Aniskina, I. A. Statnaia, M. A. Motsakov, and A. I. Pogoreltsev (2019). Simulation of the ENSO influence on the extra-tropical middle atmosphere. *Earth Planets and Space*, 71 (1), 8. ISSN: 1880-5981. DOI: `10.1186/s40623-019-0987-9`.

Ermakova, T. S., I. A. Statnaya, I. N. Fedulina, E. V. Suvorova, and A. I. Pogoreltsev (2017). Three-dimensional semi-empirical climate model of water vapor distribution and its implementation to the radiation module of the middle and upper atmosphere model. *Russ. Meteorol. Hydrol.*, 42 (9), 594–600. ISSN: 1934-8096. DOI: `10.3103/S1068373917090060`.

Fellous, J. L., R. Bernard, M. Glass, M. Massebeuf, and A. Spizzichino (1975). A study of the variations of atmospheric tides in the meteor zone. *J. Atmos. Terr. Phys.*, 37 (12), 1511 –1524. ISSN: 0021-9169. DOI: `10.1016/0021-9169(75)90030-6`.

Fleming, E. L., S. Chandra, J.J. Barnett, and M. Corney (1990). Zonal mean temperature, pressure, zonal wind and geopotential height as functions of latitude. *Adv. Space Res.*, 10 (12), 11 –59. ISSN: 0273-1177. DOI: `10.1016/0273-1177(90)90386-E`.

Fomichev, V. I., J.-P. Blanchet, and D. S. Turner (1998). Matrix parameterization of the 15 μm CO2 band cooling in the middle and upper atmosphere for variable CO2 concentration. *J. Geophy. Res.: Atmos.*, 103 (D10), 11505–11528. DOI: `10.1029/98JD00799`.

Fomichev, V.I. and G.M. Shved (1985). Parameterization of the radiative flux divergence in the 9.6 μm O3 band. *J. Atmos. Terr. Phys.*, 47 (11), 1037 –1049. ISSN: 0021-9169. DOI: `10.1016/0021-9169(85)90021-2`.

Forbes, J. M. (1982a). Atmospheric tide: 2. The solar and lunar semidiurnal components. *J. Geophy. Res.: Space Phys.*, 87 (A7), 5241–5252. DOI: `10.1029/JA087iA07p05241`.

– (1982b). Atmospheric tides: 1. Model description and results for the solar diurnal component. *J. Geophy. Res.: Space Phys.*, 87 (A7), 5222–5240. DOI: `10.1029/JA087iA07p05222`.

Forbes, J. M., X. Zhang, S. Palo, J. Russell, C. J. Mertens, and M. Mlynczak (2008). Tidal variability in the ionospheric dynamo region. *J. Geophy. Res.: Space Phys.*, 113 (A2). DOI: `10.1029/2007JA012737`.

Forbes, J.M., A.H. Manson, R.A. Vincent, G.J. Fraser, F. Vial, R. Wand, S.K. Avery, R.R. Clark, R. Johnson, R. Roper, R. Schminder, T. Tsuda, and E.S. Kazimirovsky (1994). Semidiurnal tide in the 80–150 km region: an assimilative data analysis. *J. Atmos. Sol.-Terr. Phys.*, 56 (10), 1237 –1249. ISSN: 0021-9169. DOI: `10.1016/0021-9169(94)90062-0`.

Foreman, M.G.G. and R.F. Henry (1989). The harmonic analysis of tidal model time series. *Advances in Water Resources*, 12 (3), 109 –120. ISSN: 0309-1708. DOI: `https://doi.org/10.1016/0309-1708(89)90017-1`.

Fröhlich, K. (2005). The Quasi Two-Day Wave - its impact on the zonal mean circulation and wave-wave interactions in the middle atmosphere. *PhD thesis. Universität Leipzig.*

Fröhlich, K., A. Pogoreltsev, and C. Jacobi (2003). Numerical simulation of tides, Rossby and Kelvin waves with the COMMA-LIM model. *Adv. Space Res.*, 32 (5), 863 –868. ISSN: 0273-1177. DOI: `10.1016/S0273-1177(03)00416-2`.

GSWM (2020). Amplitudes and phases of the diurnal and semidiurnal migirating tides from Global Scale Wave Model. Available at: `https://www2.hao.ucar.edu/gswm-global-scale-wave-model`. last acess: 02. March 2020.

Geißler, C. and C. Jacobi (2018). Forcing of the Quarterdiurnal Tide. *Rep. Inst. Meteorol. Univ. Leipzig*, 56, 21–30. URL: `https://nbn-resolving.org/urn:nbn:de:bsz:15-qucosa2-317929`.

Geißler, C., C. Jacobi, and F. Lilienthal (2020). Forcing mechanisms of the migrating quarterdiurnal tide. *Ann. Geophys.*, 38 (2), 527–544. DOI: `10.5194/angeo-38-527-2020`.

Gelaro, R., W. McCarty, M. J. Suárez, R. Todling, A. Molod, L. Takacs, C. A. Randles, A. Darmenov, M. G. Bosilovich, R. Reichle, K. Wargan, L. Coy, R. Cullather, C. Draper, S. Akella, V. Buchard, A. Conaty, A. M. da Silva, W. Gu, G.-K. Kim, R. Koster, R. Lucchesi, D. Merkova, J. E. Nielsen, G. Partyka, S. Pawson, W. Putman, M. Rienecker, S. D. Schubert, M. Sienkiewicz, and B. Zhao ().

Guharay, A., P. P. Batista, R. A. Buriti, and N. J. Schuch (2018). On the variability of the quarter-diurnal tide in the MLT over Brazilian low-latitude stations. *Earth Planets and Space*, 70 (1), 140. ISSN: 1880-5981. DOI: `10.1186/s40623-018-0910-9`.

Hagan, M. E., J. M. Forbes, and F. Vial (1995). On modeling migrating solar tides. *Geophys. Res. Lett.*, 22 (8), 893–896. DOI: `10.1029/95GL00783`.

Hagan, M. E., R. G. Roble, and J. Hackney (2001). Migrating thermospheric tides. *J. Geophy. Res.: Space Phys.*, 106 (A7), 12739–12752. DOI: `10.1029/2000JA000344`.

Hough, S. S. and G. H. Darwin (1898). V. On the application of harmonic analysis to the dynamical theory of the tides. Part II. On the general integration of Laplace's dynamical equations. *Philos. T. Roy. Soc. A, Containing Papers of a Mathematical or Physical Character*, 191, 139–185. DOI: `10.1098/rsta.1898.0005`.

Huang, T. Y. W. and A. K. Smith (1991). The Mesospheric Diabatic Circulation and the Parameterized Thermal Effect of Gravity Wave Breaking on the Circulation. *J. Atmos. Sci.*, 48 (8), 1093–1111. DOI: `10.1175/1520-0469(1991)048<1093:TMDCAT>2.0.CO;2`.

Jacobi, C., C. Arras, C. Geißler, and F. Lilienthal (2019). Quarterdiurnal signature in sporadic E occurrence rates and comparison with neutral wind shear. *Ann. Geophys.*, 37 (3), 273–288. DOI: `10.5194/angeo-37-273-2019`.

Jacobi, C., T. Ermakova, D. Mewes, and A. I. Pogoreltsev (2017a). El Niño influence on the mesosphere/lower thermosphere circulation at midlatitudes as seen by a VHF meteor radar at Collm (51.3° N, 13° E). *Adv. Radio Sci.*, 15, 199–206. DOI: `10.5194/ars-15-199-2017`.

Jacobi, C., K. Fröhlich, Y. Portnyagin, E. Merzlyakov, T. Solovjova, N. Makarov, D. Rees, A. Fahrutdinova, V. Guryanov, D. Fedorov, D. Korotyshkin, J. Forbes, A. Pogoreltsev, and D. Kürschner (2009). Semi-empirical model of middle atmosphere wind from the ground to the lower thermosphere. *Adv. Space Res.*, 43 (2), 239 –246. ISSN: 0273-1177. DOI: `10.1016/j.asr.2008.05.011`.

Jacobi, C., K. Fröhlich, and A. Pogoreltsev (2006). Quasi two-day-wave modulation of gravity wave flux and consequences for the planetary wave propagation in a simple circulation model. *J. Atmos. Sol.-Terr. Phys.*, 68 (3), 283 –292. ISSN: 1364-6826. DOI: `10.1016/j.jastp.2005.01.017`.

Jacobi, C., C. Geißler, F. Lilienthal, and A. Krug (2018). Forcing mechanisms of the 6 h tide in the mesosphere/lower thermosphere. *Adv. Radio Sci.*, 16, 141–147. DOI: `10.5194/ars-16-141-2018`. URL: `https://www.adv-radio-sci.net/16/141/2018/`.

Jacobi, C., A. Krug, and E. Merzlyakov (2017b). Radar observations of the quarterdiurnal tide at midlatitudes: Seasonal and long-term variations. *J. Atmos. Sol.-Terr. Phys.*, 163, 70 –77. ISSN: 1364-6826. DOI: `10.1016/j.jastp.2017.05.014`.

– (2017c). Radar observations of the quarterdiurnal tide at midlatitudes: Seasonal and long-term variations. *J. Atmos. Sol.-Terr. Phys.*, 163, 70 –77. ISSN: 1364-6826. DOI: `10.1016/j.jastp.2017.05.014`.

Jacobi, C., F. Lilienthal, C. Geißler, and A. Krug (2015). Long-term variability of mid-latitude mesosphere-lower thermosphere winds over Collm (51°N, 13°E). *J. Atmos. Sol.-Terr. Phys.*, 136, 174 –186. ISSN: 1364-6826. DOI: `10.1016/j.jastp.2015.05.006`.

Jacobi, C., Y.I. Portnyagin, T.V. Solovjova, P. Hoffmann, W. Singer, A.N. Fahrutdinova, R.A. Ishmuratov, A.G. Beard, N.J. Mitchell, H.G. Muller, R. Schminder, D. Kürschner, A.H. Manson, and C.E. Meek (1999). Climatology of the semidiurnal tide at 52–56°N from ground-based radar wind measurements 1985–1995. *J. Atmos. Sol.-Terr. Phys.*, 61 (13), 975 –991. ISSN: 1364-6826. DOI: `10.1016/S1364-6826(99)00065-6`.

Jakobs, H.J., M. Bischof, A. Ebel, and P. Speth (1986). Simulation of gravity wave effects under solstice conditions using a 3-D circulation model of the middle atmosphere. *J. Atmos. Sol.-Terr. Phys.*, 48 (11), 1203 –1223. ISSN: 0021-9169. DOI: `10.1016/0021-9169(86)90040-1`.

Koval, A. V., N. M. Gavrilov, A. I. Pogoreltsev, and N. O. Shevchuk (2018). Influence of Solar Activity on Penetration of Traveling Planetary-Scale Waves From the Troposphere Into the Thermosphere. *J. Geophy. Res.: Space Phys.*, 123 (8), 6888–6903. DOI: `10.1029/2018JA025680`.

Kovalam, S. and R. A. Vincent (2003). Intradiurnal wind variations in the midlatitude and high-latitude mesosphere and lower thermosphere. *Journal of Geophysical Research: Atmospheres*, 108 (D4). DOI: `10.1029/2002JD002500`.

Lange, M. (2001). Modellstudien zum CO2-Anstieg und O3 -Abbau in der mittleren Atmosphäre und Einfluss des Polarwirbels auf die zonale Symmetrie des Windfeldes in der Mesopausenregion. *PhD thesis. Universität Leipzig.*

Lee, C.-C., J.-Y. Liu, C.-J. Pan, and H.-H. Hsu (2003). The intermediate layers and associated tidal motions observed by a digisonde in the equatorial anomaly region. *Annales Geophysicae*, 21 (4), 1039–1045. URL: `https://hal.archives-ouvertes.fr/hal-00317051/file/angeo-21-1039-2003.pdf`.

Lilienthal, F. and C. Jacobi (2019). Nonlinear forcing mechanisms of the terdiurnal solar tide and their impact on the zonal mean circulation. *Ann. Geophys. Disc.*, 2019, 1–18. DOI: `10.5194/angeo-2019-37`.

Lilienthal, F., C. Jacobi, and C. Geißler (2018). Forcing mechanisms of the terdiurnal tide. *Atmos. Chem. Phys.*, 18 (21), 15725–15742. DOI: `10.5194/acp-18-15725-2018`.

Lilienthal, F., C. Jacobi, T. Schmidt, A. de la Torre, and P. Alexander (2017). On the influence of zonal gravity wave distributions on the Southern Hemisphere winter circulation. *Ann. Geophys.*, 35 (4), 785–798. DOI: `10.5194/angeo-35-785-2017`.

Lilienthal, L. (2019). Analysis of the Forcing Mechanisms of the Terdiurnal Solar Tide in the Middle Atmosphere. *PhD theses. Universiät Leipzig.* URL: `https://nbn-resolving.org/urn:nbn:de:bsz:15-qucosa2-341366`.

Lindzen, R. S. (1981). Turbulence and stress owing to gravity wave and tidal breakdown. *J. Geophys. Res.: Oceans*, 86 (C10), 9707–9714. DOI: `10.1029/JC086iC10p09707`.

Liou, K.-N. (1992). Radiation and Cloud Processes in the Atmosphere: Theory, Observation and Modeling. *Oxford Monographs on Geology and Geophysics, (20).*

Liu, G., D. Janches, R. S. Lieberman, T. Moffat-Griffin, D. C. Fritts, and N. J. Mitchell (2020). Coordinated Observations of 8- and 6-hr Tides in the Mesosphere and Lower Thermosphere by Three Meteor Radars Near 60°S Latitude. *Geophys. Res. Lett.*, 47 (1). DOI: `10.1029/2019GL086629`.

Liu, M. H., J. Y. Xu, J. Yue, and G. Y. Jiang (2015). Global structure and seasonal variations of the migrating 6-h tide observed by SABER/TIMED. *Science China Earth Sciences*, 58 (7), 1216–1227. ISSN: 1869-1897. DOI: `10.1007/s11430-014-5046-6`.

Liu, R., D. Lu, F. Yi, and X. Hu (2006). Quadratic nonlinear interactions between atmospheric tides in the mid-latitude winter lower thermosphere. *J. Atmos. Sol.-Terr. Phys.*, 68 (11), 1245 –1259. ISSN: 1364-6826. DOI: `10.1016/j.jastp.2006.03.004`.

MERRA-2 (2019). Monthly mean ozone fields on pressure levels 1979-date; Modern-Era Retrospective analysis for Research and Applications, Version 2, available at: `https://disc.gsfc.nasa.gov/datasets?keywords=%22MERRA-2%22`. Last access: 10 September 2019.

Manson, A. H. and C. E. Meek (1986). Dynamics of the middle atmosphere at Saskatoon (52°N, 107°W): a spectral study during 1981, 1982. *Journal of Atmospheric and Terrestrial Physics*, 48 (11), 1039 –1055. ISSN: 0021-9169. DOI: `https://doi.org/10.1016/0021-9169(86)90025-5`.

Manson, A.H., C.E. Meek, H. Teitelbaum, F. Vial, R. Schminder, D. Kürschner, M. J. Smith, G. J. Fraser, and R. R. Clark (1989). Climatologies of semi-diurnal and diurnal tides in the middle atmosphere (70–110 km) at middle latitudes (40–55°). *J. Atmos. Sol.-Terr. Phys.*, 51 (7), 579 –593. DOI: `10.1016/0021-9169(89)90056-1`.

Matsuno, T. (1966). Numerical Integrations of the Primitive Equations by a Simulated Backward Difference Method. *J. Meteor. Soc. Jap.*, 44 (1), 76–84. DOI: `10.2151/jmsj1965.44.1_76`.

Medvedev, A. S. and G. P. Klaassen (2003). Thermal effects of saturating gravity waves in the atmosphere. *J. Geophy. Res.: Atmos.*, 108 (D2), ACL 4–1–ACL 4–18. DOI: `10.1029/2002JD002504`.

Miyahara, S. and J. F. Forbes (1991). Interactions between gravity waves and the diurnal tide in the mesosphere and lower thermosphere. *J. Meteor. Res. Japan. Ser. II*, 69 (5), 523–531. DOI: `10.2151/jmsj1965.69.5_523`.

Mlynczak, M. G. and S. Solomon (1993). A detailed evaluation of the heating efficiency in the middle atmosphere. *J. Geophy. Res.: Atmos.*, 98 (D6), 10517–10541. DOI: `10.1029/93JD00315`.

Morton, Y. T., J. D. Mathews, and Q. Zhou (1993). Further evidence for a 6-h tide above Arecibo. *J. Atmos. Terr. Phys.*, 55 (3). Arecibo initiative dynamics of the atmosphere, AIDA act '89, 459 –465. ISSN: 0021-9169. DOI: `10.1016/0021-9169(93)90081-9`.

NOAA ESRL Global Monitoring Division (2018). Atmospheric Carbon Dioxide Dry Air Mole Fractions from quasi-continuous measurements at Mauna Loa, Hawaii, National Oceanic and Atmospheric Administration (NOAA), Earth System Research Laboratory (ESRL), Global Monitoring Division (GMD), Boulder, Colorado, USA, available at: `https://www.esrl.noaa.gov/gmd/ccgg/trends/data.html`. last access: 10 September 2019.

Ogibalov, V., V. I. Fomichev, and A. Kutepov (2000). Radiative Heating affected by Infrared CO2 bands in the middle and upper atmosphere. *Izv. Atmos. Ocean. Phys.*, 34 (4), 454–464.

Oikonomou, C., H. Haralambous, C. Haldoupis, and C. Meek (2014). Sporadic E tidal variabilities and characteristics observed with the Cyprus Digisonde. *Journal of Atmospheric and Solar-Terrestrial Physics*, 119, 173 –183. ISSN: 1364-6826. DOI: `https://doi.org/10.1016/j.jastp.2014.07.014`.

Pancheva, D., N.J. Mitchell, M.E. Hagan, A.H. Manson, C.E. Meek, Yi Luo, Ch. Jacobi, D. Kürschner, R.R. Clark, W.K. Hocking, J. MacDougall, G.O.L. Jones, R.A. Vincent, I.M. Reid, W. Singer, K. Igarashi, G.I. Fraser, T. Nakamura, T. Tsuda, Yu. Portnyagin, E. Merzlyakov, A.N. Fahrutdinova, A.M. Stepanov, L.M.G. Poole, S.B. Malinga, B.L. Kashcheyev, A.N. Oleynikov, and D.M. Riggin (2002). Global-scale tidal structure in the mesosphere and lower thermosphere during the PSMOS campaign of June–August 1999 and comparisons with the global-scale wave model. *J. Atmos. Sol.-Terr. Phys.*, 64 (8). PSMOS 2000 Workshop - Planetary Scale Mesopause Observing System, 1011 –1035. ISSN: 1364-6826. DOI: `10.1016/S1364-6826(02)00054-8`.

Pogoreltsev, A. I. (2007). Generation of normal atmospheric modes by stratospheric vacillations. *Izvestiya, Atmos. Ocean. Phys.*, 43 (4), 423–435. ISSN: 1555-628X. DOI: `10.1134/S0001433807040044`.

Pogoreltsev, A.I., A.A. Vlasov, K. Fröhlich, and C. Jacobi (2007). Planetary waves in coupling the lower and upper atmosphere. *J. Atmos. Sol.-Terr. Phys.*, 69 (17), 2083 –2101. ISSN: 1364-6826. DOI: `10.1016/j.jastp.2007.05.014`.

Pokhotelov, D., E. Becker, G. Stober, and J. L. Chau (2018). Seasonal variability of atmospheric tides in the mesosphere and lower thermosphere: meteor radar data and simulations. *Ann. Geophys.*, 36 (3), 825–830. DOI: `10.5194/angeo-36-825-2018`.

Portnyagin, Y., T. Solovjova, E. Merzlyakov, J. Forbes, S. Palo, D. Ortland, W. Hocking, J. MacDougall, T. Thayaparan, A. Manson, C. Meek, P. Hoffmann, W. Singer, N. Mitchell, D. Pancheva, K. Igarashi, Y. Murayama, Ch. Jacobi, D. Kuerschner, A. Fahrutdinova, D. Korotyshkin, R. Clark, M. Taylor, S. Franke, D. Fritts, T. Tsuda, T. Nakamura,

S. Gurubaran, R. Rajaram, R. Vincent, S. Kovalam, P. Batista, G. Poole, S. Malinga, G. Fraser, D. Murphy, D. Riggin, T. Aso, and M. Tsutsumi (2004). Mesosphere/lower thermosphere prevailing wind model. *Adv. Space Res.*, 34 (8), 1755 –1762. ISSN: 0273-1177. DOI: `10.1016/j.asr.2003.04.058`.

Press, W. H., B. P. Flannery, S. A. Teukolsky, and W. T. Vetterling (1989). Numerical Recipes in FORTRAN: The Art of Scientific Computing. *2nd ed. Cambridge, England: Cambridge University Press*, 407–411.

Randel, W. J. and F. Wu (2007). A stratospheric ozone profile data set for 1979–2005: Variability, trends, and comparisons with column ozone data. *Journal of Geophysical Research: Atmospheres*, 112 (D6). DOI: `10.1029/2006JD007339`.

Revah, I. (1970). Partial reflections of gravity waves observed by means of a meteoric radar. *J. Atmos. Terr. Phys.*, 32 (7), 1313 –1317. ISSN: 0021-9169. DOI: `10.1016/0021-9169(70)90061-9`.

Ribstein, B. and U. Achatz (2016). The interaction between gravity waves and solar tides in a linear tidal model with a 4-D ray-tracing gravity-wave parameterization. *J. Geophy. Res.: Space Phys.*, 121 (9), 8936–8950. DOI: `10.1002/2016JA022478`.

Riese, M., D. Offermann, and G. Brasseur (1994). Energy released by recombination of atomic oxygen and related species at mesopause heights. *J. Geophys. Res.: Atmos.*, 99 (D7), 14585–14593. DOI: `10.1029/94JD00356`.

Rose, K. (1983). On the influence of nonlinear wave-wave interactions in a 3-D primitive equation model for Sudden stratospheric warmings. *Beiträge zur Physik der Atmosphäre, 56, 14–41.*

SPARC (2020). Monthly mean global ozone data set 1979-2005 from Stratosphere-troposphere Processes And their Role in Climate, available at: `https://www.sparc-climate.org/data-centre/data-access/reference-climatology/randals-climatologies/updated-ozone-trends/`. Last access: 05. October 2020.

Samtleben, N., C. Jacobi, P. Pišoft, P. Šácha, and A. Kuchař (2019). Effect of latitudinally displaced gravity wave forcing in the lower stratosphere on the polar vortex stability. *Ann. Geophys.*, 37 (4), 507–523. DOI: `10.5194/angeo-37-507-2019`.

She, C. Y., S. Chen, B. P. Williams, Z. Hu, D. A. Krueger, and M. E. Hagan (2002). Tides in the mesopause region over Fort Collins, Colorado (41°N, 105°W) based on lidar temperature observations covering full diurnal cycles. *J. Geophy. Res.: Atmos.*, 107 (D18), ACL 4–1–ACL 4–12. DOI: `10.1029/2001JD001189`.

Sivjee, G.G. and R.L. Walterscheid (1994). Six-hour zonally symmetric tidal oscillations of the winter mesopause over the South Pole Station. *Planet Space Sci.*, 42 (6), 447 –453. ISSN: 0032-0633. DOI: `10.1016/0032-0633(94)00085-9`.

Smith, A. K. (2012). Global Dynamics of the MLT. *Surv Geophys.*, 33 (6), 1177–1230. ISSN: 1573-0956. DOI: `10.1007/s10712-012-9196-9`.

Smith, A. K. and D. A. Ortland (2001). Modeling and analysis of the structure and generation of the terdiurnal tide. *J. Atmos. Sci.*, 58 (21), 3116–3134. DOI: `10.1175/1520-0469(2001)058<3116:MAAOTS>2.0.CO;2`.

Smith, A. K., D. V. Pancheva, and N. J. Mitchell (2004). Observations and modeling of the 6-hour tide in the upper mesosphere. *J. Geophys. Res.: Atmos.*, 109 (D10). DOI: `10.1029/2003JD004421`.

Strobel, D. F. (1978). Parameterization of the atmospheric heating rate from 15 to 120 km due to O2 and O3 absorption of solar radiation. *J. Geophys. Res.: Oceans*, 83 (C12), 6225–6230. DOI: `10.1029/JC083iC12p06225`.

Suvorova, E. V. and A. I. Pogoreltsev (2011). Modeling of nonmigrating tides in the middle atmosphere. *Geomagn. Aeron.*, 51 (1), 105–115. ISSN: 1555-645X. DOI: `10.1134/S0016793210061039`.

Swinbank, R. and D. A. Ortland (2003). Compilation of wind data for the Upper Atmosphere Research Satellite (UARS) Reference Atmosphere Project. *J. Geophys. Res.: Atmos.*, 108 (D19). DOI: `10.1029/2002JD003135`.

Teitelbaum, H. and F. Vial (1991). On tidal variability induced by nonlinear interaction with planetary waves. *J. Geophy. Res.: Space Phys.*, 96 (A8), 14169–14178. DOI: `10.1029/91JA010192`.

Teitelbaum, H., F. Vial, A. H. Manson, R. Giraldez, and M. Massebeuf (1989). Nonlinear interaction between the diurnal and semidiurnal tides: terdiurnal and diurnal secondary waves. *Journal of Atmospheric and Terrestrial Physics*, 51 (7). International Middle Atmosphere Program Symposium, 627 –634. ISSN: 0021-9169. DOI: `https://doi.org/10.1016/0021-9169(89)90061-5`.

Thoning, K. W., P. P. Tans, and W. D. Komhyr (1989). Atmospheric carbon dioxide at Mauna Loa Observatory: 2. Analysis of the NOAA GMCC data, 1974–1985. *J. Geophys. Res.: Atmos.*, 94 (D6), 8549–8565. DOI: `10.1029/JD094iD06p08549`.

Tong, Y., J. D. Mathews, and W. P. Ying (1988). An upper E region quarterdiurnal tide at Arecibo? *J. Geophy. Res.: Space Phys.*, 93 (A9), 10047–10051. DOI: `10.1029/JA093iA09p10047`.

Wang, H., J. Boyd, and R. Akmaev (Jan. 2016). On computation of Hough functions. *Geoscientific Model Development Discussions*, 9, 1–17. DOI: `10.5194/gmd-2015-282`.

Xu, J., A. K. Smith, G. Jiang, W. Yuan, and H. Gao (2012). Features of the seasonal variation of the semidiurnal, terdiurnal and 6-h components of ozone heating evaluated from Aura/MLS observations. *Ann. Geophys.*, 30 (2), 259–281. DOI: `10.5194/angeo-30-259-2012`.

Xu, J., A. K. Smith, M. Liu, X. Liu, H. Gao, G. Jiang, and W. Yuan (2014). Evidence for nonmigrating tides produced by the interaction between tides and stationary planetary waves in the stratosphere and lower mesosphere. *J. Geophy. Res.: Atmos.*, 119 (2), 471–489. DOI: `10.1002/2013JD020150`.

Yiğit, E., A. D. Aylward, and A. S. Medvedev (2008). Parameterization of the effects of vertically propagating gravity waves for thermosphere general circulation models: Sensitivity study. *J. Geophys. Res.: Atmos.*, 113 (D19). DOI: `10.1029/2008JD010135`.

Yiğit, E. and A. S. Medvedev (2015). Internal wave coupling processes in earth's atmosphere. *Adv. Space Res.*, 55 (4), 983 –1003. ISSN: 0273-1177. DOI: `10.1016/j.asr.2014.11.020`.

Yiğit, E., A. S. Medvedev, A. D. Aylward, P. Hartogh, and M. J. Harris (2009). Modeling the effects of gravity wave momentum deposition on the general circulation above the turbopause. *J. Geophys. Res.: Atmos.*, 114 (D7). DOI: `10.1029/2008JD011132`.

Younger, P. T., D. Pancheva, H. R. Middleton, and N. J. Mitchell (2002). The 8-hour tide in the Arctic mesosphere and lower thermosphere. *J. Geophy. Res.: Space Phys.*, 107 (A12), SIA 2–1–SIA 2–11. DOI: `10.1029/2001JA005086`.

A. Supplement

A.1. Background reference climatology

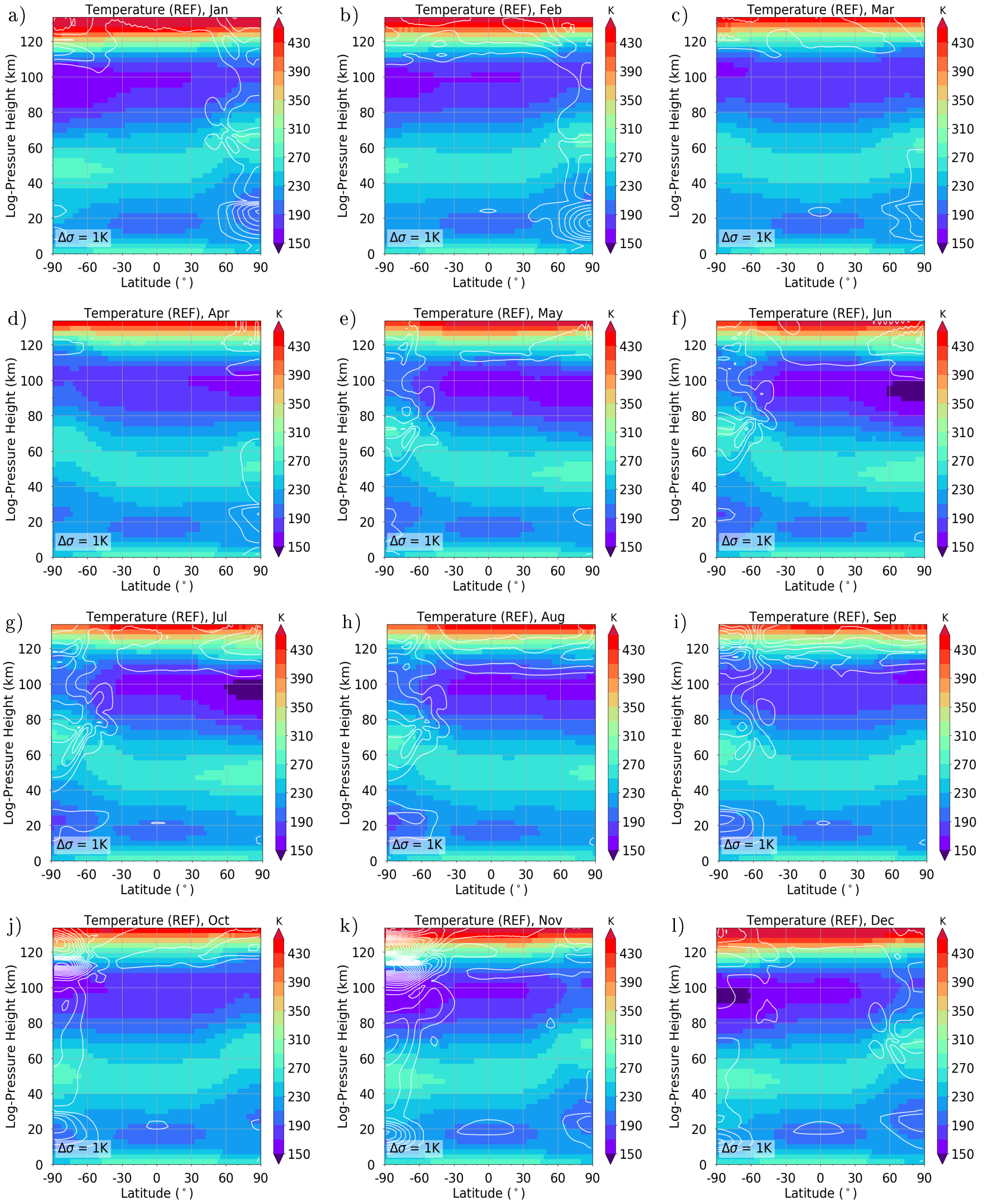

Figure S1.: Background temperature as color, white lines are standard deviation from ensemble runs.

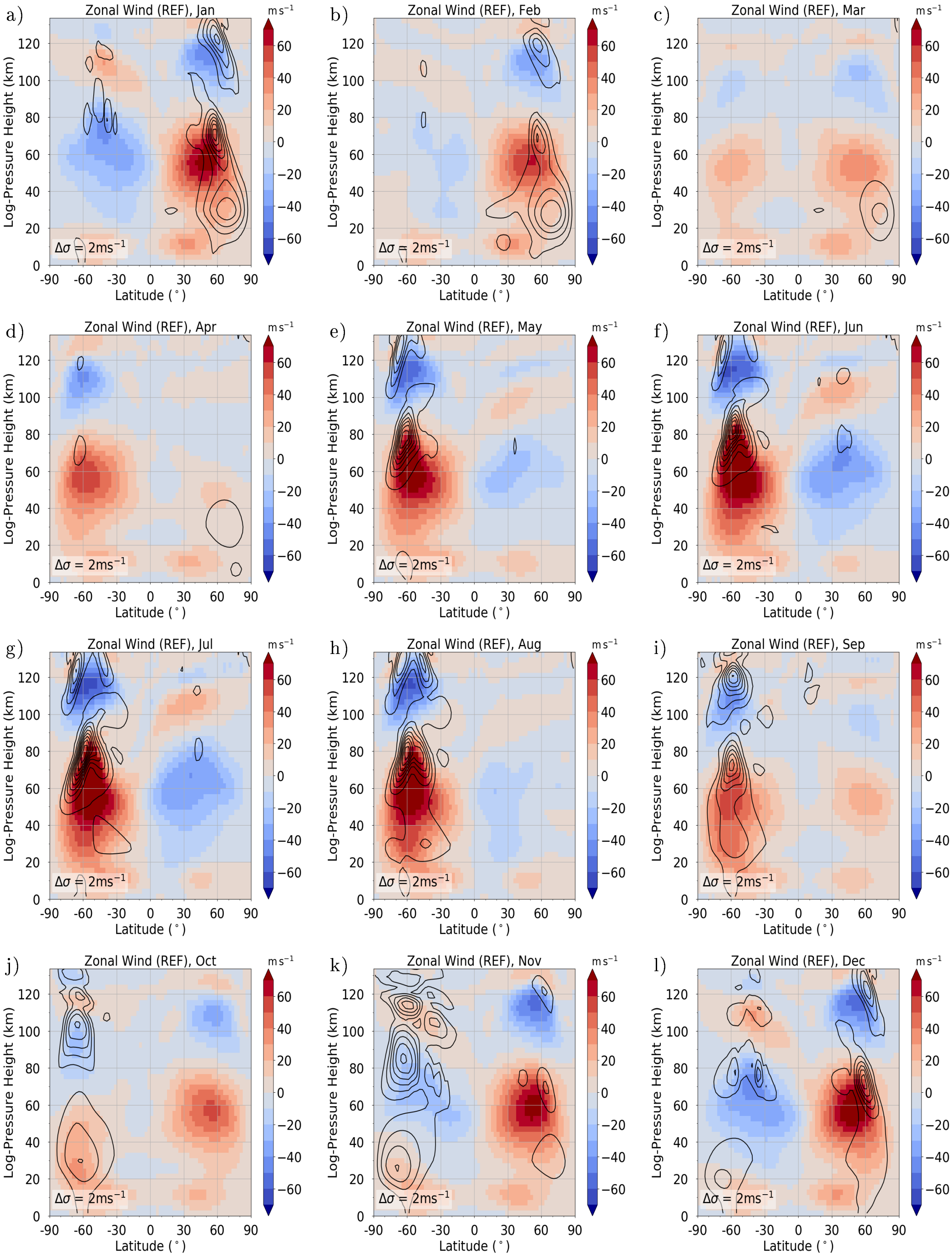

Figure S2.: Background zonal wind as color, black lines are standard deviation from ensemble runs.

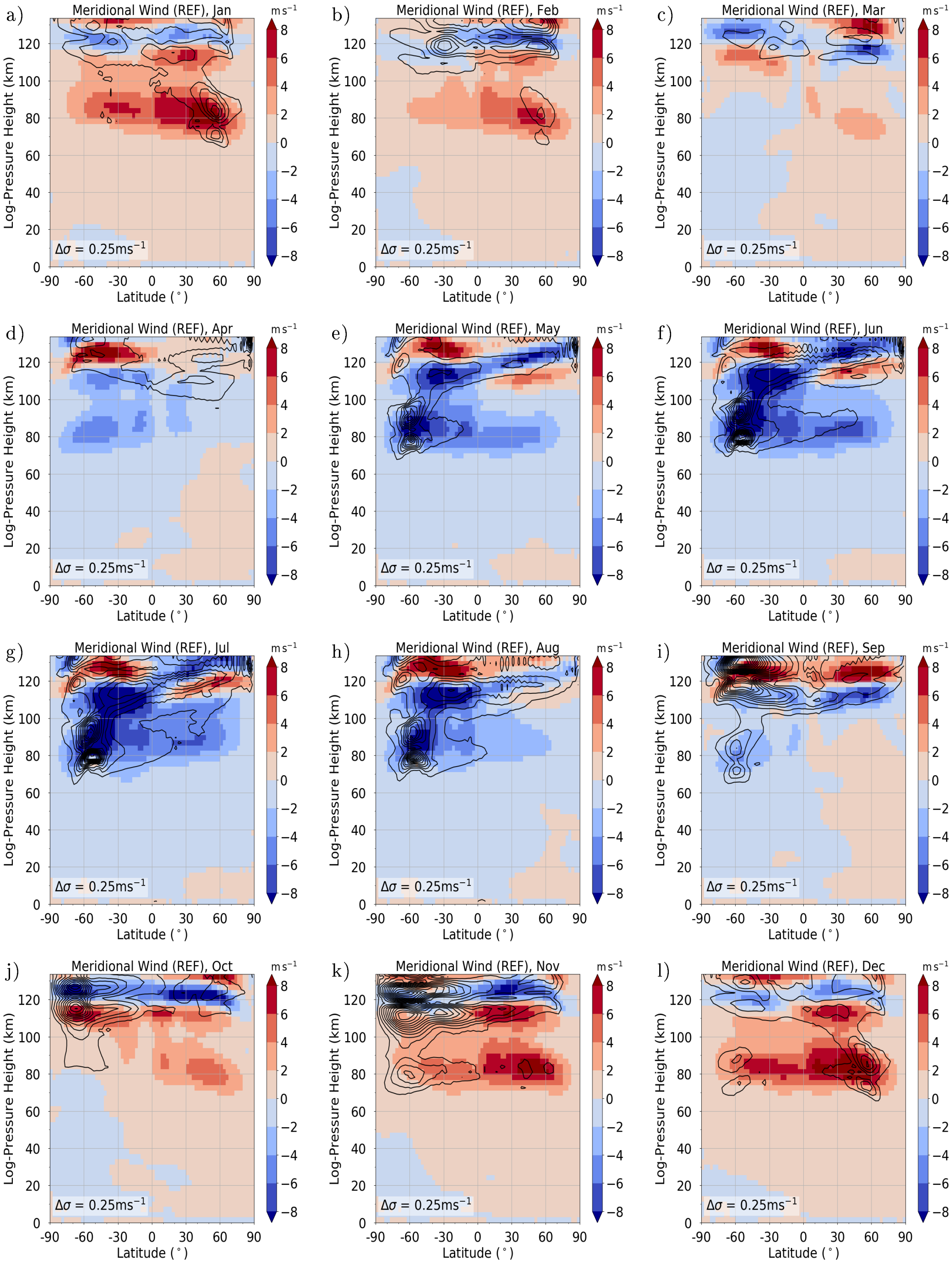

Figure S3.: Background meridional wind as color, black lines are standard deviation from ensemble runs.

A.2. QDT Amplitudes

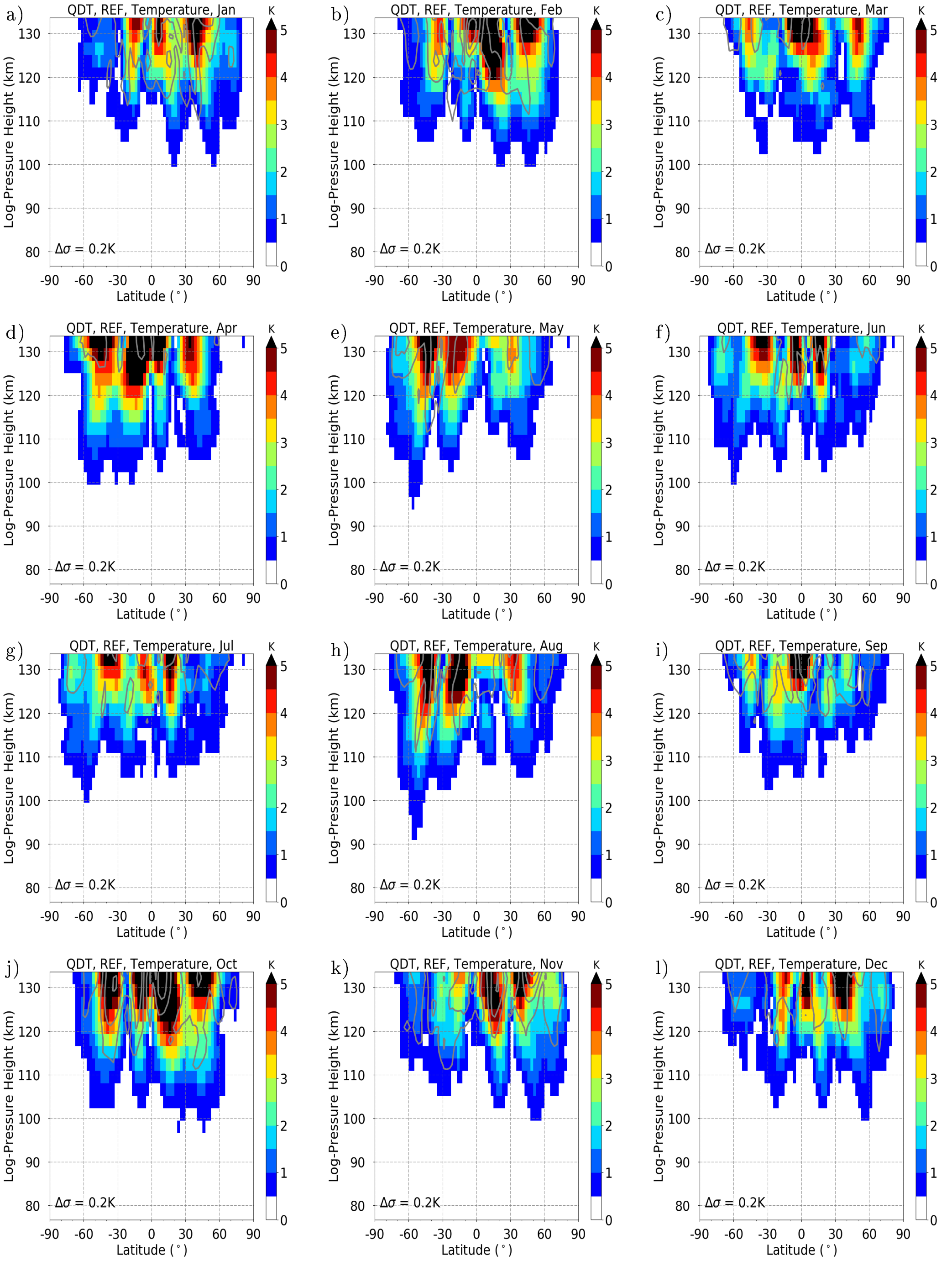

Figure S4.: QDT temperature amplitudes as color, black lines are standard deviation from ensemble runs.

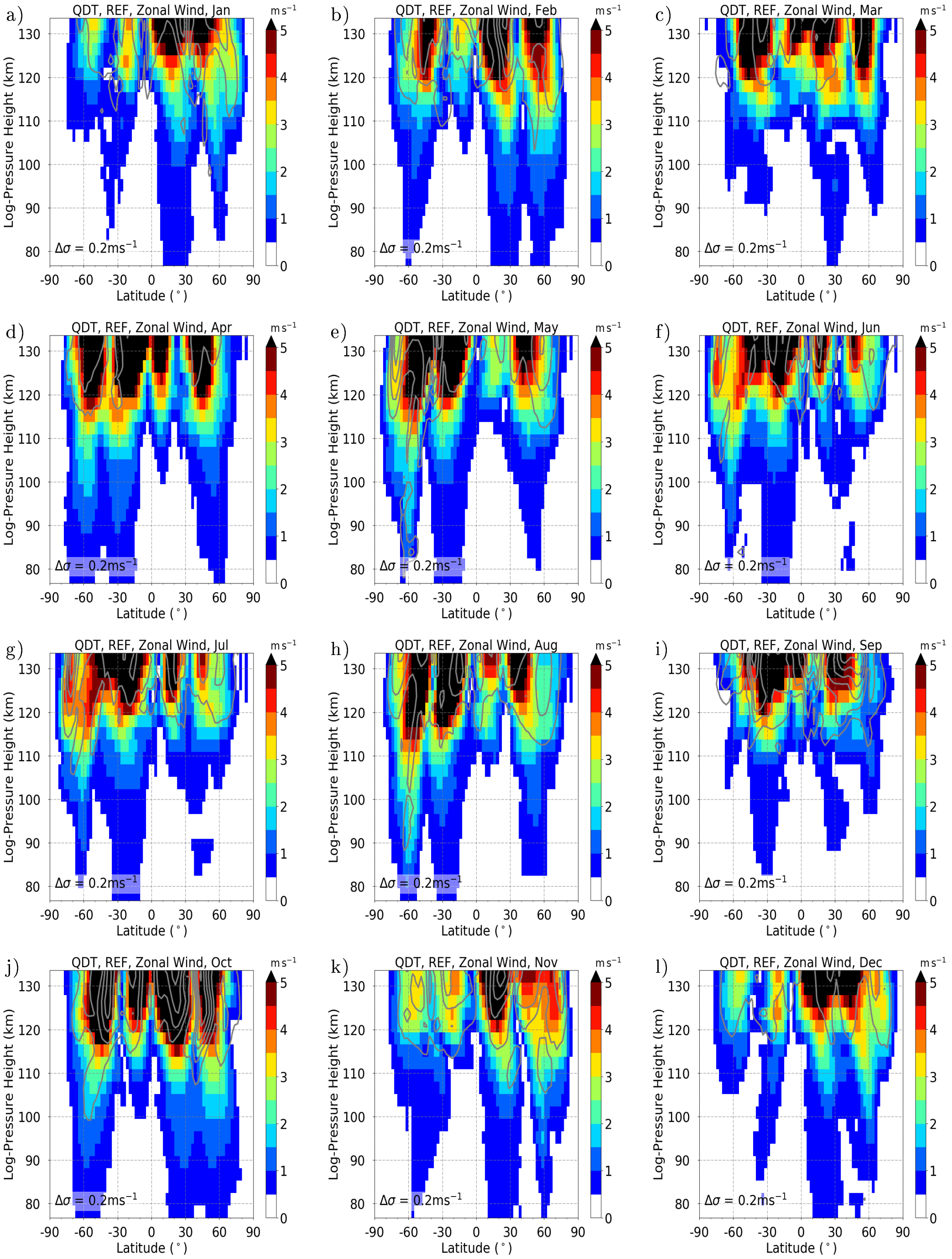

Figure S5.: QDT zonal wind amplitudes as color, black lines are standard deviation from ensemble runs.

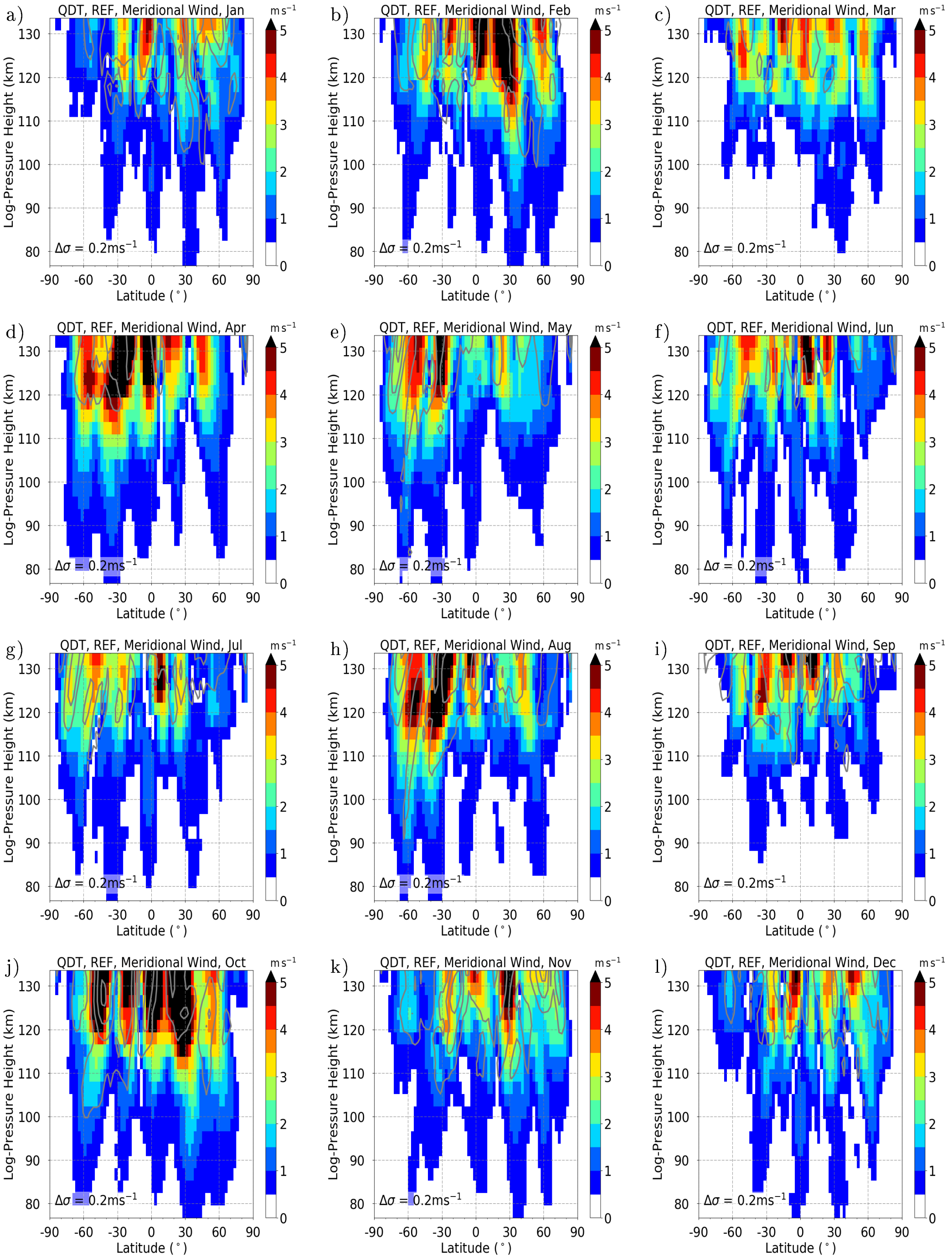

Figure S6.: QDT meridional wind amplitudes as color, black lines are standard deviation from ensemble runs.

A.3. QDT Phases

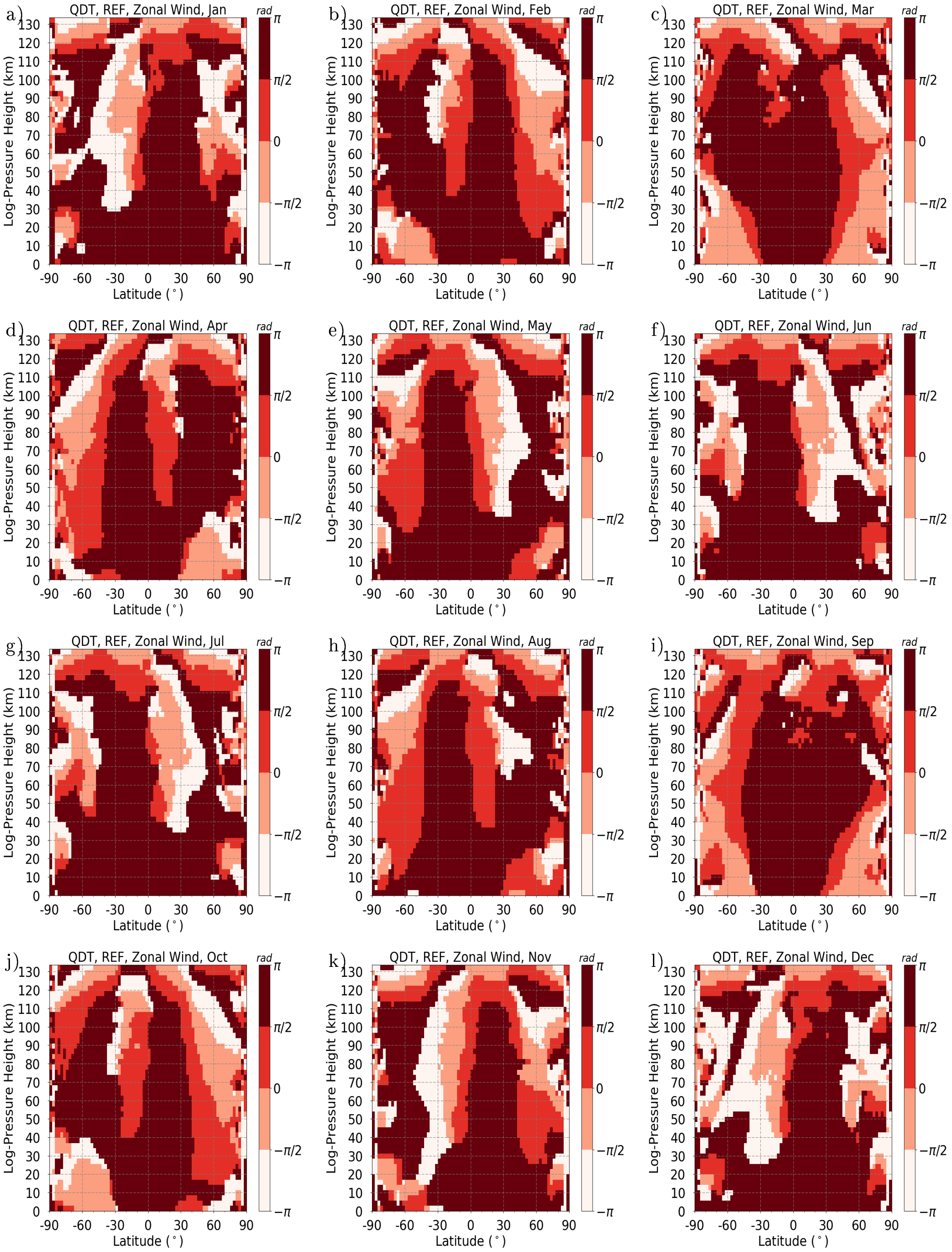

Figure S7.: QDT zonal wind phases as color.

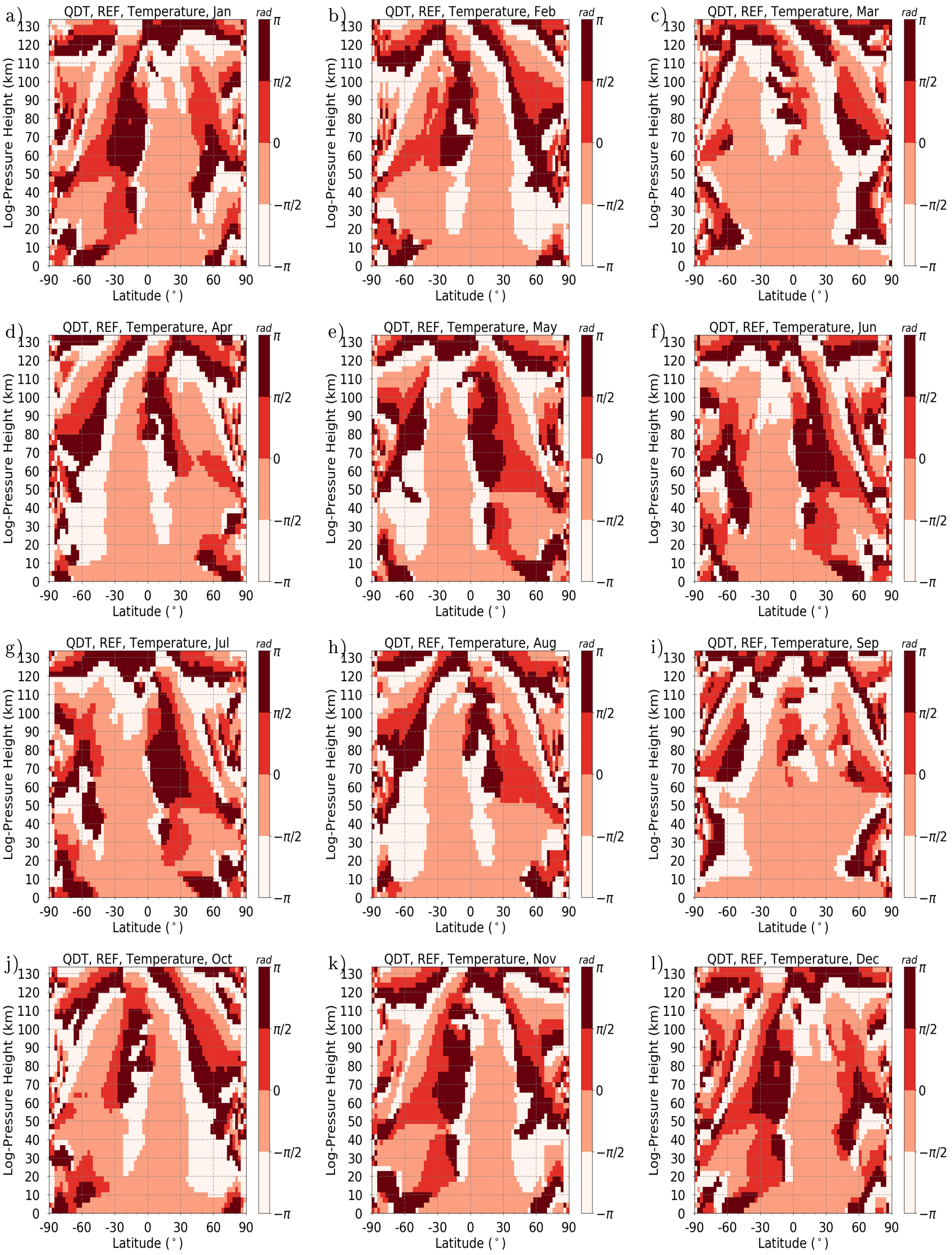

Figure S8.: QDT temperature phases as color.

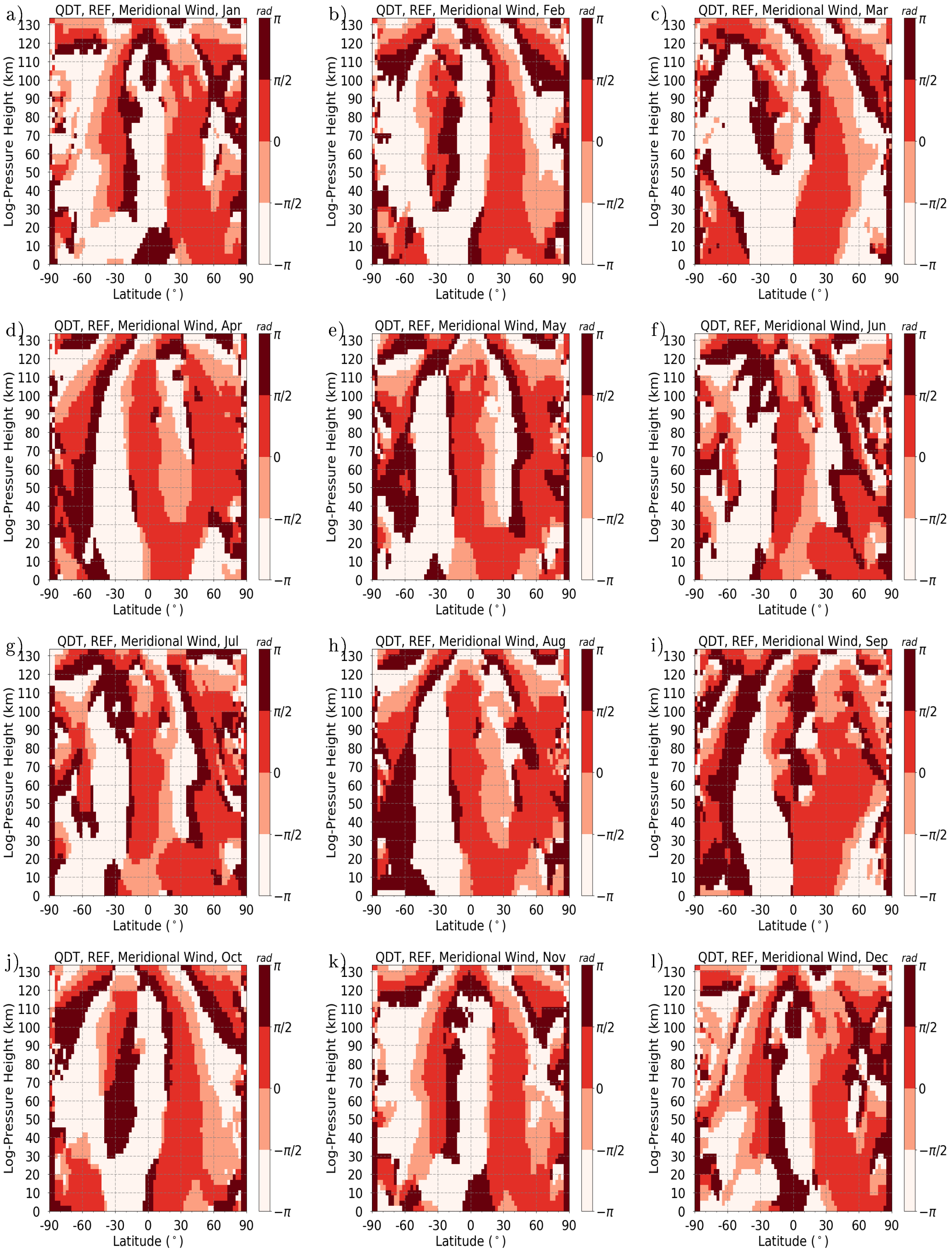

Figure S9.: QDT meridional wind phases as color.

A.4. QDT Vertical Wavelength

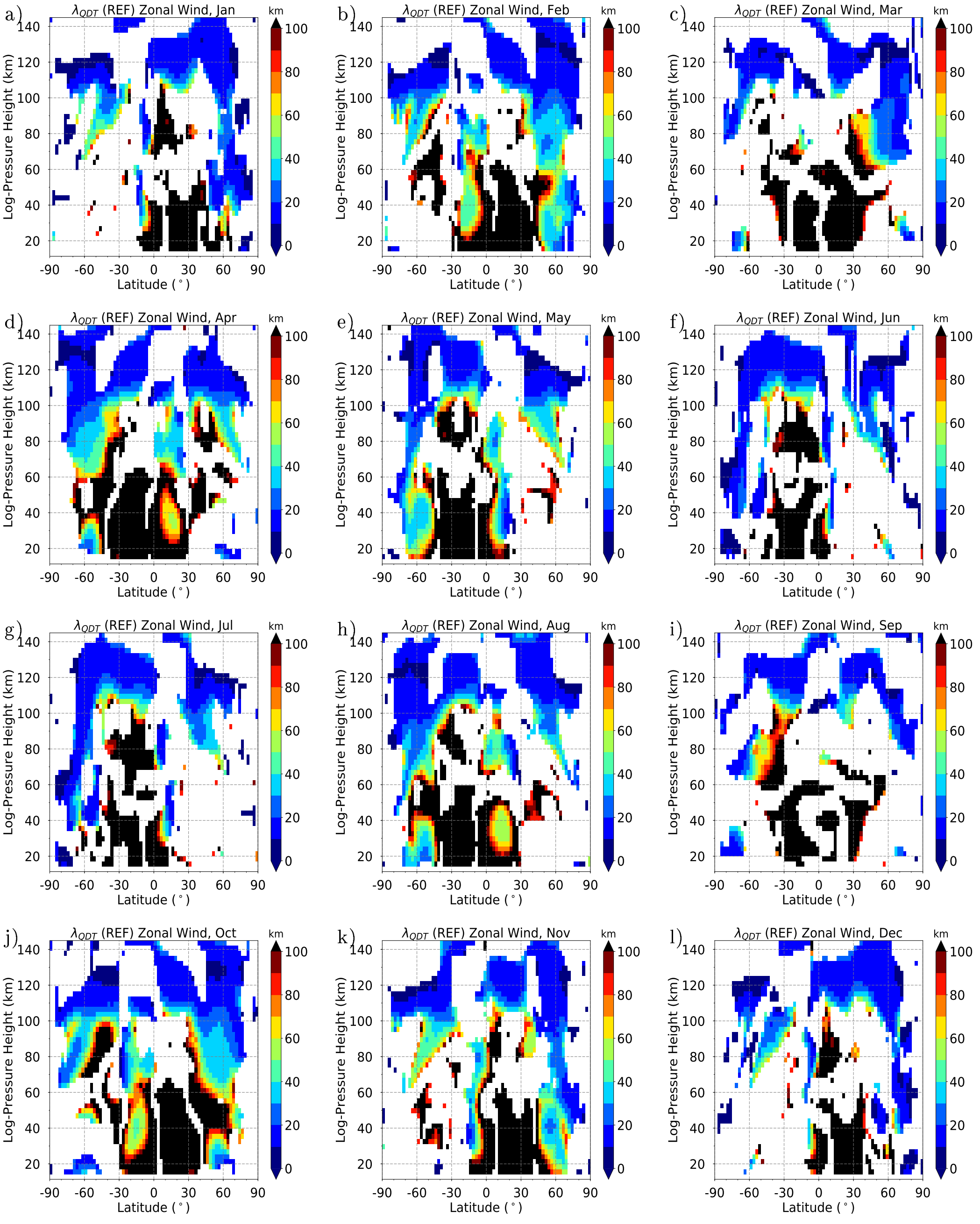

Figure S10.: QDT zonal wind vertical wavelengths, which are a result of a linear fit of vertical phase gradients over a range of 30 km and plottet for areas with correlation coefficient of $R \leq 0.6$.

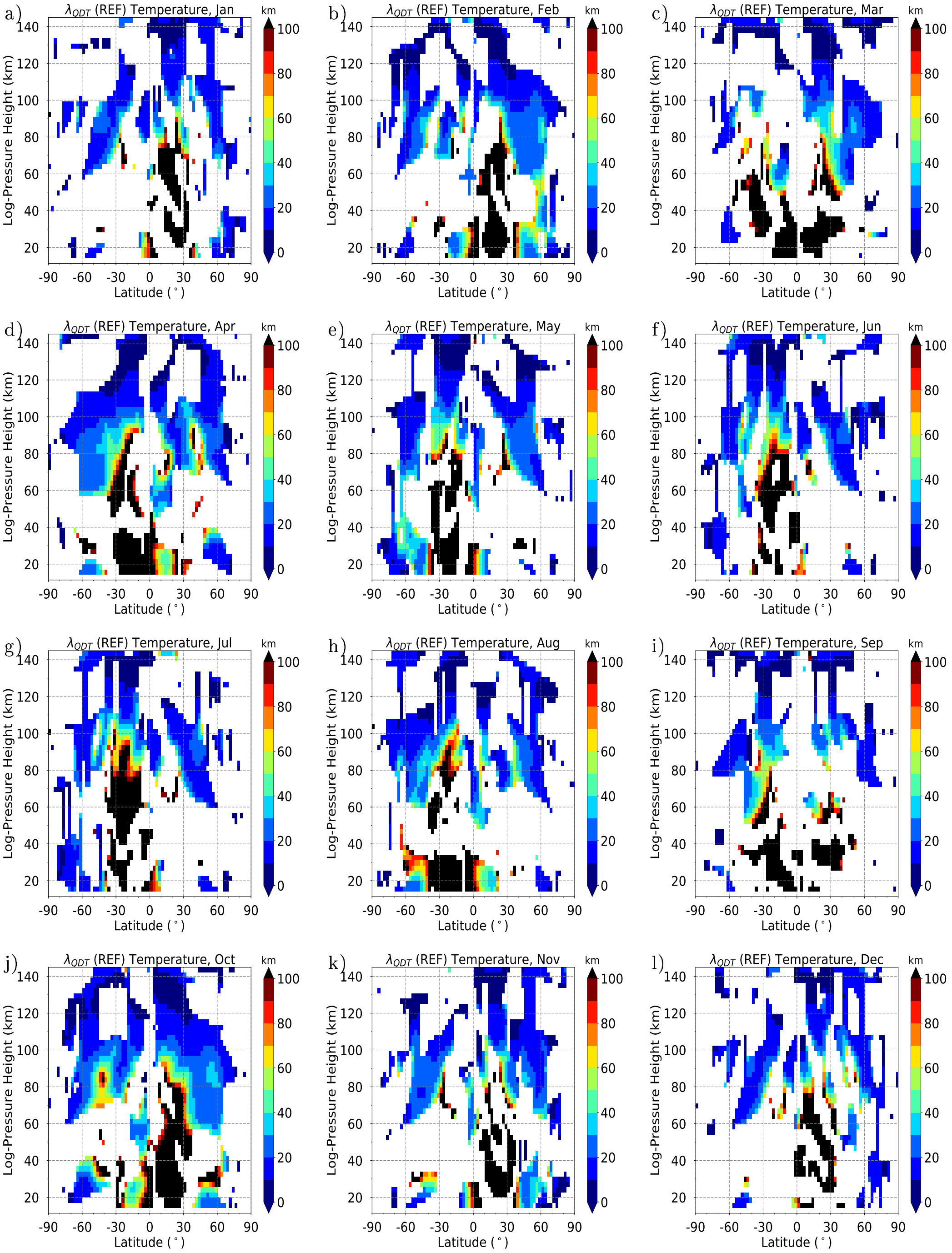

Figure S11.: QDT temperature vertical wavelengths, which are a result of a linear fit of vertical phase gradients over a range of 30 km and plottet for areas with correlation coefficient of $R \leq 0.6$.

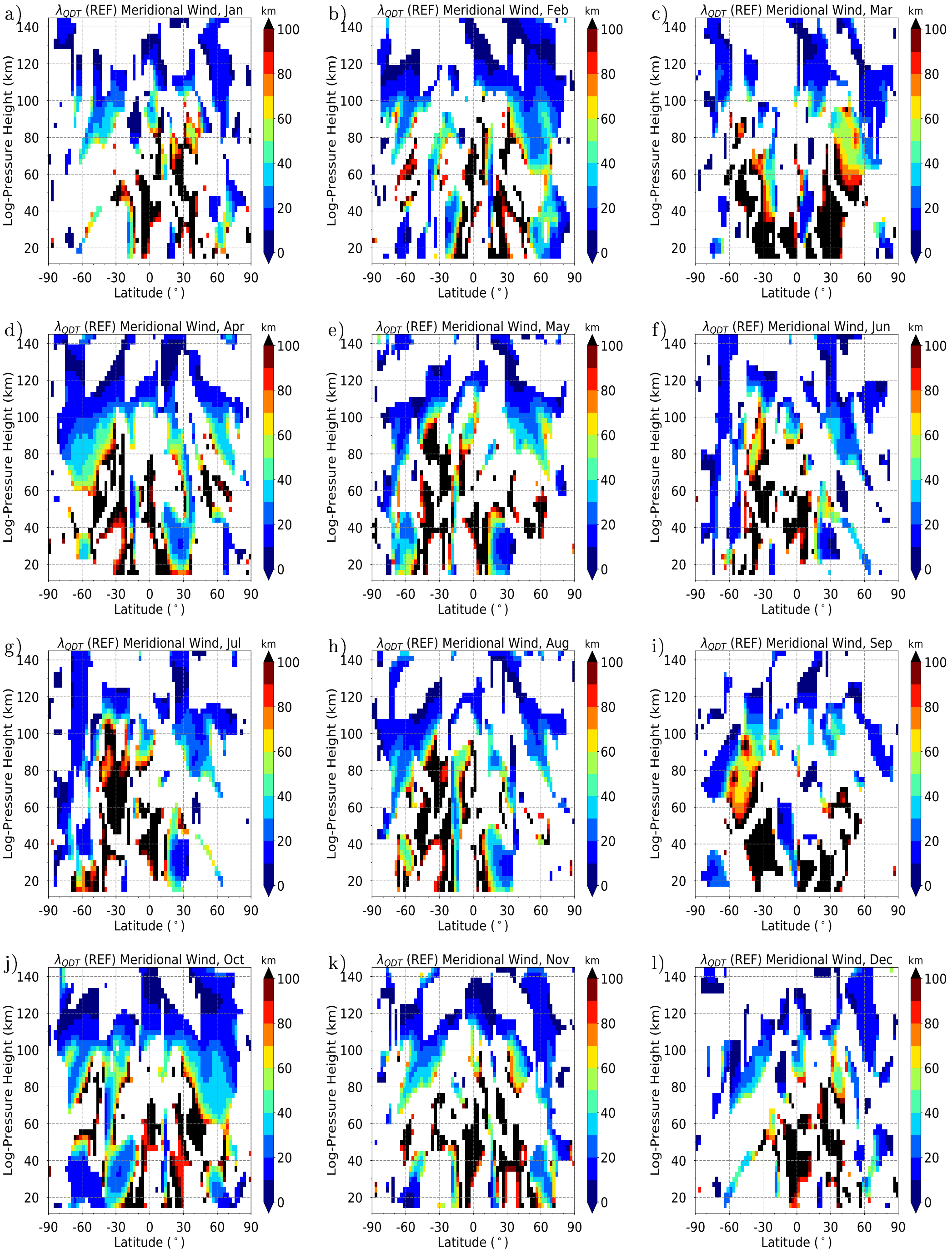

Figure S12.: QDT vertical wavelengths, which are a result of a linear fit of vertical phase gradients over a range of 30 km ($R^2 = 0.6$).

A.5. DT, SDT and TDT Wind Amplitudes and Phases for January

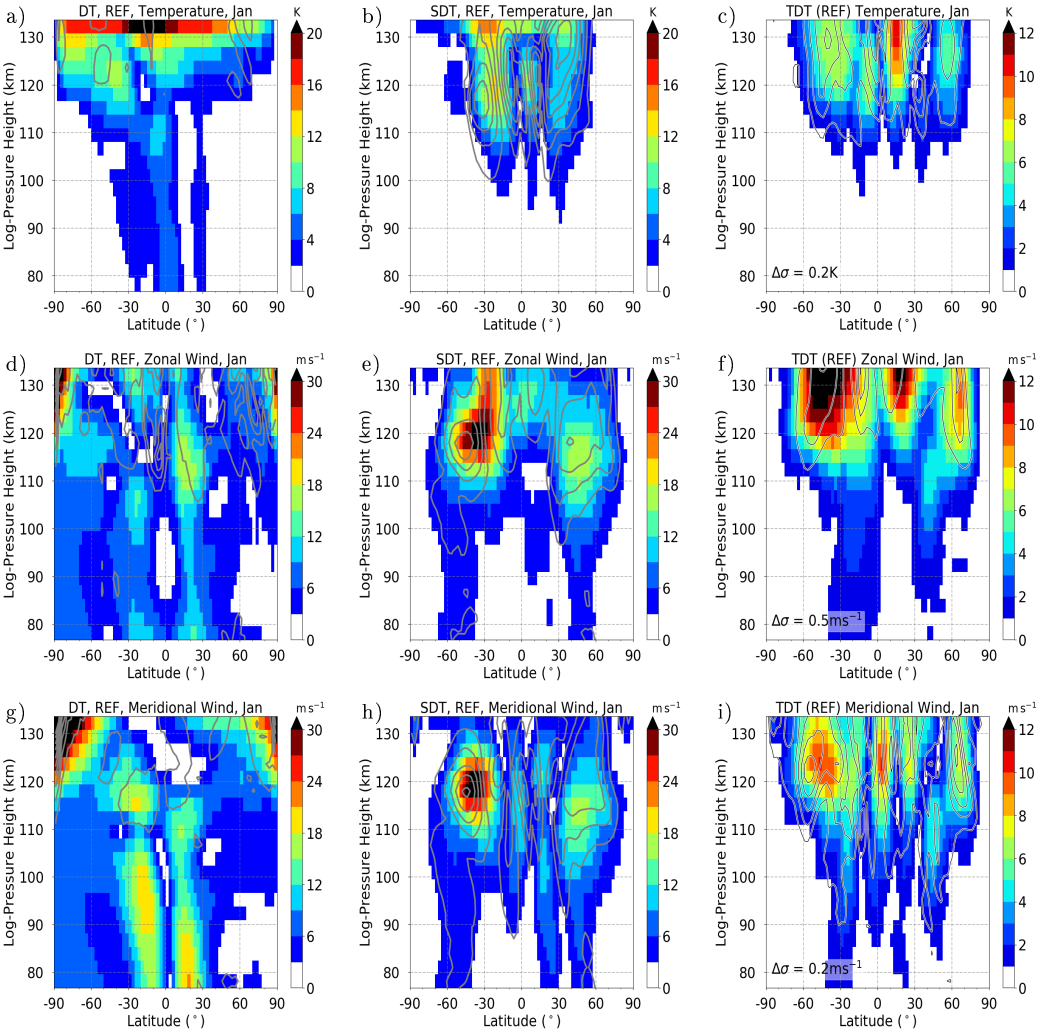

Figure S13.: DT (left), SDT (mid) and TDT (right) temperature (top), zonal wind (mid) and meridional wind (bottom) amplitudes for January as color, black lines are standard deviation from ensemble runs.

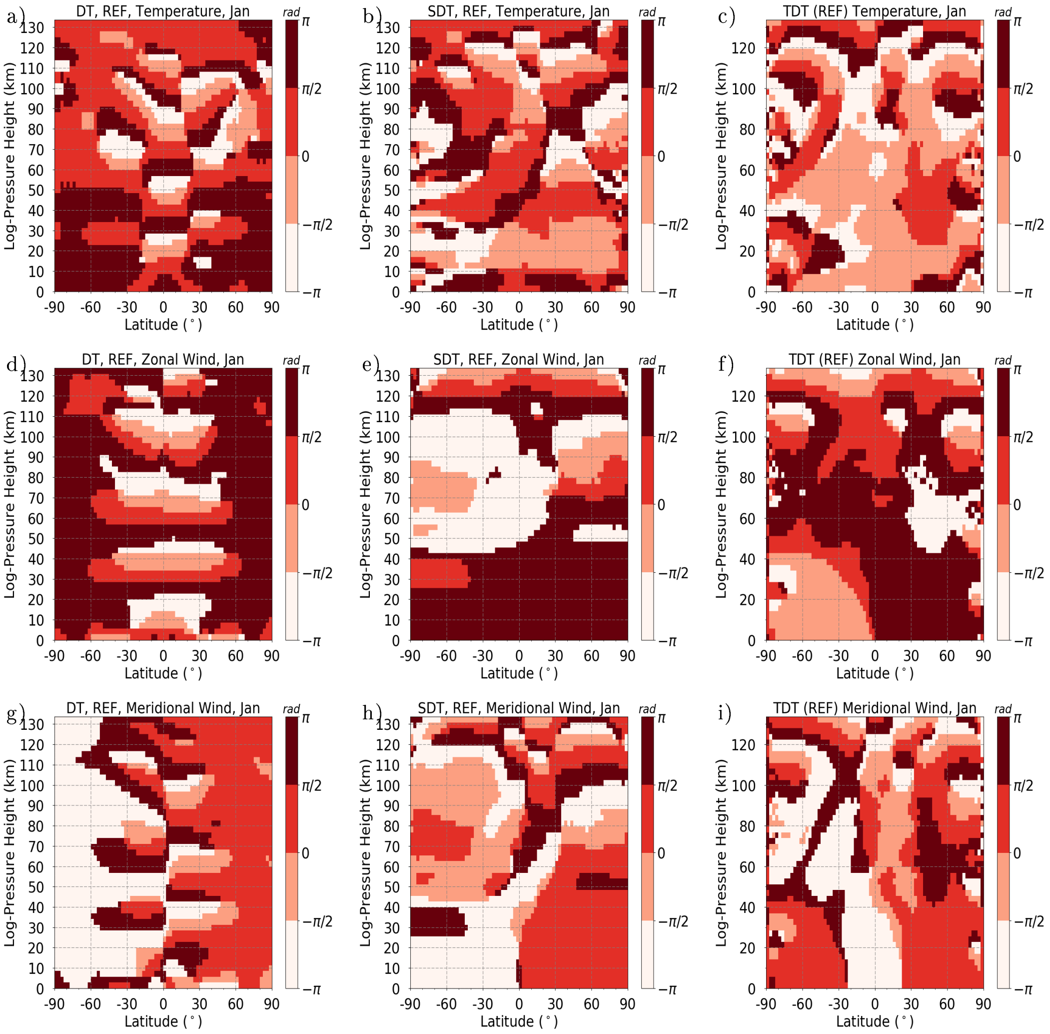

Figure S14.: DT (left), SDT (mid) and TDT (right) temperature (top), zonal wind (mid) and meridional wind (bottom) phases for January as color

A.6. QDT reconstruction with Hough modes

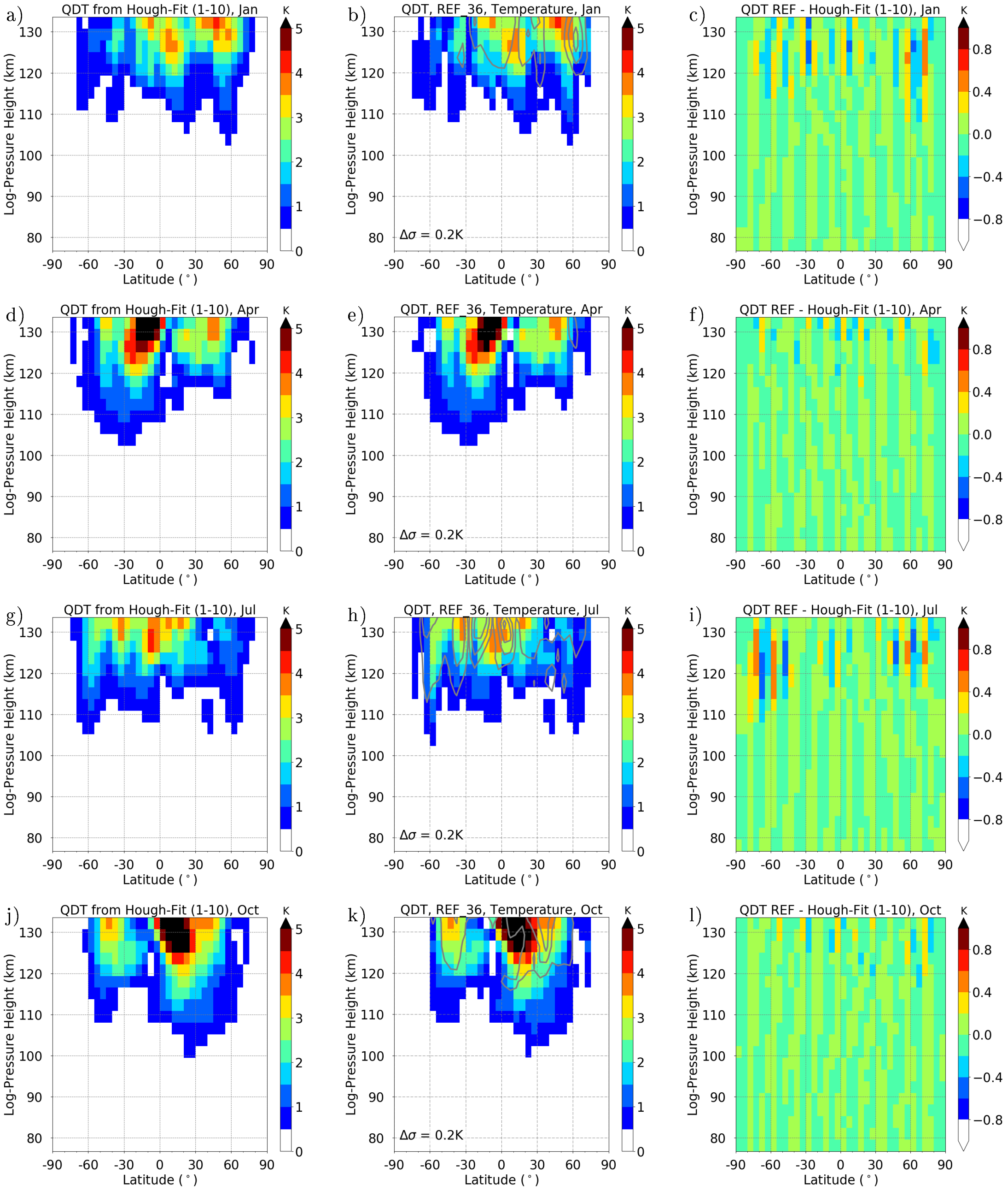

Figure S15.: Calculated QDT temperature amplitudes from Hough modes 1 to 10 with the least squares fit method after Eq. 6.2 (left), REF simulation (mid) and differences between calculations and REF simulations (right) for a resolution of 36 latitudes. For January (top), April, July and October (bottom).

A.7. QDT Forcing Terms

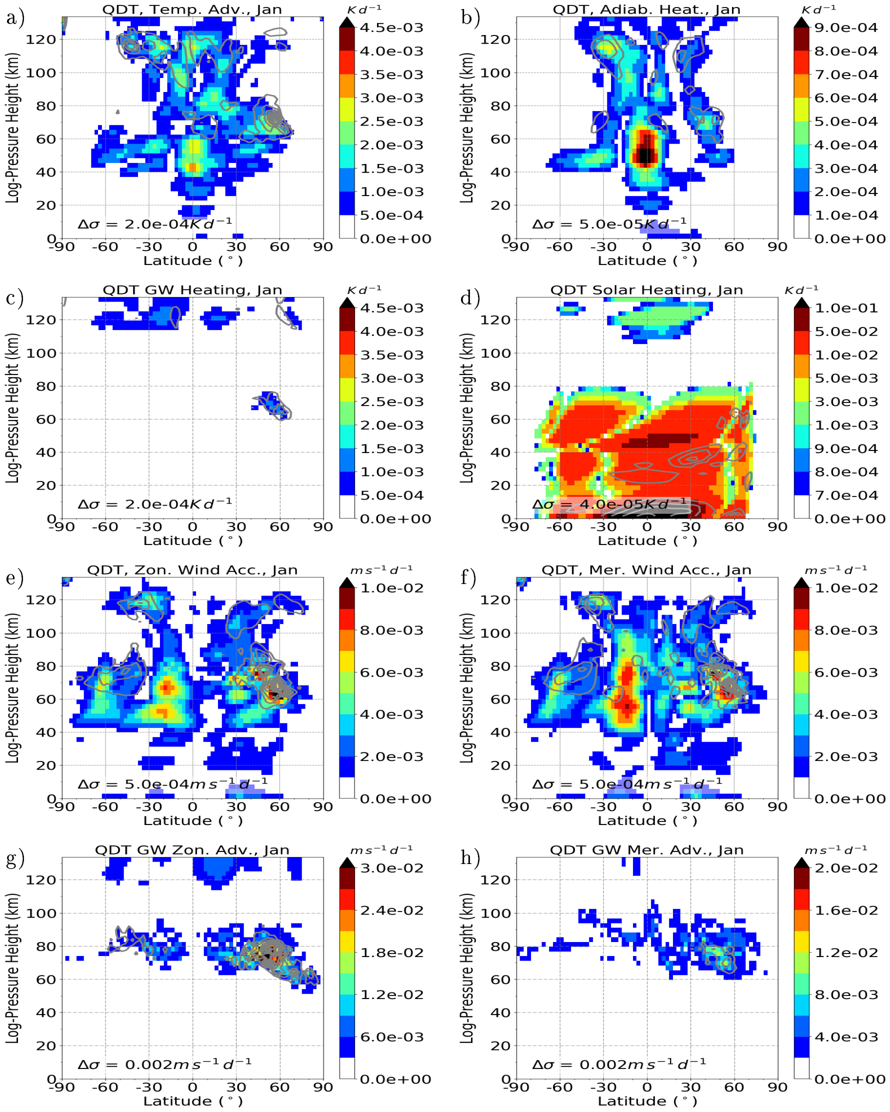

Figure S16.: Quarterdiurnal component of thermal tendency terms in the REF simulation. Amplitudes are scaled by $\exp{-z(2H)^{-1}}$. Results are an average of the 11 ensemble members. Standard deviations (σ) are added as grey lines. Temperature advection (nonlinear component), adiabatic heating (nonlinear component), heating due to gravity wave activity (tendency term from gravity wave parameterization), solar heating (tendency term from solar radiation parameterization), zonal wind advection (nonlinear component), meridional wind advection (nonlinear component), zonal and meridional acceleration due to gravity waves (tendency terms from gravity wave parameterization). Note the different color scales.

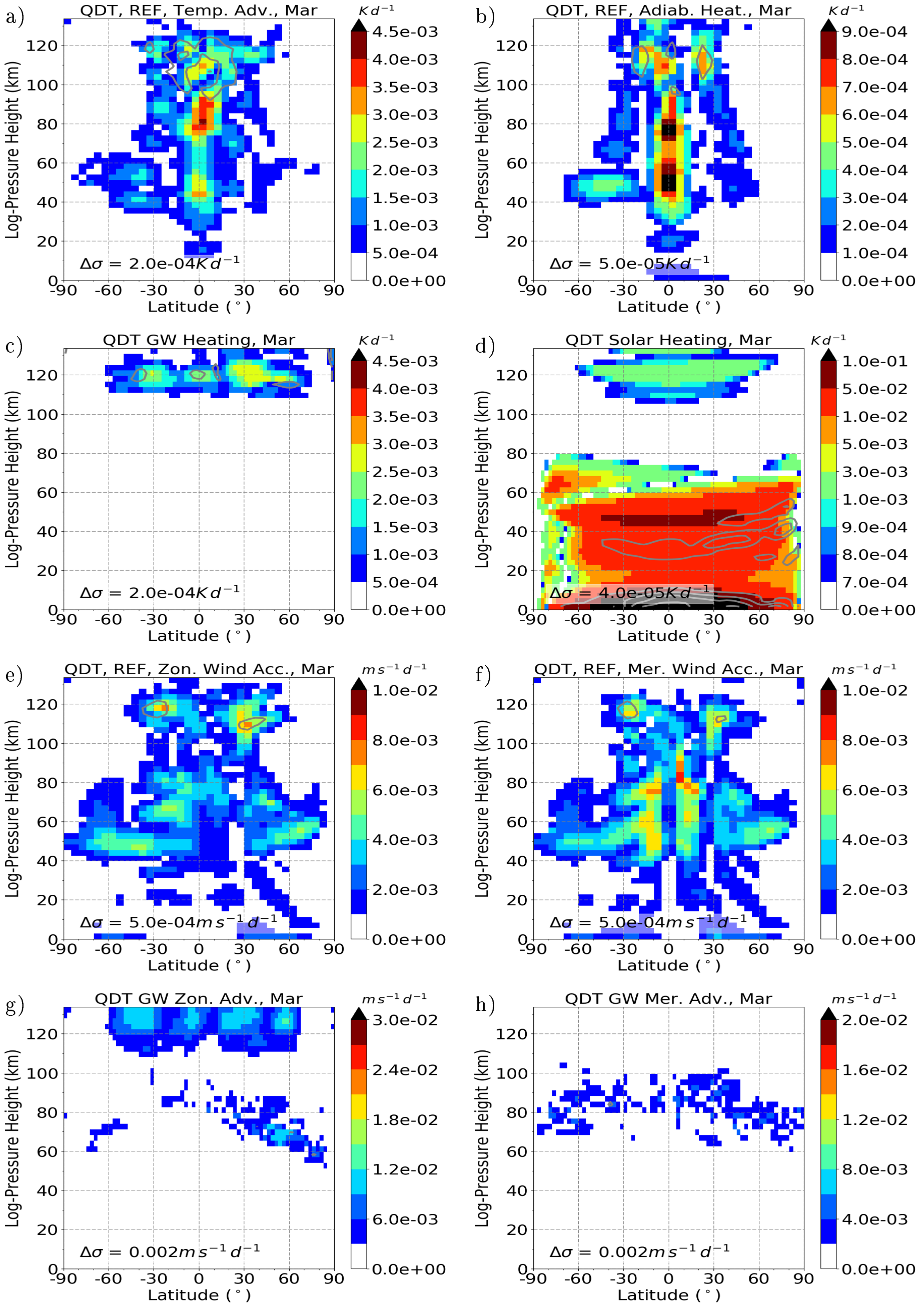

Figure S17.: Same as Fig. S16 but for March.

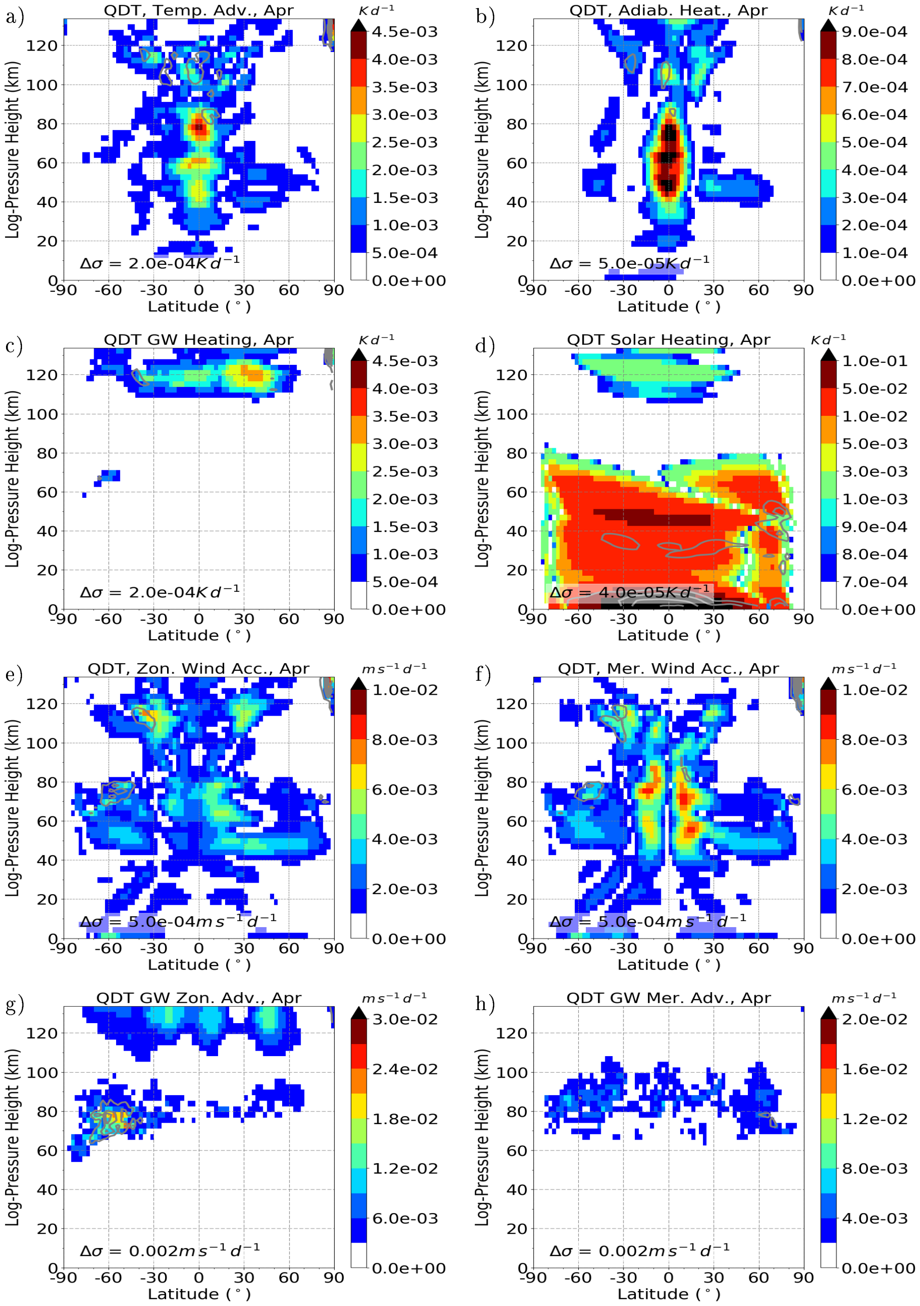

Figure S18.: Same as Fig. S16 but for October.

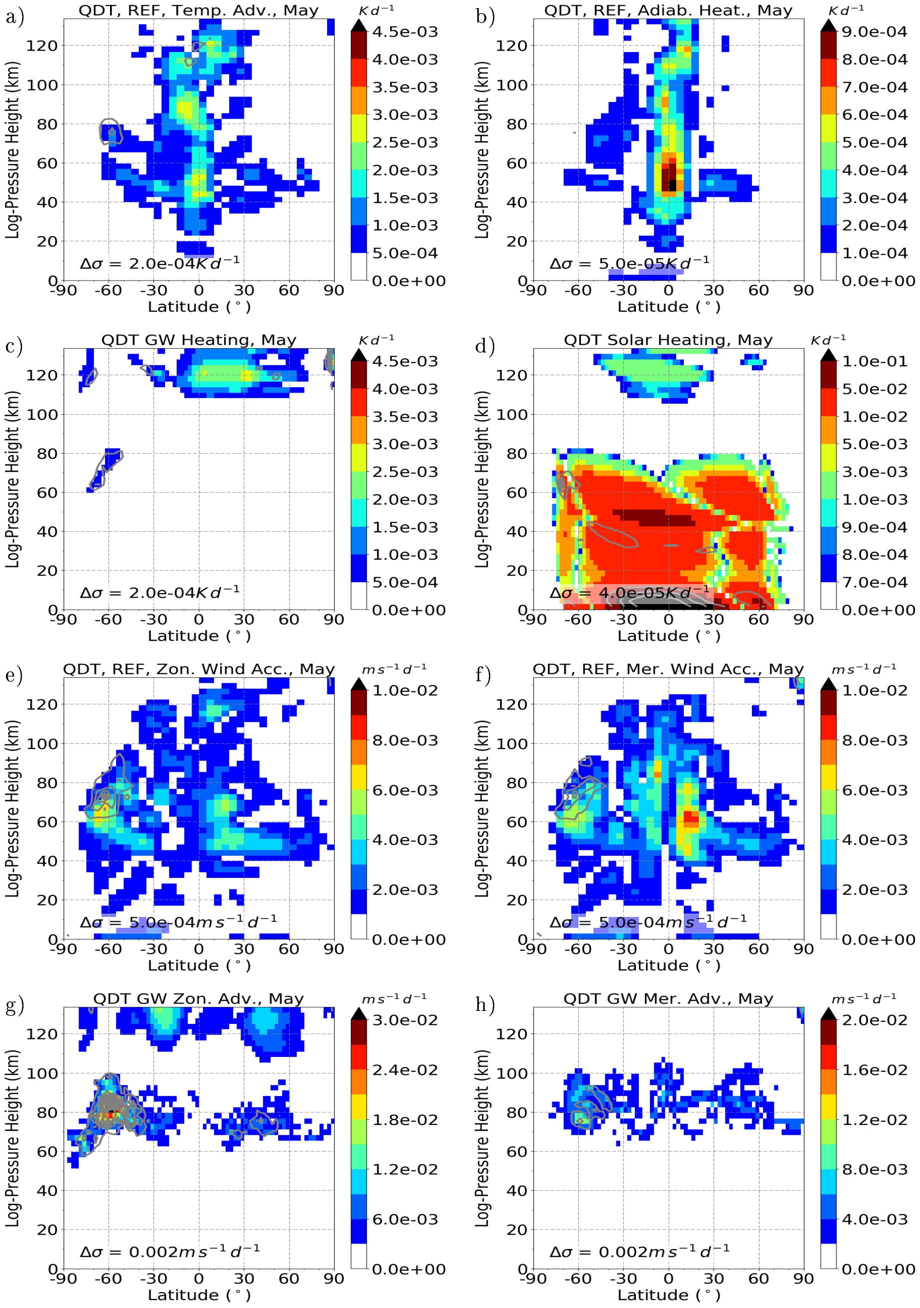

Figure S19.: Same as Fig. S16 but for May.

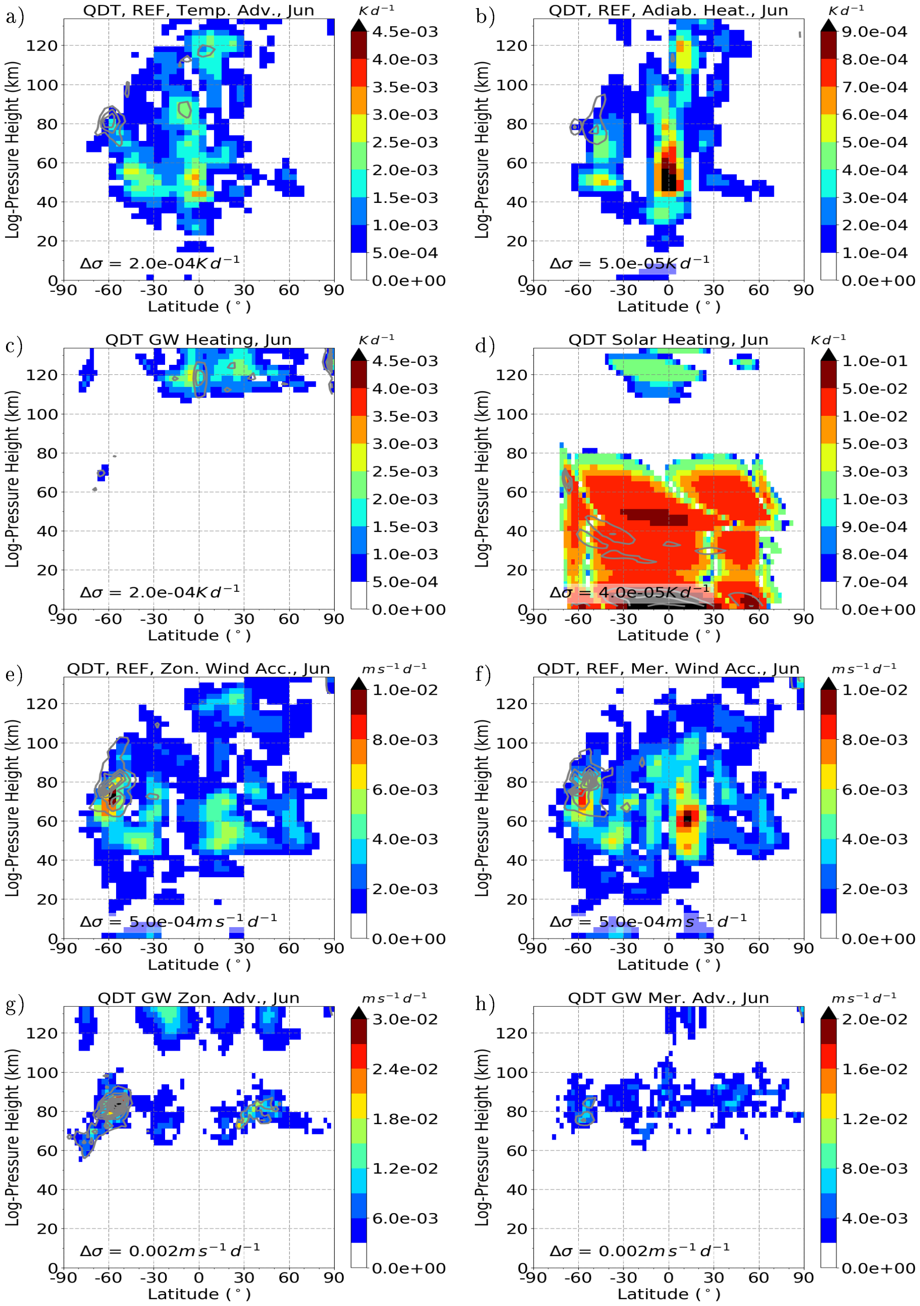

Figure S20.: Same as Fig. S16 but for June.

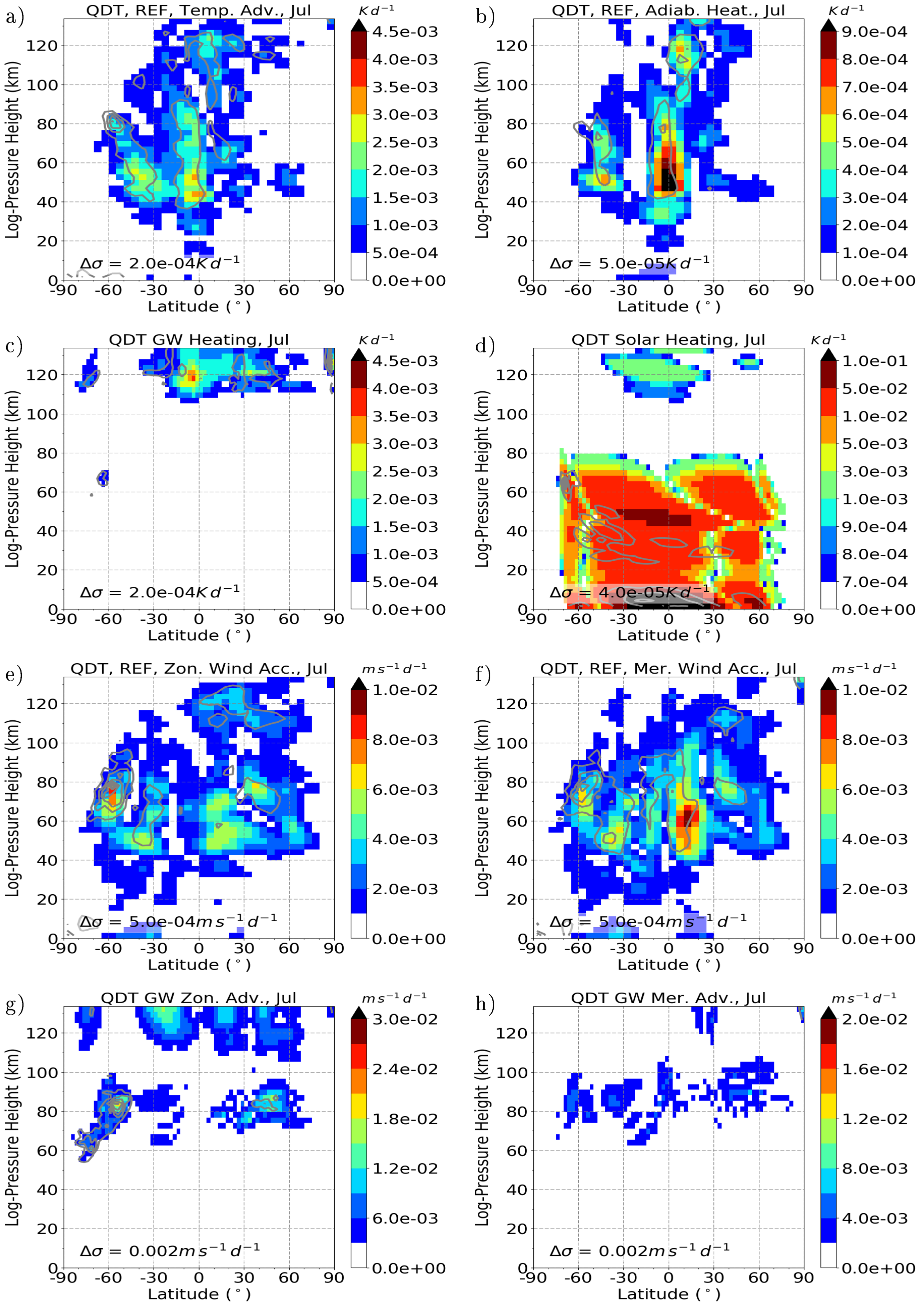

Figure S21.: Same as Fig. S16 but for July.

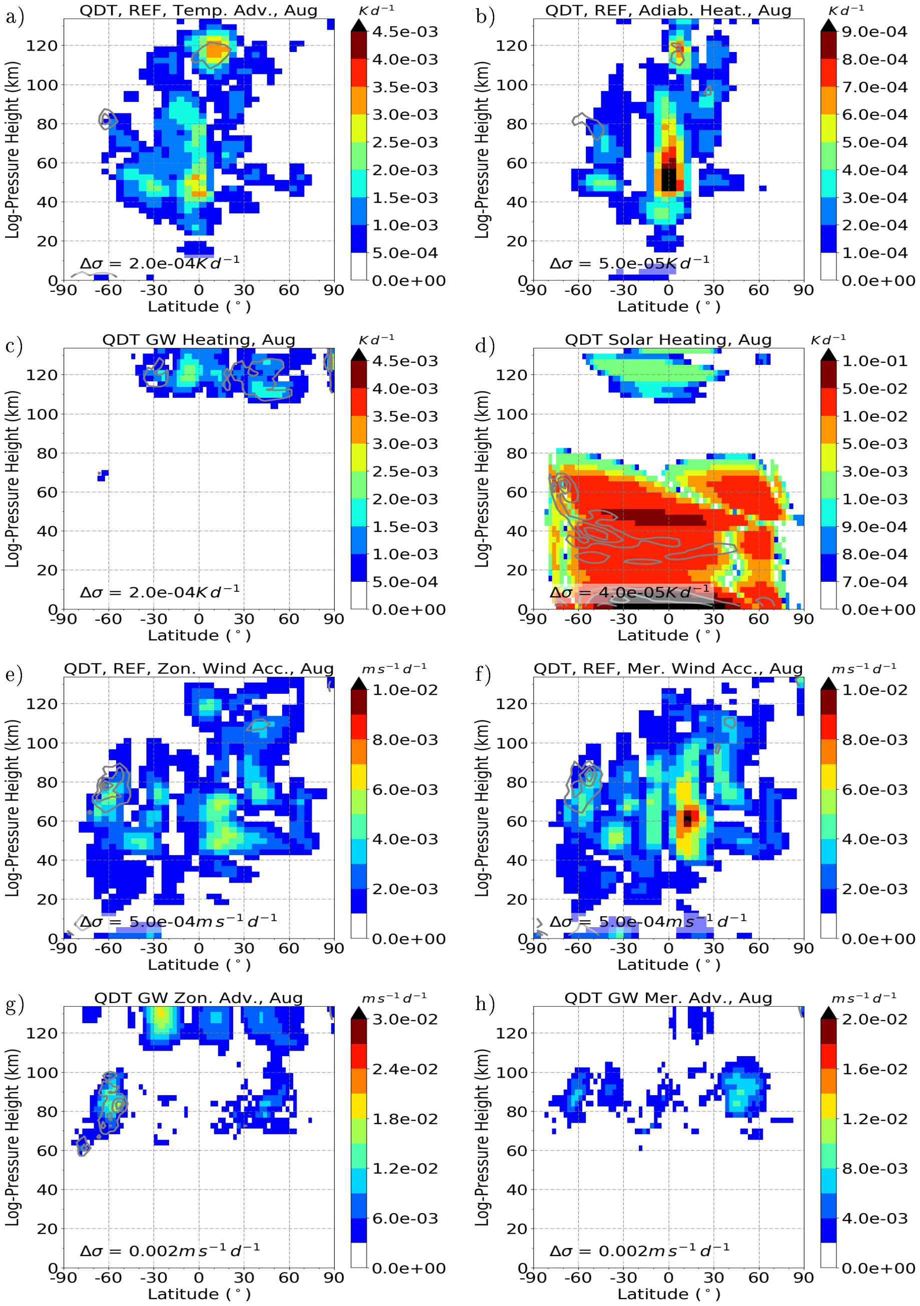

Figure S22.: Same as Fig. S16 but for August.

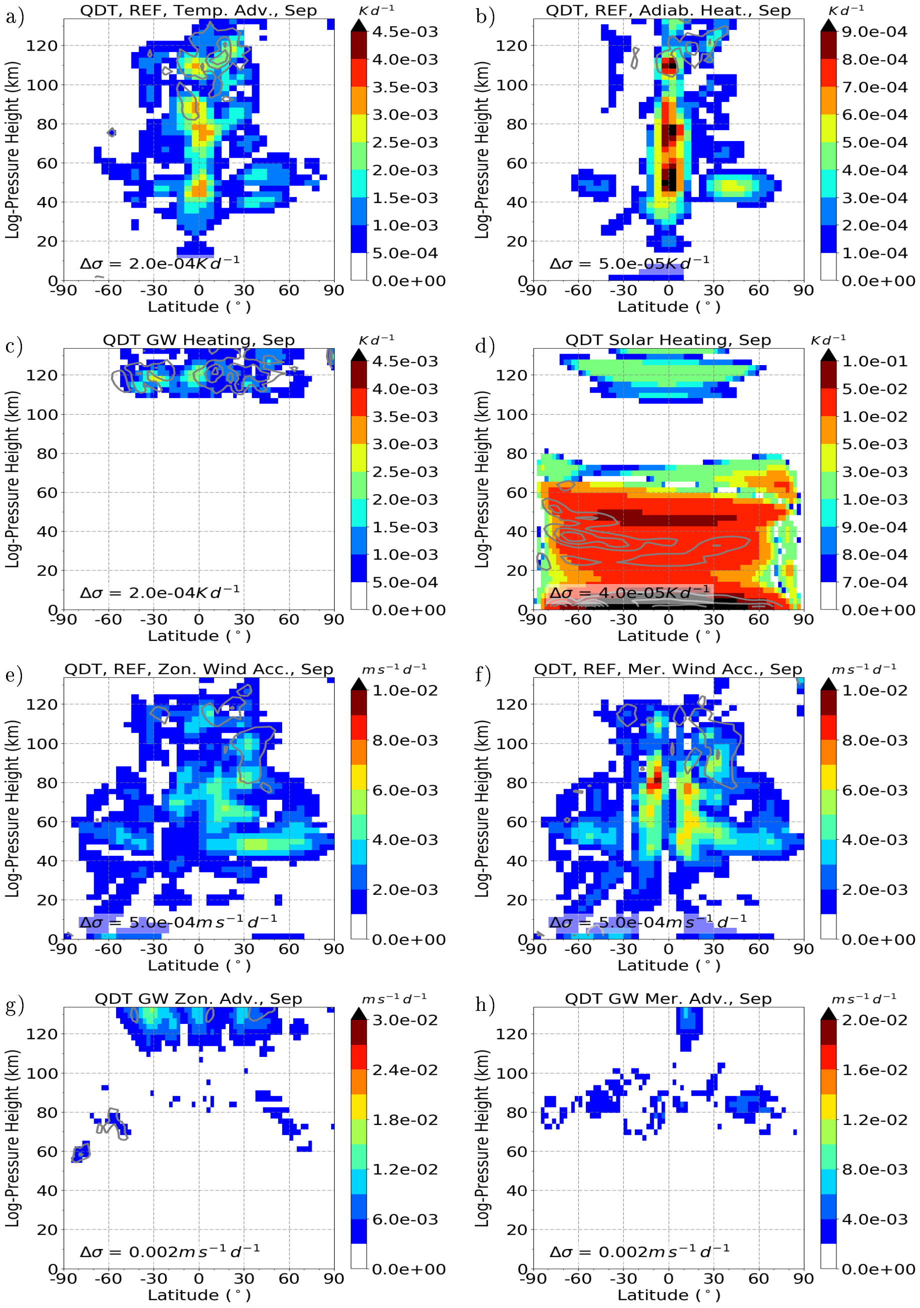

Figure S23.: Same as Fig. S16 but for September.

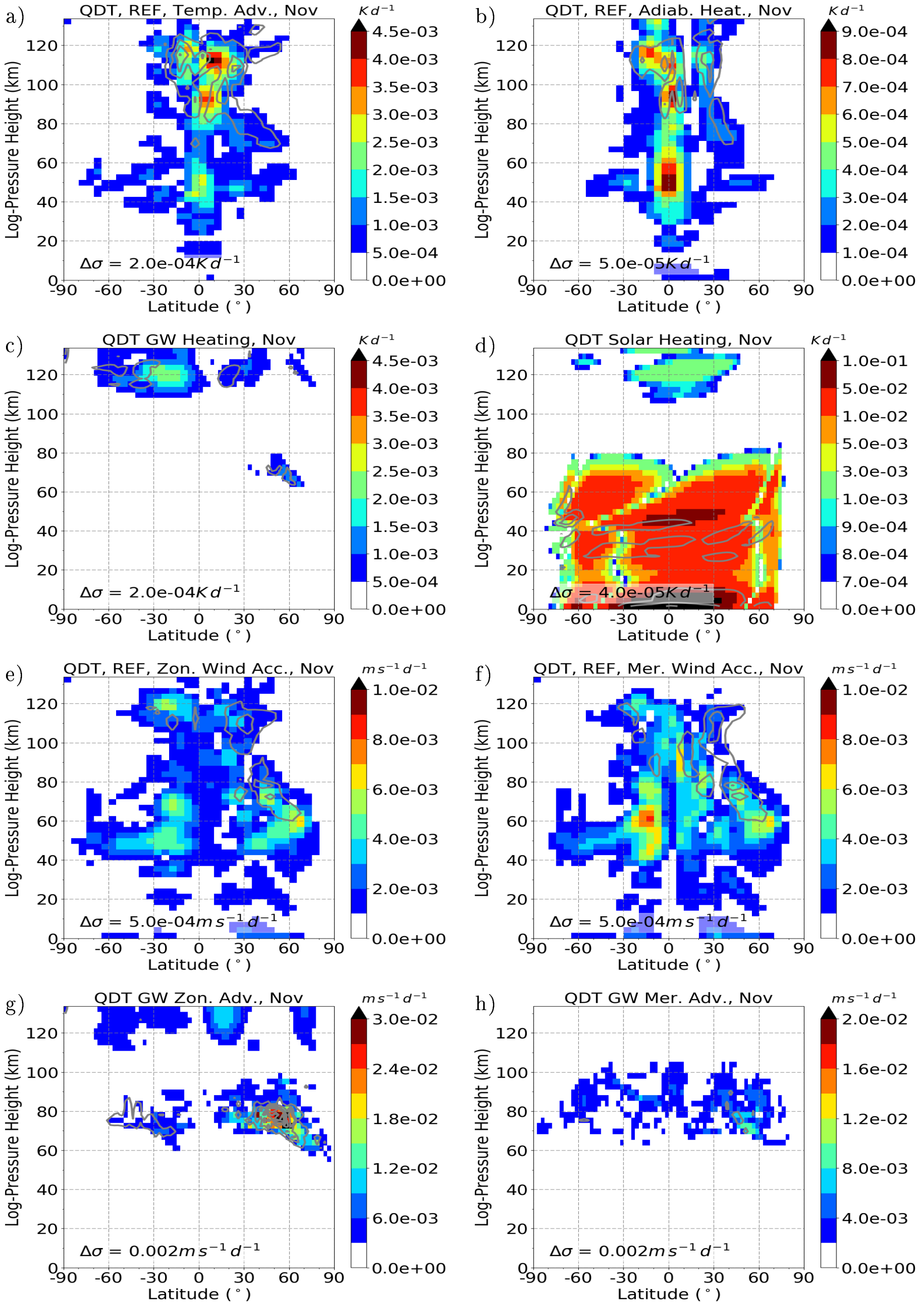

Figure S24.: Same as Fig. S16 but for November.

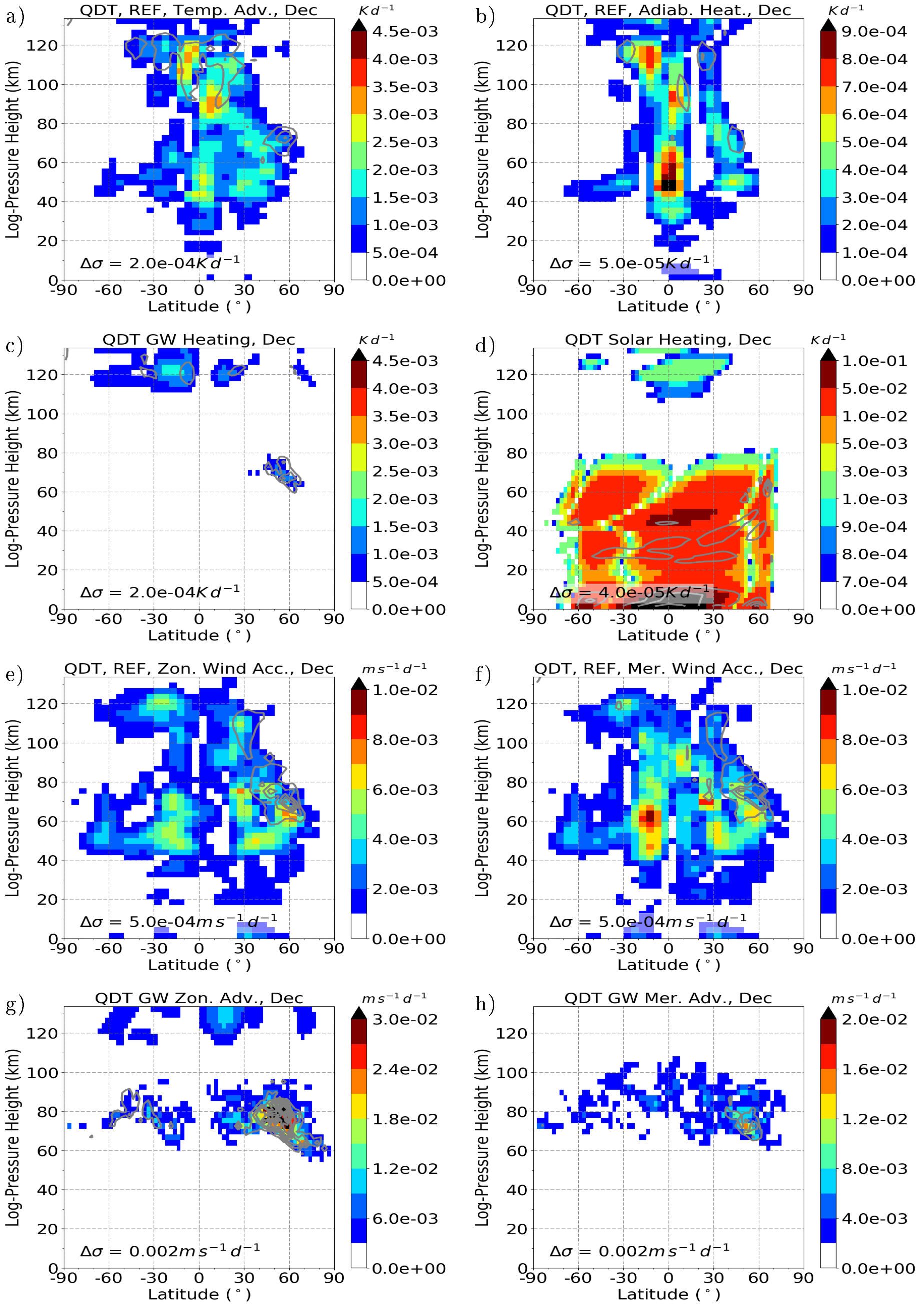

Figure S25.: Same as Fig. S16 but for December.

A.7.1. Terms of Tendency Equation with different meridional resolution

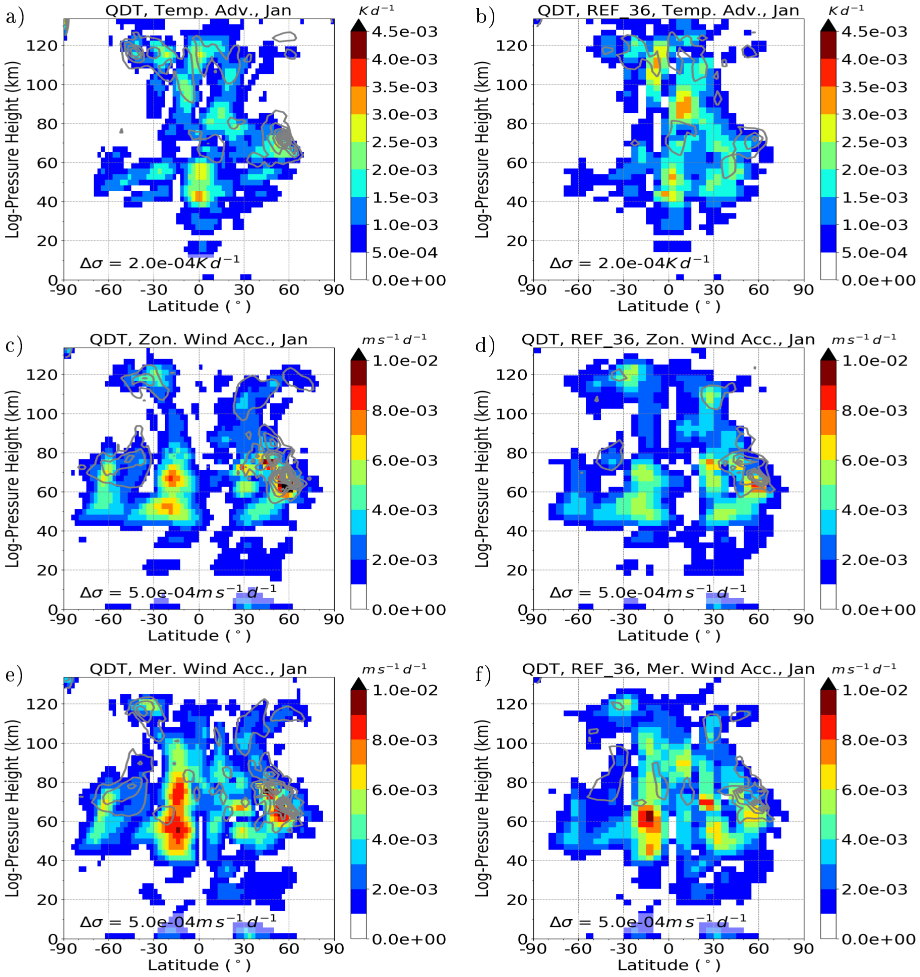

Figure S26.: Quarterdiurnal component of tendency terms in the REF simulation for January. Left REF simulation with 72 latitudinal resolution, right with 36 latitudinal resolution. Amplitudes are scaled by $\exp{-z(2H)^{-1}}$. Results are an average of the 11 ensemble members (shaded color). Standard deviations (σ) are added as grey contour lines. Temperature advection (nonlinear component), zonal wind advection (nonlinear component), meridional wind advection (nonlinear component). Note that the color scales are different.

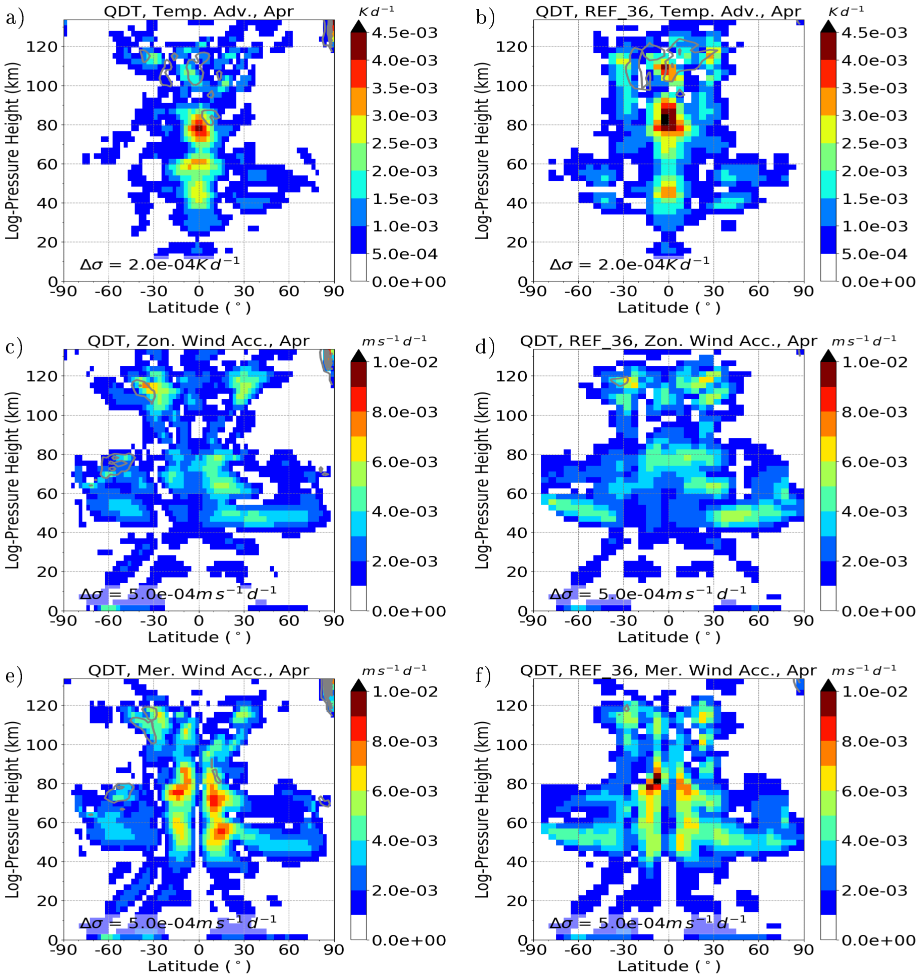

Figure S27.: Quarterdiurnal component of tendency terms in the REF simulation for April. Left REF simulation with 72 latitudinal resolution, right with 36 latitudinal resolution. Amplitudes are scaled by $\exp{-z(2H)^{-1}}$. Results are an average of the 11 ensemble members (shaded color). Standard deviations (σ) are added as grey contour lines. Temperature advection (nonlinear component), zonal wind advection (nonlinear component), meridional wind advection (nonlinear component). Note that the color scales are different.

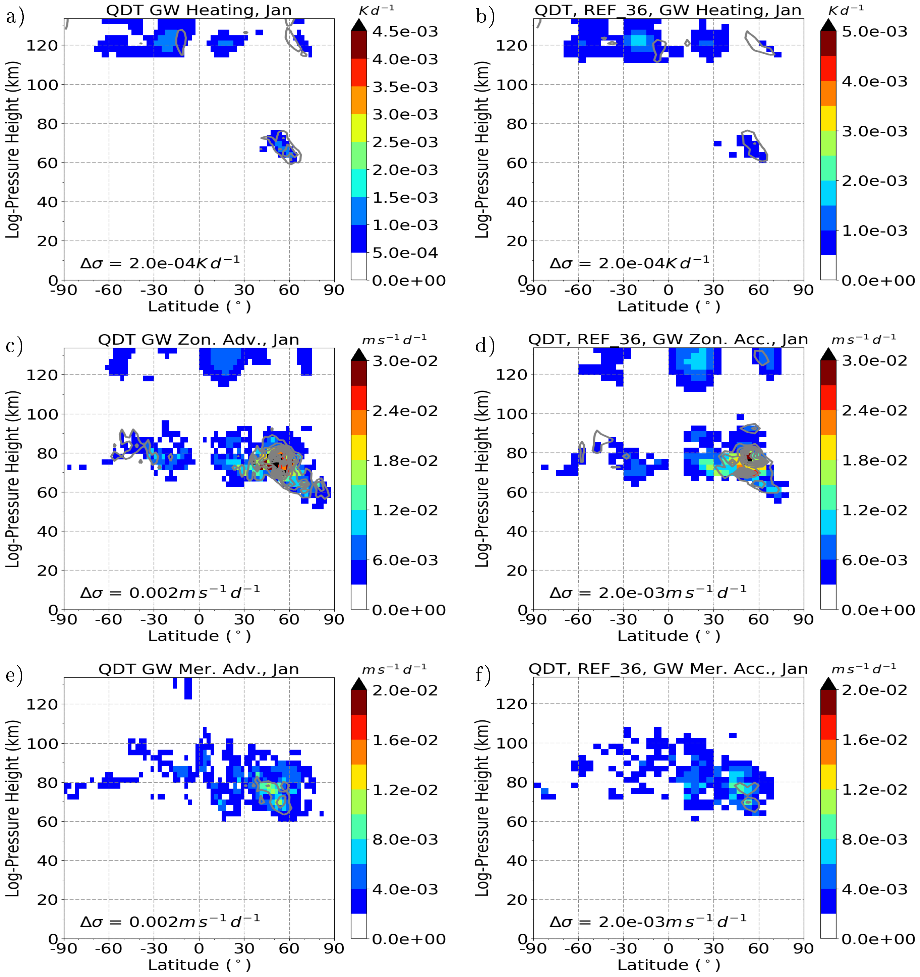

Figure S28.: Quarterdiurnal component of tendency terms in the REF simulation for January. Left REF simulation with 72 latitudinal resolution, right with 36 latitudinal resolution. Amplitudes are scaled by $\exp{-z(2H)^{-1}}$. Results are an average of the 11 ensemble members (shaded color). Standard deviations (σ) are added as grey contour lines. Heating due to gravity wave activity (tendency term from gravity wave parameterization), zonal and meridional acceleration due to gravity waves (tendency terms from gravity wave parameterization). Note that the color scales are different.

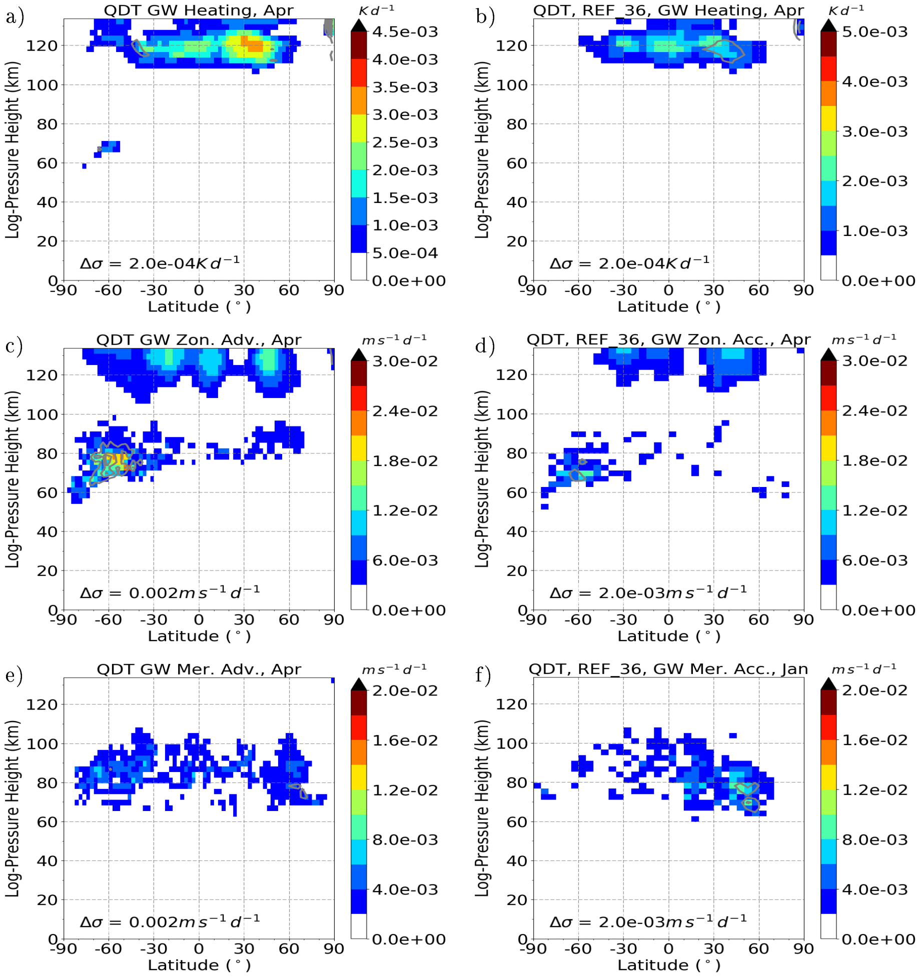

Figure S29.: Quarterdiurnal component of tendency terms in the REF simulation for April. Left REF simulation with 72 latitudinal resolution, right with 36 latitudinal resolution. Amplitudes are scaled by $\exp{-z(2H)^{-1}}$. Results are an average of the 11 ensemble members (shaded color). Standard deviations (σ) are added as grey contour lines. Heating due to gravity wave activity (tendency term from gravity wave parameterization), zonal and meridional acceleration due to gravity waves (tendency terms from gravity wave parameterization). Note that the color scales are different.

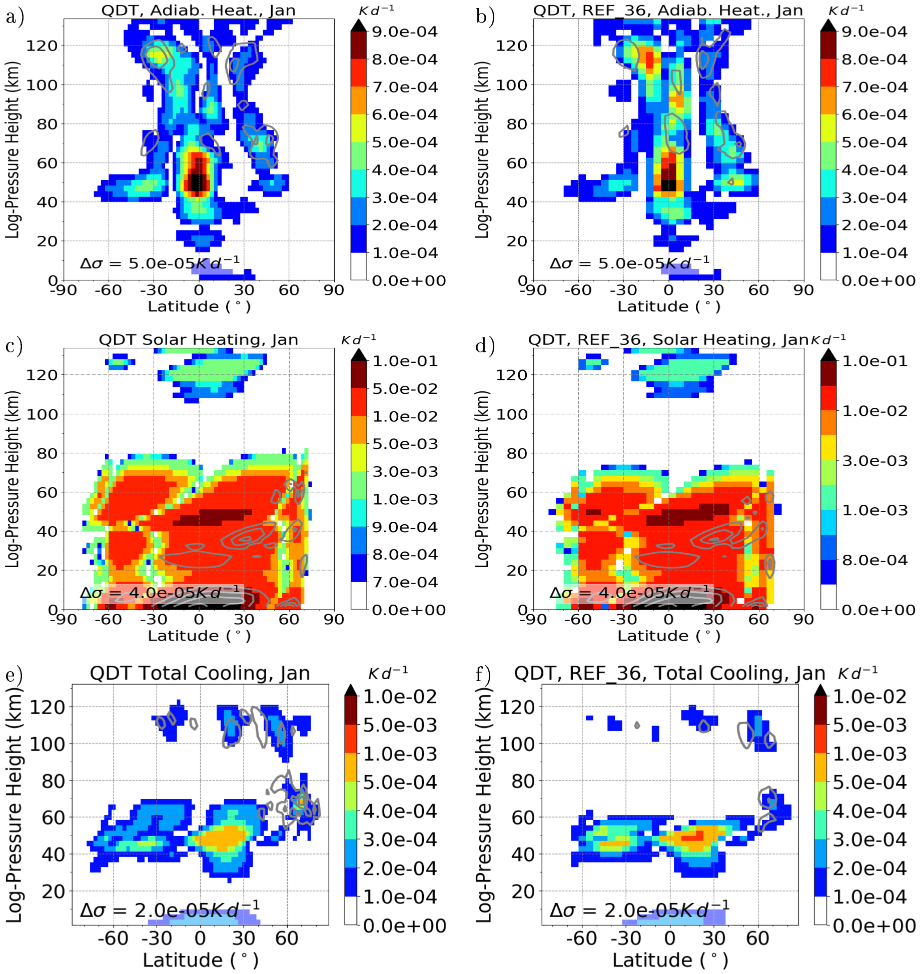

Figure S30.: Quarterdiurnal component of thermal tendency terms in the REF simulation for January. Left REF simulation with 72 latitudinal resolution, right with 36 latitudinal resolution. Amplitudes are scaled by exp$-z(2H)^{-1}$. Results are an average of the 11 ensemble members (shaded color). Standard deviations (σ) are added as grey contour lines. Adiabatic heating (nonlinear component), solar heating (tendency term from solar radiation parameterization), radiative cooling (tendency term from radiative cooling parameterization).

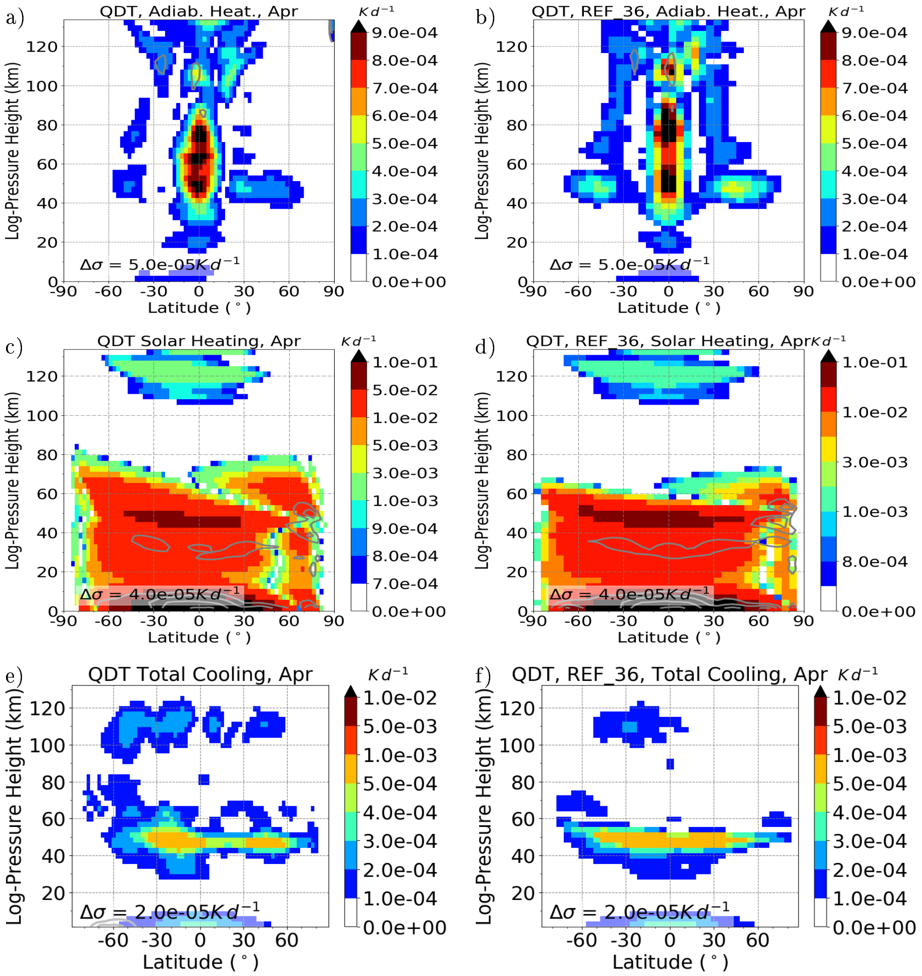

Figure S31.: Quarterdiurnal component of thermal tendency terms in the REF simulation for April. Left REF simulation with 72 latitudinal resolution, right with 36 latitudinal resolution. Amplitudes are scaled by $\exp{-z(2H)^{-1}}$. Results are an average of the 11 ensemble members (shaded color). Standard deviations (σ) are added as grey contour lines. Adiabatic heating (nonlinear component), solar heating (tendency term from solar radiation parameterization), radiative cooling (tendency term from radiative cooling parameterization).

A.8. The solar Forcing

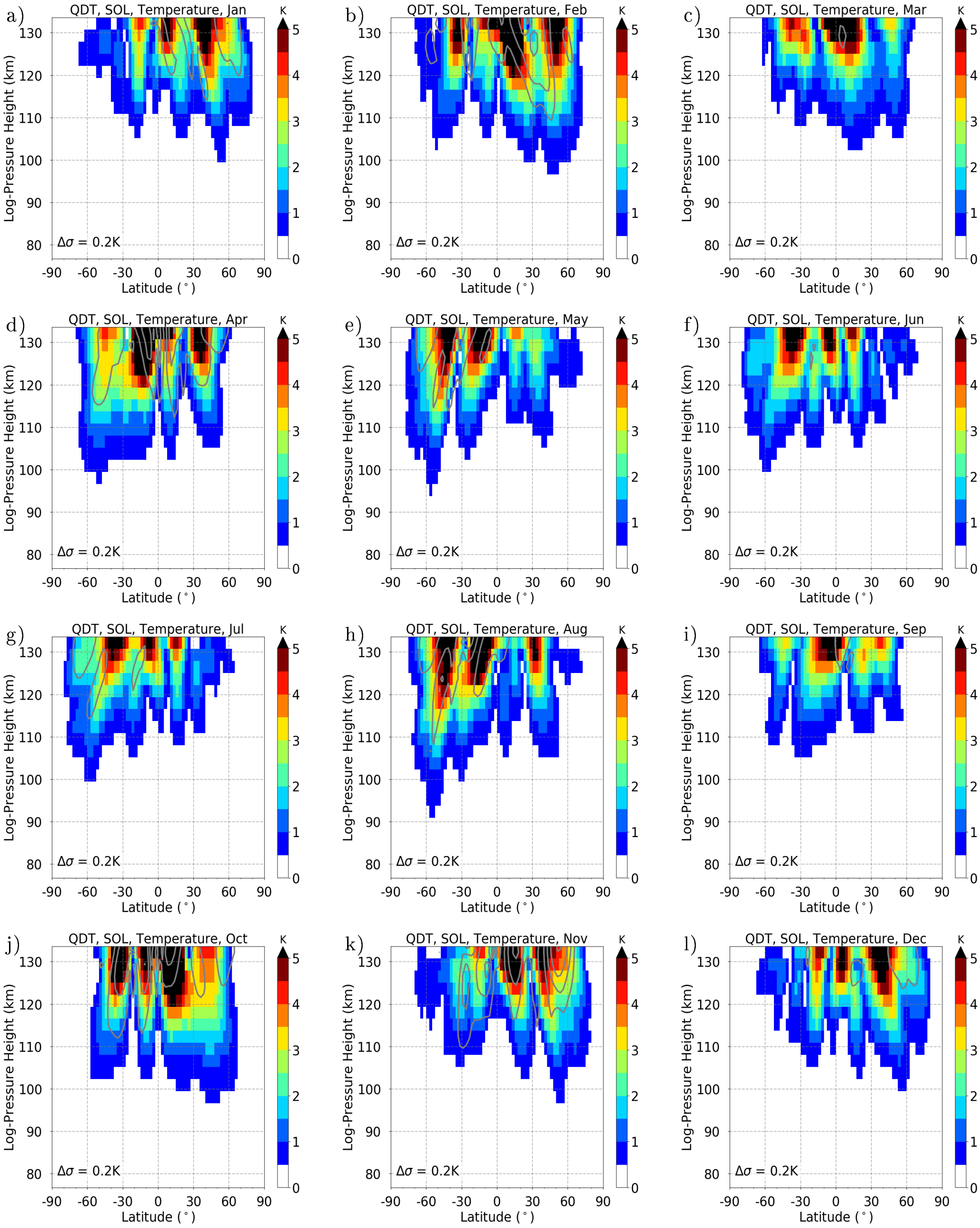

Figure S32.: SOL run QDT temperature amplitudes as color, black lines are standard deviation from ensemble runs.

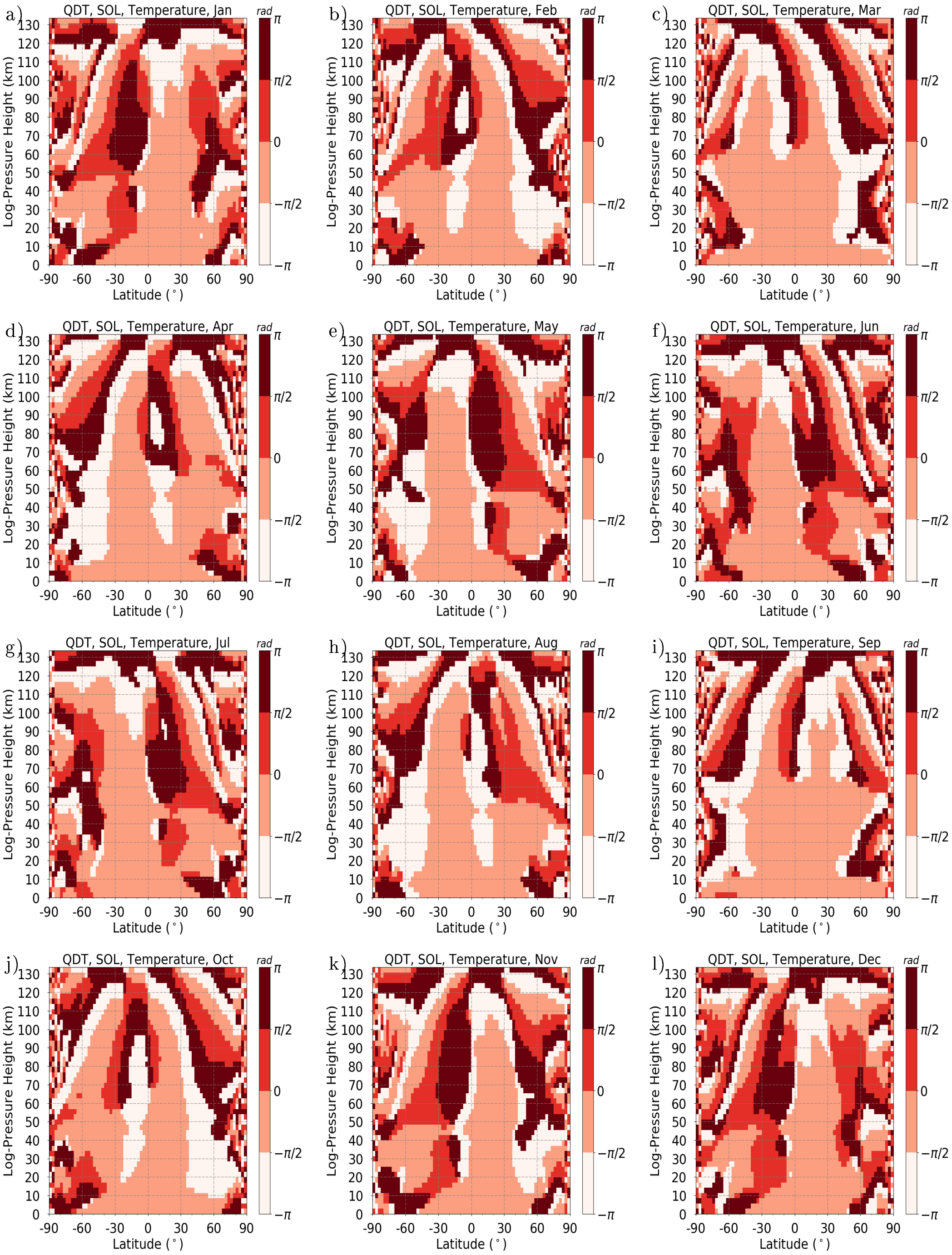

Figure S33.: SOL run QDT temperature phases as color.

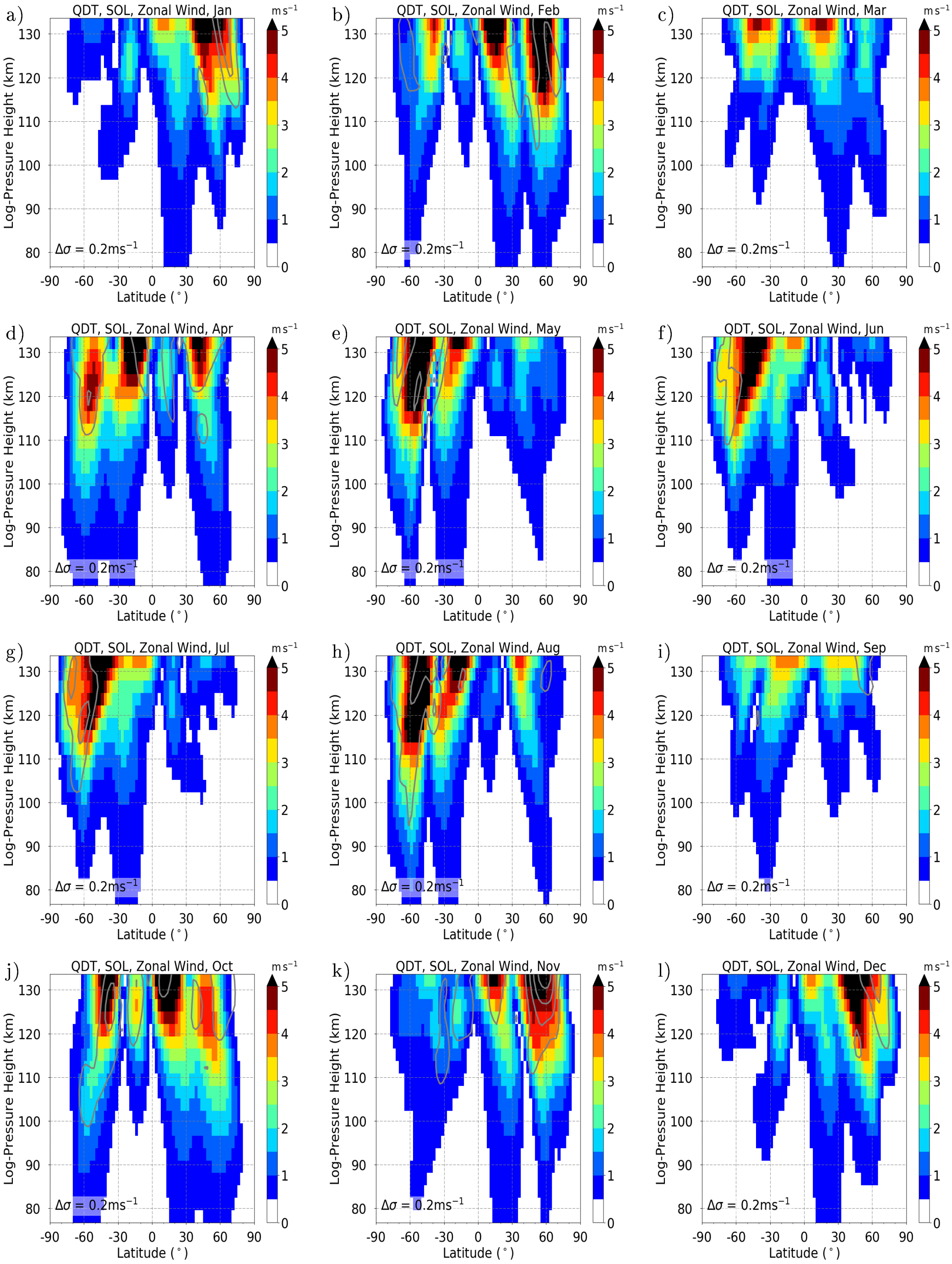

Figure S34.: SOL run QDT zonal wind amplitudes as color, black lines are standard deviation from ensemble runs.

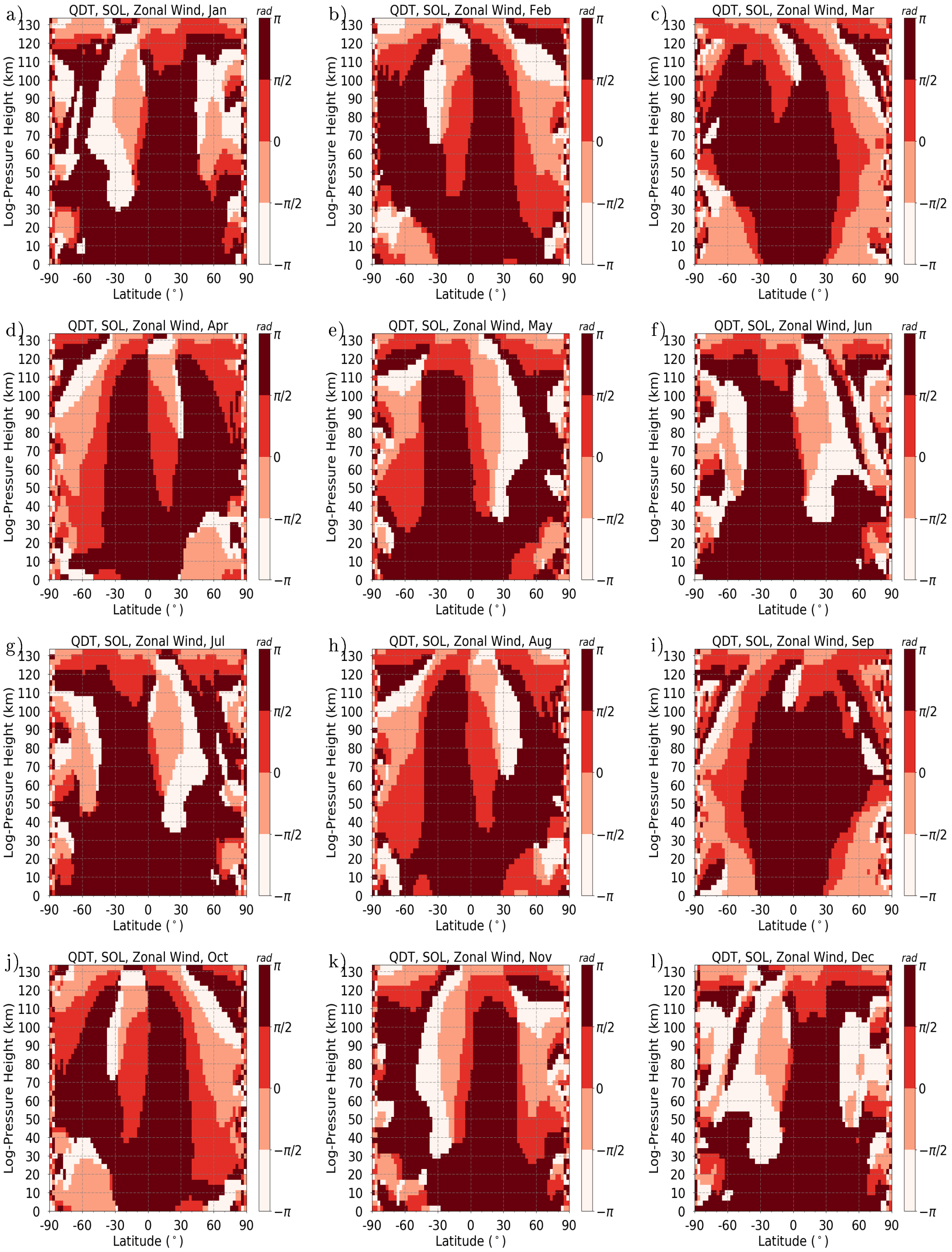

Figure S35.: SOL run QDT zonal wind phases as color.

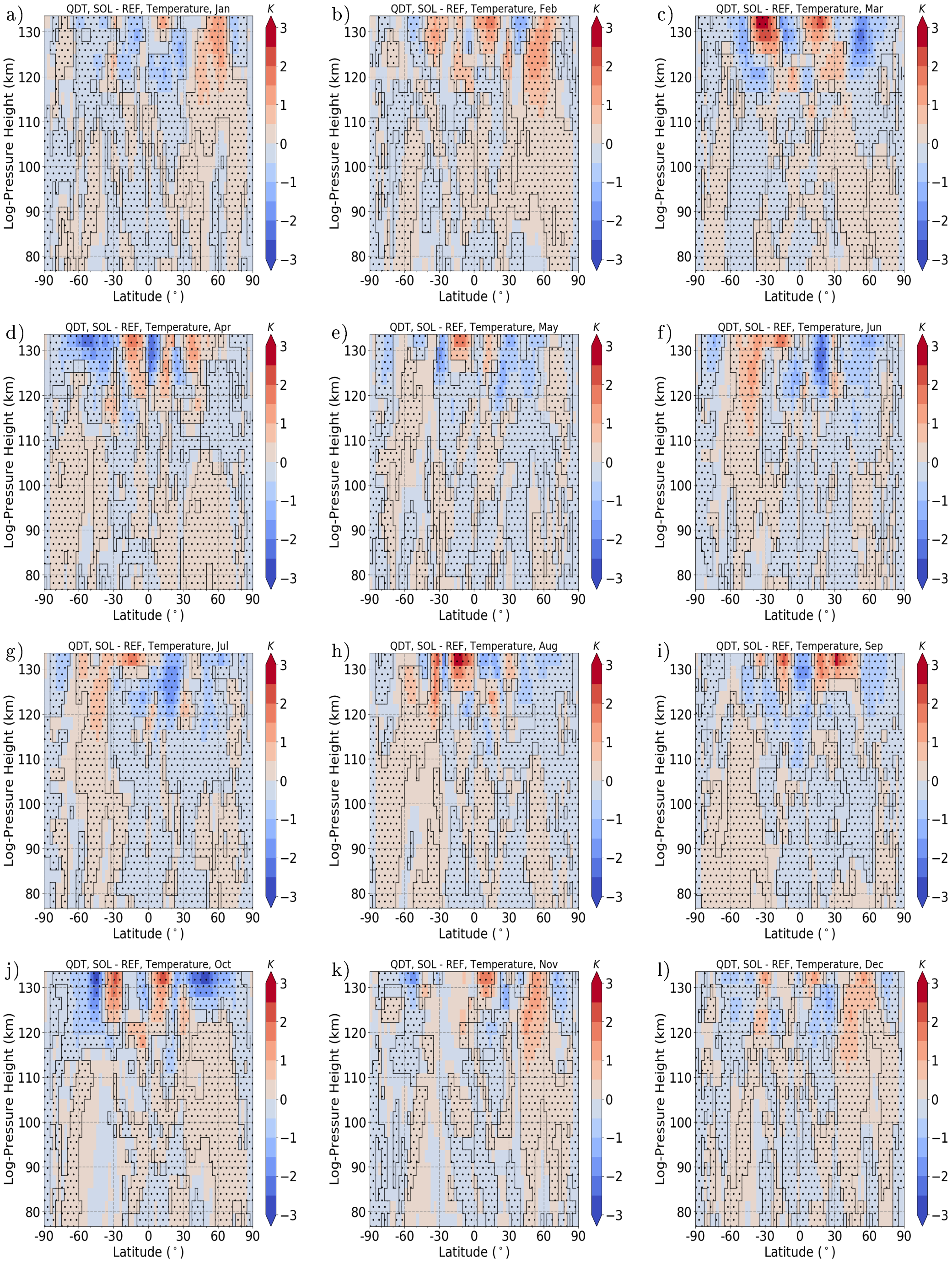

Figure S36.: QDT temperature amplitude differences between SOL and REF run as color. Significance larger than 99% as dotted area.

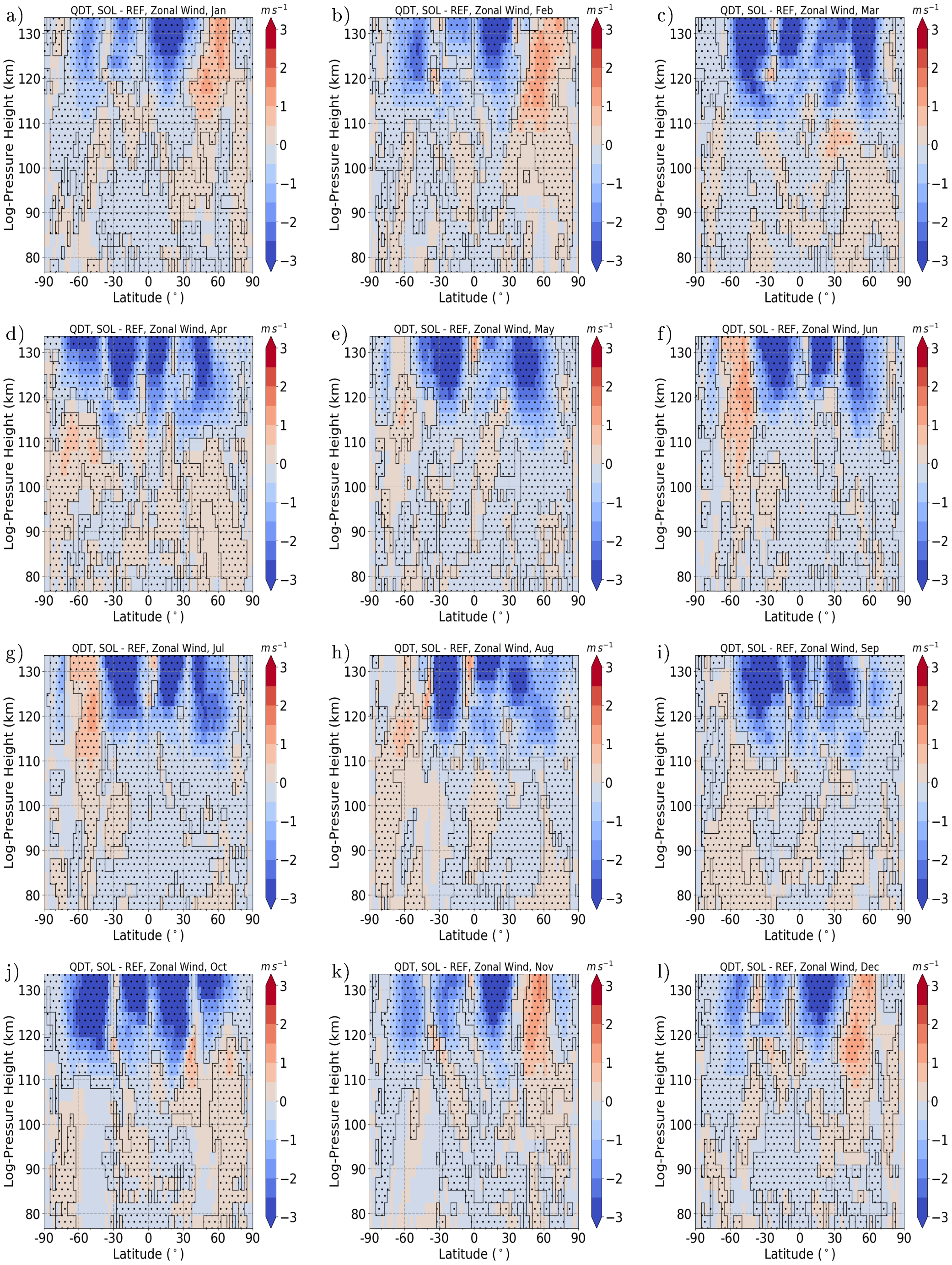

Figure S37.: QDT zonal wind amplitude differences between SOL and REF run as color. Significance larger than 99% as dotted area.

A.9. The gravity wave Forcing

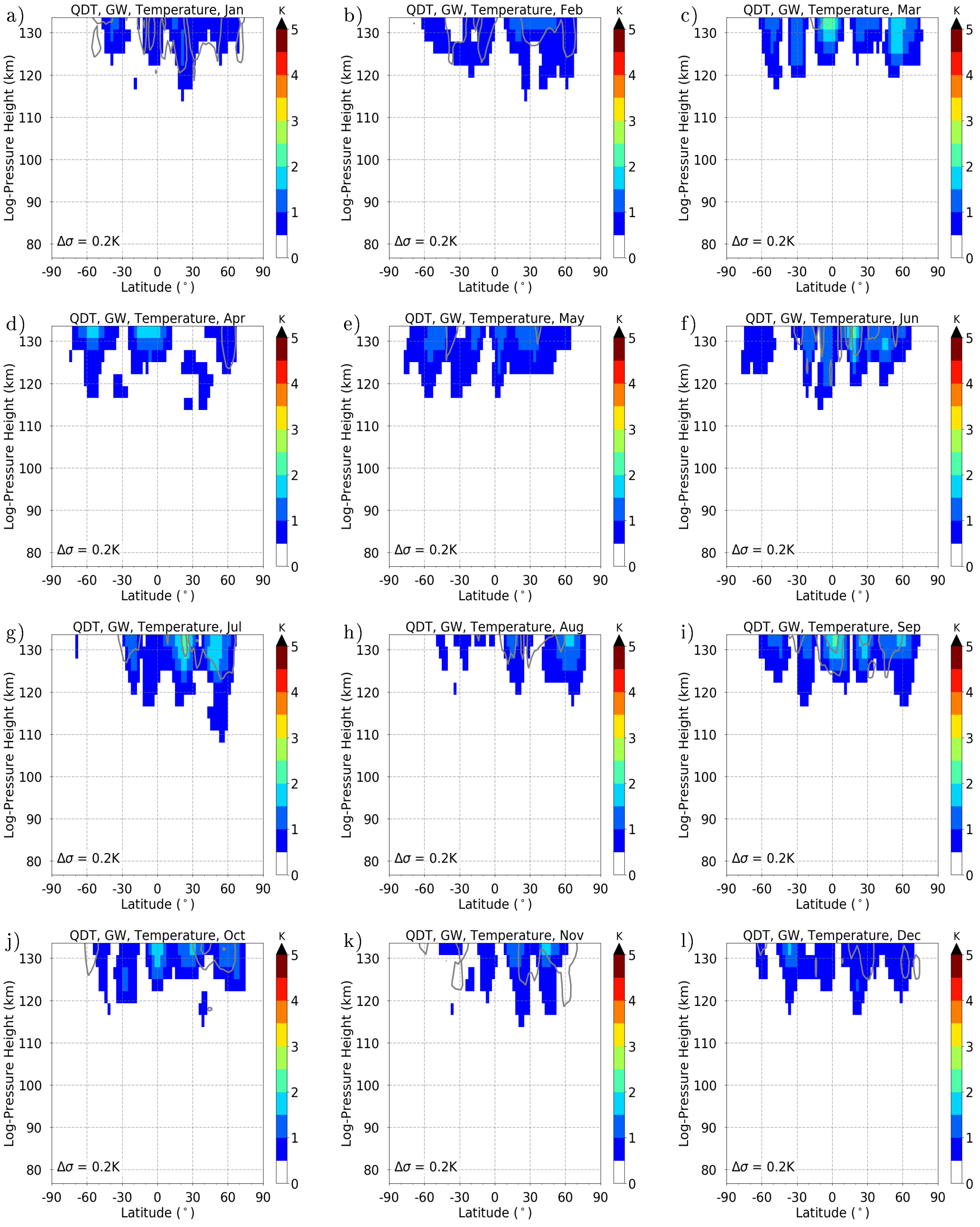

Figure S38.: GW run QDT temperature amplitudes as color, black lines are standard deviation from ensemble runs.

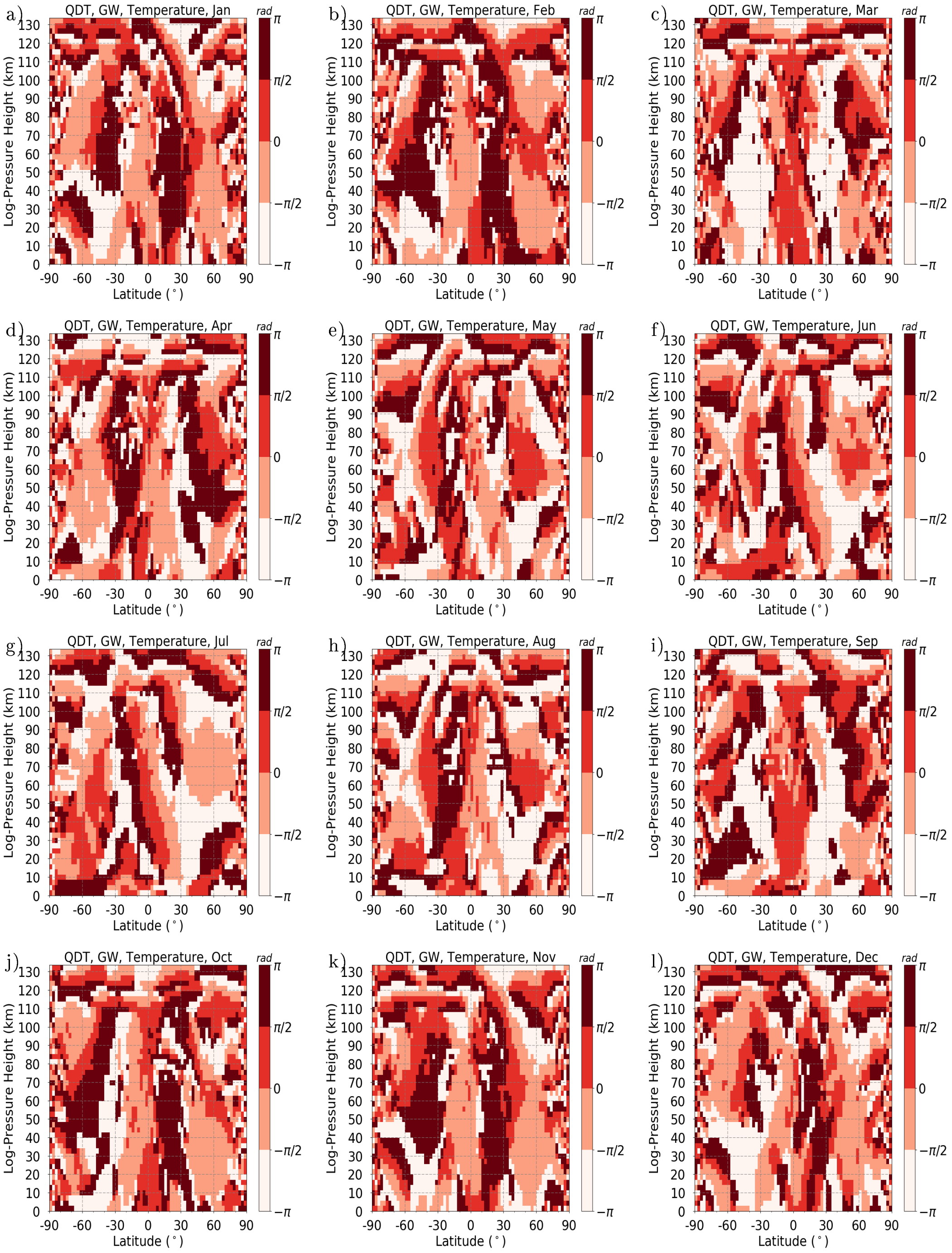

Figure S39.: GW run QDT temperature phases as color.

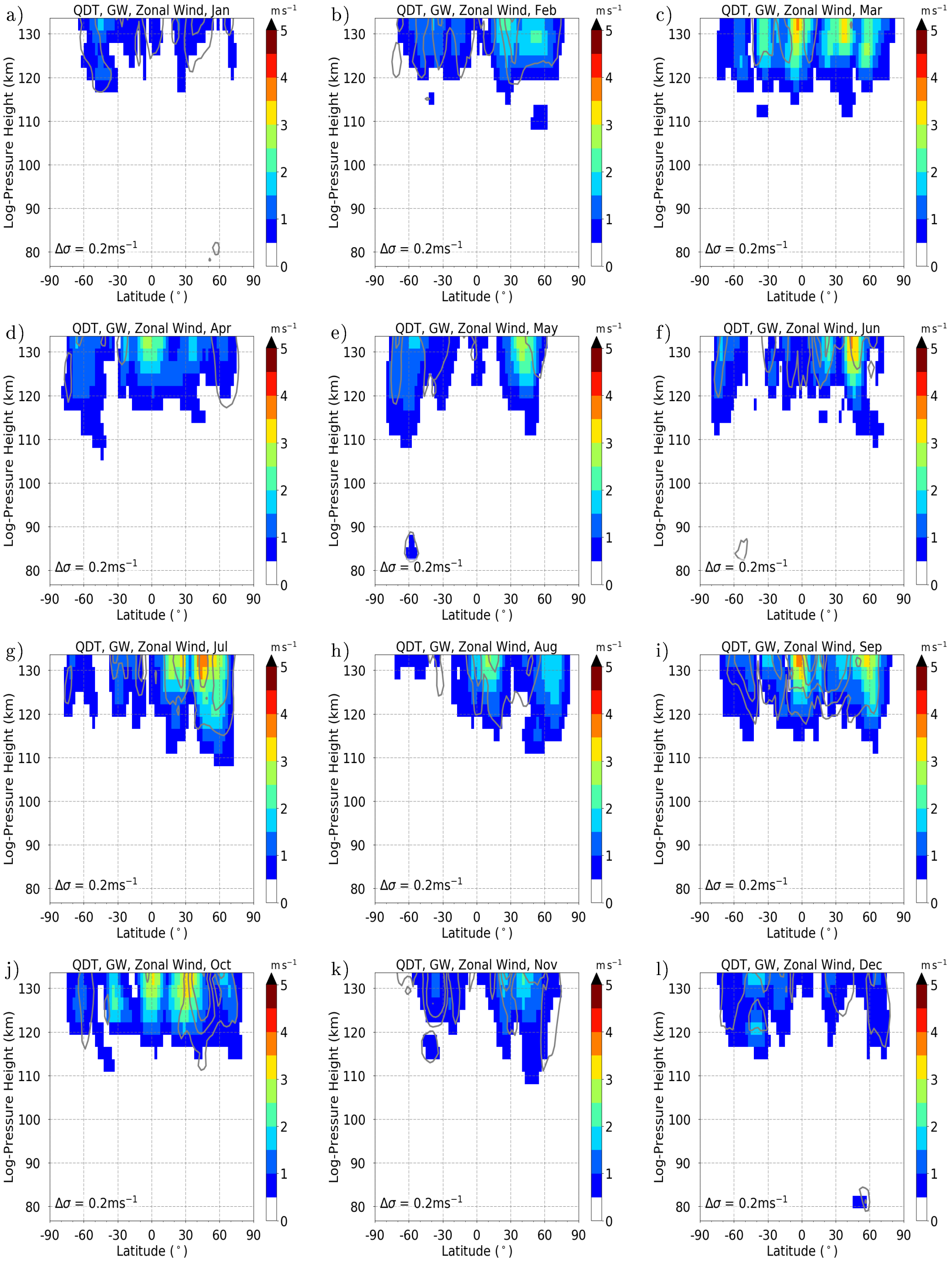

Figure S40.: GW run QDT zonal wind amplitudes as color, black lines are standard deviation from ensemble runs.

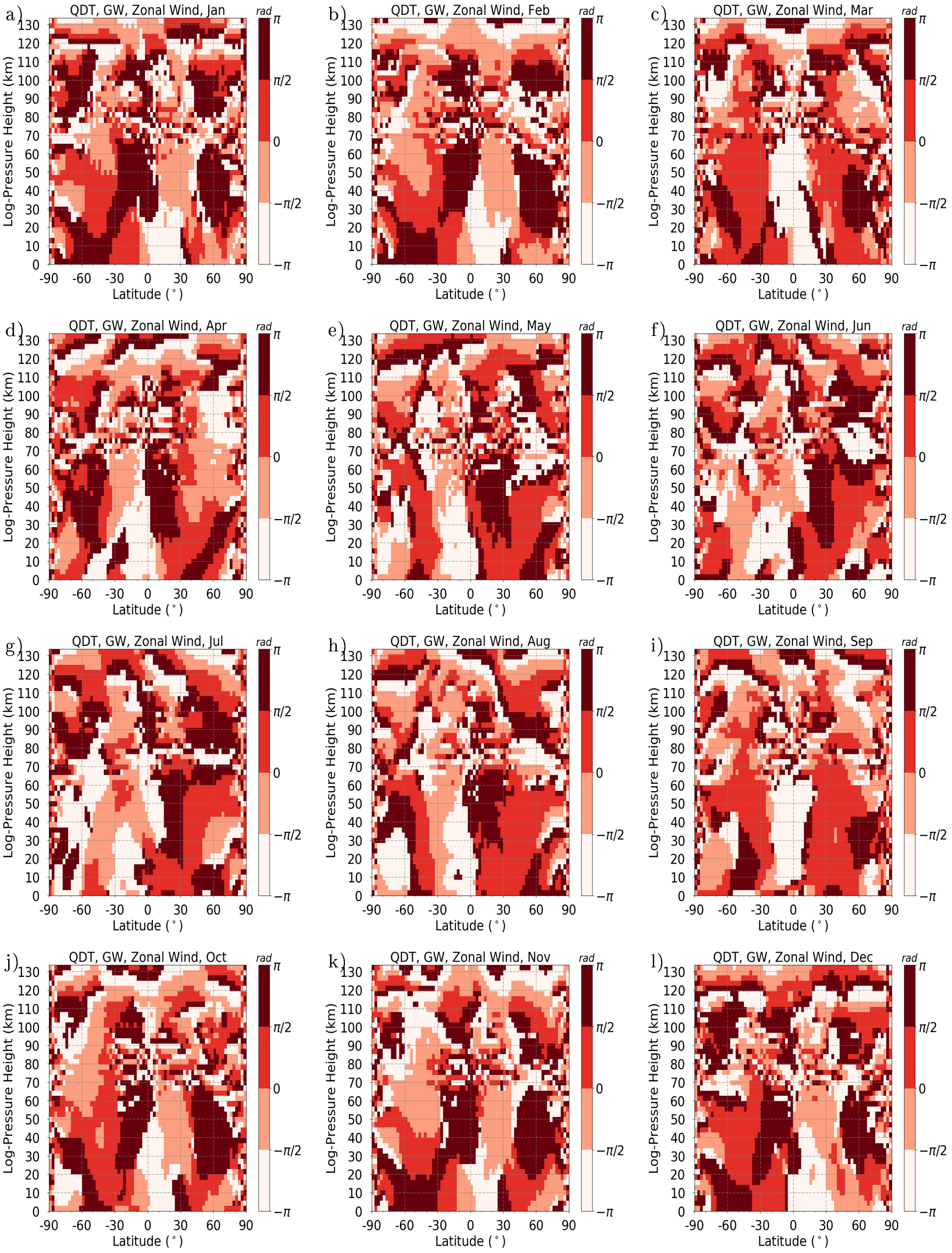

Figure S41.: GW run QDT zonal wind phases as color.

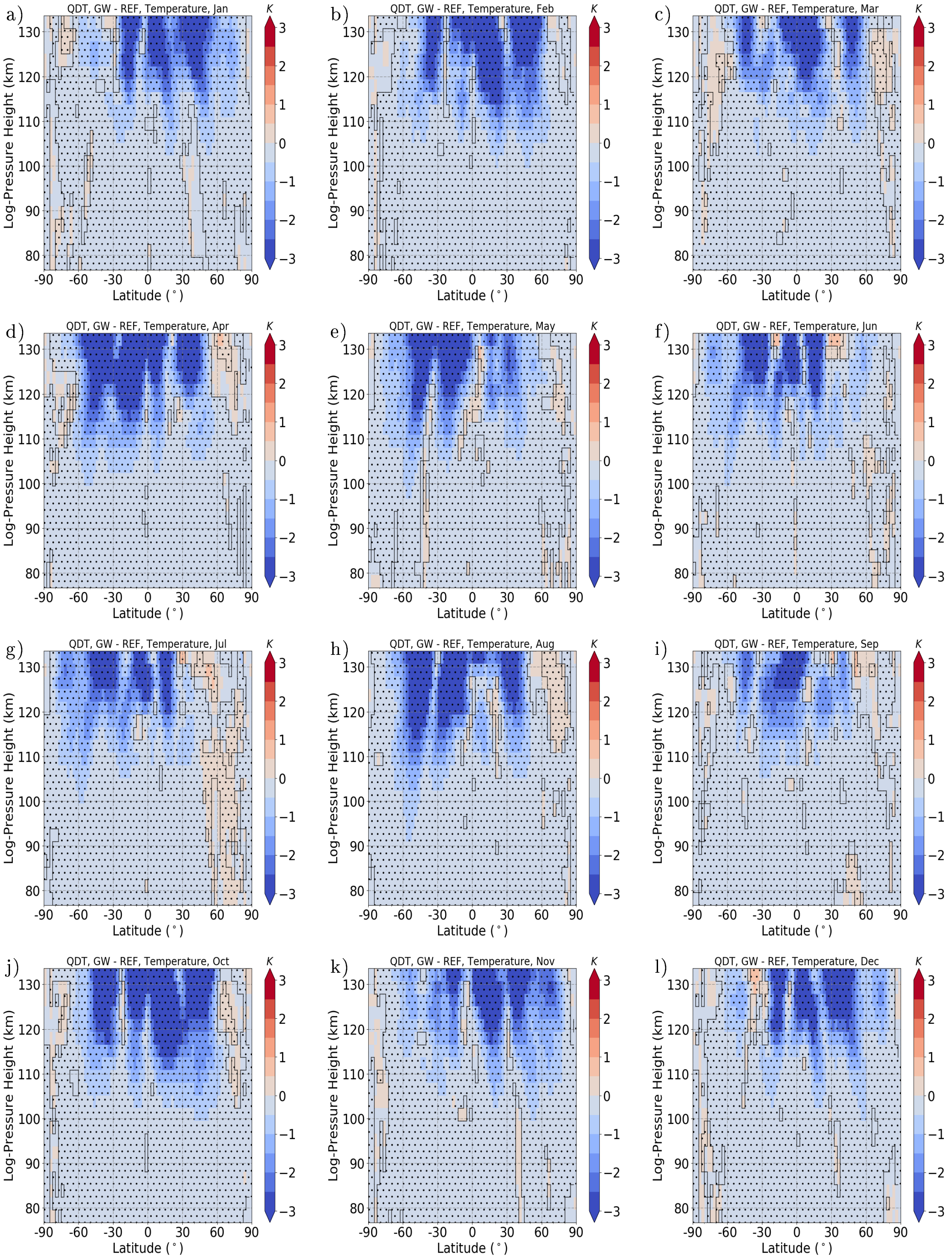

Figure S42.: QDT temperature amplitude differences between GW and REF run as color. Significance larger than 99% as dotted area.

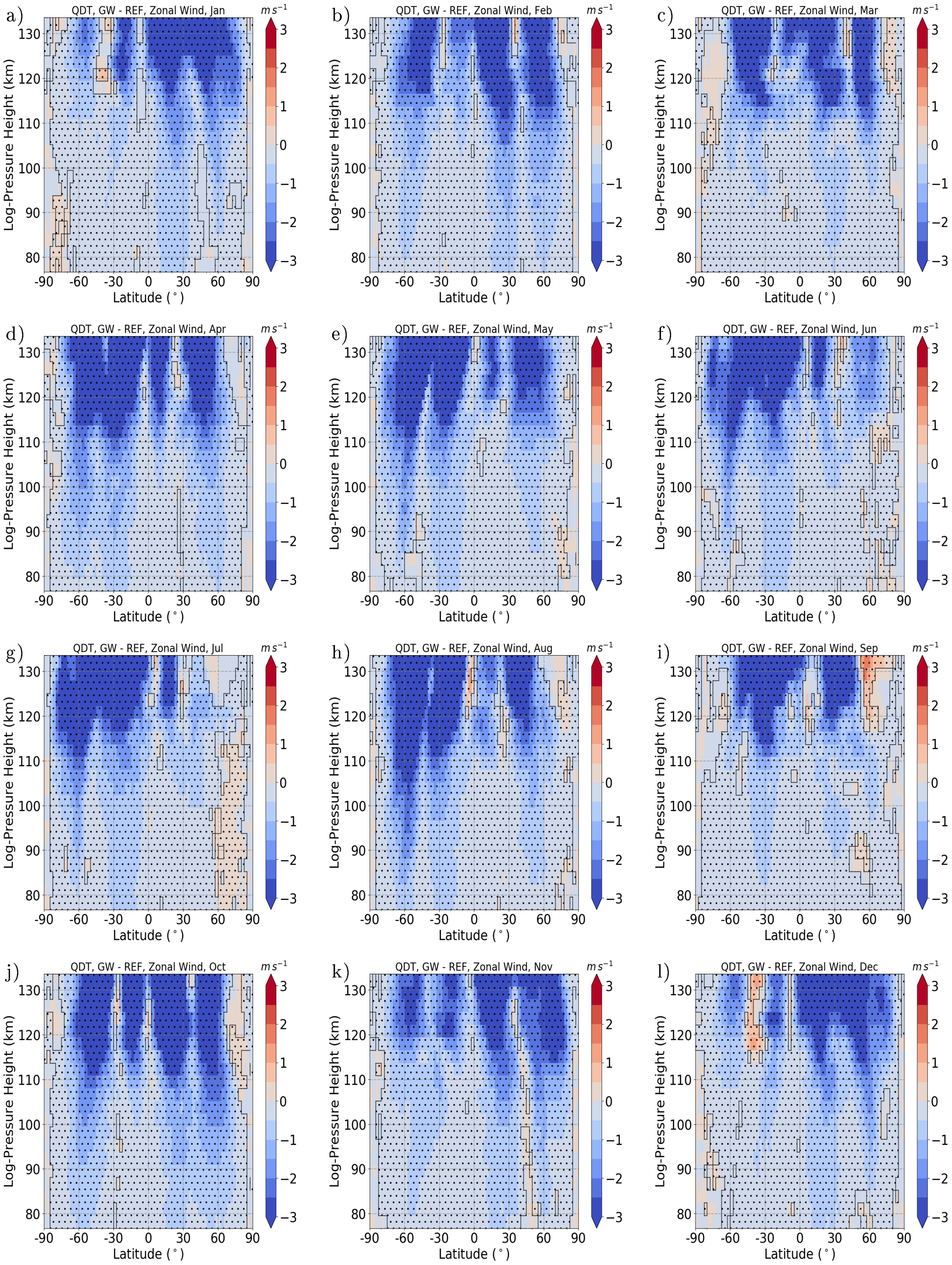

Figure S43.: QDT zonal wind amplitude differences between GW and REF run as color. Significance larger than 99% as dotted area.

A.10. The nonlinear Forcing

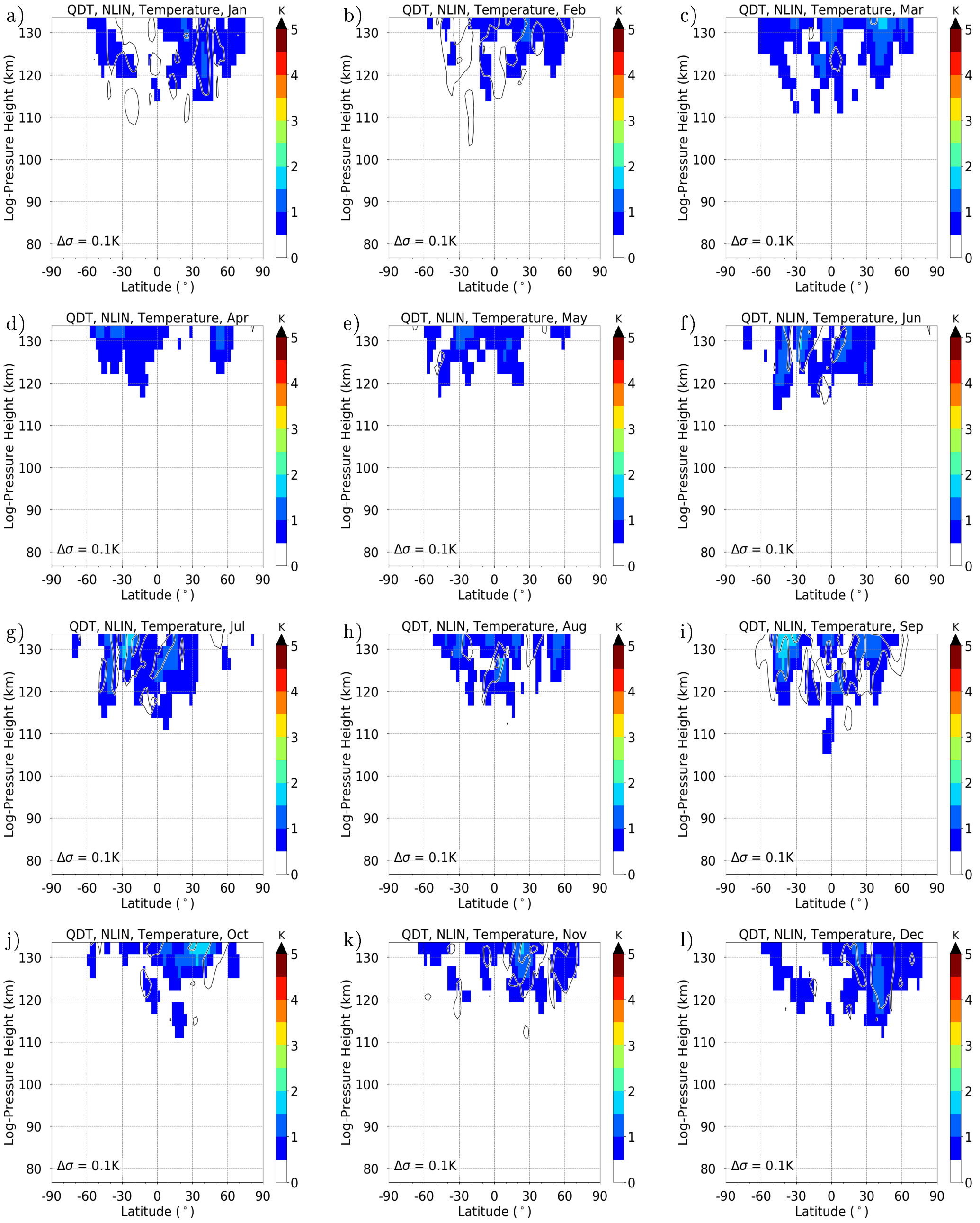

Figure S44.: NLIN run QDT temperature amplitudes as color, black lines are standard deviation from ensemble runs.

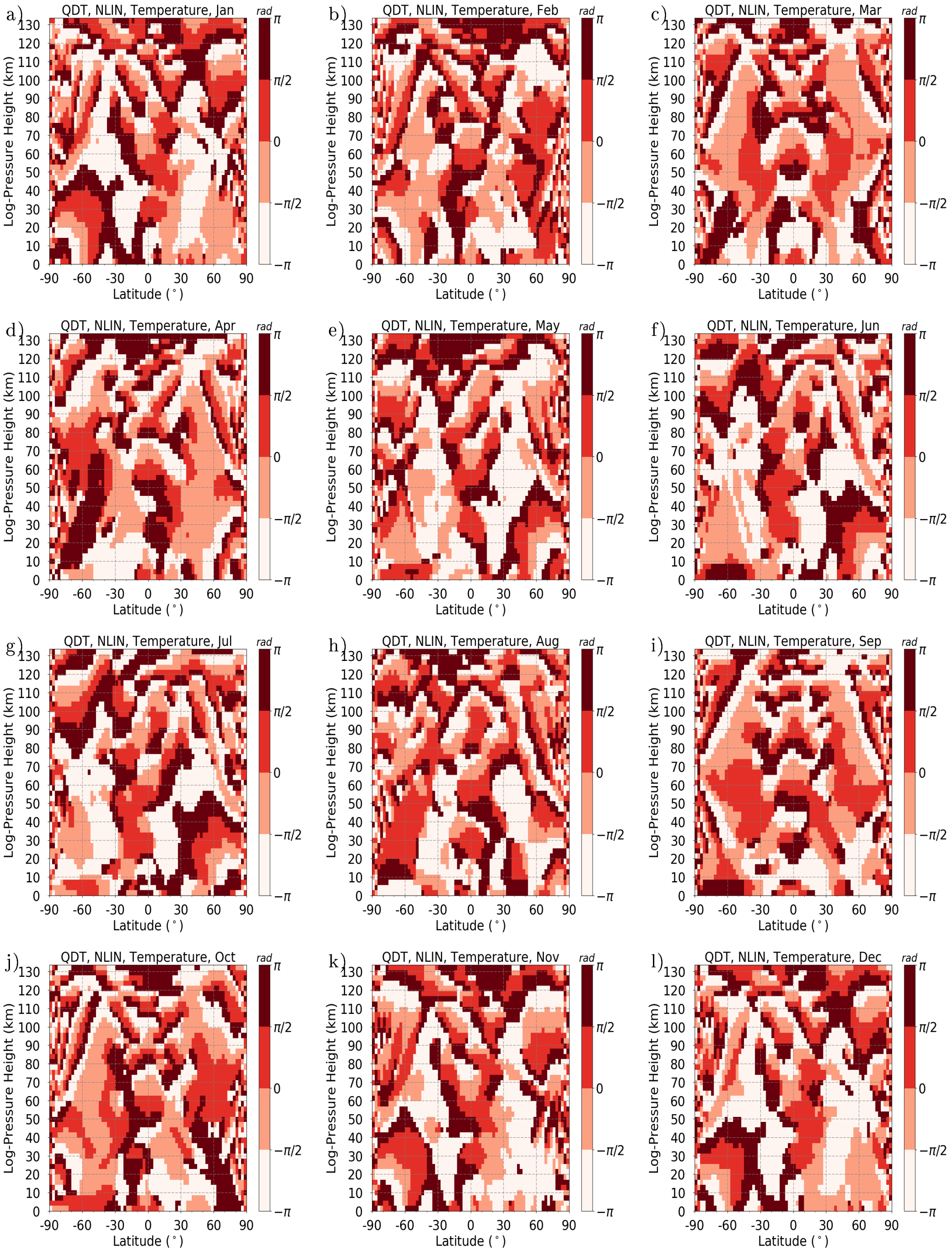

Figure S45.: NLIN run QDT temperature phases as color.

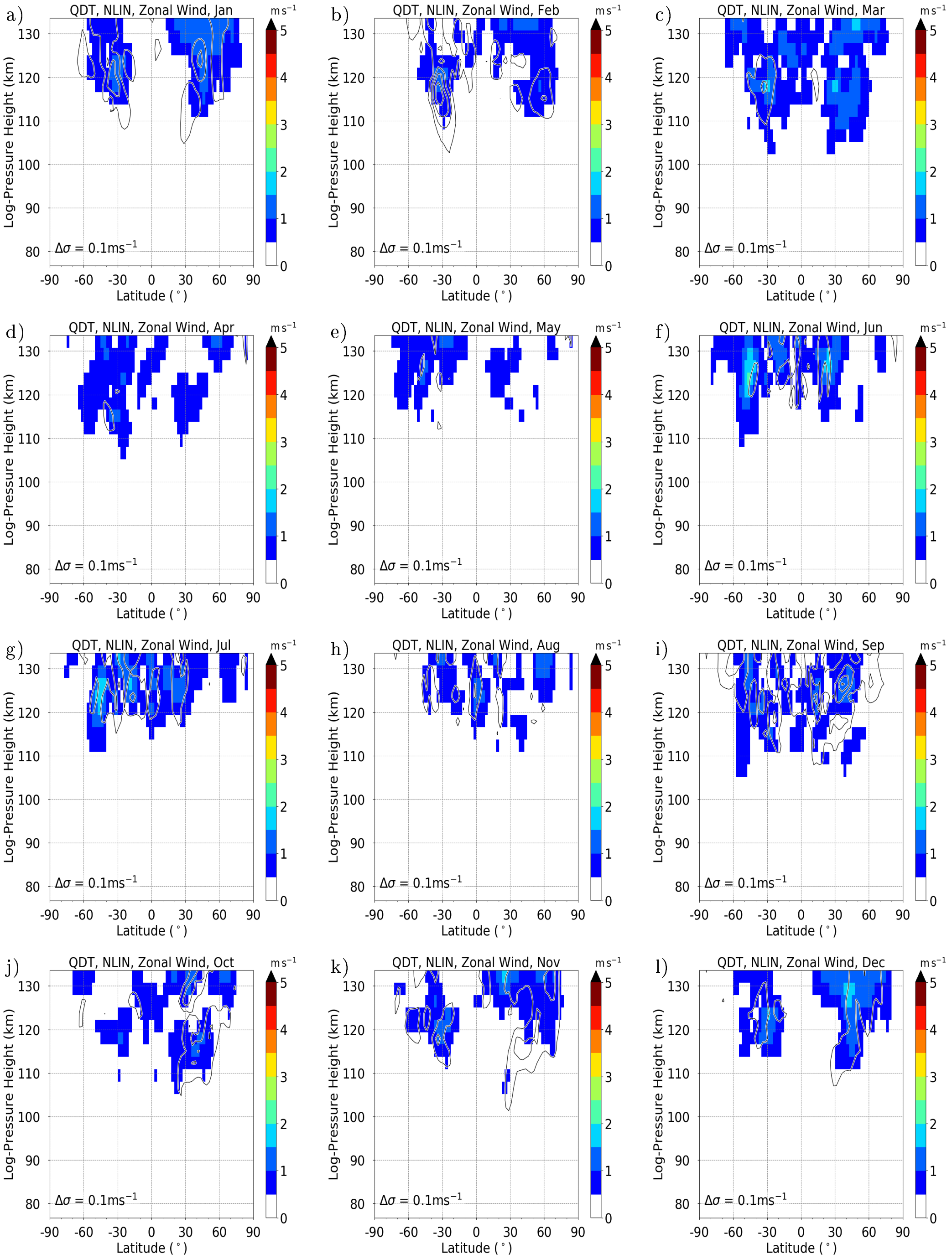

Figure S46.: NLIN run QDT zonal wind amplitudes as color, black lines are standard deviation from ensemble runs.

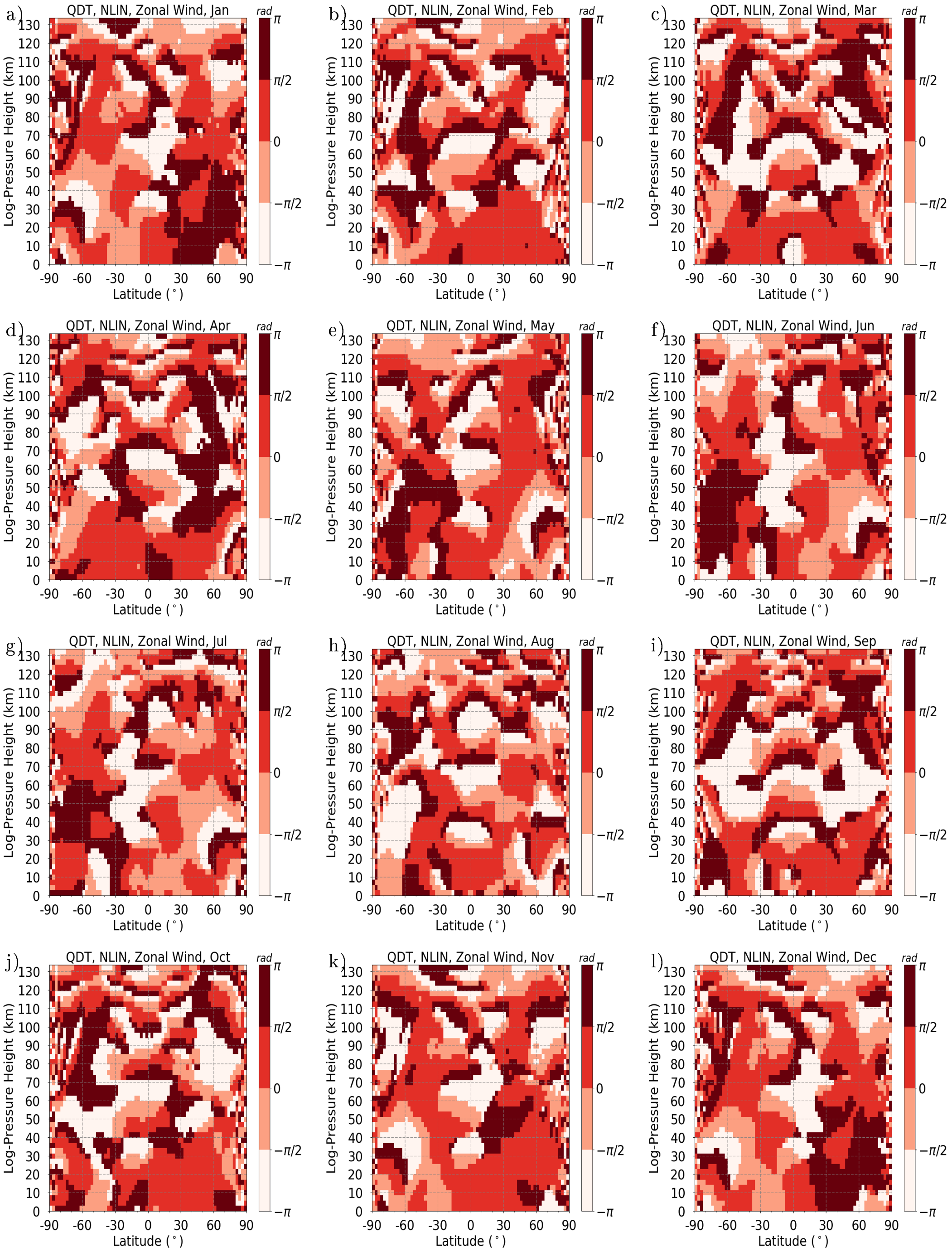

Figure S47.: NLIN run QDT zonal wind phases as color.

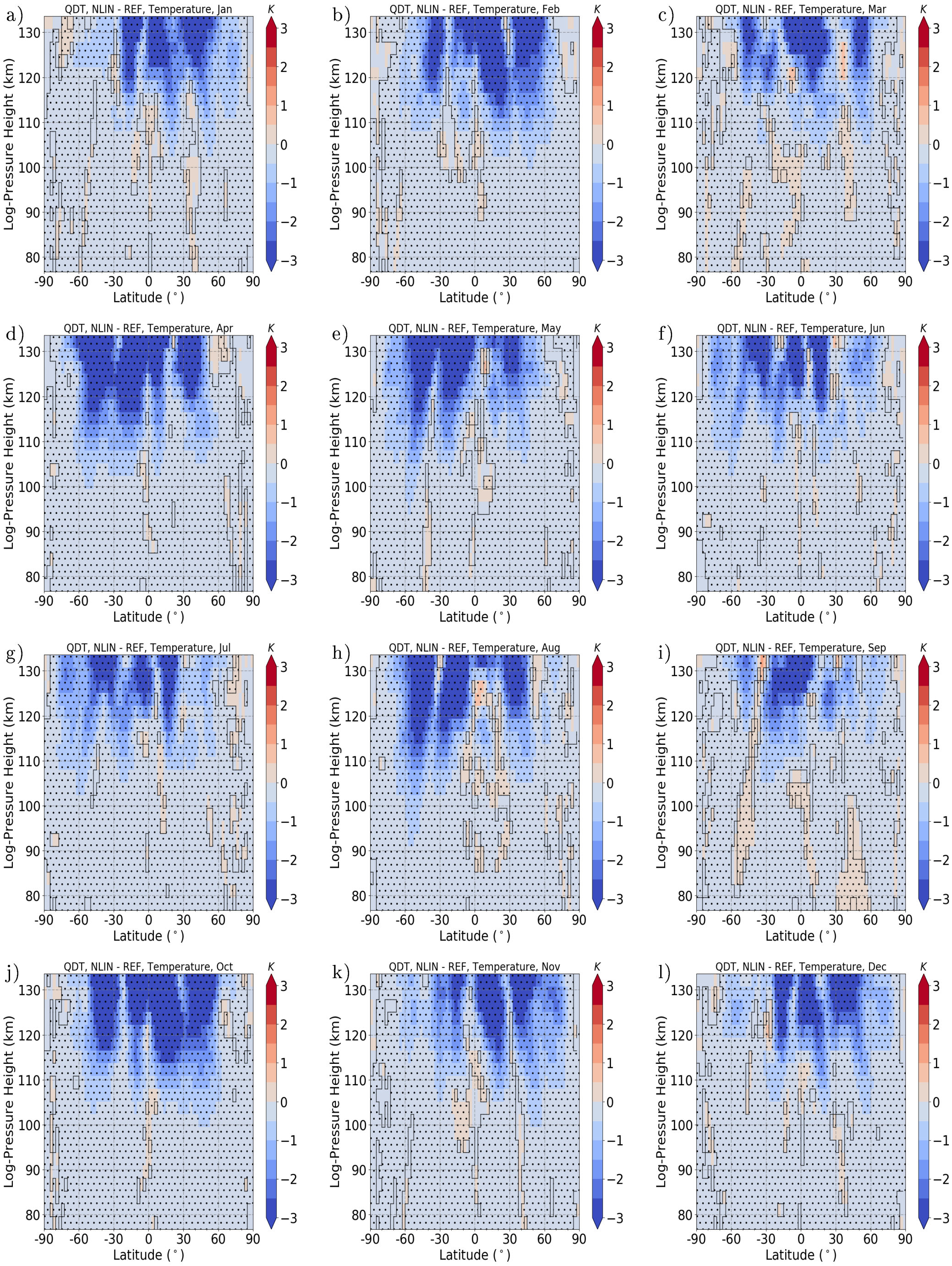

Figure S48.: QDT temperature amplitude differences between NLIN and REF run as color. Significance larger than 99% as dotted area.

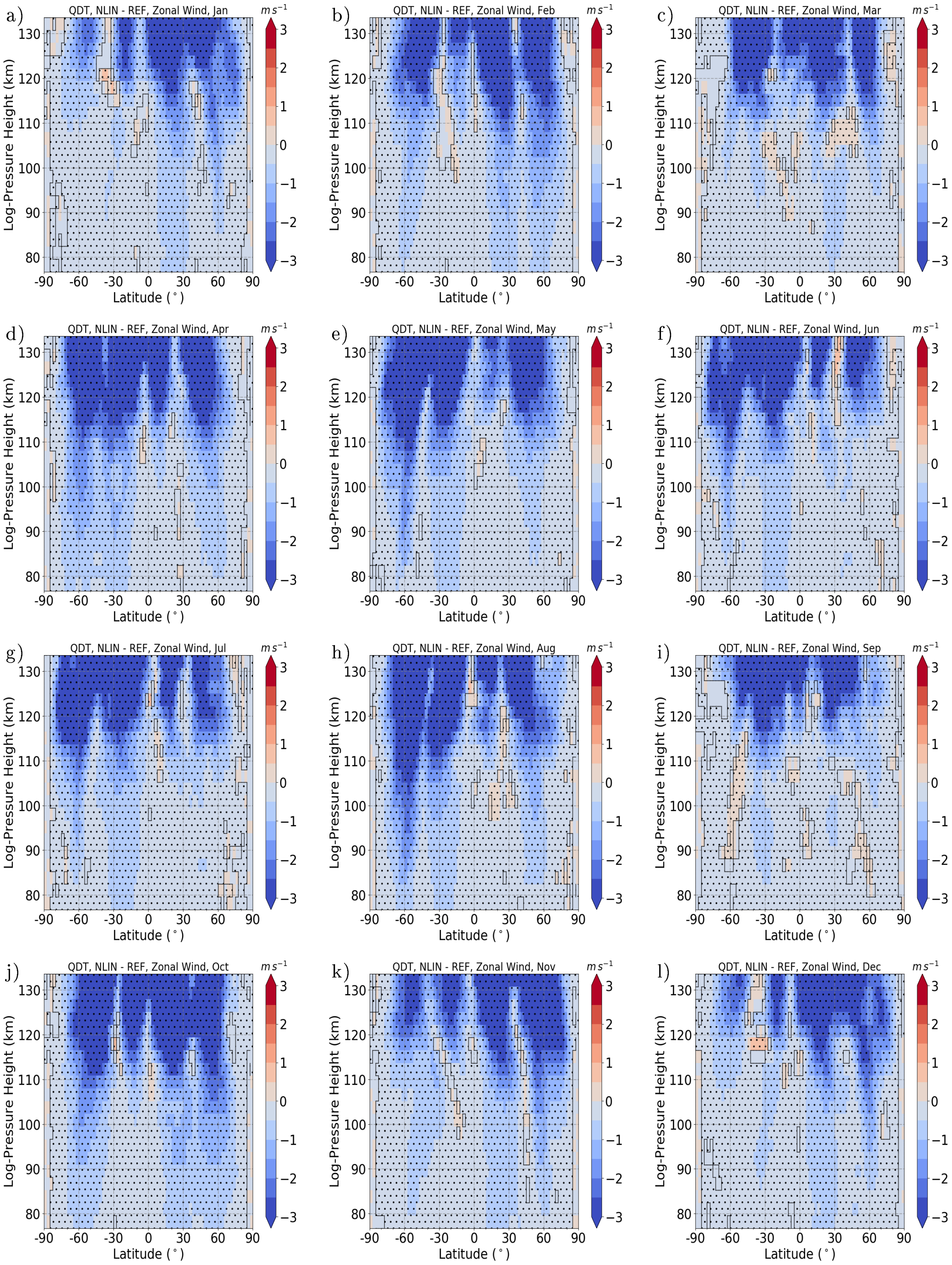

Figure S49.: QDT zonal wind amplitude differences between NLIN and REF run as color. Significance larger than 99% as dotted area.

A.11. No Gravity Wave Forcing

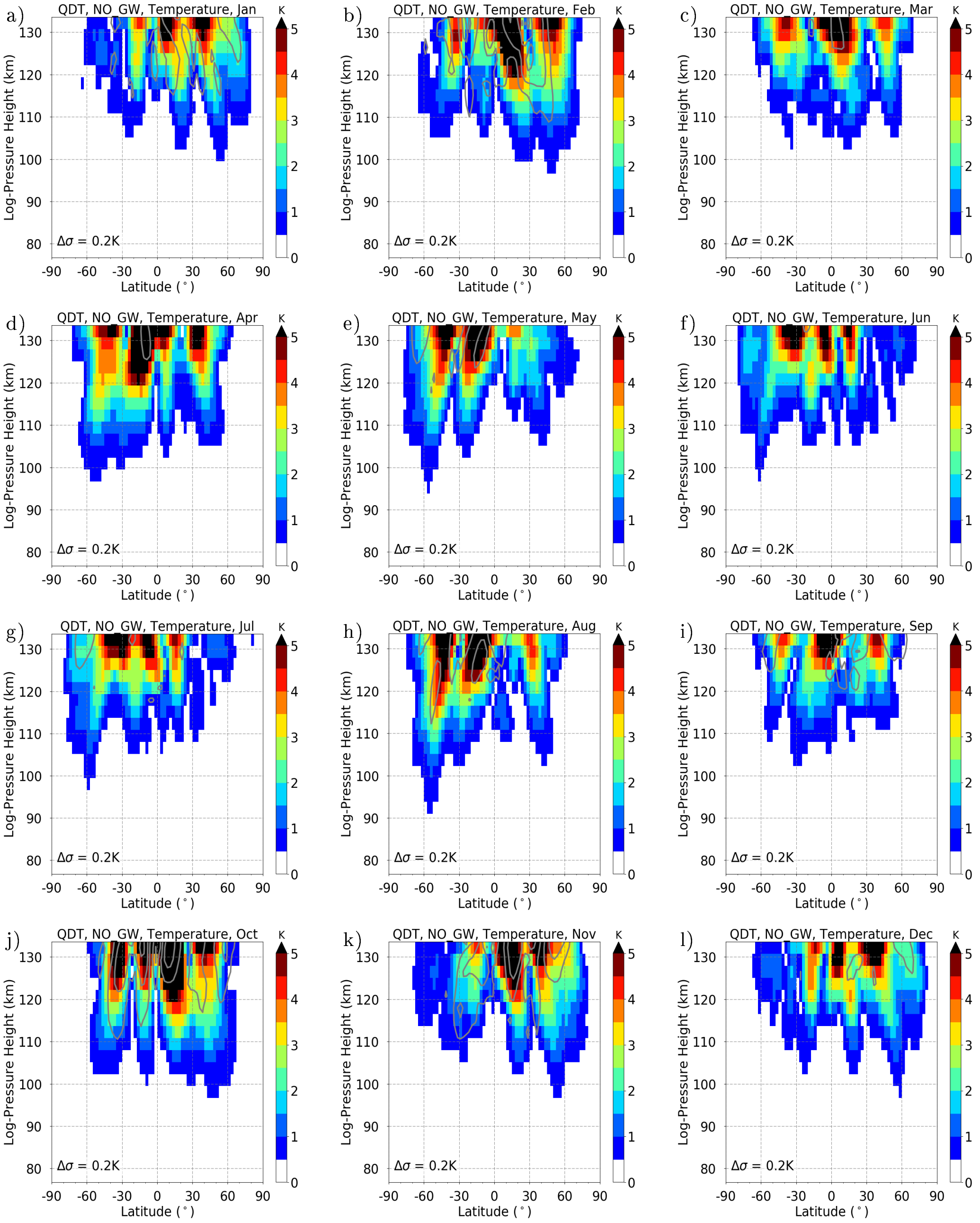

Figure S50.: NO_GW run QDT temperature amplitudes temperature as color, black lines are standard deviation from ensemble runs.

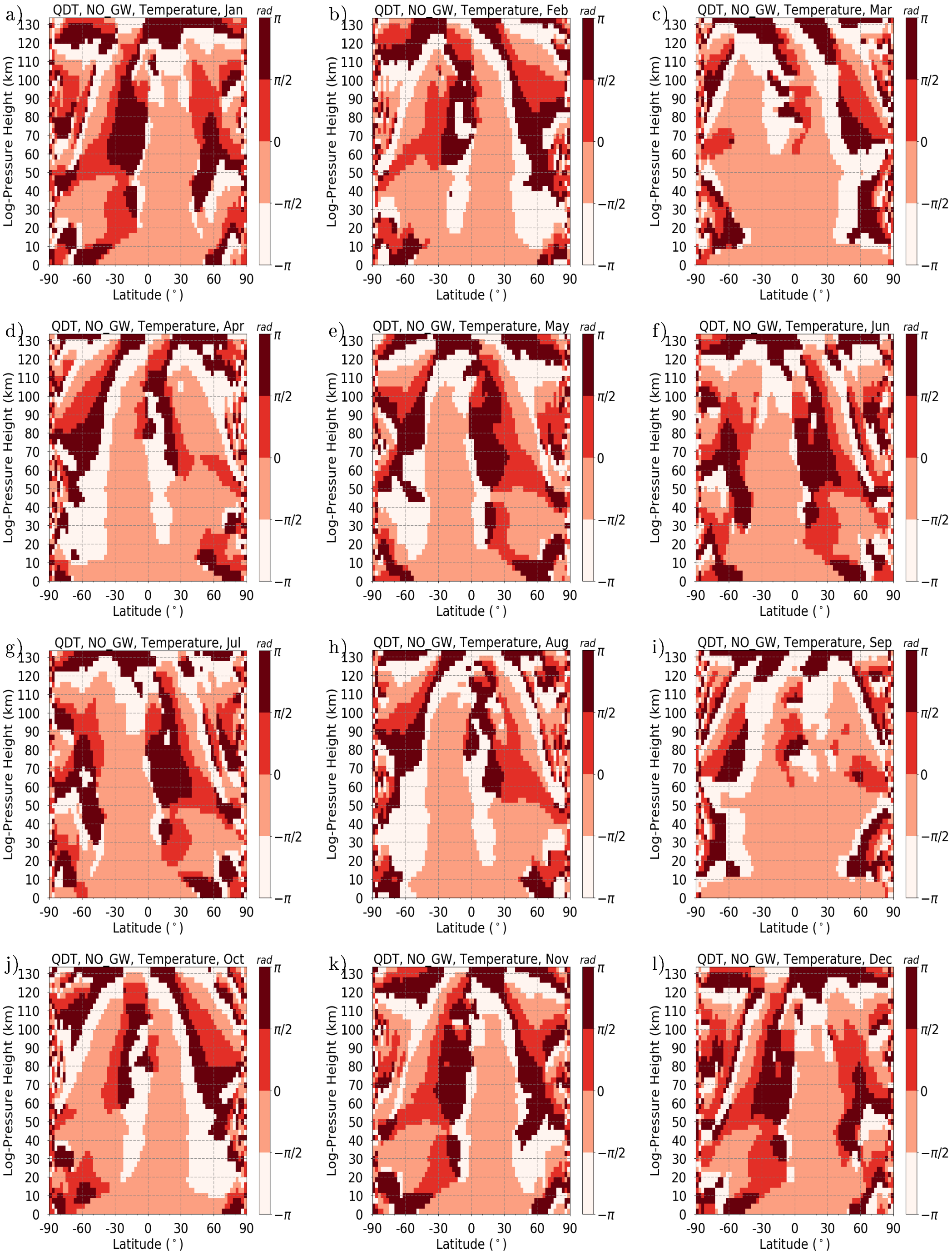

Figure S51.: NO_GW run QDT temperature phases as color.

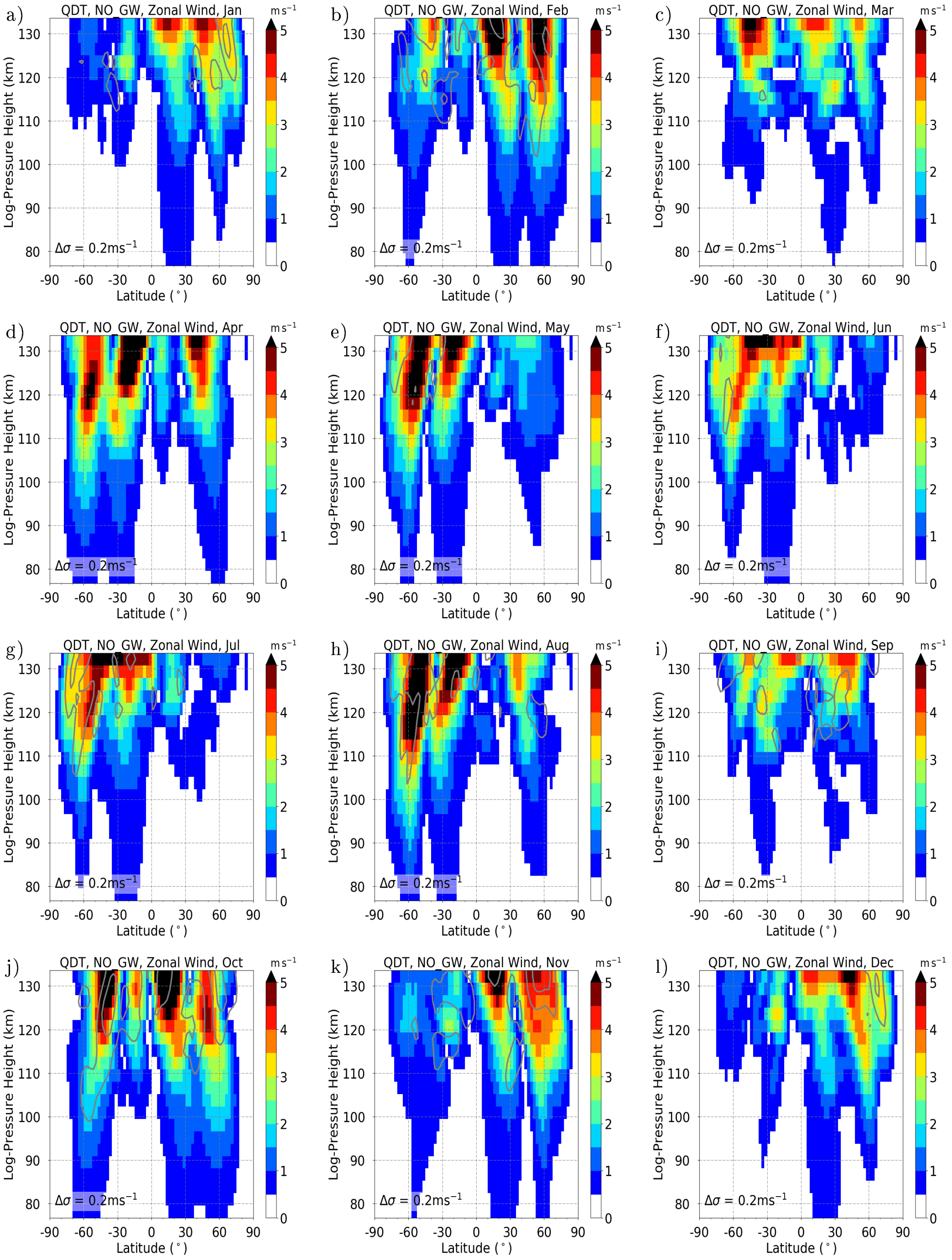

Figure S52.: NO_GW run QDT zonal wind amplitudes as color, black lines are standard deviation from ensemble runs.

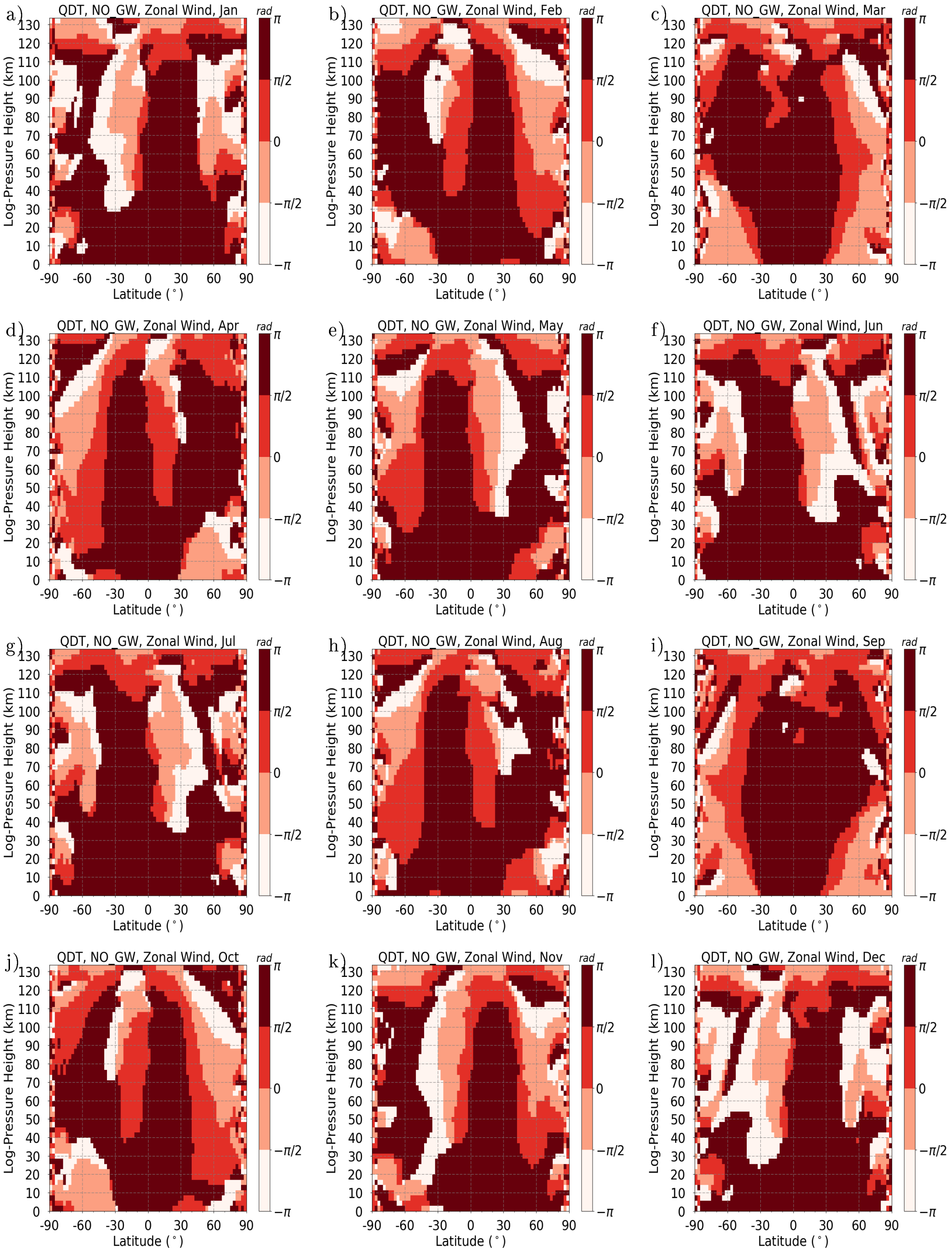

Figure S53.: NO_GW run QDT zonal wind phases as color.

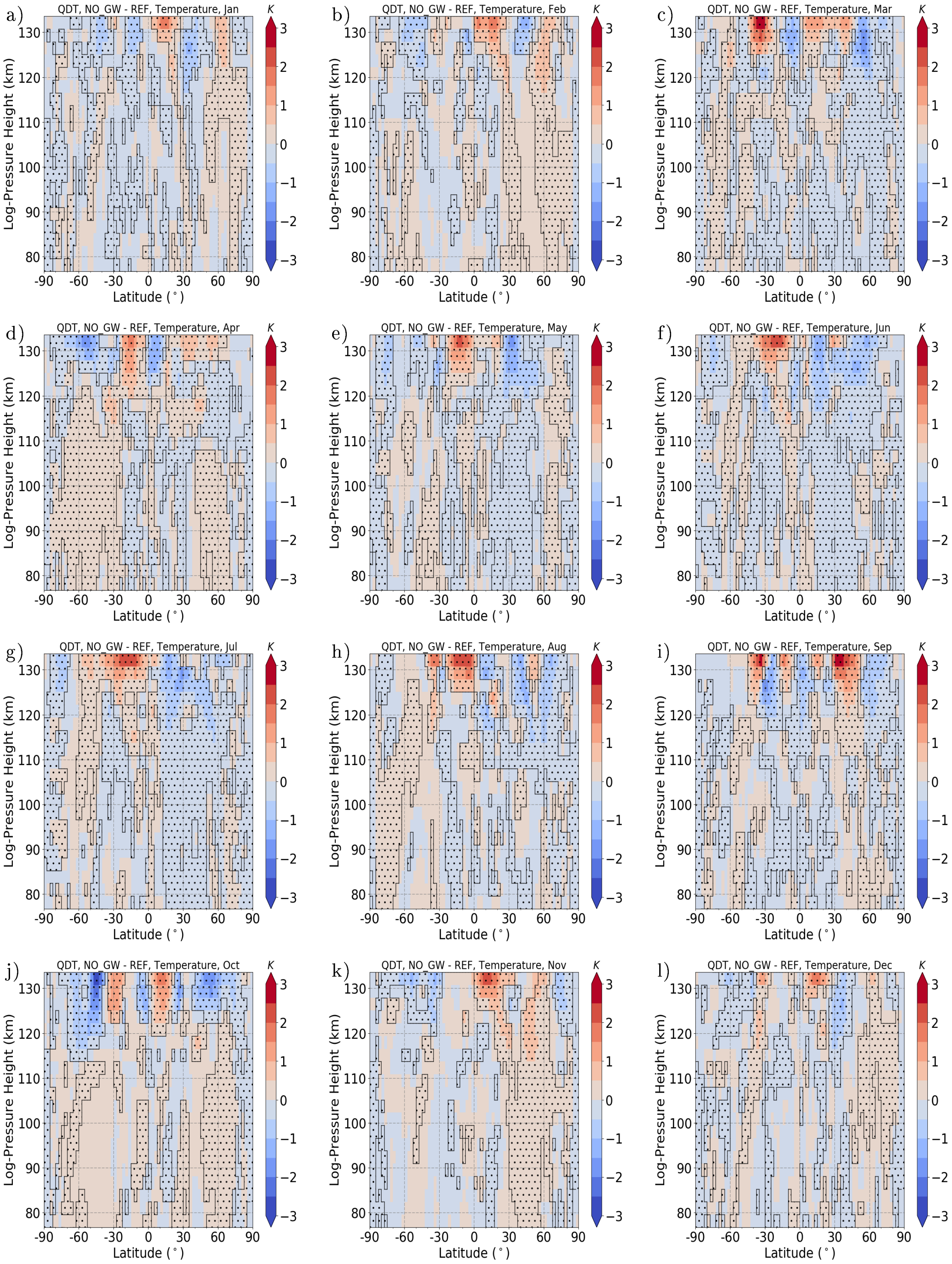

Figure S54.: QDT dtemperature amplitude differences between NO_GW and REF run as color. Significance larger than 99% as dotted area.

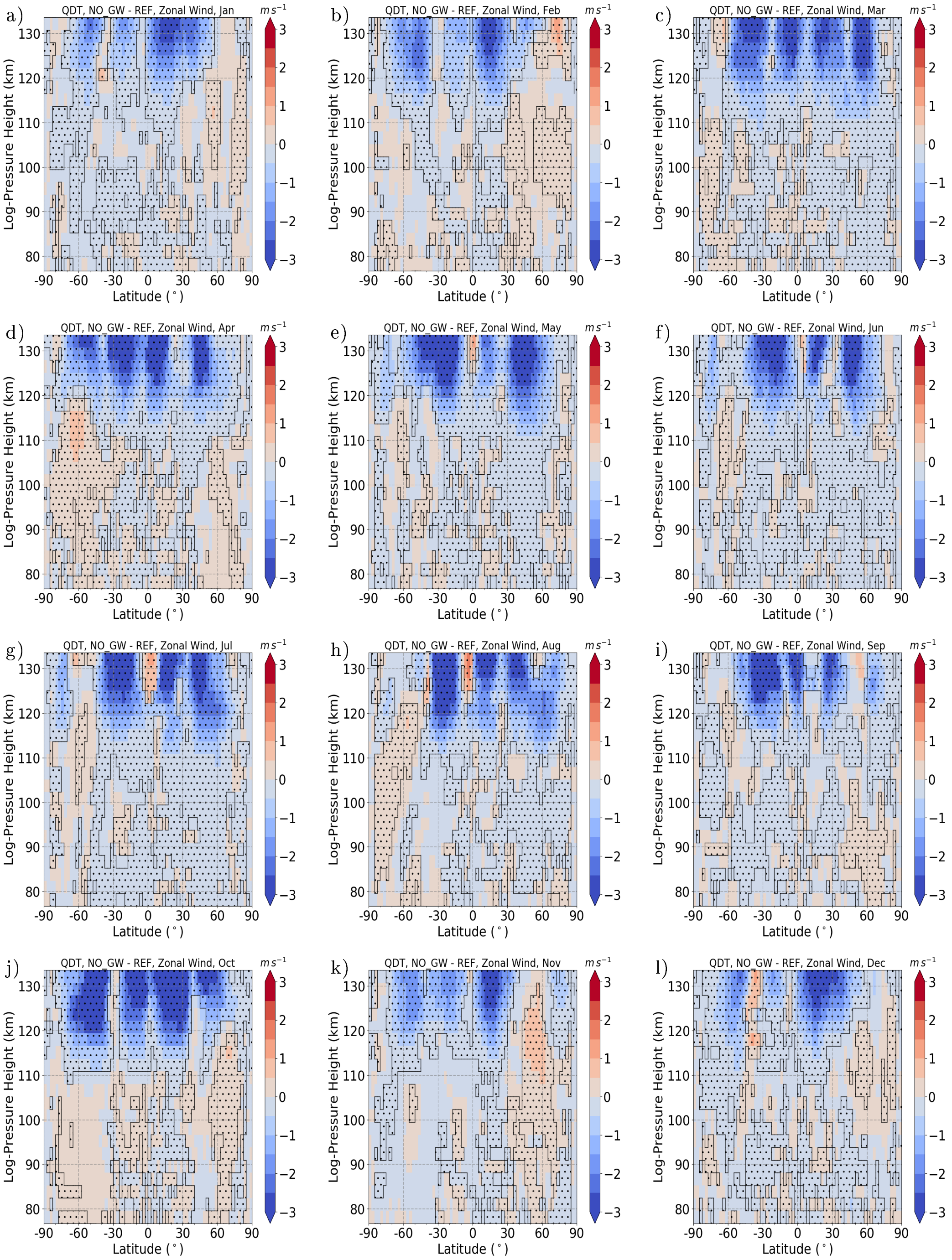

Figure S55.: QDT zonal wind amplitude differences between NO_GW and REF run as color. Significance larger than 99% as dotted area.

A.12. No nonlinear Forcing

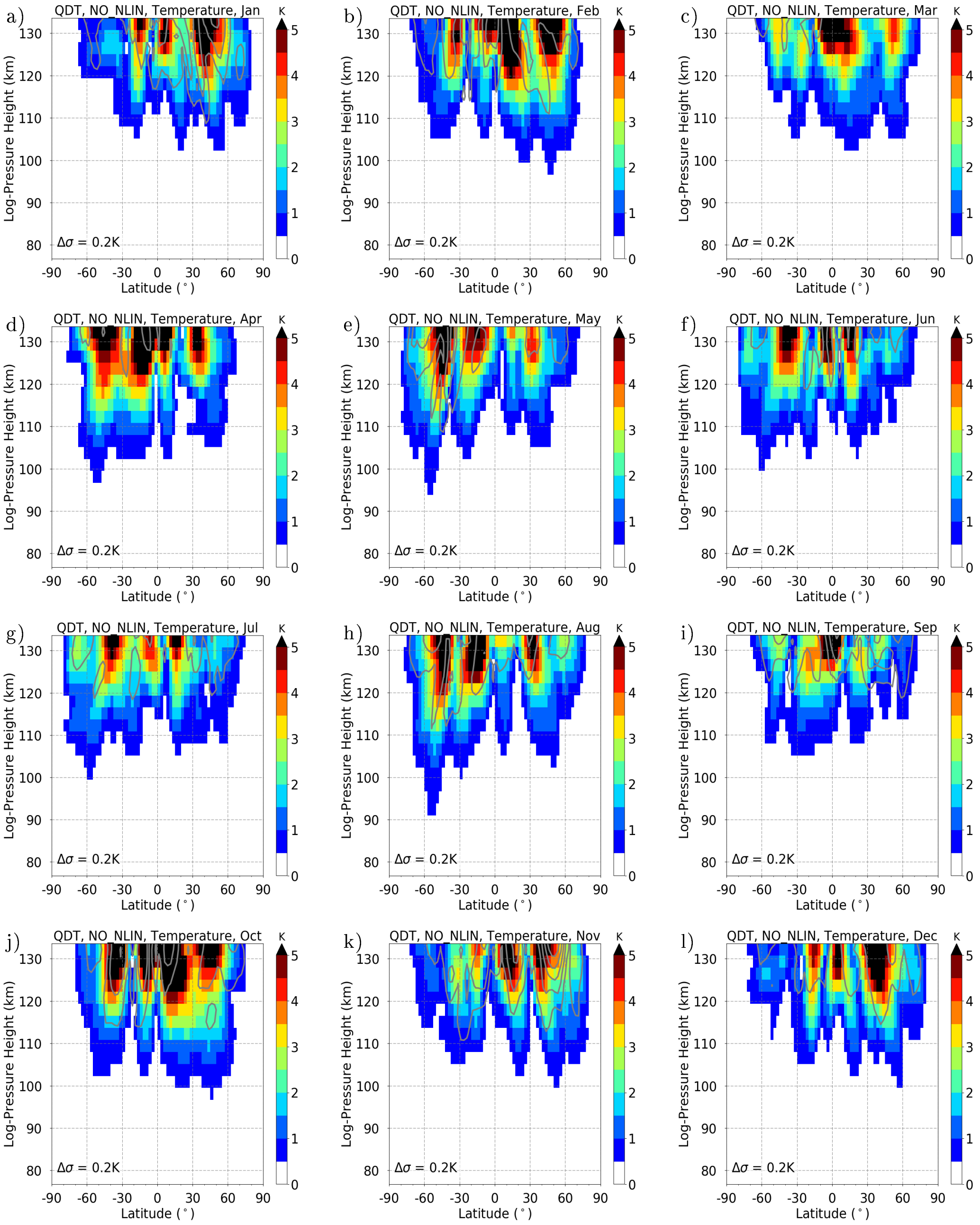

Figure S56.: NO_NLIN run QDT temperature amplitudes as color, black lines are standard deviation from ensemble runs.

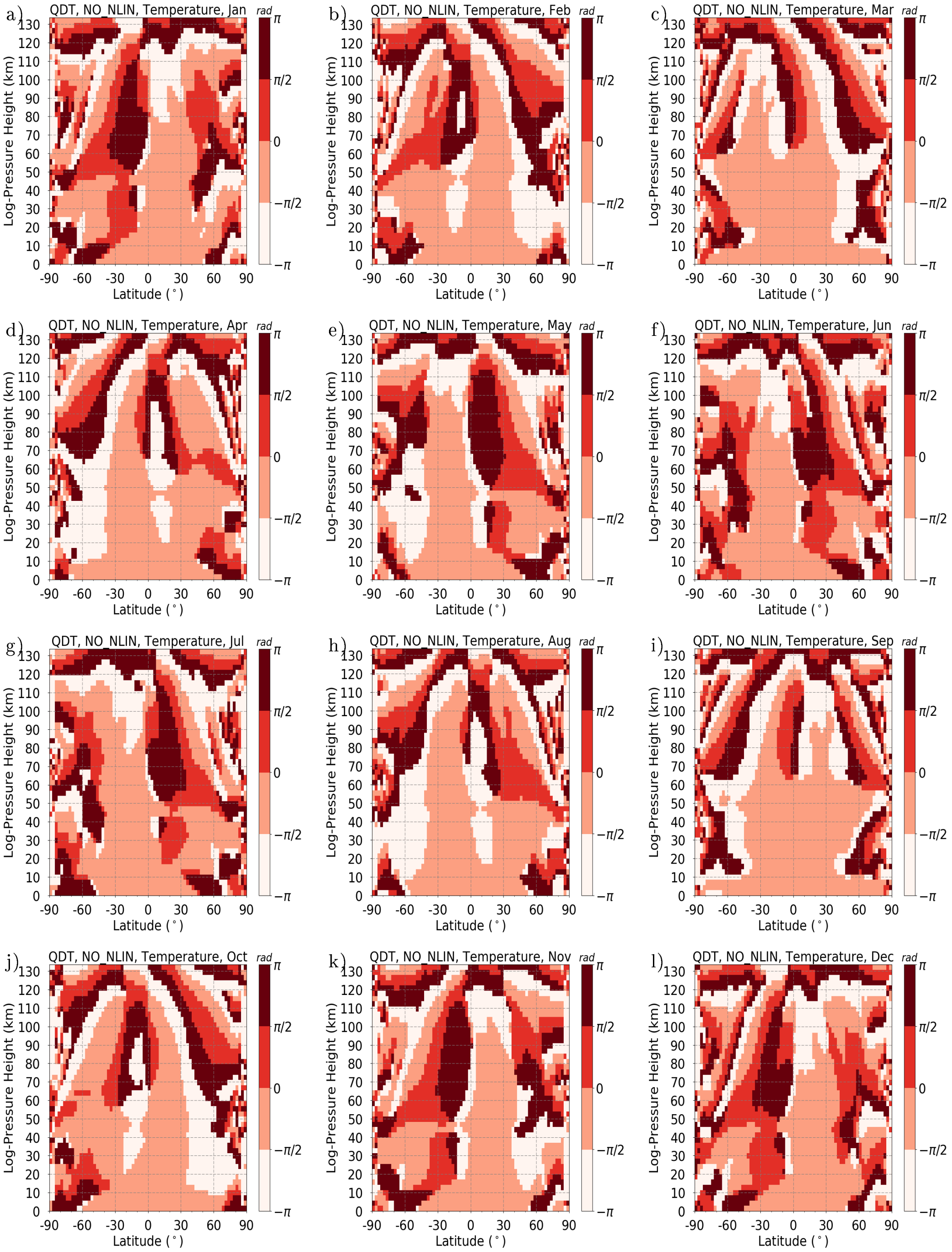

Figure S57.: NO_NLIN run QDT temperature phases as color.

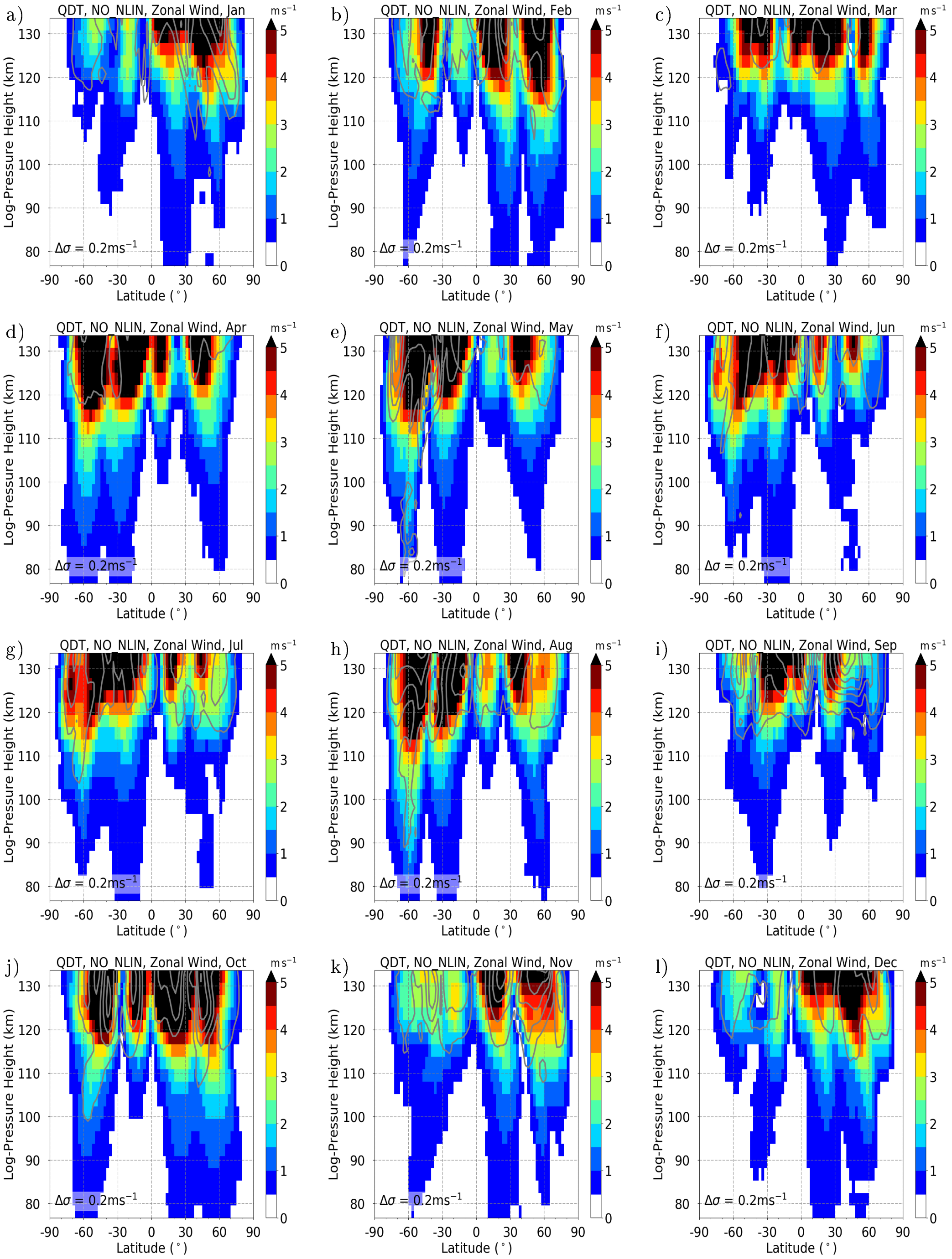

Figure S58.: NO_NLIN run QDT zonal wind amplitudes as color, black lines are standard deviation from ensemble runs.

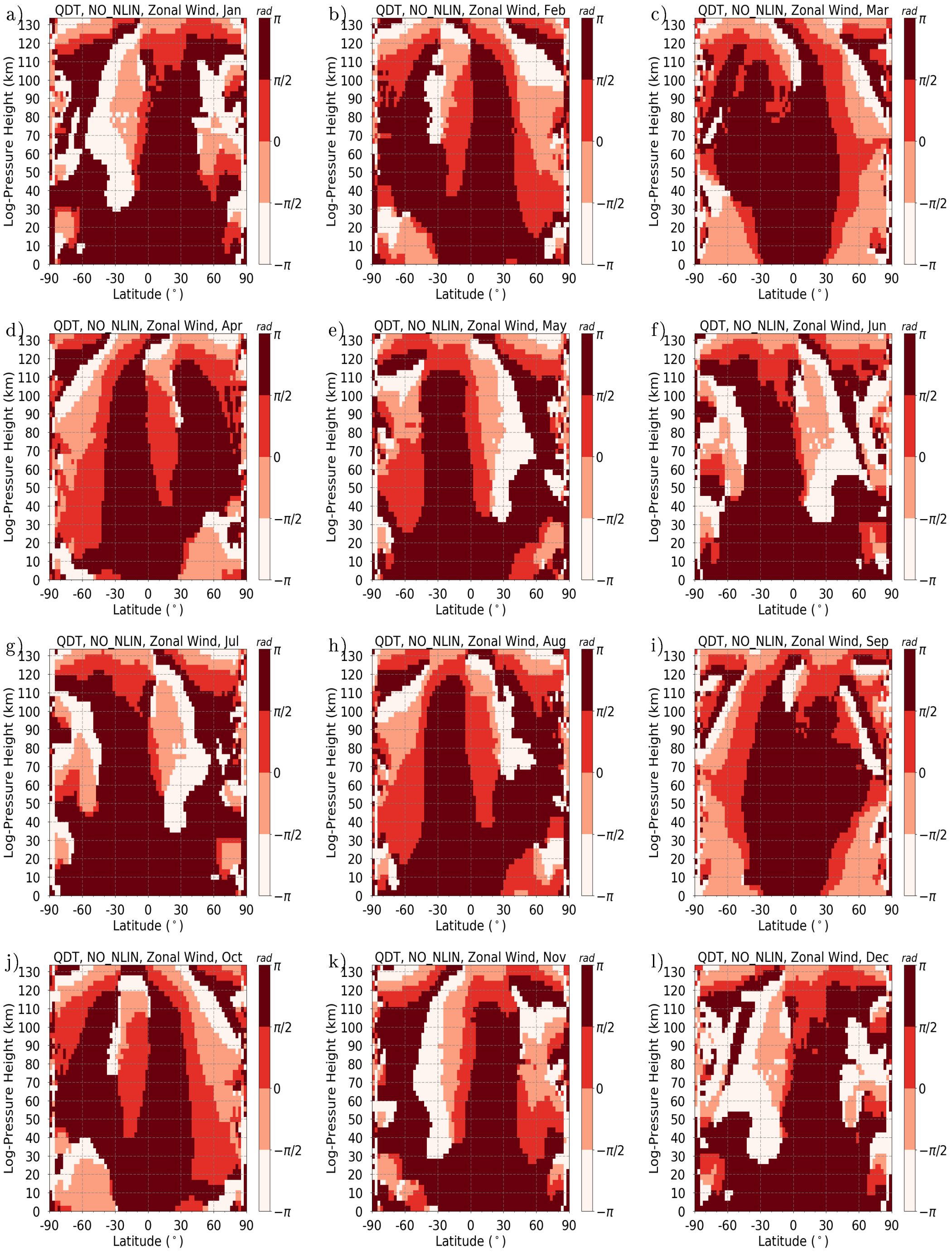

Figure S59.: NO_NLIN run QDT zonal wind phases as color.

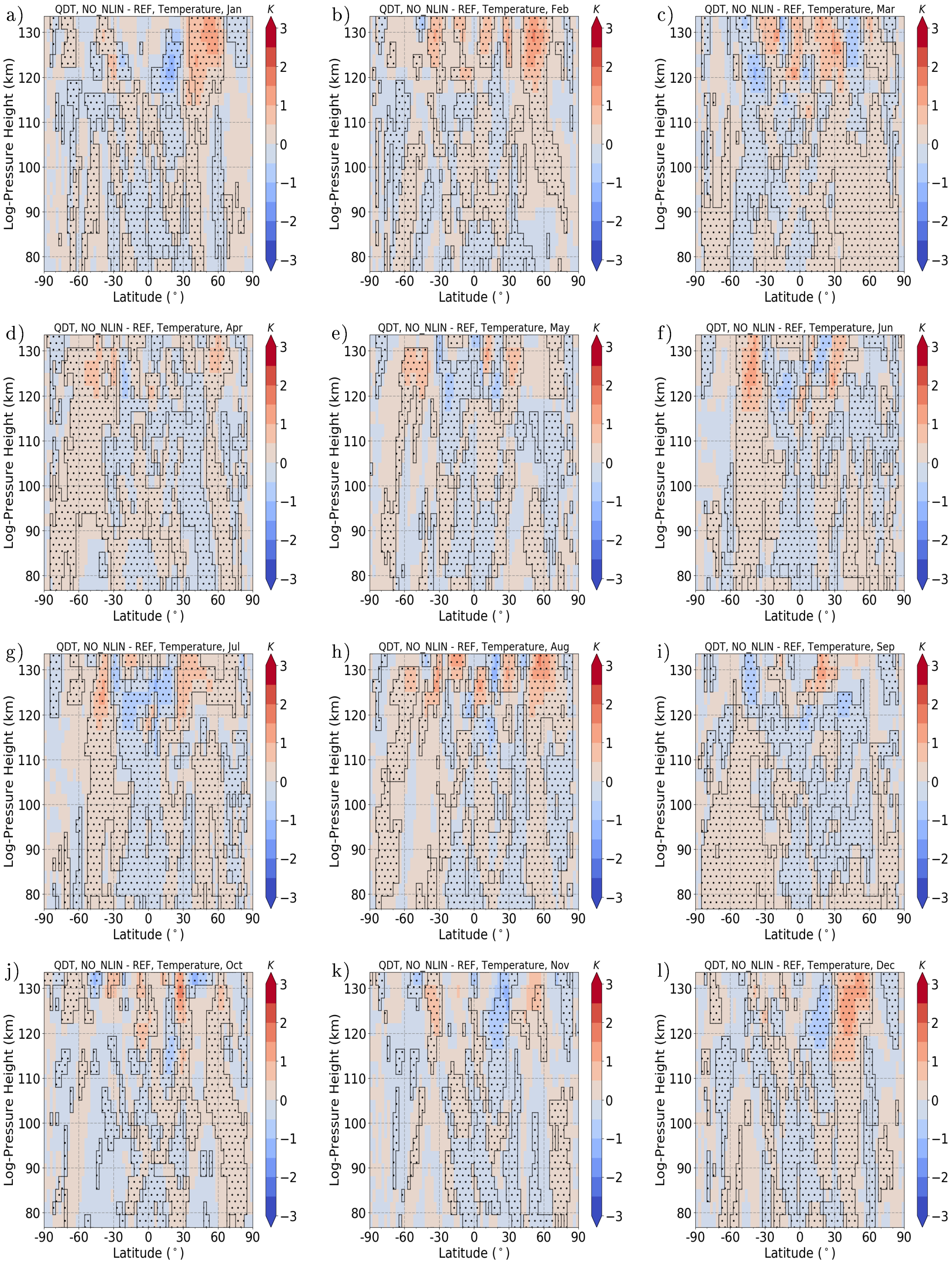

Figure S60.: QDT temperature amplitude differences between NO_NLIN and REF run as color. Significance larger than 99% as dotted area.

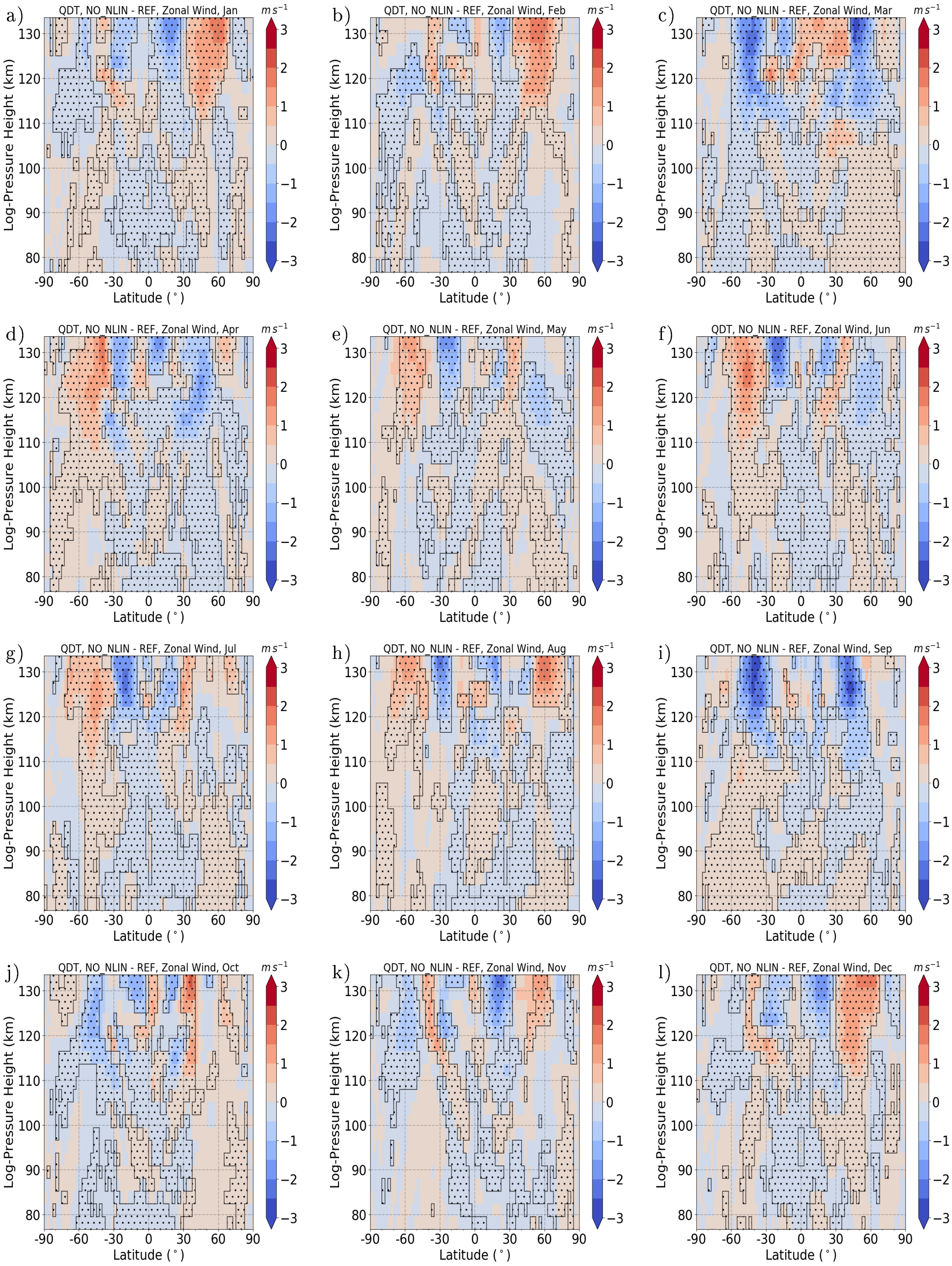

Figure S61.: QDT zonal wind amplitude differences between NO_NLIN and REF run as color. Significance larger than 99% as dotted area.

A.13. Interactions of Different Forcing Mechanisms

A.13.1. Interaction between Nonlinear and Solar Forcing

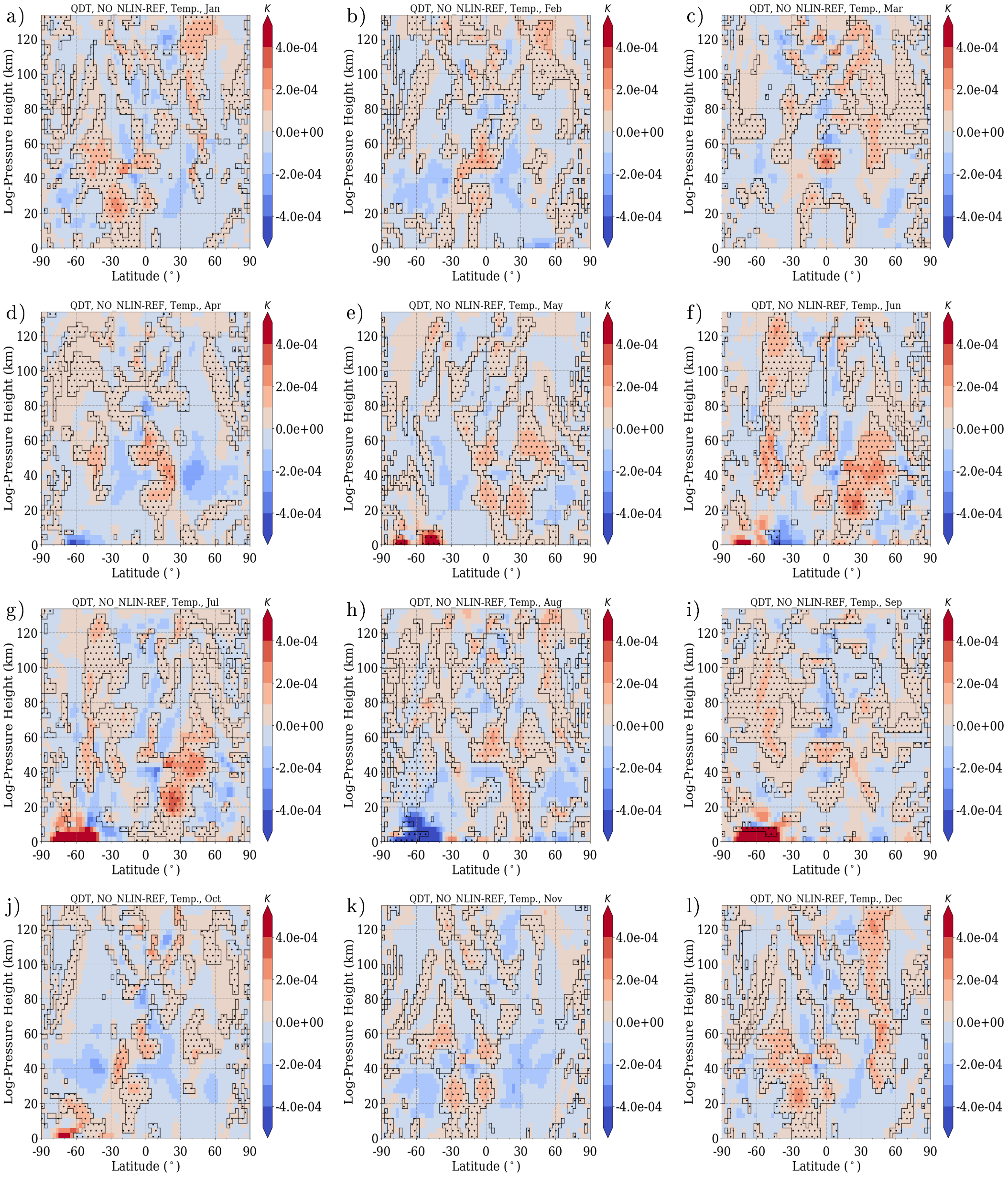

Figure S62.: Difference of QDT temperature amplitudes between NO_NLIN and REF simulation, scaled by density. Areas of destructive interference (120° $\leq$ $\Delta\Phi$ $\leq$ 240°) between NLIN and SOL phases are hatched.

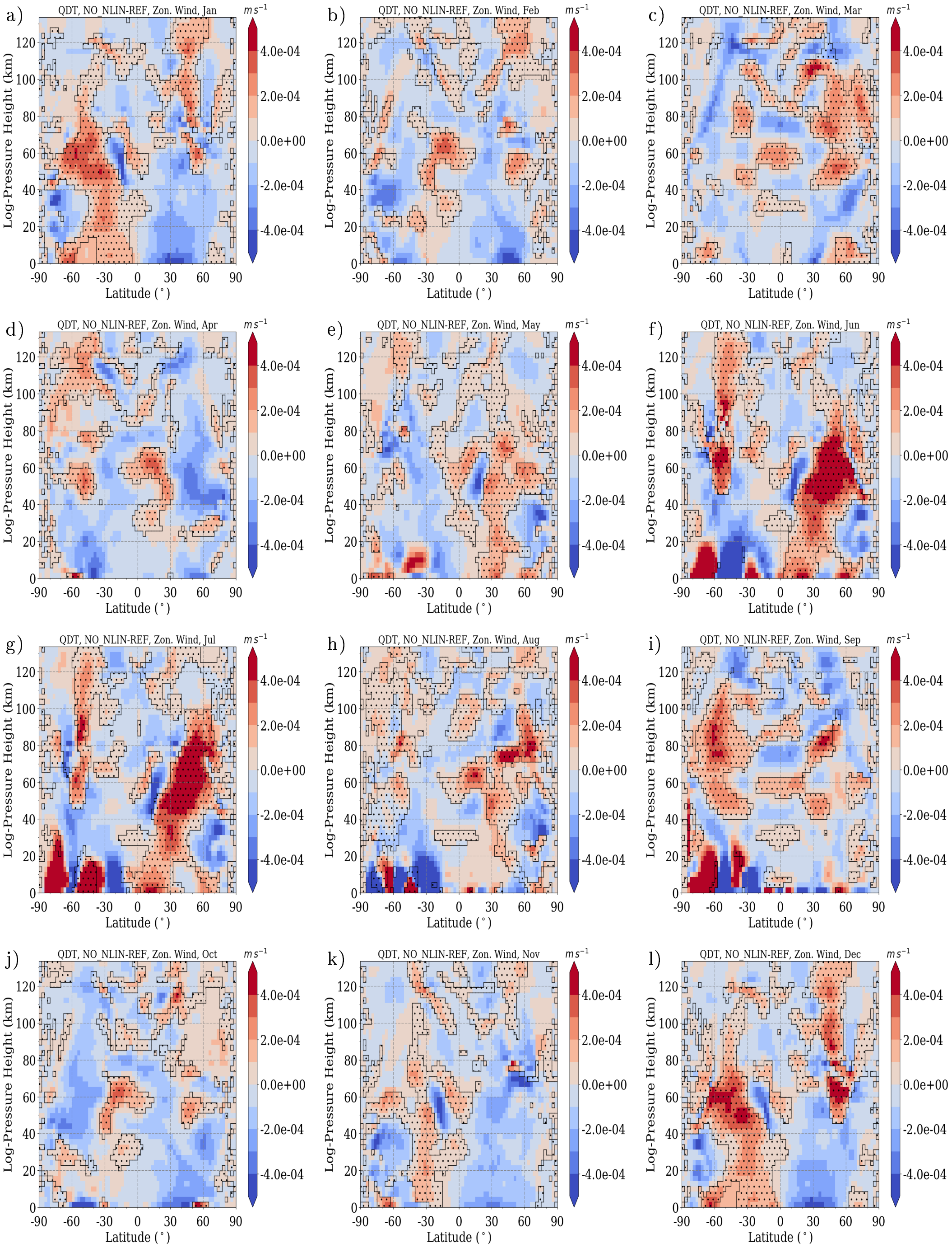

Figure S63.: Difference of QDT zonal wind amplitudes between NO_NLIN and REF simulation, scaled by density. Areas of destructive interference ($120° \leq \Delta\Phi \leq 240°$) between NLIN and SOL phases are hatched.

A.13.2. Interaction between Gravity wave and Solar Forcing

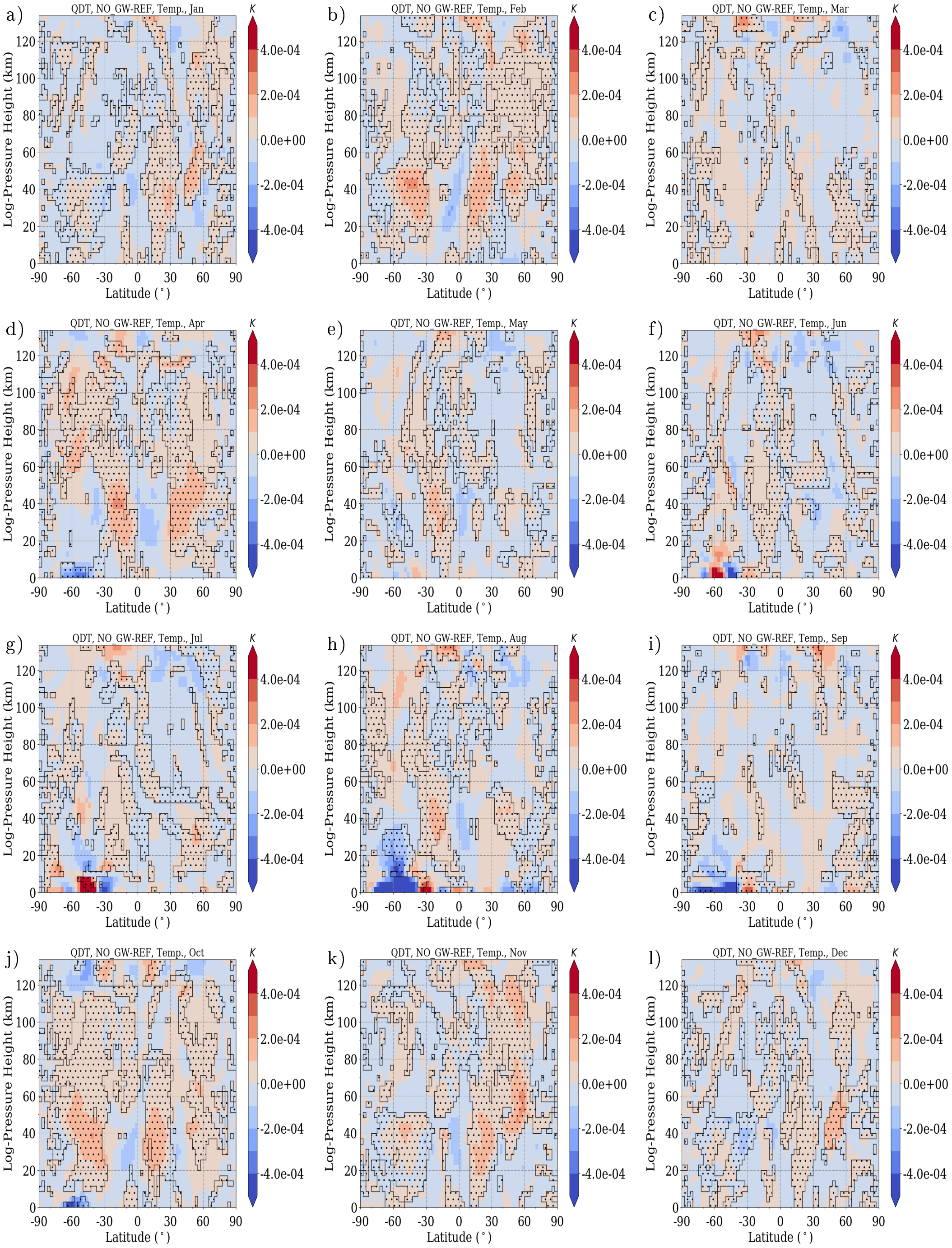

Figure S64.: Difference of QDT temperature amplitudes between NO_GW and REF simulation, scaled by density. Areas of destructive interference ($120° \leq \Delta\Phi \leq 240°$) between GW and SOL phases are hatched.

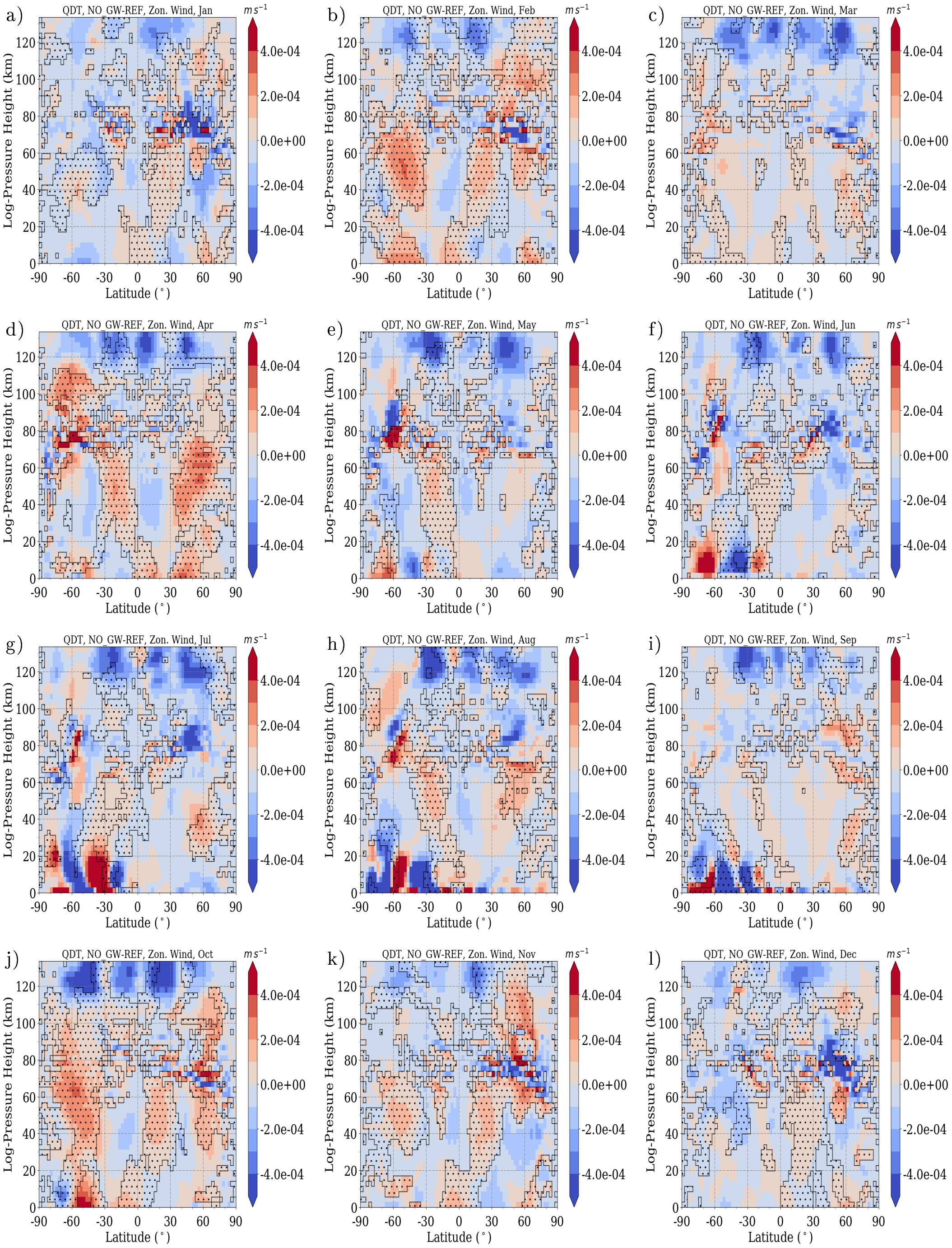

Figure S65.: Difference of QDT zonal wind amplitudes between NO_NLIN and REF simulation, scaled by density. Areas of destructive interference ($120° \leq \Delta\Phi \leq 240°$) between NLIN and SOL phases are hatched.

A.14. Influence of Enhanced Forcing Mechanisms

A.14.1. Influence of Enhanced Solar Forcing Mechanisms

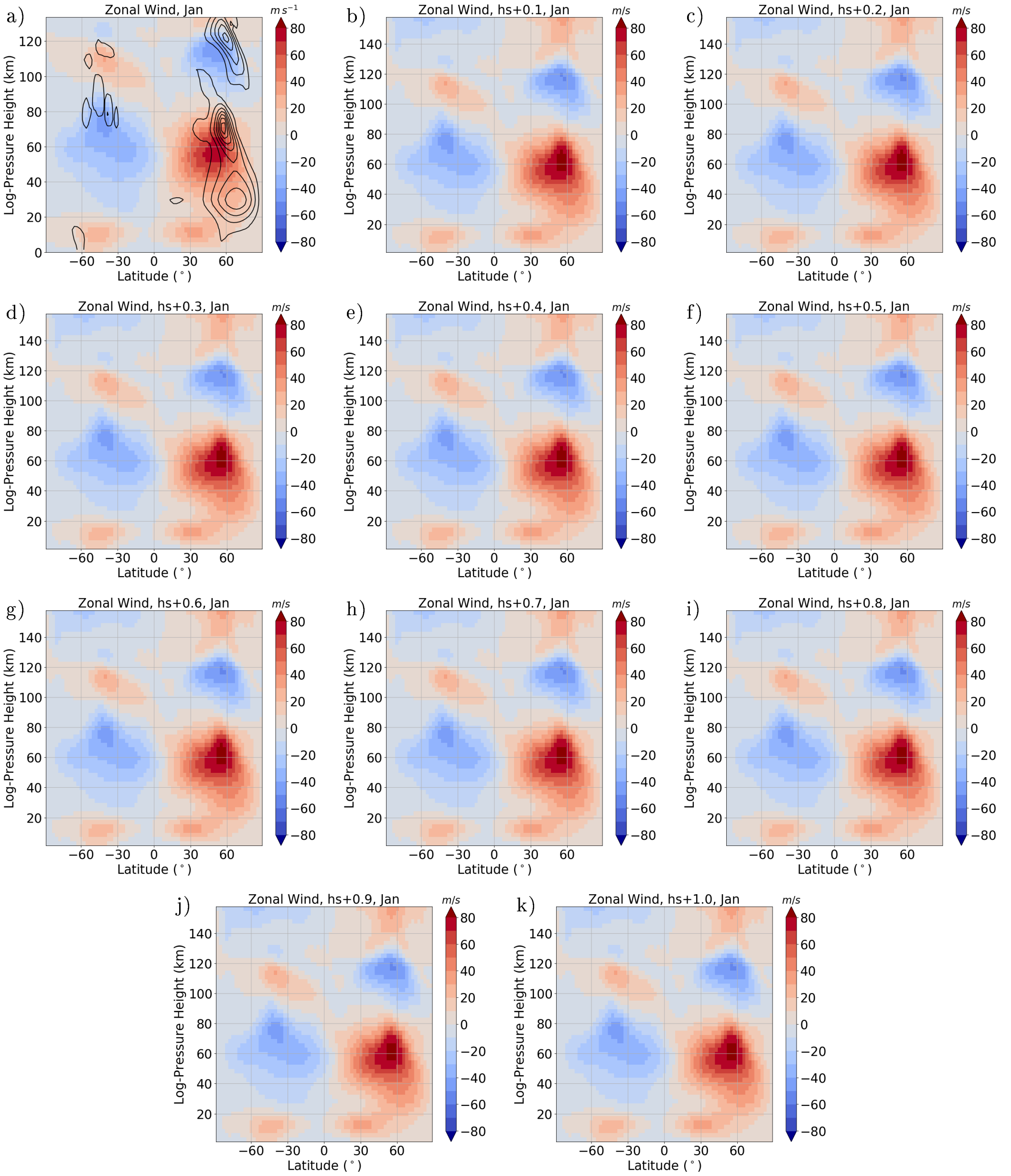

Figure S66.: Zonal wind for January for runs with enhanced solar forcing. In the REF run black lines show the standard deviation from ensemble runs.

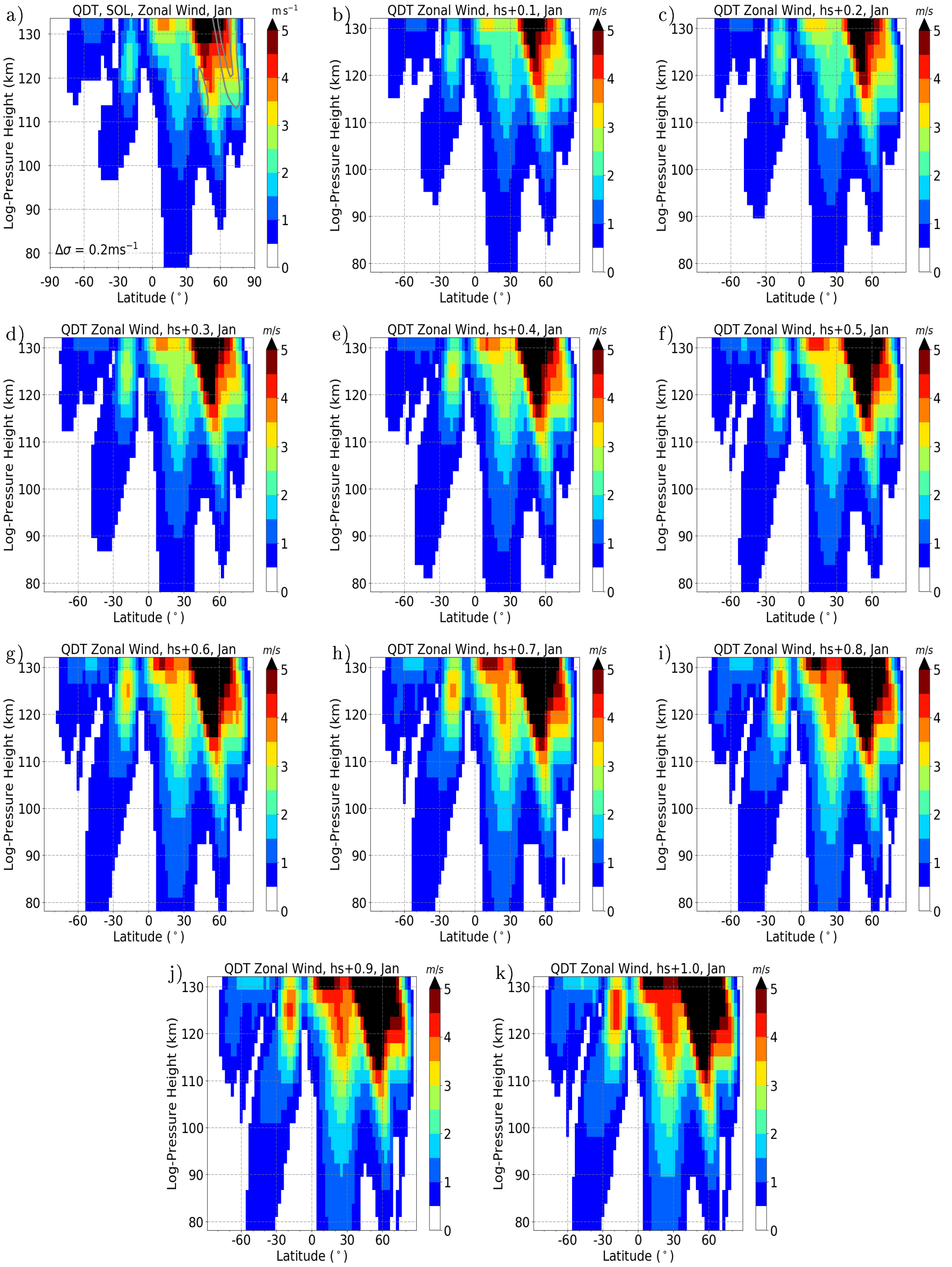

Figure S67.: QDT zonal wind amplitudes for January for runs with enhanced solar forcing. In the REF run black lines show the standard deviation from ensemble runs.

A.14.2. Influence of Enhanced Gravity Wave Forcing Mechanisms

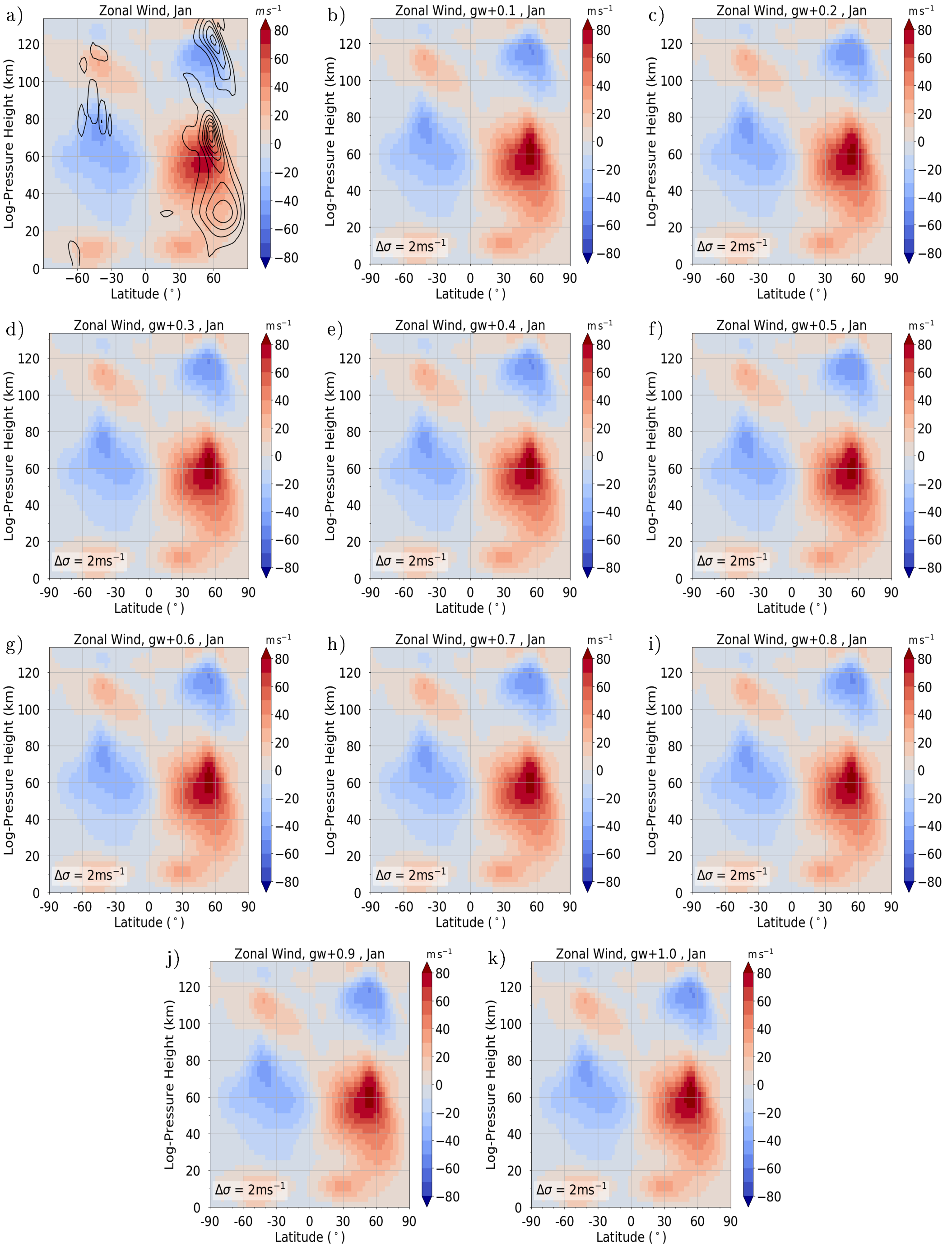

Figure S68.: Zonal wind for January for run with enhanced gravity wave forcing. In the REF run black lines show the standard deviation from ensemble runs.

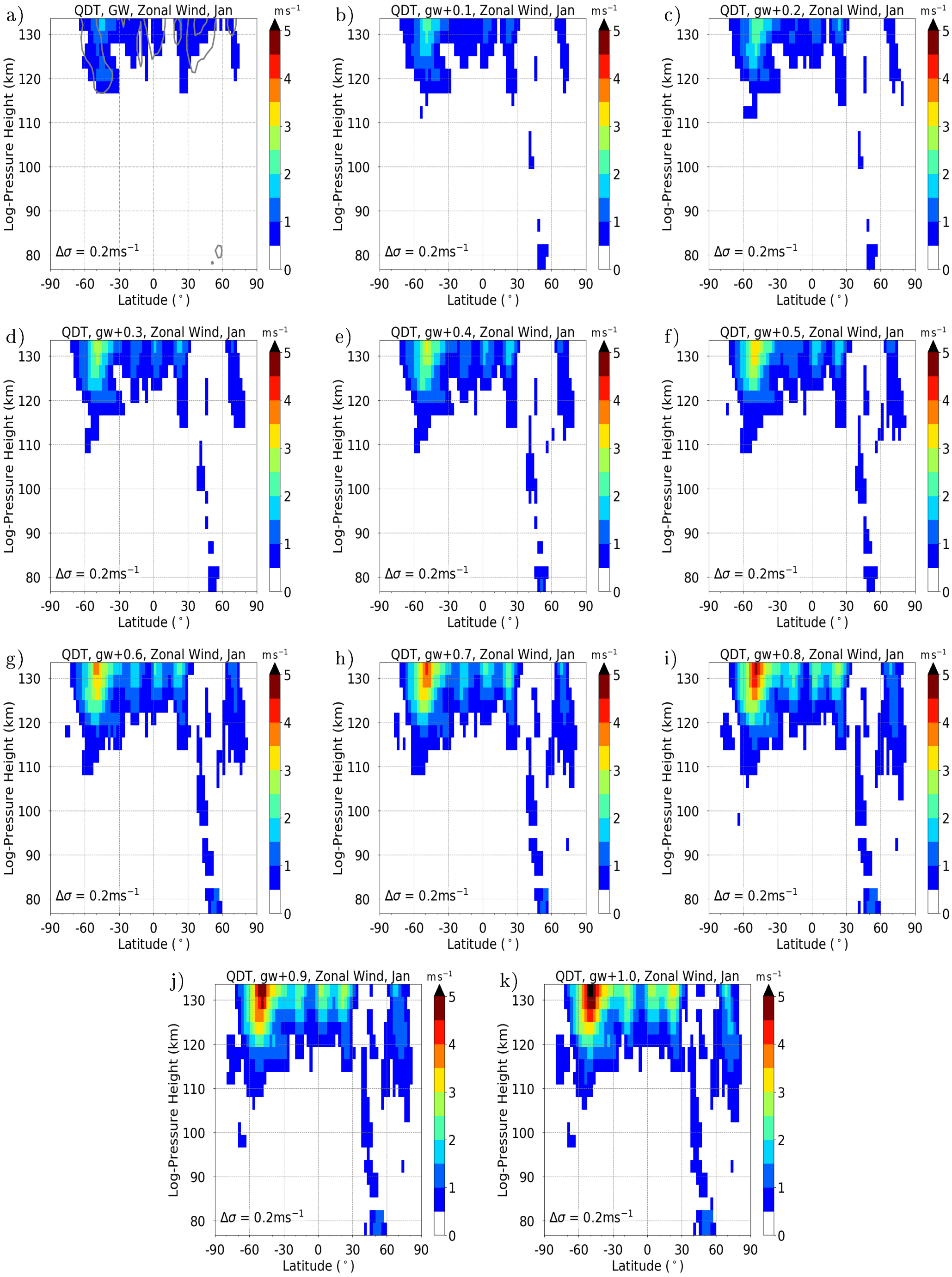

Figure S69.: QDT zonal wind amplitudes for January for run with enhanced gravity wave forcing. In the REF run black lines show the standard deviation from ensemble runs.

A.14.3. Influence of Enhanced Nonlinear Forcing Mechanisms

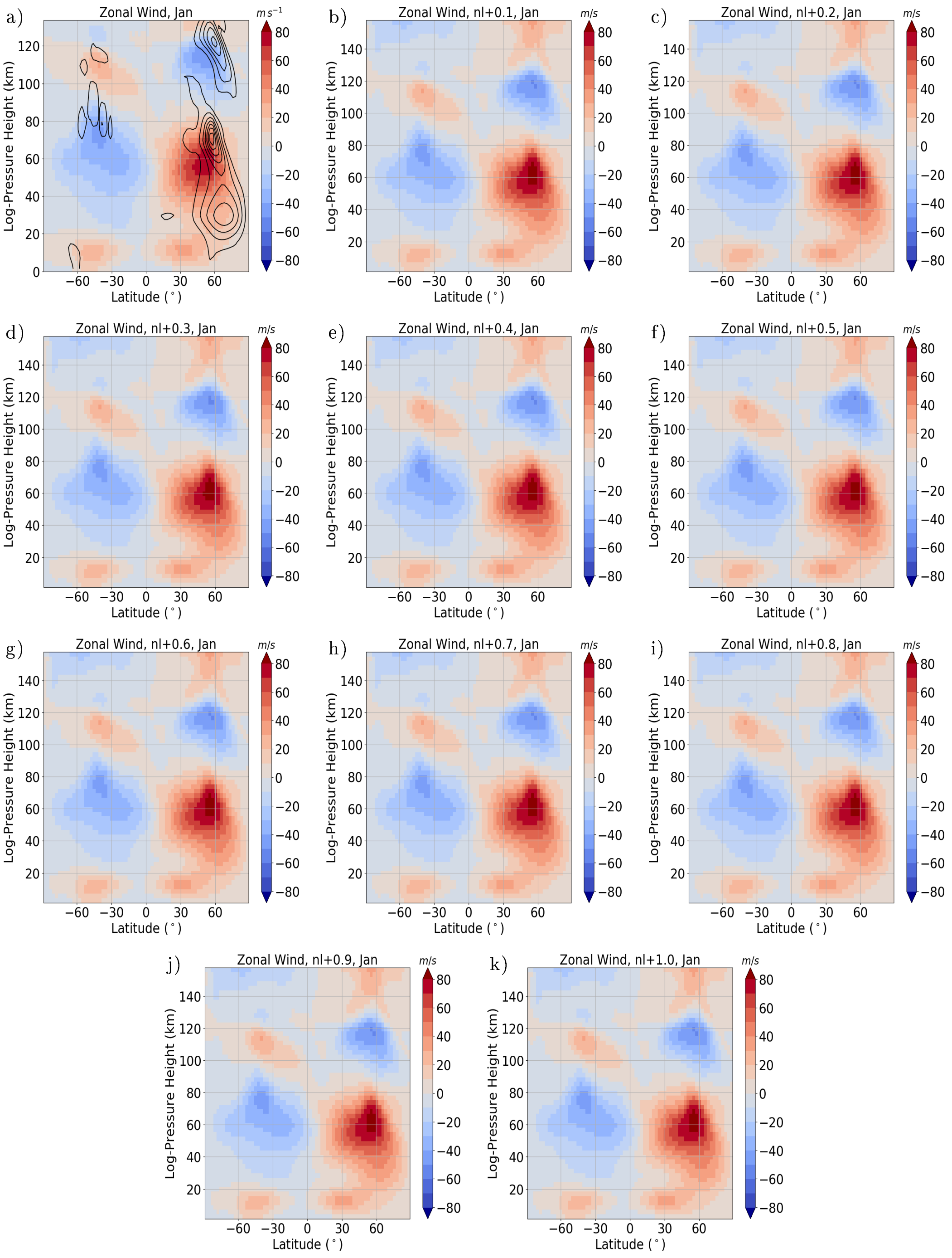

Figure S70.: Zonal wind for January for run with enhanced nonlinear forcing. In the REF run black lines show the standard deviation from ensemble runs.

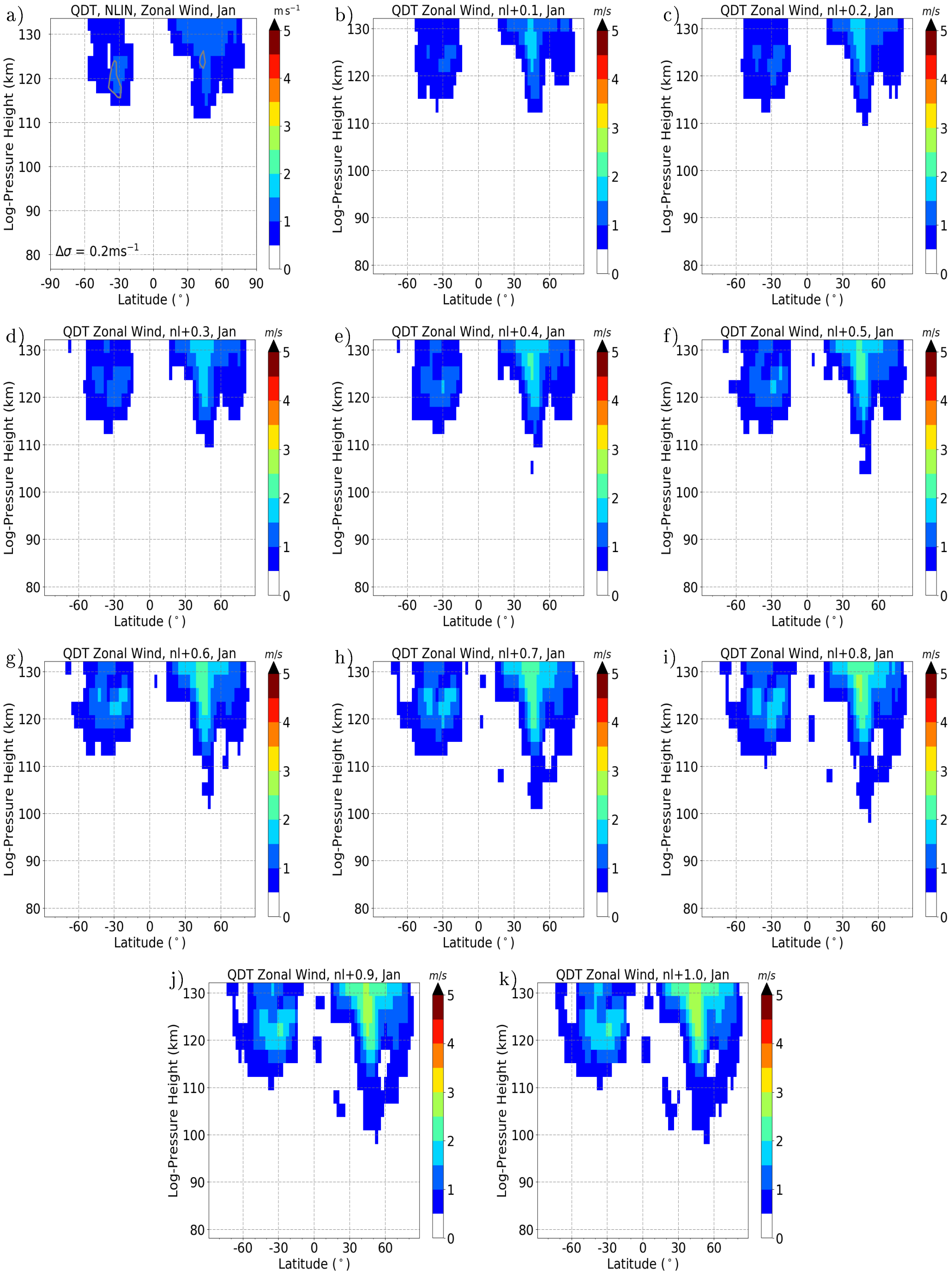

Figure S71.: QDT zonal wind amplitudes for January for run with enhanced nonlinear forcing. In the REF run black lines show the standard deviation from ensemble runs.

Acknowledgements

This project was supported by Deutsche Forschungsgemeinschaft under grant 836/34-1, for which I would like to thank the DFG.

The greatest THANKS go to my supervisor Prof. Dr. Christoph Jacobi for his continuous helpful input and the permanent availability for questions. I would also like to thank him for his comprehensive insight into the scientific work at the university, especially regarding the writing of scientific articles, proposals, networking, teaching and supervising of student, as well as politics at the faculty. This strengthened me in dealing with problems that arose in this direction and prepared me for future tasks.

Furthermore, I would like to thank the whole working group of the middle and upper atmosphere at the Leipzig Institute for Meteorology (LIM), around Friederike, Nadja, Daniel, Rajesh and Ales. The scientific discussion, the help in various problematic situations and the communication in the working group was very helpful, motivating and friendly.

I would also like to thank my family and friends for their moral support and assistance.

I would also like to thank the open source policy of the MERRA-2 project database under the leadership of NASA for the lower boundary conditions and the ozone data, as well as NOAA for the carbon dioxide data from the mauna loa observatory.

Furthermore, I would like to thank Wang et al. (2016) for providing the source code for calculating the theoretical Hough modes according to the Chebyshev method.